The Turbulent Structure of the Jet in Cross-Flow

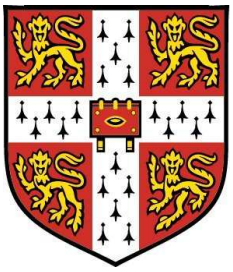

Nicolas Lanitis

Trinity College

University of Cambridge

A thesis submitted for the degree of

Doctor of Philosophy

February 2014

Declaration

This dissertation is the result of my own work and includes nothing which is the outcome of work done in collaboration except where specifically indicated in the text. No parts of this dissertation has already been, or is currently being reviewed for any other degree, diploma or qualification. This thesis contains approximately 50,000 words and 120 figures.

Nicolas Lanitis
February 2014

To my parents Egly and Marios Lanitis.

Acknowledgements

First and foremost I extend my greatest gratitude for the love and support of my parents and two sisters which has been the main driving force behind the completion of this study. I would like to acknowledge the patient guidance, supervision and encouragement I have received from Dr. James Dawson throughout the course of this study. I would also like to acknowledge all members of the fluids group Dr. Tom Clark, Dr. Nicholas Worth, Dr. Lian Gan, Dr. Jose Cardesa-Duenas, Dr. Erdogan Aydemir, John Lawson and Dhiren Mistry for their kind friendship and many discussions which have helped me immensely. This study could not have been completed without the help from Mick Underwood and all other CUED technicians in designing and manufacturing all of the experimental apparatus. I would like to give special thanks to all of my close personal friends whose spiritual support is greatly appreciated. Finally I wish to acknowledge the funding from the Engineering and Physical Sciences Research council, through a Cambridge University Doctoral Training Award.

Abstract

In this thesis the structure of the jet in cross flow in the far field was investigated experimentally using time-resolved, multi-scale and statistically independent Stereoscopic Particle Image Velocimetry measurements to reveal the mean and instantaneous three-dimensional (3D) structures. All of the measurements were performed in the Counter-rotating Vortex Pair (CVP) plane for a high velocity ratio and jet Reynolds number. Statistical measurements at various downstream locations and velocity ratios are presented. Probability density functions of the streamwise vorticity field showed that each CVP core is instantaneously made of a number of small vortex tubes rather than a single vortex core. The characteristic 'kidney' shape was illustrated in the rms velocity profiles and the Reynolds stress profiles exhibited a high level of organisation which showed an evolving shape with downstream distance and persisted well into the far field. Two point spatial correlations pointed to a common structure for all conditions whose mean shape generates the 'kidney' shape, as well as evidence of wake structures. Time-resolved measurements were carried out in a moving and stationary frame of reference, converted to 3D measurements via the use of Taylor's hypothesis. The origin of the 'kidney' shape and large degree of spatial order in the far field was found to be a result of an organised 'train' of consecutive hairpin, roller and wake structures. Together, these structures provide a physical explanation that reconciles the statistical and instantaneous structure of the CVP.

Contents

List of Figures

Nomenclature

Roman Symbols

$\dot{m}$	Mass flow rate
$\hat{\mathbf{e}}$	Unit vector
$\mathbf{A_r}$	Reduced velocity gradient tensor
$\mathbf{A}$	Velocity gradient tensor
$\mathbf{U}$	Velocity vector
$\mathbf{x}$	Position vector
$\mathcal{P}$	Production of TKE
ρ_p	Mean particle density
A, m	Trajectory scaling constants
c	Wave propagation speed
C'	Concentration fluctuation
C_d	Discharge Coefficient
$C_{U_iU_j}$	Spatially averaged velocity correlation
d_τ	Particle image diameter
d_i	Nozzle inlet diameter

d_j Nozzle/Jet exit diameter

d_k Turbulent transport terms of TKE equation

d_o Orifice diameter

d_p Mean particle diameter

DT Time between vector fields

dt Time between image pairs

$f/\#$ 'f-number' aperture setting

f Longitudinal velocity correlation function

f_{cam} Camera frame-rate

f_c Flow coefficient

f_s Sampling frequency

J Momentum ratio

k Turbulent kinetic energy

l Global length-scale

$l_{1/2}$ Half-width at half maximum

L_{int} Integral length-scale

L_n Nozzle profile length

l_{turb} Characteristic turbulent length scale

m, n Sample index

N Number of samples

P Pressure

P, Q, R Topological Invariants of velocity gradient tensor

p' Fluctuating pressure

Q Correlation coefficient

q Recorded vector field index

R Core spacing

$R_{u_i u_i}$ Velocity correlation function

Re Reynolds number

Re_Γ Circulation Reynolds number

Re_{cf} Cross-flow Reynolds number

Re_{crit} Critical Reynolds number

Re_j Jet Reynolds number

Re_{turb} Characteristic turbulent Reynolds number

s Length along jet centreline

s_x^2 Sampling variance multiplied by N

s'_{ij} Strain rate tensor of fluctuating velocities

S_{ij} Strain rate tensor

St Stokes number

T Sampling Time

t Time

T_{int} Integral time-scale

t_{turb} Characteristic turbulent time scale

U, V, W Instantaneous velocity components

u', v', w' Fluctuating velocity components

u_η Kolmogorov velocity scale

U_Γ Induced velocity magnitude

U_∞ Cross-flow velocity

U_c Convection velocity

U_{jet} Jet velocity

u_{turb} Characteristic turbulent velocity

U_t Towing speed

V_r Velocity ratio

x, y, z Cartesian Coordinates

x_{bp} Branch point x-location

Greek Symbols

β Orifice to pipe diameter

Δp Pressure drop across orifice

Δt Time between vector fields in Taylor reconstruction

δt Temporal spacing

δx, δy, δz Grid spacing

δ_{ω_c} Jet width (distance between vorticity centroids)

δ_ω Jet width (distance between 5% peak values)

ϵ Uncertainty

Γ Circulation

κ Wave number

Λ Viscous to Kolmogorov length scale ratio

λ Taylor microscale

λ_κ, η Kolmogorov length scale

λ_ν Viscous length scale

λ_{ci} Swirling Strength

λ_p Measurement resolution

μ_x True mean

ν Viscosity

Ω Enstrophy

ω Vorticity

ω_{0+} Peak positive vorticity

ω_{0-} Peak negative vorticity

ϕ Scheimpflug angle

ρ Density

τ_η Kolmogorov time scale

τ_f Flow time-scale

τ_p Seeding particles response time

θ Stereo camera angle

ε Dissipation rate of TKE

ϱ Temporal autocorrelation coefficient

Superscripts

$(\cdots)'$ Fluctuation

Subscripts

$_{iso}$ Iso-surface

$_{i,\ j,\ k}$ Index

$_{max}$ Maximum

$_{x,\ y,\ z}$ Cartesian component

Other Symbols

$\overline{(\cdots)}$ Mean

$det[\cdots]$ Determinant of matrix

$tr[\cdots]$ Trace of matrix

Acronyms

$2D-3C$ Two Dimensional - Three Velocity Component

CVP Counter Rotating Vortex Pair

FoV Field Of View

IW Interrogation Window

$JICF$ Jet In Cross-Flow

$LFoV$ Large-scale Field of View

PIV Particle Image Velocimetry

$PLIF$ Planar Laser Induced Fluorescence

$SFoV$ Small-scale Field of View

TT Tow Tank

VGT Velocity Gradient Tensor

WC Water Channel

$SPIV$ Stereoscopic Particle Image Velocimetry

Introduction

The Jet in a Cross Flow (JICF) has been studied for many years due to its fundamental significance as a turbulent flow as well as its widespread environmental and engineering applications. The JICF, as the name suggests, consists of a jet issuing at an angle into a cross flow. There are many variations of the JICF, depending on the area of application. Examples include different nozzle exit shapes (circular, elliptical and square), the jet issuing perpendicularly or at an angle to the cross flow and the jet exit being flush to the surface or extruding into the flow. They are widely used in effusion cooling applications where cooling films are formed to keep surface temperatures below critical values. Initial interest in this flow, dates back to 1932 [38]. Environmental applications, where thermal plumes rise into the atmosphere where a significant cross-flow can exist, include erupting volcanoes and chimney stacks from industrial plants. The latter formed a necessity to study the cross flow jet from the desire to predict the path and concentration field of contaminants at a given distance downstream. Other applications of the JICF include the area of aerodynamics with Vertical and/or Short TakeOff/Landing (V/STOL) aircrafts and thrust vector control (control of missiles and rockets). Research in this area was related with the cross sectional shape, the trajectory and the induced forces on the aircraft. Finally, and very importantly, the JICF is used in mixing applications such as air dilution jets (figure 1b) and fuel injectors in gas turbine engines, due to its suggested superior mixing properties when compared to a normal jet issuing into a quiescent flow [9, 32, 38, 57, 58].

One of the most important features of the cross flow jet is the creation of a Counter Rotating Vortex Pair in the far field of the flow, after the jet is bent along the cross-flow direction. In the early years, research concentrated on quali-

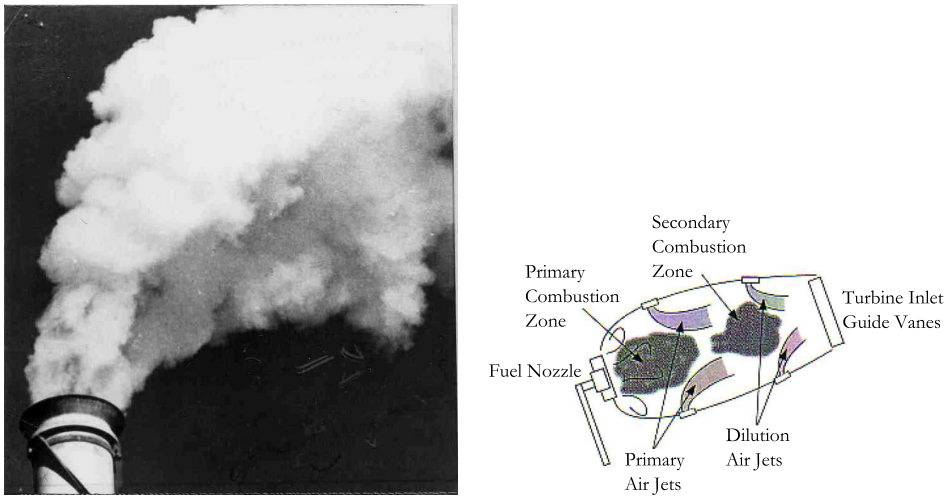

(a) (b)

Figure 1: Examples of applications of a JICF. (a) Chimney stack. (b) Schematic of air dilution system. Taken from Karagozian [32].

tative measurements of the cross flow jet using flow visualization to look at the jet trajectory and structures that existed within the the different regions of the flow. Early experiments with pressure probes measurements and hot wire anemometry, gave access to the mean velocity field and showed the existence of the counter rotating vortex pair in the cross-plane far field [22]. Due to the complexity of the flow, a number of researchers tried to model the flow using various techniques [9, 22]. The most notable one is the one by Broadwell & Breidenthal [9] who modelled the average field as a pair of counter rotating vortex lines which form due to the momentum impulse of the jet on the cross-flow, similar to the one that appear off the tips of an aircraft wing. With the introduction of laser techniques, Particle Image Velocimetry (PIV) and Planar Laser Induced Fluorescence (PLIF) researchers began to look at the evolution of the near field and the mechanisms involved in the formation of the CVP [33, 37, 44]. A large amount of work, especially during the 1990s, was dedicated to understand the process by which the jets deforms and rolls-up into a CVP. Interestingly, it is only recently that researchers have began to look at the mixing field by studying the scalar concentration field and the turbulent velocity field in various cross sectional planes

measuring Reynolds fluxes and scalar probability distribution functions for various boundary conditions [57, 58, 59]. Perhaps this was because the techniques and equipment to do so have only recently become available. Performing such measurements and trying to understand what they imply for the turbulent mixing field has proven a difficult task.

It is true that the JICF is central to a number of problems and has a very widespread area of application. This alone justifies the amount of research taking place. However it must not be forgotten that the flow itself is turbulent and is not fully understood yet, in particular the turbulent structure of the CVP. The addition of the evolution and presence of the CVP makes this flow even harder to understand. Turbulent flows are not purely random and are known to contain coherent structures which interact with each other from the large-scales down to the small-scales, known as turbulent eddies. With the most recent advancements of PIV, such as Stereoscopic PIV and Tomographic PIV, it is now possible to measure the three dimensional (3D) velocity field and in some cases allows the full 9-component velocity gradient tensor to be extracted. This contains all the information about the deformation (rotation and stretching) of fluid elements within the turbulent field. This gives the opportunity to measure the turbulent structure of the JICF similar to the studies by Adrian *et al.* [2], Hutchins *et al.* [30], Elsinga *et al.* [20] and Dennis & Nickels [18] which give insight into the structure of turbulent boundary layers.

One of the main applications of the JICF that is often cited is that it is a superior configuration for mixing applications. Here the reference is the round jet. This formed, and still forms, one of the main drives for research in the quest to try and understand why. The literature of the JICF spans almost a century, however despite this there is very little work dedicated to try and understand the fundamental turbulent field of the cross flow jet. It is therefore important to do so from a scientific point of of view which can then be extended to practical applications. Therefore the aim of the current investigation is to study the large-scale turbulent field structure of the JICF, predominantly in the far field, for a high velocity ratio and jet Reynolds number via a series of experiments using the technique of Stereoscopic PIV. The simplest case of a round jet flush with the wall surface and injected normally into a cross-flow of the same fluid is consid-

ered. Both statistically independent measurements and high-speed time resolved measurements were undertaken to understand the turbulent structure from both a statistical and structural point of view. This leads to new information that would help further develop models for the far field like the one from Broadwell & Breidenthal [9]. Furthermore, knowledge of the turbulent structure could help in understanding the reason why the JICF has superior mixing properties as well as turbulent mixing in general.

Chapter 1 presents a literature review for the JICF, describing the findings from previous studies in different areas of the flow and the methods used to study the turbulent field. Chapter 2 describes the experimental apparatus and methods used in the current investigation. The following two chapters present the results from the measurements. Chapter 3 focuses on the mean flow properties of the CVP plane, whereas the results from the 3D reconstructions are presented in chapter 4 identifying what structures the JICF is comprised of. The thesis finishes with chapter 5 which contains a summary and conclusions from the current investigation before outlining future work.

Chapter 1

Literature Review

1.1 Overview

This chapter introduces a literature review relevant to the current study. This includes previous research on the Jet in Cross-Flow (JICF) and techniques used to study turbulent flows. Important nomenclature is firstly introduced which help to characterise the flow as well as an introduction to the overall structure of the JICF. The chapter ends with a summary of the literature review and the main objectives of the thesis.

1.2 Governing Equations

The Continuity equation (conservation of mass) and Navier-Stokes equation (conservation of momentum) governing the instantaneous motion of an incompressible, isothermal Newtonian fluid parcel in the absence of body forces, written in tensor notation for brevity, are given by:

$$\frac{\partial U_i}{\partial x_i} = 0 \tag{1.1}$$

$$\frac{\partial U_i}{\partial t} + U_j \frac{\partial U_i}{\partial x_j} = -\frac{1}{\rho}\frac{\partial P}{\partial x_i} + \nu \frac{\partial^2 U_i}{\partial x_j \partial x_j}, \tag{1.2}$$

where ρ is the density, P is the pressure and ν is the kinematic viscosity. Repeated indices indicate a summation, and the *i-th* component of the position vector $\mathbf{x}$ and

velocity vector **U** are defined in a three-dimensional (3D), orthogonal coordinate system. The left hand side of the Navier-Stokes equation 1.2 is the material derivative, which can be denoted by $D(\mathbf{.})/Dt$, which gives the rate of change of a quantity, in this case a velocity component, associated with a fluid element moving through a flow field. A complete solution of the left hand side would require knowledge of the complete velocity gradient tensor (VGT):

$$\mathbf{A} = \frac{\partial U_i}{\partial x_j}. \tag{1.3}$$

To study the turbulent field a Reynolds decomposition is carried out by by splitting the flow into a mean and fluctuating component:

$$U_i(\mathbf{x}, t) = \overline{U_i(\mathbf{x}, t)} + u'(\mathbf{x}, t) \tag{1.4}$$

$$P(\mathbf{x}, t) = \overline{P(\mathbf{x}, t)} + p'(\mathbf{x}, t). \tag{1.5}$$

Applying this decomposition to equation 1.1 and 1.2 and averaging gives the Reynolds averaged equation:

$$\frac{\partial \overline{U}_i}{\partial x_i} = 0 \tag{1.6}$$

$$\frac{\partial \overline{U}_i}{\partial t} + \overline{U}_j \frac{\partial \overline{U}_i}{\partial x_j} = -\frac{1}{\rho}\frac{\partial \overline{P}}{\partial x_i} + \nu \frac{\partial^2 \overline{U}_i}{\partial x_j \partial x_j} - \frac{\partial \overline{u_i' u_j'}}{\partial x_j}. \tag{1.7}$$

The differential in the last term on the right hand side of the Reynolds averaged momentum equation 1.7, after multiplying both sides by ρ, $-\rho\overline{u_i' u_j'}$ is the Reynolds stress, representing the flux of *i-th* momentum in the *j-th* direction by a velocity fluctuation in the *j-th* direction. However the term $\overline{u_i' u_j'}$ is also referred to as the Reynolds stress [51]. Furthermore, subtracting equation 1.6 from equation 1.1 shows that:

$$\frac{\partial u_i'}{\partial x_i} = 0. \tag{1.8}$$

The governing equation for the turbulent kinetic energy per unit mass $k = (1/2)\overline{u_i' u_i'}$ is obtained by subtracting the Reynolds average equation (1.7) from

the Navier-Stokes equation (1.2), multiplying by u_i' and finally averaging to give:

$$\frac{\partial k}{\partial t} + \overline{U}_j \frac{\partial k}{\partial x_j} = -\frac{1}{\rho}\frac{\partial \overline{u_j' p'}}{\partial x_j} - \frac{1}{2}\frac{\partial \overline{u_i' u_i' u_j'}}{\partial x_j} + 2\nu \frac{\partial \overline{u_i' s_{ij}'}}{\partial x_j} - \overline{u_i' u_j'}\,\overline{S}_{ij} - 2\nu \overline{s_{ij}' s_{ij}'}. \quad (1.9)$$

The term S_{ij} is the strain-rate tensor which is also split into a mean and fluctuating component, $\overline{S}_{ij} = (1/2)(\partial \overline{U}_i/\partial x_j + \partial \overline{U}_j/\partial x_i)$ and $s_{ij}' = (1/2)(\partial u_i'/\partial x_j + \partial u_j'/\partial x_i)$. The left hand side of equation 1.9 represents the change of TKE moving through a flow field, both in space and time. This is an important equation as it introduces the origin of two important quantities, namely the production and dissipation of TKE, which will be used further on. The right-hand side can be split into three main parts:

$$d_k = -\frac{1}{\rho}\frac{\partial \overline{u_j' p'}}{\partial x_j} - \frac{1}{2}\frac{\partial \overline{u_i' u_i' u_j'}}{\partial x_j} + 2\nu \frac{\partial \overline{u_i' s_{ij}'}}{\partial x_j} \quad (1.10)$$

$$\mathcal{P} = -\overline{u_i' u_j'}\,\overline{S}_{ij} \quad (1.11)$$

$$\varepsilon = 2\nu \overline{s_{ij}' s_{ij}'}, \quad (1.12)$$

The three terms in the group d_k represent the turbulent transport of TKE by pressure gradient work by the pressure fluctuations, turbulent diffusion and molecular diffusion respectively which redistribute energy in the flow. The second term $\mathcal{P}_k$ represents the production of TKE where the action of the Reynolds stresses $\overline{u_i' u_j'}$, on the mean velocity gradients, which are usually of opposite sign, serves as a source. The last term ε is the viscous dissipation of TKE, and from its definition it can be seen that it is always non-negative and thus acts as a sink.

Turbulent flows cover a very wide range of length-scales, ranging from the large-scales which are of the order of the width of the flow, down to the smallest scales where dissipation takes place. The following definitions are made by considering statistically stationary (i.e mean quantities do not change with time), homogeneous isotropic turbulence. The *large-scale eddy length-scale* l_{turb} is of the order of the width of the flow, i.e the size of the largest eddy. Using a characteristic turbulent velocity defined as $u_{turb} = \sqrt{2k/3}$, a *large-scale eddy-turnover time* can be defined as $t_{turb} = l_{turb}/u_{turb}$, which is a representation of the lifetime of a large eddy. An *integral time-scale* can be defined through the autocorrelation

coefficient

$$\varrho(\tau) = \frac{\overline{u_i'(t)u_i'(t+\tau)}}{\overline{u_i'^2}}, \tag{1.13}$$

which ranges between -1 and 1, and τ represents a time delay. For stationary turbulence, the time t is arbitrary. The integral time-scale is obtained by integrating the autocorrelation coefficient as shown in equation 1.14, which gives a time-scale over which the velocity component remains correlated.

$$T_{int} = \int_0^\infty \varrho(\tau)\,\mathrm{d}\tau \tag{1.14}$$

From this an *integral length-scale* can be obtained from $L = \sqrt{\overline{u_i'^2}}T_{int}$. However the integral length scale is more often defined as the length scale extracted from the longitudinal velocity correlation function:

$$f(r) = \frac{\overline{u_1'(\mathbf{x})u_1'(\mathbf{x}+\hat{\mathbf{e}}_\mathbf{1}r)}}{\overline{u_1'^2}}, \tag{1.15}$$

where $\hat{\mathbf{e}}_\mathbf{1}$ is a unit vector in the x_1 direction, and r is the length between the two points in space. The integral length-scale is obtained by integrating $f(r)$, as shown in equation 1.16, which gives a measure of the extent of the region over which the velocities remain correlated.

$$L_{int} = \int_0^\infty f(r)\,\mathrm{d}r \tag{1.16}$$

The *Taylor microscale* λ is defined by:

$$\overline{\left(\frac{\partial u_1'}{\partial x_1}\right)^2} = \frac{u_{turb}^2}{\lambda^2}. \tag{1.17}$$

It is also associated with the curvature of the velocity correlation function 1.15 near $r = 0$, and lies somewhere between the integral length scale L_{int} and the smallest scales of turbulence, the *Kolmogorov length-scale* [16, 51].

The characteristic length-scale associated with the smallest turbulent motion, at which viscous dissipation takes place, is defined as the *Kolmogorov* length-

scale given by equation 1.18, with the associated time and velocity-scale given by equations 1.19 and 1.20 respectively. These equation are derived from the argument that the small scales would only depend on the dissipation ε, assumed to be equal to the rate of supply of energy from the large scales, and the viscosity ν [61]. These quantities are important as they are used later on to assess aspects of the experimental measurements.

$$\eta \equiv \left(\frac{\nu^3}{\varepsilon}\right)^{1/4} \tag{1.18}$$

$$\tau_\eta \equiv \left(\frac{\nu}{\varepsilon}\right)^{1/2} \tag{1.19}$$

$$u_\eta \equiv (\nu\varepsilon)^{1/4} \tag{1.20}$$

In the following chapters the symbol λ_κ is used to denote the Kolmogorov length-scales, instead of η, for consistency with other symbols in the related analysis.

1.3 The Structure of a Jet in Cross-Flow

The cross flow jet can be split up into three main areas. The near field (close to the exit of the jet), the far field (after the jet has turned into the cross flow) and the wake (the area between the jet and the wall). The complex interaction between the cross-flow and the jet leads to the formation of different vortical structures in each of these areas, as can be seen in figure 1.1. A Cartesian coordinate system is used, with streamwise direction $x_1 = x$, spanwise direction $x_2 = y$, wall-normal direction $x_3 = z$ and corresponding velocity components $U_1 = U$, $U_2 = V$, $U_3 = W$. The near field is dominated by jet shear layer vortices, the far field by a Counter-rotating Vortex Pair (CVP), and the wake by a horseshoe vortex and upright vortices, also known as wake structures. The region of the near field and far field are not strictly defined in the literature and different authors use different definitions. However, the general consensus is that the near field is the region where the CVP develops and the far field is the region where the CVP is fully developed [58].

There are two main parameters used to characterise the cross flow jet. One is the momentum flux ratio J, defined as the ratio of the jet momentum to the

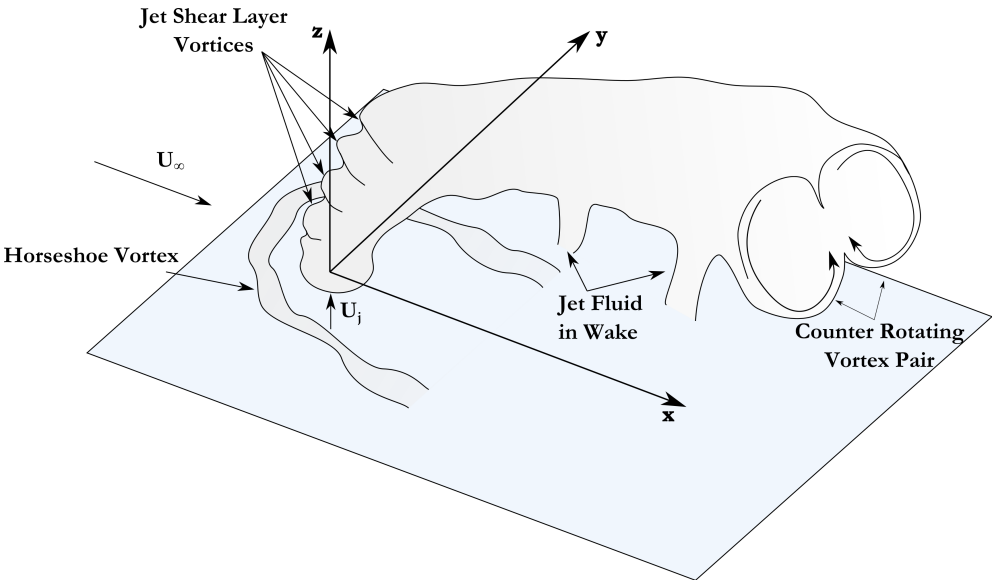

Figure 1.1: Schematic of a Jet in a cross flow depicting the dominant vortical structures.

crossflow momentum. For flows where the jet fluid and the cross-flow fluid are the same and hence have the same density the momentum flux ratio reduces to the velocity ratio V_r, which is the most commonly used parameter to describe the cross-flow jet in literature. These are defined as:

$$\text{Momentum Ratio:} \quad J = \frac{\rho_j U_{jet}^2}{\rho_\infty U_\infty^2} \tag{1.21}$$

$$\text{Velocity Ratio:} \quad V_r = \frac{U_{jet}}{U_\infty} \tag{1.22}$$

where ρ_j is the jet fluid density, U_{jet} is the jet exit bulk velocity, ρ_∞ is the cross-flow fluid density and U_∞ is the cross-flow velocity.

The second parameter is the jet Reynolds number, or sometimes the cross flow Reynolds number:

$$\text{Jet Reynolds number:} \quad Re_j = \frac{U_{jet} d_j}{\nu} \tag{1.23}$$

$$\text{Cross-Flow Reynolds number:} \quad Re_{cf} = \frac{U_\infty d_j}{\nu} \tag{1.24}$$

where ν is the kinematic viscosity.

From the image of figure 1.1 it can be easily seen that one of the main issues in performing research on a cross flow jet is that it is a highly dynamic 3D flow. In such cases, where complicated 3D flows are under investigation, it is very hard to study the whole field at once. As a result different parts of such flow fields are studied depending on the area of application or interest. Indeed over the years different researchers have focused on different areas of the JICF according to the field they were involved in. Furthermore, advances in experimental techniques allow researchers to access more information about the flow which was previously inaccessible. The literature review will be presented in terms of the different areas and aspects various researchers have looked at starting with the vorticity field structure.

1.3.1 The Near Field

How the near field of the jet evolves into a counter rotating vortex pair in the far field has received considerable attention as it is one of the most striking features of the flow. The near field, otherwise known as the developing region, is defined as the region close to the jet exit (after the potential core which is approximately 5 jet diameters) where the CVP is developing. Early research on the mechanism of formation of the CVP includes work from Moussa *et al.* [42] and Coelho & Hunt [14]. Both concluded that the CVP is formed from the thin vortex sheet (shear layer) that emanates from the nozzle exit which, as shown in figure 1.2b, rolls up creating vortex rings which are swept with the cross-flow at different rates thus being deformed and bundled into the CVP.

Kelso *et al.* [33] studied the evolution of the jet in more detail using flow visualization and flying-hot-wire experiments for Velocity ratios ranging from 2 to 6 and Re_{cf} numbers ranging from 440 to 6200. Kelso *et al.* [33] suggest that the formation of the CVP is a result of two processes. First is the shear layer roll up of the upstream side of the jet like a Kelvin-Helmholtz instability (which was observed for all velocity ratios studied), illustrated by dye visualisations as shown in figure 1.2a. At Re_{cf} values above 940 the authors postulate that vortex rings resulting from this roll up are shed near the exit of the jet, much like the case of

a free jet, and that this roll-up contributes to the enhanced entrainment of the JICF. In the second process the side and downstream part of the shear layer (lee side of the jet) folds to begin forming the CVP. The proposed mechanism for the formation of the CVP, which is the superposition of these two processes, is shown in figure 1.2b. The vortex rings emanating from the pipe initially roll up like a Kelvin Helmholtz instability. The upstream plane of the jet ring tilts with the mean curvature of the jet, remaining perpendicular to it. The downstream plane aligns itself with the direction of the jet so that the sides of the ring contribute to the vorticity of the CVP.

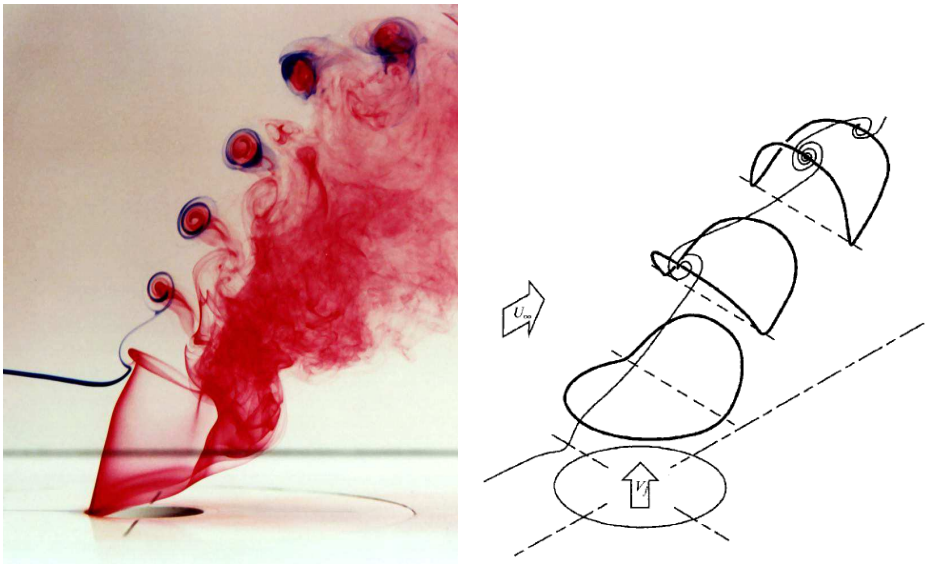

(a) Kelvin Helmholtz roll up

(b) Suggested near field evolution mechanism

Figure 1.2: Near field jet evolution results of Kelso *et al.* [33]

Cortelezzi & Karagozian [15] performed inviscid numerical simulations by modelling the flow using three-dimensional (3D) vortex filaments to characterise the generation and evolution of the vorticity field. The velocity ratios studied varied from 2 to 12 with emphasis on the $V_r = 5.4$ case. Their results agree with the proposed mechanism of Kelso *et al.* [33]. The authors conclude that the formation of the folded rings begins with the initial roll up of the jet shear layer forming a starting vortex ring. The folding on the lee side of this first vortex

ring then triggers the roll-up of the cylindrical vortex sheet which starts the formation of a second ring. The secondary ring also undergoes the folding process thus triggering the roll up of a new ring. The initiation of the formation of the CVP comes from the rollup and lee-side bending of the jet vortex sheet leading to, as they put it, 'tight columnar vorticity isosurface' which form the cores of the CVP, shown in figure 1.3.

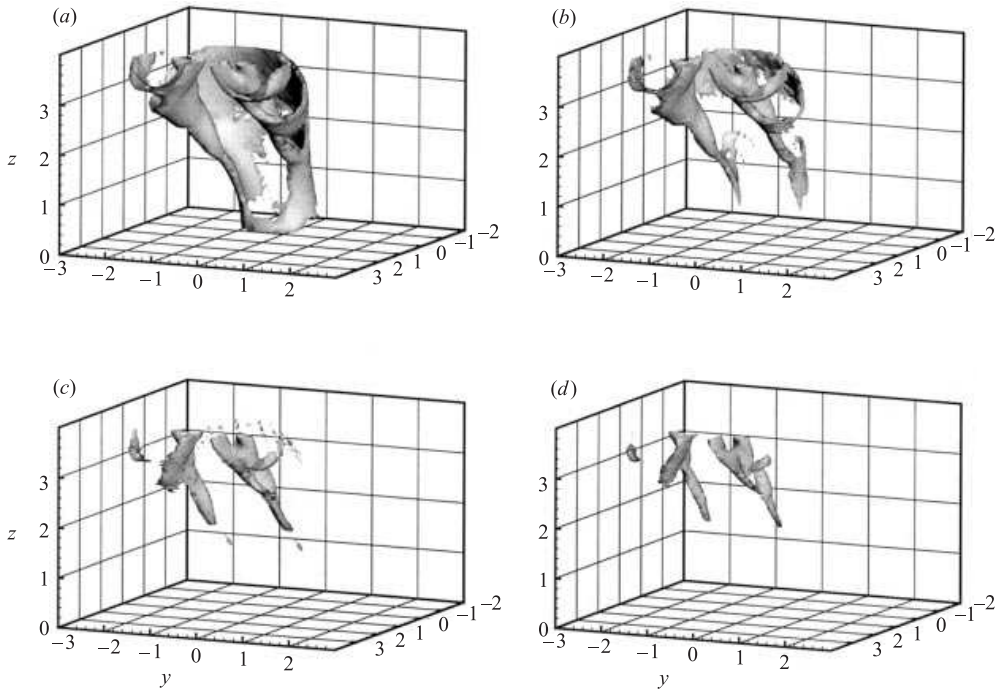

Figure 1.3: Ensemble averaged vorticity field from Cortelezzi & Karagozian [15] for a $V_r = 5.4$ showing initiation of CVP formation. Plots (a) to (d) show iso-contours of increasing vorticity iso-value.

Lim *et al.* [37] however postulate that vortex rings do not form in the near region of the JICF unless V_r reaches infinity (meaning a free jet). The experiment they performed was for a $V_r = 4.6$ and $Re_j = 1600$. By performing both normal and laser dye visualisations they concluded that there was no evidence of vortex rings being formed at the exit of the jet. Furthermore, the initial formation of the CVP by the folding of the sides of the cylindrical shear layer prevents it from rolling up into a ring. The suggested mechanism is that the whole shear layer deforms as shown in figure 1.4. Two vortex loops are formed, one on the upstream

side and one on the downstream (or lee side) of the jet as shown in section B-B in the figure. As the shear layer develops these two loops eventually merge to form the CVP in the far field.

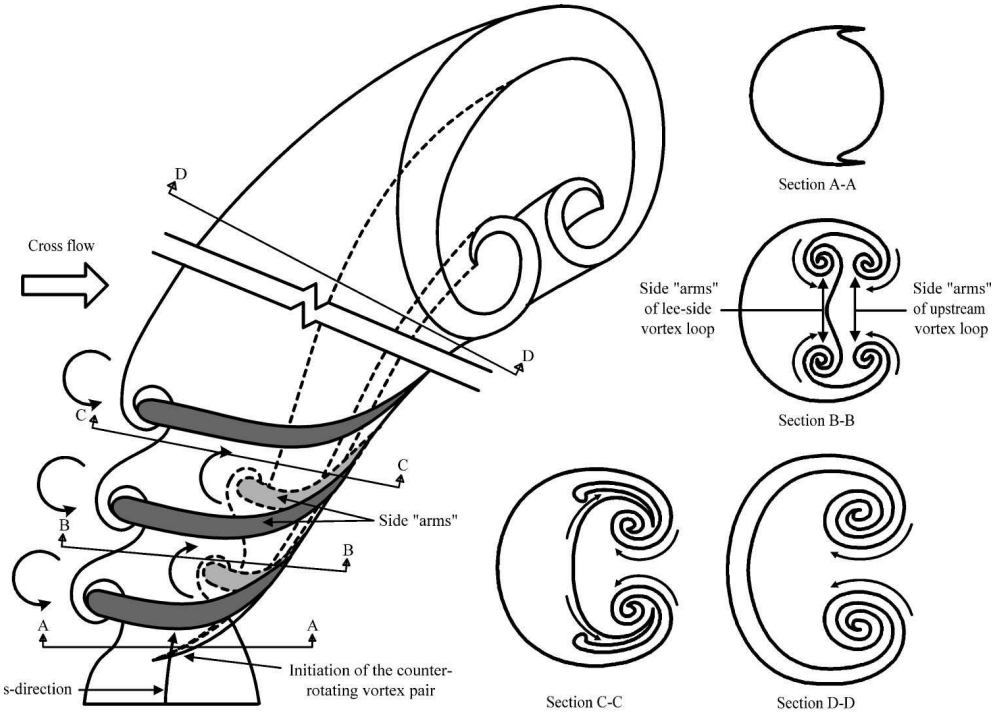

Figure 1.4: Schematic of the development of the shear layer according to Lim *et al.* [37]. Adapted from Lim *et al.* [37]

Schlegel *et al.* [56] looked at the contribution of the wall boundary layer to the formation of the CVP through high resolution three-dimensional vortex simulations. The investigations were performed for a cross-flow jet with $V_r = 5$ and $Re_j = 1225$. Viscous simulations where the boundary layer was suppressed gave similar results to the formation of the CVP as Cortelezzi & Karagozian [15] with a rollup of the jet shear layer and lee-side deformation of the jet's azimuthal vorticity leading to the initiation of the CVP. However, the addition of viscosity showed a delay in the roll up of the shear layer on the windward side and that the initiation of the CVP formation does not require a preceding shear layer roll up. With the influence of the boundary layer a number of near-wall structures

appear. Vorticity from the boundary layer is entrained into the jet and merges with the CVP contributing to an increase in its total circulation via the presence of tornado-like wall-normal vortices on the lee side of the jet. This is shown in figure 1.5. Furthermore the presence of the windward roll-up structures is similar to the previous inviscid models.

In addition to the complexity of the near field, it is also very sensitive to inlet condition. New *et al.* [44] studied the effect of top hat and parabolic jet velocity profiles on the development of the near field of a round jet in a cross flow for $2.3 < V_r < 5.8$. The study was experimental and the techniques of Planar Laser Induced Fluorescence (PLIF) and Particle Image Velocimetry (PIV) were used to obtain flow visualisations and velocity measurements respectively in the centre plane of the jet. The main conclusions are that for a parabolic velocity profile there is a delay in the formation of the upstream and downstream shear layer vortices due to the thicker shear layer associated with the velocity profile. This leads to less entrainment and therefore an increased jet penetration into the cross flow. For a top hat profile, where the shear layer is thinner, there is a more regular and coherent formation of the shear layer vortices. However the resulting two flows shared many of the salient features.

The evolution of the jet in the near field is a very complex phenomenon due to the fact that there are a number of vortical structures which continuously interact with each other. The question of how the jet develops to form the CVP is not fully understood yet, especially for higher velocity ratios and Reynolds number, as most near field studies are for low velocity ratios ($V_r < 10$) and low Reynolds numbers.

1.3.2 The Wake

As shown in figure 1.1 the wake of the JICF contains upright vortices. These vortical structures in the wake look similar to that of vortex shedding from a solid cylinder. McMahon *et al.* [40] and Moussa *et al.* [42] measured the characteristic wake frequencies using hot-wire measurements and found that the Strouhal numbers were similar to that of solid cylinder, not only in value but also the fact that it was almost independent of cross-flow Reynolds number, in the same range

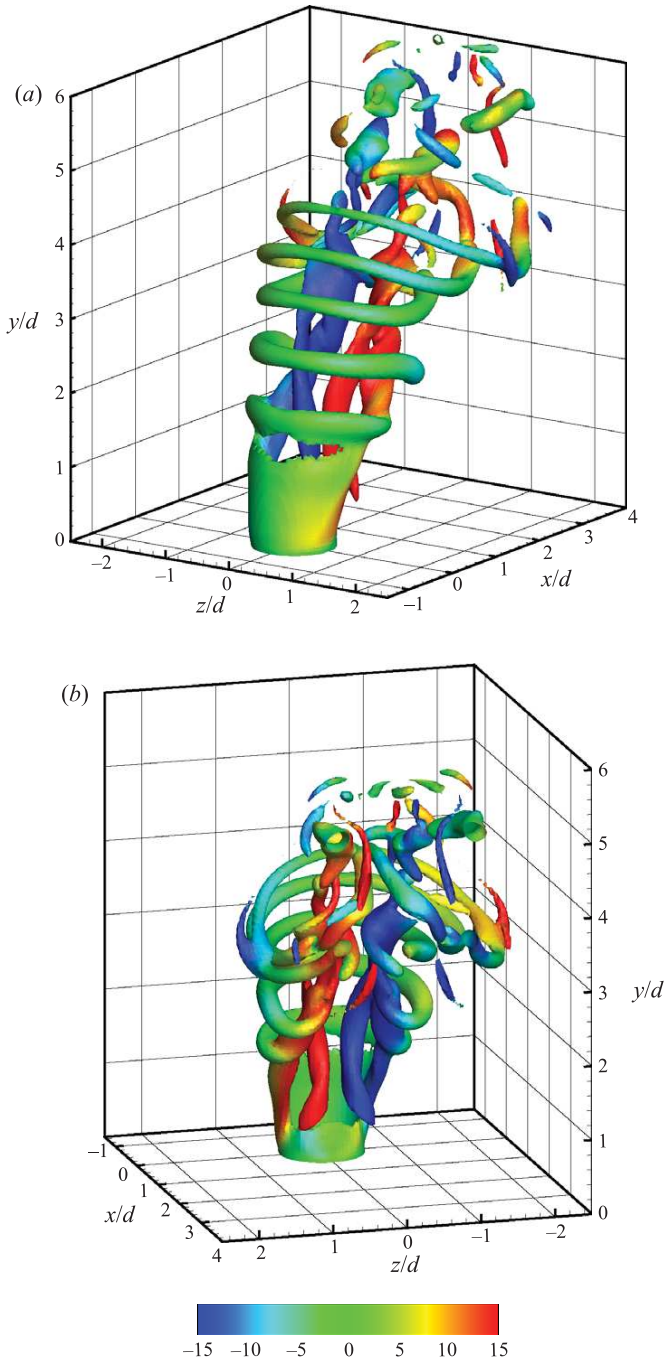

Figure 1.5: Near wall vorticity magnitude iso-surfaces with colors indicating wall normal vorticity from simulation of Schlegel *et al.* [56] for $V_r = 5$ and $Re_j = 1225$. Contours show the windward rollup structures as well as the CVP formation via the jet shear layer folding with contribution from boundary layer vorticity.

of $10^3 < Re_d < 10^5$ where the Strouhal number for a solid cylinder remains approximately constant [8]. This led them to conclude that the vortices in the wake were analogous the the shedding observed off solid cylinders, i.e a von Karman vortex street.

Fric & Roshko [23] studied the wake vortices in more detail using flow visualization to see the vortices and hot wire anemometry for frequency measurements for $2 < V_r < 10$ and $3800 < Re_{cf} < 11400$. The main finding was that the vortical structures in the wake are not shed from the jet but are formed from vorticity which originates in the cross-flow boundary layer. This is shown in their smoke visualisations reproduced in figure 1.6 by separately tagging the two possible sources of vorticity, the jet (figure 1.6a) and the cross-flow boundary layer (1.6b). The images show a side view of the jet, an $x - z$ cross section using the coordinate system of figure 1.1.

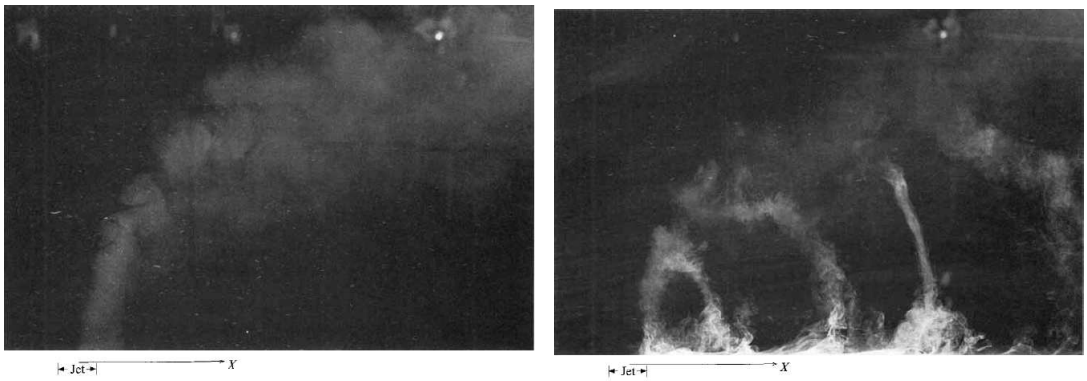

(a) Smoke tags in jet

(b) Smoke tags in cross-flow boundary layer

Figure 1.6: Origin of wake vortices for $V_r = 4$ and $Re_{cf} = 3800$. Figure 1.6a has smoke tags in the jet whereas figure 1.6b has them in the cross-boundary layer. Results from Fric & Roshko [23]

Briefly the postulated mechanism of how the wake structures form involves the following steps. First the cross-flow boundary layer separates close to the downstream edge of the jet orifice due to the adverse pressure gradient of the curved streamlines around the jet. The separated boundary layer then rolls up into a vortex parallel to the wall. The separated vortex nearest to the jet is entrained into the jet and convected with it. It is therefore pulled vertically upwards,

'turning up' (terminology used by Wu & Wu [67]), which creates the wall normal vortex wake structure. While convecting downstream along the widening wake area it becomes stretched with boundary layer fluid and vorticity continuously being pumped upwards into its base. The wake structures have been observed to persist to up to at least 100 jet diameters downstream of the jet exit (Kuzo & Roshko [35]). The authors note that the most coherent wake structures (with peakiest Strouhal frequency) occur at $V_r = 4$. At higher velocity ratios close to 10 it is noted the efficiency of entrainment of the separated cross-flow boundary layer is low and the wakes vortices are very thin as they are stretched more[1]. Kelso *et al.* [33] also performed visualizations of the wake vortices and agree with the fact that when $V_r > 3$ with increasing Reynolds number the wake structures are more coherent.

Smith & Mungal [58] performed concentration measurements in various cross sectional planes of the cross-flow jet using air seeded with acetone. The parameters covered were $5 < V_r < 25$ and $8400 < Re_j > 41500$. The results of their measurements will be discussed in more detail in section 1.4, but their observations in the wake are discussed here. For velocity ratios greater than 10 they observed jet fluid in the wake vortices rather than cross-flow boundary layer fluid, the opposite of that suggested by Fric & Roshko [23]. This is shown in figure 1.7, where only the jet was tagged. The authors loosely suggest that this is due to the steeper trajectory (increased penetration) of the $V_r > 10$ cross flow jets which reduces interactions with the cross-flow boundary layer. Importantly, the Vr = 5 case was classed as belonging to 'a different regime, where wall effects (image vortices) are important'. So the velocity ratio for the cross flow jet can be separated into two regimes:

- $V_r < 10$ where cross flow boundary layer fluid is present in the wake structures and the interaction of the jet with the wall is important.
- $V_r > 10$ where jet fluid is present in the wake structures and there is no interaction with the wall.

[1]The jet trajectory will be discussed in section 1.4.1 but a larger velocity ratio means that the jet penetrates further into the cross stream thus increasing the wall normal height of the jet

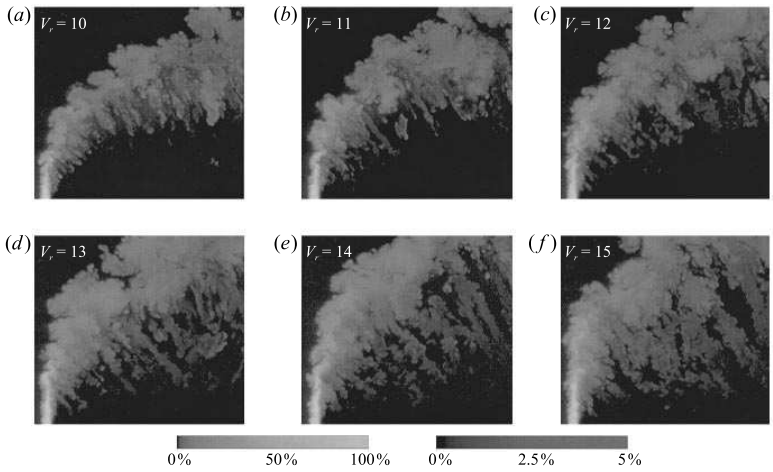

Figure 1.7: Side view PLIF images showing jet fluid in wake for $V_r > 10$ and $Re_{cf} = 3300$. From Smith & Mungal [58]

This change in flow regime in the wake has not been explored further and it is generally agreed that $V_r = 10$ is the critical velocity ratio where this transition occurs. Furthermore the interaction between the wake vortices and the CVP for $V_r > 10$ has also not been explored to the authors best knowledge.

1.3.3 The Far Field

The far field of the JICF is dominated by a counter-rotating vortex pair. Early studies such as Fearn & Weston [22] and Moussa *et al.* [42] concentrated on measurements of the mean velocity field. Fearn & Weston [22] confirmed that the CVP is the dominant flow structure by taking average velocity measurements with a rake of 7 yaw pitched pressure probes in one half of the cross-sectional 'vortex' planes of a transverse jet. The parameters studied were for $3 < V_r < 10$ and $2.6 \times 10^3 < Re_{cf} < 3.6 \times 10^5$. The circulation of the CVP was measured by fitting the data to vortex models and assuming symmetry about the centre plane. The two models used were, the filament model, which assumes vorticity is concentrated in 2 infinite straight vortex filaments and the diffuse model which assumes that each vortex is composed of a Gaussian distribution of vorticity. The authors found that the diffuse model gave a better fit to their mean data indicating that the average CVP vorticity field has a Gaussian distribution. Furthermore,

they concluded that the strength of the CVP decreases with downstream distance.

Kuzo [34] performed 2D PIV measurements in the CVP cross section (y-z plane of figure 1.1) at various downstream positions. This work is one of the few studies, to the authors best knowledge, that resembles the measurements performed in the experiments of the current research in that the whole cross section of the far field is measured using the technique of PIV. The measurements were performed for $Vr = 5, 10, 20$ and a Reynolds number range of $2079 < Re_j < 13087$. The measurements showed the existence of an alternate state for the CVP, specifically unsteadiness, asymmetry and multiple vortices, below a critical Re number which increased with velocity ratio. The plot describing this states is shown in figure 1.8. The blown up areas are loci plots of maximum/minimum vorticity.

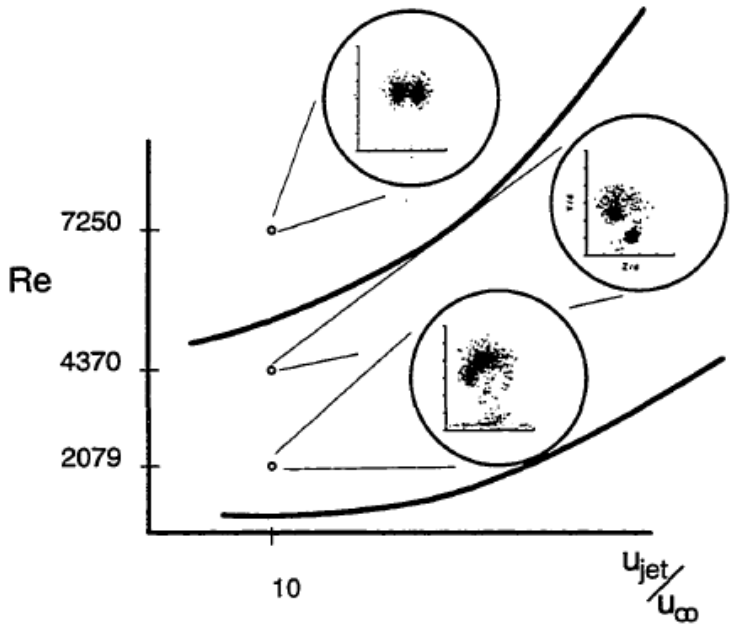

Figure 1.8: Alternate mean flow states. Blown up areas show loci plots of maximum/minimum vorticity in the CVP cross section, used to illustrate and distinguish the dynamic nature of the alternate flow states in $Re - V_r$ space. From Kuzo [34]

From the data, information about the vorticity of the CVP was extracted

showing that each vortex followed a Gaussian distribution as shown in figure 1.9. In the figure the Y coordinate is the wall normal direction and Z is the spanwise direction (different from the coordinate system used in figure 1.1), Y_0 and Z_0 are the centre of the vortex, R^* is the equivalent radius and Γ_0 is the total circulation. Furthermore the strength/circulation decreased with downstream distance in what seems like a power low relationship when the downstream distance is scaled with d_j. The word 'seems' is used as the author only took measurements at 4 downstream positions spanning approximately $100d_j$ and did not try a curve fit to describe this decay. This is shown in figure 1.10a.

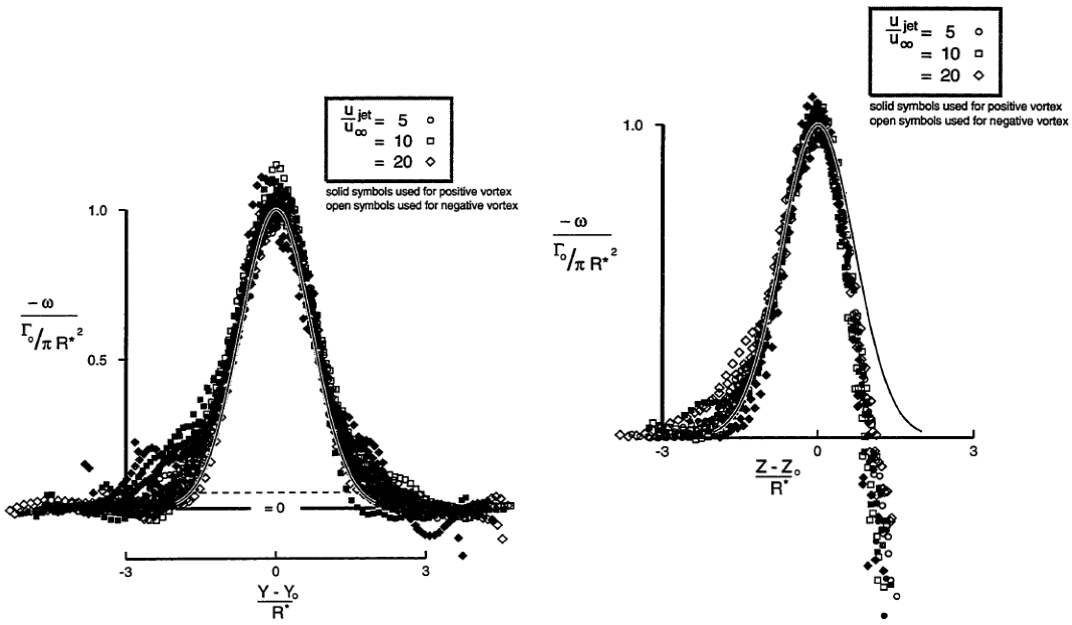

(a) Vorticity distribution in CVP along wall normal direction

(b) Vorticity distribution in CVP along spanwise direction

Figure 1.9: Vorticity distribution of the CVP. Results from Kuzo [34]

Perharps the most notable work in modelling the behaviour of the CVP came from Broadwell & Breidenthal [9]. The authors simplify the problem by considering the jet, in the limiting case where $d_j \to 0$, as a point source of momentum, 'a lift force of vanishing drag', which generates a CVP much like a lifting wing generates a trailing vortex pair. This allowed them to postulate that, ignoring vis-

cosity assuming it has no global effect and is only important in the small (energy dissipation) scales, the only global length scale based on dimensional reasoning is

$$l = \left(\frac{\dot{m}_j U_{jet}}{\rho_\infty U_\infty^2} \right)^{\frac{1}{2}}, \tag{1.25}$$

where $\dot{m}_j$ is the mass flow rate of the jet $\dot{m}_j = \rho_j (1/4)\pi d_j^2 U_{jet}$. For the case where the jet and cross flow fluids are the same ($\rho_j = \rho_\infty$) this length scale reduces to $l = (\pi/4)^{\frac{1}{2}} V_r d_j$. Using this assumption they then performed an analysis for the downstream evolution of the trajectory and circulation of the CVP, modelled as two line vortices. With the spacing of the cores R in the far field, where the flow is independent of l, also assumed to be proportional to the distance from the wall z, two important results are extracted:

$$\frac{z}{V_r d_j} = c \left(\frac{x}{V_r d_j} \right)^{\frac{1}{3}}, \tag{1.26}$$

$$Re_\Gamma = \left(\frac{x}{V_r d_j} \right)^{\frac{-1}{3}} Re_j. \tag{1.27}$$

It should be noted that in addition to the assumption of inviscid flow the model only applies to the average far field. Equation 1.26 describes the jet trajectory along the centre plane, with x being the cross-flow direction and z the wall normal direction with origin at the jet exit. Equation 1.27 is the Circulation Reynolds number defined as $Re_\Gamma = \Gamma/\nu$ and shows how the strength of the CVP scales with downstream distance x as $Re_\Gamma \backsim x^{\frac{-1}{3}}$ and the global length scale $V_r d_j$ as $Re_\Gamma \backsim (V_r d_j)^{\frac{1}{3}}$.

Kuzo [34] also plotted the decay of normalised circulation against downstream distance x scaled by l, shown as D in figure 1.10b. The quantity plotted on the vertical axis is actually equal to Re_Γ/Re_j for $\rho_\infty = \rho_j$. The plot shows that the data does not collapse perfectly but does indicate that the suggested scaling by Broadwell & Breidenthal [9] encapsulates the basic physics of the flow correctly. Surprisingly, apart from the limited data of Kuzo [34], nobody has tried to measure the circulation field of the far field in order to verify the model suggested and the resulting scaling.

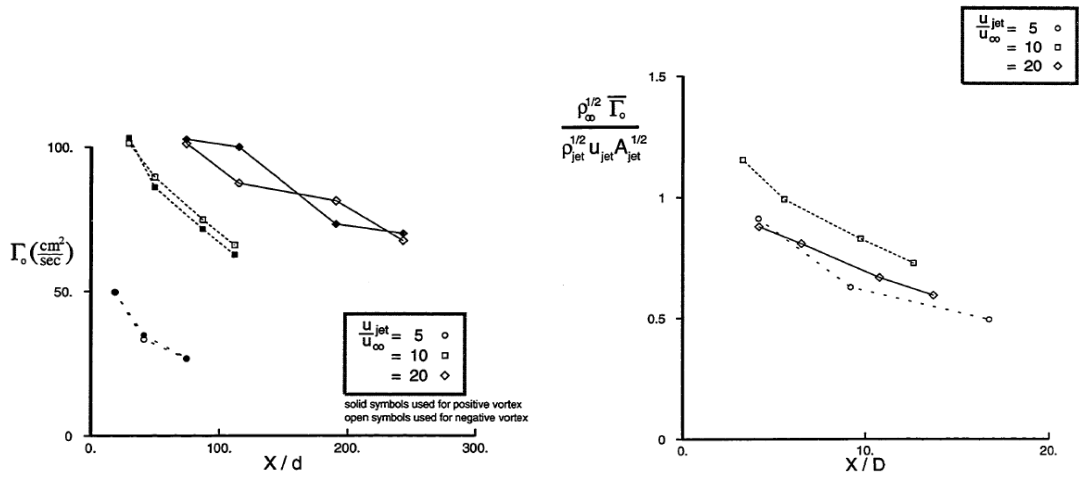

(a) Downstream decay of circulation (b) Downstream decay of normalised circulation

Figure 1.10: Circulation decay of the CVP. Results from Kuzo [34]

Rivero *et al.* [55] performed an experimental study to investigate the structures present in the JICF for $V_r = 3.8$ and $Re_{cf} = 6600$. This was carried out by using hot-wire velocity data measured using a rake of $8 \times -$ wires together with a pattern recognition technique, and PLIF visualisations in the far field. Their results showed that the CVP is not a steady feature with the strength of the two cores modulated by the wake structures, whose own strength is higher than that of the CVP. A mechanism for this was given via 'handle type' vortices, shown in figure 1.11, which explained the modulation and interaction between the CVP and the wake, 'Karman-like' vortices. Furthermore, the existence of 'folded rings' in the main body of the CVP was noted which originate from the azimuthal vorticity in the inner pipe wall of the jet.

During the course of this study Johnson *et al.* [31] performed Stereo-PIV measurements in the far field CVP cross-plane (similar to the measurements which will be presented later). Measurements were performed on both a heated and unheated jet for a momentum ratio 4.57 and 4.2 and jet Reynolds number of $43,600$ and $41,000$ respectively. A Proper Orthogonal Decomposition (POD) analysis revealed that the large scale motions of the CVP are predominantly responsible for the overall contribution to the Reynolds shear stresses and Turbulent Kinetic

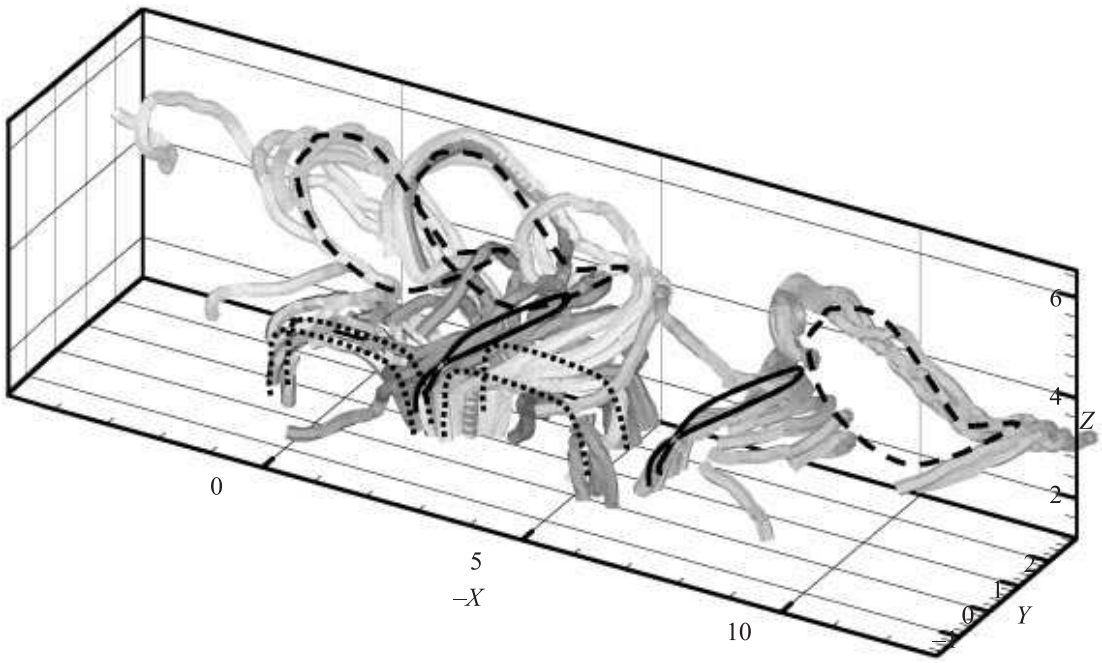

Figure 1.11: Total vorticity field of JICF from hot wire measurements of Rivero *et al.* [55] for $V_r = 3.8$ and $Re_{cf} = 6600$. Figure shows the 'handle type' and 'folded ring' structures identified.

Energy (TKE) components. The heated and unheated jets were found to behaved very similarly, indicating that the behaviour of the flow is dominated by the kinematics of the interaction between the jet and the cross-flow.

The scaling laws governing other properties of the JICF have also been examined in the literature. The aim was to examine if the JICF exhibits different scaling characteristics in the 3 different areas mentioned in this section and whether it shows any signs of self similarity. This is discussed in the next section.

1.4 Scaling

1.4.1 Jet Trajectory

The trajectory of the JICF is the most frequently reported property of the flow in the literature. Pratte & Baines [53] were amongst the first to quantify the trajectory by using visualization of an oil aerosol jet issuing from a pipe extending into the crossflow and suggested an $V_r d_j$ scaling to collapse the trajectories. The expression they suggested was

$$\frac{z}{V_r d_j} = A \left(\frac{x}{V_r d_j} \right)^m \tag{1.28}$$

with $A = 2.05$ and $m = 0.28$ to describe jet trajectories for V_r ranging from 5 to 35. As discussed in section 1.3.3 the analysis of Broadwell & Breidenthal [9] resulted in the same trajectory scaling of $V_r d_j$ although the constant $m = 1/3$. Hasselbrink & Mungal [26] obtained scaling laws for the cross flow jet using conservation of mass and momentum and extracted the same scaling for the jet trajectory as Broadwell & Breidenthal [9]. However it should be noted that their analysis is only valid for velocity ratios $V_r \geq 10$.

One of the biggest issues with the jet trajectory is that reported cases have different jet inlet conditions, e.g. flush mounted or extruding nozzle, as well as different definitions for the trajectory. Amongst these are the locus of maximum concentration, locus of maximum velocity magnitude, locus of maximum wall normal mean velocity, locus of maximum cross-flow direction mean velocity and the path of the streamline exiting from the centre of the jet nozzle, just to name

a few. However, most researchers agree with the scaling of $V_r d_j$ being best suited to best collapse the data for the jet trajectory, albeit with a scatter in the values of A and m ranging from $1.2 < A < 2.6$ and $0.28 < m < 0.38$ [26].

1.4.2 Concentration and Velocity Field

Smith & Mungal [58] performed extensive measurements of the concentration field in various cross sectional planes of the JICF to observe the various length scales that affect the flow field. Their results for $10 < V_r < 25$ are summarised in figure 1.12.

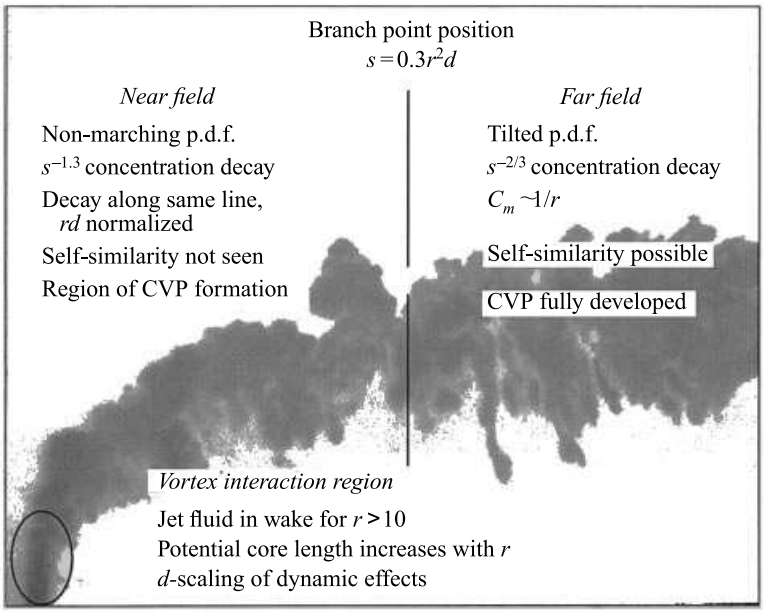

Figure 1.12: Summary of results from Smith & Mungal [58] showing scaling features of the JICF. Authors denote the velocity ratio V_r as r.

Their measurements showed two important things. First, when the decay in centreline concentration is plotted against the length along jet centreline, s, the concentration decayed with $s^{-1.3}$ for the near field and $s^{-2/3}$ in the far field. The centreline concentration for a free round jet goes with s^{-1}. When the concentration decay is plotted against $s/V_r^2 d_j$ the position where the rate changes from $s^{-1.3}$ to $s^{-2/3}$ line up at $s/V_r^2 d_j = 0.3$, which corresponds to $x_{bp}/V_r^2 d_j \approx 0.2$. This

'branch point' position (hence the subscript 'bp') was used by Smith & Mungal [58] to define transition point in the flow separating the near field from the far field. Furthermore comparing the decay rates since the higher concentration decay is in the near field, it is the structural formation of the CVP that corresponds to the enhanced mixing region, compared to the normal jet. The reason why these branch points exist is still an open question.

The second conclusion involves self-similarity. When the concentration profile in the centre plane is normalised by the maximum local concentration, at a given downstream x-position before the branch point, and plotted against $y/l_{1/2}$, $l_{1/2}$ being the half-width at half maximum, the profiles do collapse showing self-similarity. However, the corresponding profiles in the CVP plane (y-z plane of figure 1.1) do not show self-similarity. Thus full self similarity has yet to be observed. However the authors postulate about the possibility of self-similarity beyond the branch points but have not expanded on it.

Su & Mungal [59] performed simultaneous velocity and concentration measurements in off-centreplanes and the centre plane of the cross-flow jet for a $V_r = 5.7$ and a $Re_j = 5000$. Two configurations were studied, one having the pipe flush to the wall and the second protruding into the cross-flow. The authors looked at the near field and far field and compared the scaling observed in the mean velocity and concentration field with that observed in free jets. The near field showed indications of free jet scaling for both velocity and concentration field decay rate of s^{-1}. In the far field however the velocity profile does exhibit a wake decay rate of $s^{-2/3}$ but the concentration decay is much faster. Departure from jet scaling in the near field and especially wake scaling in the far field for the concentration field was attributed to the fact that the relevant field is not axisymmetric observed by looking at the cross-stream profiles.

Interestingly, looking at the centreline concentration decays, the results of Su & Mungal [59] note a contradiction with those of Smith & Mungal [58] with the centreline concentration decaying with s^{-1} in the near field and faster then $s^{-2/3}$ in the far field. Given that the results were consistent for both nozzle configurations the authors attribute this to the fact that the jet exit velocity profile was a pipe flow profile, compared to the top hat profile of Smith & Mungal [58]. However, no experiment was performed to confirm this. Smith & Mungal [58] did note that

the $V_r = 5$ case belonged to a different class of JICF due to interaction with the wall as described in section 1.3.3. So the discrepancy in the results could also be due to the fact that the results of Smith & Mungal [58] are valid for $V_r > 10$.

The results from the various scaling investigations in the literature mainly show that the JICF is not a fully self similar flow. This is due to the dynamic 3D nature of the flow as well the different complex interaction of the jet and the cross flow at different areas of the flow. However, scaling various properties by $d_j, V_r d_j$ and $V_r^2 d_j$ helps to compare flows with different velocity ratios for large scale features.

1.5 Mixing

Su & Mungal [59] also measured the fluctuating concentration and velocity turbulence quantities $\overline{C'}, \overline{u'}, \overline{v'}$. Their results show that mixing intensity, quantified by the scalar variance and the magnitude of the turbulent scalar fluxes, is initially higher on the upstream side of the jet and increases on the downstream/wake side with downstream distance. This indicates how the vortical structure of the JICF mentioned in section 1.3 could affect the mixing process. Initial entrainment takes place on the upstream side through the roll-up of vortices creating a high initial mixing intensity on the upstream side. The development of the CVP and the generation of wake vortices then increases the mixing intensity in the wake side of the jet. This shows that understanding the structures present in the turbulent velocity and scalar field can help to understand the mixing processes.

Shan & Dimotakis [57] performed PLIF measurements in the CVP cross section of the far field of the JICF for a $V_r = 10$. The effect of jet Reynolds number on the concentration field was studied for $1 \times 10^3 \leq Re_j \leq 20 \times 10^3$. The effect of Reynolds number on turbulent mixing is shown in the PDF distributions of the scalar concentration in figure 1.13. The PDF shows that the concentration develops a peak with increasing Re above 5×10^3. This peak development shows that the scalar field becomes more spatially homogeneous with increasing Reynolds number.

Comparing the PDF of the JICF in figure 1.13a with the PDF of a free jet in figure 1.13b, taken from Shan & Dimotakis [57] who perfomred a previous similar

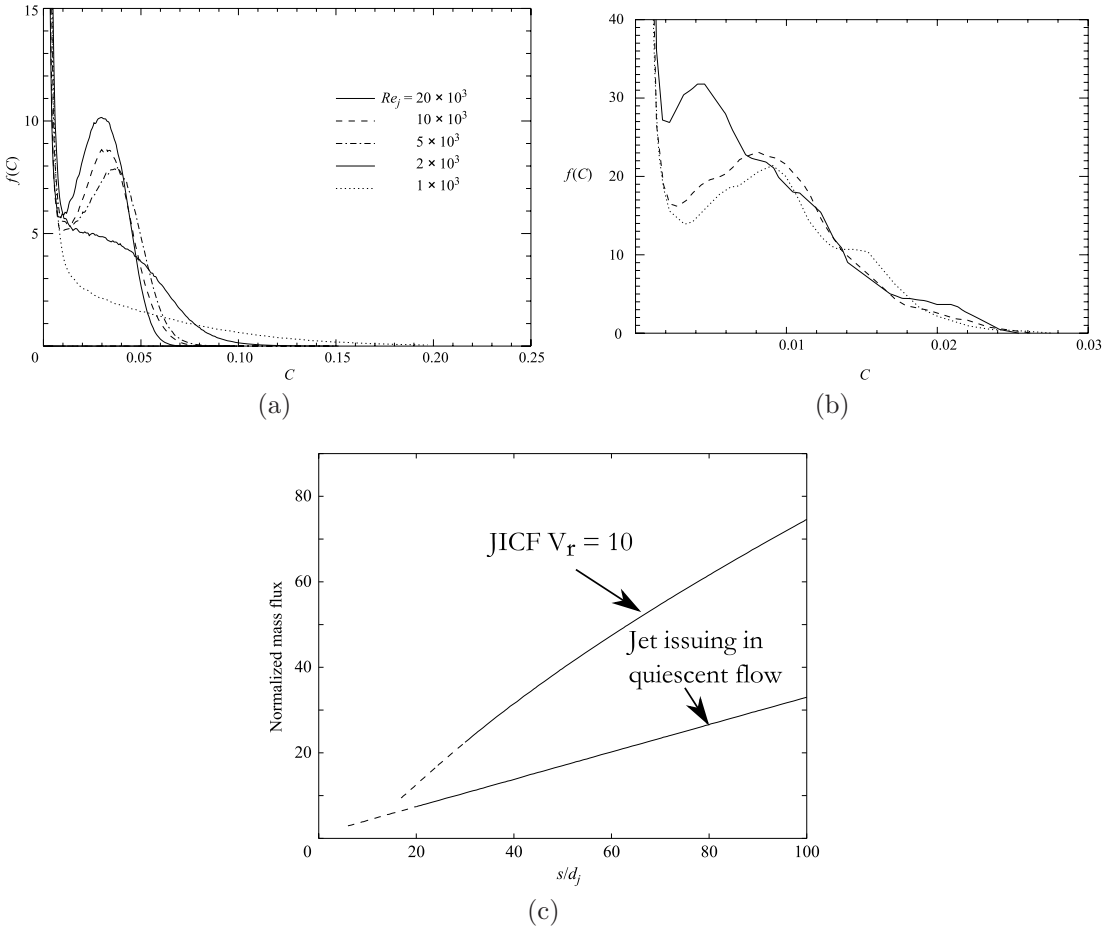

Figure 1.13: Scalar PDF results from from Shan & Dimotakis [57] showing enhanced mixing abilities of the $V_r = 10$ JICF. (a) PDF of jet fluid concentration for increasing Reynolds number of a JICF with $V_r = 10$. (b) PDF of jet fluid for a free jet issuing into quiescent flow for $Re_j = 4.5, 9, 18 \times 10^3$ represented by lines of increasing solidity. (c) Normalised total mass flux plotted against length along jet centre line s. Amended from figure 20 of Shan & Dimotakis [57].

investigation for free jets, shows that the free jet develops a smooth monotonic decreasing distribution in the scalar field. Using the scaling results for the far field from Hasselbrink & Mungal [26] of the jet mass flow rate, Shan & Dimotakis [57] also performed an analysis to compare the entrainment rates between the JICF for $V_r \geq 10$ and a free jet. Their result, shown in figure 1.13c, of the normalised jet mass flow rate by jet inlet mass flow rate show that the JICF has a higher entrainment rate. Coupling this with the enhanced mixing/homogenisation of the JICF to the free jet the authors concluded that the JICF is a more efficient mixer.

The question of whether the cross-flow jet is a more 'efficient' mixer is still open however. Based only on the fact that cross-flow jet entrains more fluid than a free jet and achieves better homogenisation, then the cross-flow jet can be called a better mixer. However, this is somewhat misleading as the total momentum has not been considered. If the question is looked from the point of view of a 'momentum budget' then it can be seen that this might not be the case. This can explained by looking at the cross-flow jet and the free jet mixing as a 'black box' shown in figure 1.14. The difficulty with this analysis is quantifying the

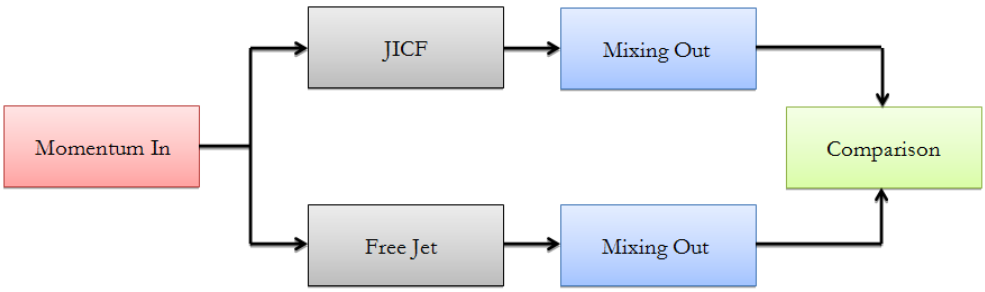

Figure 1.14: 'Black Box' analysis for the mixing efficiency of a JICF

'Momentum In' and 'Mixing Out' terms from each flow in a way that makes them comparable. This would have to be done in non dimensional quantities that encapsulate the physics behind each flow. It is suggested to use the analogy of a JICF suggested by Broadwell & Breidenthal [9] with the lift force on a wing.

Shan & Dimotakis [57] also looked at the isotropy of the scalar field both for the large-scales and small-scales using scalar increment statistics. The result, which were consistent across all Reynolds numbers studied, was that the scalar

field is made of large scale plateaux in concentration which are separated by small scale cliffs of sharp concentration. By looking at the scalar increments in the two different directions as well as power spectra the authors concluded that the cliffs were preferentially aligned along the vertical (wall normal) direction showing small scale anisotropy in the scalar field. The authors suggested that this is due to the straining action of the CVP along the vertical thus suggesting a link between the large scale vortical structure and the resulting small scale scalar field. Their conclusion was that the scalar isotropy (referring to the internal structure of the scalar field based on the distribution of scalar increments and scaler differences, power spectra and scalar microscales) does not necessarily exist for the cross-flow jet and that the detailed turbulent mixing structure depends on the large-scale dynamics. This is not surprising if a CVP still exists in the mean. However, the authors only looked at $V_r = 10$ and it would be interesting to see if this anisotropy persists for higher velocity ratios and how any changes to the large scale dynamics affect it.

1.6 Outstanding Issues

The JICF has a very complicated flow structure which is not well understood and yet very important to a variety of engineering applications. The complex interactions between the cross flow and the jet make it very hard to predict let alone understand the resulting flow field. Furthermore, the flow is sensitive to inlet conditions and, apart from the centre plane, shows no signs of self similarity. In summary there is a large number of studies concentrating on the near field dynamics of the jet, restricted to mainly low velocity ratios and Reynolds numbers, with studies concentrating on the long term behaviour of the jet being limited. The evolution of the near field into a CVP is an interesting area in terms of the physics involved, but the resulting underlying turbulent field is more important as it controls the mixing characteristics. Evidence of a link between the large scale vortical structures and the scalar field has been shown by Shan & Dimotakis [57]. The study of the underlying turbulent field therefore cannot be fully understood from a statistical point of view and so more effort needs to be put into understanding the turbulent structure of the JICF.

Table 1.1 summarises the important experimental studies from the literature, discussed in the literature review above. The table exposes the key areas that have yet to be investigated in the literature, which are listed below:

- Complete similarity of the CVP plane in the far field has not been established.
- Instantaneous turbulent structure of the JICF in the far field is not fully understood.
- Downstream evolution of instantaneous CVP structure has not been explored.

Although the JICF can potentially be considered a canonical flow, similar to how a turbulent jet or a turbulent boundary layer is, a self-similarity solution has not not been established. A rigorous analysis would be required to investigate this with a large number of statistical measurements at various downstream position extending well into the far-field, and as such is not the main focus of this thesis. The final two points above will be the focal point of the thesis. Hasselbrink & Mungal [26] state that "the transverse jet has become an example of turbulent flow composed of 'coherent structures' - dominant vortical systems, which have offered the hope of a mechanistic, rather than statistical, understanding of turbulence". The aim of this thesis is to try and understand the turbulent structure of the JICF, which will in turn help in answering other questions such as its superior mixing properties.

1.7 Project Objectives

The far field structure of the JICF will be investigated by looking at the three-dimensional far field structure, together with statistical properties of the CVP plane. A summary of the parameters studied by other researchers are shown in table 1.1. In order to choose which parameters to study it is best to separate the JICF flow field into different classes based on the relevant parameters using the literature available.

1. Velocity Ratio V_r (from Fric & Roshko [23] and Smith & Mungal [58])

(a) $V_r < 10$: Interaction of the jets main body with wall boundary layer through wake structures.

(b) $V_r > 10$: No interaction with bounding wall + Jet fluid in wake

2. Jet Reynolds number Re_j (from Kuzo [34])

(a) $Re_j < Re_{crit} = f(V_r)$: Large unsteadiness and assymetry of CVP large scale structure and tertiary vortices in far field.

(b) $Re_j > Re_{crit} = f(V_r)$: Higher degree of symmetry and no tertiary vortices in far field

The subject of the wall interactions with the CVP is still open and is not the aim of the present study to answer. For this reason this study will concentrate on $V_r > 10$. From table 1.1 studies with velocity ratio above 10 extend up to a maximum of 25. Furthermore since the study concentrates on the underlying turbulent field in the CVP it is more beneficial to study high Reynolds numbers cases above the critical value. From the results of Kuzo [34] (figure 1.8) the critical jet Reynolds numbers corresponding to velocity ratios of 10 and 25 are 5500 and 7250 respectively. Therefore the velocity ratios to be studied are restricted between $10 < V_r < 25$ with a jet Reynolds number safely above the critical value of $Re_{j,crit} > 10 \times 10^3$. The maximum Reynolds number was selected, within the resolution of the measuring technique to be used, as $Re_j = 20 \times 10^3$.

The proposed research will be carried out through a series of experiments with water as the main fluid for both the cross-flow and jet. The experimental technique of Stereoscopic-PIV has been chosen to carry out the measurements as it allows for all three velocity components to be measured in a single plane at a high temporal speeds, thus allowing for 3D reconstructions of the velocity field to be made via the use of an appropriate technique and access to the full 9-component velocity gradient tensor. Three main experiments are performed. Mean flow measurements characterising the flow are performed using a novel Multi-Scale technique which aims to increase the dynamic range of the measurements. The second experiment, measures the downstream evolution of the turbulent CVP in the far field in a novel experimental set up. Instead of having a cross flow, a jet

is towed through a quiescent tank of water. This effectively allows the measurement set up to remain stationary whilst the flow passes through it. The result is that a 3D volume of the velocity field can be reconstructed representing the large-scale temporal evolution of the CVP within the cross-plane. The final experiment identifies the size and shape of large-scale coherent structures at various downstream locations, whose relative orientation explains the underlying turbulent field. Two-dimensional time resolved measurements are performed at given downstream location and are reconstructed into 3D spatial measurements via the use of Taylor's Hypothesis. Details of the techniques mentioned will be discussed in chapter 2.

Table 1.1: Summary of previous experimental studies. Last row indicates the contribution of the research presented in this thesis.

Authors	Technique	Study	V_r	Jet Parameters		Cross-flow Parameters	
				$Re_j \times 10^3$	Profile	δ_{cf}/d_j[a]	B.L[b]
Shan & Dimotakis [57]	PLIF	CVP Plane	10	$2, 5, 10, 20$	Top Hat	0.067 - 0.3	Laminar
New *et al.* [44]	PIV & PLIF	Near Field	$2.3 \leftrightarrow 5.8$	$0.625 \leftrightarrow 1.645$	Top Hat & Parabolic	2.4	Laminar
Su & Mungal [59]	PIV & PLIF	Centre Plane	5.7	5	F.D.T.P.F[c]	1.3	-
Hasselbrink & Mungal [27]	PIV & PLIF	Centre Plane	$10, 21$	$6, 12.8$	-	0	-
Rivero *et al.* [55]	H.W.A	CVP plane	3.8	25	Top Hat	0.27	Laminar
Smith & Mungal [58]	PLIF	Various Planes	$5, 10, 15, 20, 25$	$8.4 \leftrightarrow 41.5$	Top Hat	0.11-0.55	Turbulent
Kelso *et al.* [33]	Flow Vis. & H.W.A	Wake & Near Field	$2 \leftrightarrow 6$	-	Top Hat	0.28 - 1.3	Laminar
Kuzo [34]	PIV	CVP Plane	$5, 10, 15$	$2 \leftrightarrow 20$	-	-	-
Fric & Roshko [23]	Flow Vis. & H.W.A	Wake	$2 \leftrightarrow 10$	$7.6 \leftrightarrow 114$	Top Hat	0.026 - 0.087	Laminar
Lanitis & Dawson	Stereo PIV	CVP Plane	$10 \leftrightarrow 25$	20	Top Hat	-	Laminar

[a] δ_{cf} is the displacement thickness of the cross flow boundary layer
[b] Boundary Layer
[c] Fully Developed Turbulent Pipe Flow

Chapter 2

Experimental Facilities and Method

This Chapter introduces details of the experiments performed. The two main experimental facilities and details of the associated jet and cross-flow set ups and operating conditions are firstly introduced. Details of the Stereoscopic PIV set ups and procedures followed are then explained after limitations to the measurements to be performed are outlined. An overview of how the raw image data is processed is then introduced as well as post-processing details, together with a discussion on the application of Taylor's hypothesis for the reconstruction of the high-speed measurements.

2.1 Tow Tank Facility

A Tow Tank was used to tow a jet at the cross-flow speed. A schematic of the dimensions of the Tow Tank is shown in figure 2.1. The tank has a $1m \times 1m$ internal cross section. The tank is $7m$ long, with the middle $2m$ section, shown in green, made of transparent perspex and thus allows optical access to the flow for PIV measurements. The remaining $2.5m$ and $2m$ sections are made of opaque PVC. There is also a glass window at one end of the tank positioned in the lower left corner. The tank is supported by a steel frame as shown in figure 2.1. The whole tank is in a wooden enclosure to both darken the room for optimal PIV

measurements and for the safe use of the laser. Pictures of the tank are shown in figure 2.2.

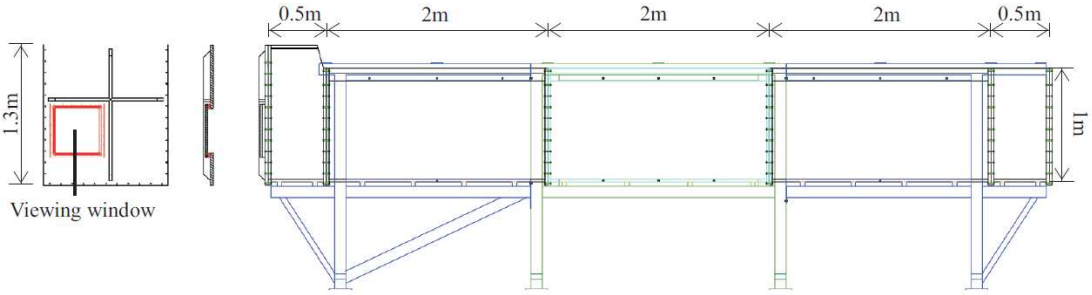

Figure 2.1: Dimensions of the Towing Tank facility

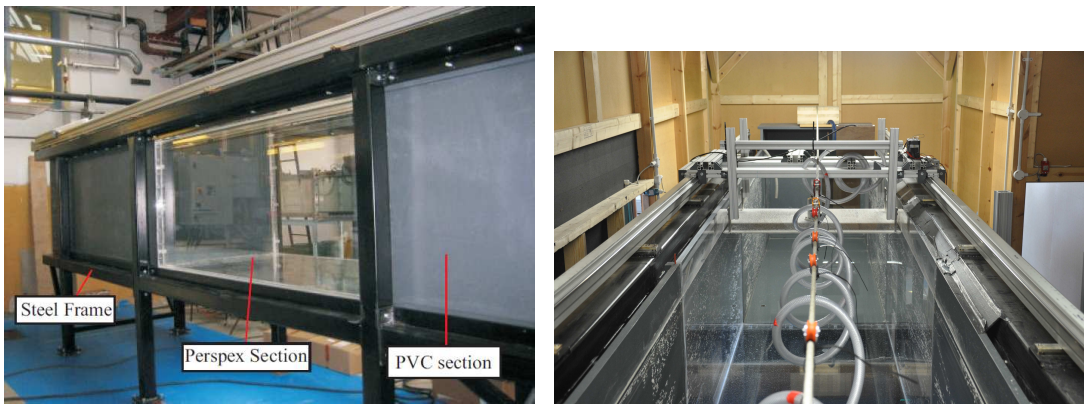

(a) Side view

(b) Top view

Figure 2.2: Pictures of the Tow Tank. Figure (a) shows the $2 \times 1m$ perspex working section with optical access. Figure (b) shows the carriage and the 'umbilical cord' system used for the supply of the jet to the moving carriage

As shown in figure 2.2b, the tank is open on the top where a carriage sits on two rails along the frame of the tank. The carriage is connected to a servo motor at the end of the tunnel by two belts on both sides of the tank running along the entire length of the tunnel. The servo motor is rated at $3kW$ and can generate a torque of $4.7Nm$ up to a speed of $6000rpm$. This corresponds to a maximum carriage speed of $4.75m/s$. The motor is powered by a three phase supply and

controlled by a Compax 0500 unit which is connected to a PC via an RS232 cable. The carriage is controlled by the Servo Manager 6.0 software. A program can be written which controls the position, speed and acceleration of the carriage which is downloaded to the controller.

2.2 Water Channel Facility

The majority of experiments were performed in a recirculating open water channel. A schematic of the Water Channel is shown in figure 2.3. The inlet of the channel has a series of sieves and flow straighteners of reducing size followed by a third order polynomial contraction. The working section of the channel, shown again in green, is 8m long with an internal cross section, shown on the right of the schematic, height and width of $500mm \times 900mm$ and is made entirely out of Perspex thus providing full optical access. The channel is supported by a steel frame and, similar to the Tow Tank facility, the whole channel is in a wooden enclosure. The primary use of this facility is for the study of turbulent boundary layers generated by tripping the flow at the working section entrance, but for the experiments discussed here the trip wire was removed.

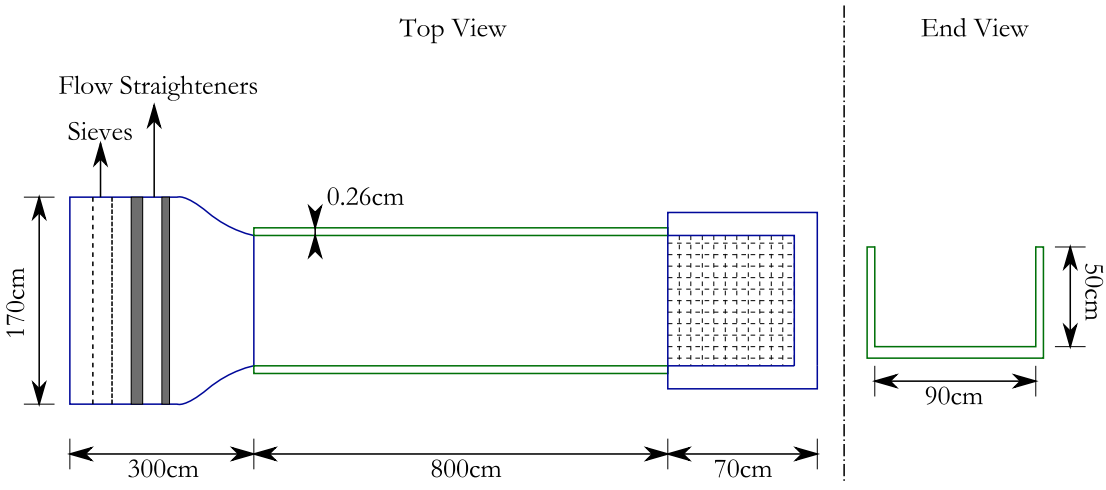

Figure 2.3: Dimensions of the Water Channel facility

Two centrifugal pumps are used to circulate the water. The speed of the

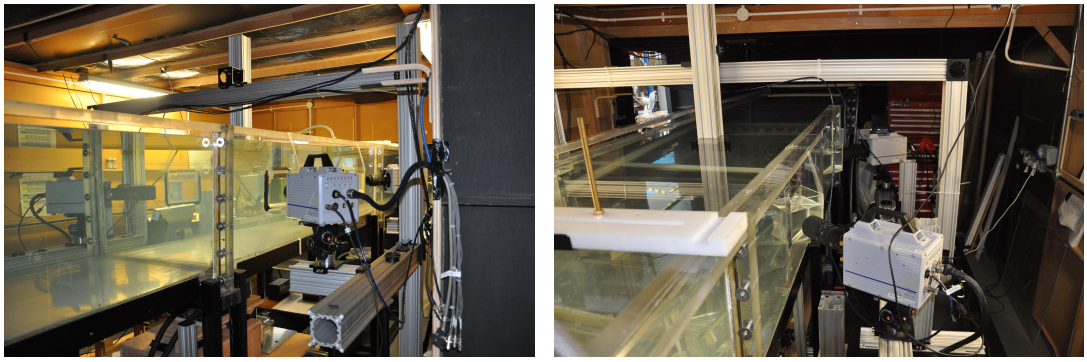

(a) Side view (b) Top view

Figure 2.4: Pictures of the Water Channel. Figure (a) shows the $8m$ long perspex working section with full optical access, with the water flow from right to left. Figure (b) shows the top part of the channel.

pumps could be gradually adjusted via a control unit which translated to free stream velocities in the working section which ranged from $0m/s$ to $0.9m/s$.

2.3 Jet Design: Operating Conditions

2.3.1 Nozzle Design

The jet nozzles used (a cross-section of which is shown in figure 2.5), with jet exit diameters of $d_j = 10mm$, $5mm$, and $4mm$, were made out of aluminium and had a 5^{th} order polynomial contour with the inflection point at the centre (mid-point) with an area contraction ratio of 25. Furthermore the nozzle length L_n to nozzle inlet diameter d_i ratio was kept constant at $L_n/d_i = 2$. A flow straightener made out of bundled plastic round tubes was added just upstream of the nozzle inlet to straighten out the flow. The jet exit profile was not measured but due to the large contraction ratio, the high Reynolds numbers and the small size of the exit diameters of the jets used it was assumed to be top hat. Detailed drawings of the nozzles, including details of the nozzle's top half housing the flow straightener, used can be found in Appendix A.

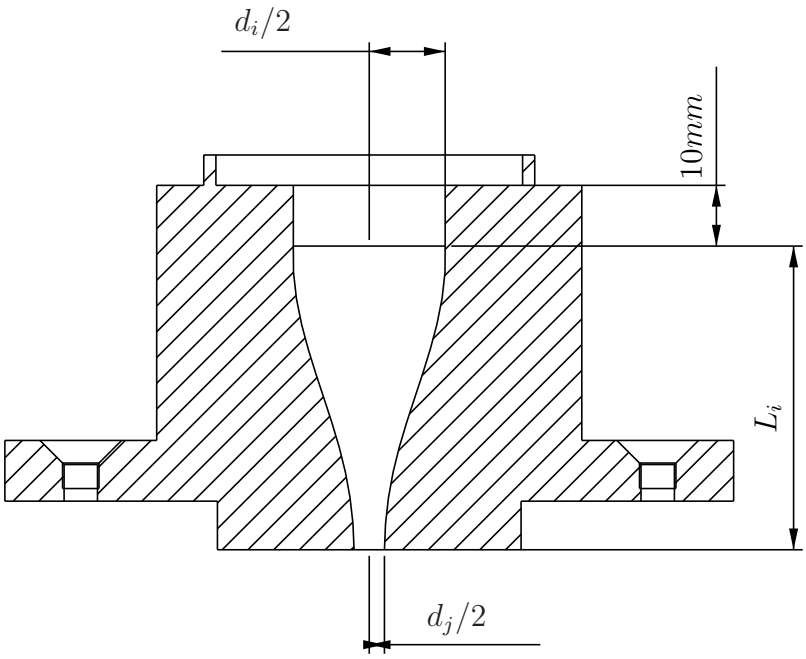

Figure 2.5: Cross-section of 5th order polynomial nozzle

2.3.2 Flow Control

A schematic of the jet supply control unit is shown in figure 2.6. For the experiment performed in the Tow Tank facility the water for the jet was supplied from a large reservoir tank but for the experiment performed in the Water Channel water was drawn from the channel itself, thus allowing for long, statistically independent, measurements to be performed.

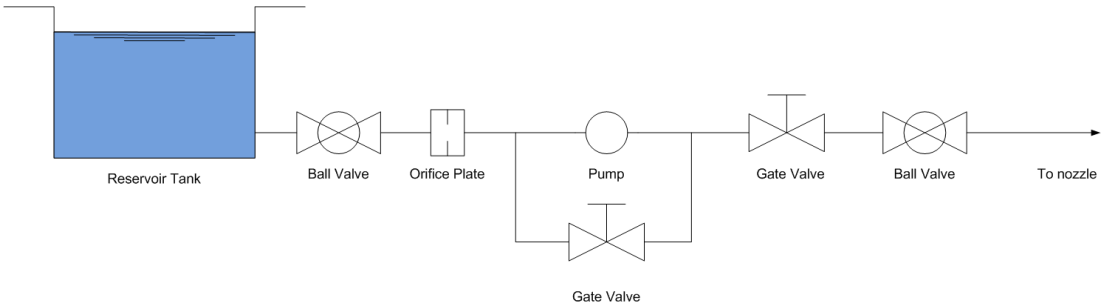

Figure 2.6: Schematic of the Jet Control Unit

The water was pumped to the nozzle using a using a $5m$ head Grundfos pump. The jet velocity was set by controlling the mass flow rate using two valves, one for coarse control and the other for finer control. An orifice plate, which was designed and constructed to the British Standard specifications of EN ISO 5167-2:2003 for an orifice to pipe diameter ratio $\beta = 0.5$, was used to measure the mass flow rate. The equation for the mass flow rate through the orifice plate is given in equation 2.1 below with d_o being the orifice plate diameter, C_d the discharge coefficient and Δp the pressure drop across the orifice.

$$\dot{m} = f_c \frac{\pi}{4} d_o^2 \sqrt{2 \times \Delta p \times \rho} \tag{2.1}$$

$$where \qquad f_c = \frac{C_d}{\sqrt{1 - \beta^4}}$$

The pressure drop was measured using the voltage output from a *Honeywell* pressure transducer, which had a linear voltage-pressure difference calibration. f_c is the flow coefficient for the configuration used which is calculated from the calibration of the orifice plate. The mass flow rate for the calibration was calculated by measuring the mass and time it took to fill up a small tank with water. Due to the fact that experiments were performed in two different facilities the jet control unit had slightly different pipe arrangement which is why separate calibration were performed. The results of the calibrations are shown in figure 2.7. The voltage output from the pressure transducer was monitored and recorded using a *National Instruments* data-logger, controlled via the software 'Lab-View', during all measurements which was then converted into a jet velocity. This was done to ensure that the jet velocity was constant during any of the runs performed.

2.3.3 Tow Tank Experimental Set-up

The end of the jet supply control unit was connected to the jet nozzle, which is attached to the carriage, via a PVC hose. The connection had to accommodate the fact that the carriages moves relative to the control unit. As such it was set up as an 'umbilical cord', with similar configurations found in production line factories. A rope was tightly suspended above and along the centreline of

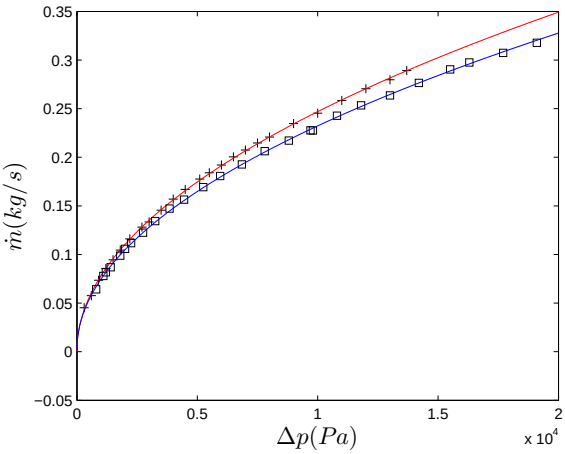

(a) Calibration Curves: + points with red curve fit are from Tow Tank (TT) facility. □ points with blue curve fit are from Water Channel (WC) facility.

	β	f_c	C_d
TT	0.5	0.657	0.636
WC	0.5	0.703	0.681

(b) Curve fit Results

Figure 2.7: Orifice plate calibration results

the tunnel on which a series of pulleys were attached to suspend the PVC pipe in a helical shape. The helical shape of the hose coupled with the pulleys used allowed it to compress and expand smoothly with the movement of the carriage. Care was taken so that the hose did not touch the surface of the water at any carriage position. The set up can be seen in figure 2.2b. Additional images of the experimental set up can be found in Appendix A.

An $985 \times 690 \times 8mm$ aluminium plate was attached to the carriage via the use of four supporting legs. The water level in the tank was such that the whole plate was just submerged beneath it. The part of the supporting legs that were attached to the plate were made of thin stainless-steel plates that had knife edge leading and trailing edge profiles aligned with the towing direction. This was done to ensure minimum disturbance to the free water surface. The leading edge of the aluminium plate also had a knife edge profile. This was done to prevent water splashing outside the tunnel. A $50mm$ hole was drilled in the centre of the plate to attach the jet nozzle and was secured via the use of 4 screws. It was ensured that the screws were flash with the bottom surface (jet exit plane) of the plate.

The program written for the speed profile of the carriage had the carriage accelerating from rest to the required cross flow speed over 3 seconds and would then continue to move at a constant speed. The carriage was stopped 1.5 meters after the first image was recorded.

The speed of the carriage was recorded during runs using a set up that was independent from the carriage's Compax control unit. This was accomplished by placing a printed grid of $4mm$ black and white bars on the frame of the tank and using on optical switch to detect them. The switch was designed and manufactured to give a high or low voltage signal (i.e turn on and off) and thus the resulting signal was a square wave. The frequency of this signal was a direct measure of the instantaneous carriage velocity.

2.3.4 Water Channel Experimental Set-up

The end of the jet supply control unit was connected to the jet nozzle via a PVC hose pipe. Water was drawn from a position far enough downstream so as not to disturb the the flow at the jet exit and chosen measurement positions.

With the nozzle attached in the same way as the aluminium plate, the jet was injected into the cross-flow through a $900 \times 800 \times 15mm$ Perspex plate suspended over the channel and submerged just under the free water surface. The supporting legs holding the plate were made of thin rods so as to minimise the disturbance to the free water surface. The leading edge of the plate had an elliptic profile and was tapered to ensure the oncoming cross-flow did not separate. The jet exit was located halfway along its length. The cross flow velocity was measured before every run using the PIV set up, with the jet supply turned off, to ensure that the cross-flow velocity remain constant across the various runs performed on different days. The free stream turbulence intensity of the channel was previously measured using an LDA system and in-situ using the PIV system and was found to be just below 1% in both cases.

2.3.5 Limitations and Flow Characteristics

The required jet and cross flow velocity was set by the required jet Reynolds number and velocity ratio as well as the diameter of the jet nozzle exit. There

were 2 main considerations taken into account before the diameter of the jet was chosen, the jet size in the far field and the jet trajectory. Smith & Mungal [58] show that the size of the jet in the far field scales with $V_r d_j$ and, as shown in section 1.4.1 so does the jet trajectory. The limitation set on the jet trajectory was that the distance between the edge of the jet and the bottom wall of the tunnel at the most downstream measurement position was at least twice the size of the jet at said downstream position. This limitation was coupled with the jet size being large enough so that the estimated turbulent viscous length scales were resolved by the PIV measurements. With the exception of a single set, measurements were taken in the far-field of the cross-flow jet where the CVP is fully developed, defined by Smith & Mungal [58] as being after the branch point located at $x_{bp} = 0.2V_r^2 d_j$.

As mentioned in section 1.4 and by observation of the jet trajectory (1.26) and Circulation Reynolds number (1.27) equation, the cross-flow jet scales with downstream distance x, velocity ratio V_r and jet diameter d_j. Since the jet nozzle exit diameter is controlled by the considerations mentioned above, this left the velocity ratios and downstream locations to be selected. Given that the aim of this study is to examine the far field structure of the cross-flow jet for $V_r > 10$ and if it shows any signs of self-similarity, three different values of each parameter were chosen to be studied. Mean flow measurements at three downstream locations of $x/d_j = 30, 55, 85$ for $V_r = 10$, as well as at 3 different velocity ratios of $V_r = 10, 15, 20$ at a downstream location of $x/d_j = 85$ were performed to characterise the mean flow. The coherent structures at three downstream locations of $x/d_j = 15, 30, 85$ for a velocity ratio of $V_r = 10$ were measured via the use of Taylor's Hypothesis to examine how their shape and relative orientation evolves. Finally the downstream evolution of the towed jet for three velocity ratios of $V_r = 10, 20, 25$ was measured.

2.3.6 Uncertainty

The uncertainty in the jet velocity and carriage speed was estimated from the accuracy of the instruments used to measure them. For the jet speed that was the accuracy of the pressure transducer used quoted as a percentage full scale, and

for the carriage speed the sampling frequency of 1kHz, i.e $\pm 1ms$. The uncertainties in each quantity was calculated using the partial differential method, which involves calculation of the influence coefficients for the quantity in question, and are summarised in table 2.1. The uncertainty changes based on the magnitude of the quantity measured and thus a minimum to maximum range is shown in the table. The error in the free stream velocity for the Water Channel experiment,

Table 2.1: Uncertainties in Flow Parameters

	Uncertainty ϵ	
	Tow-Tank	Water Channel
U_{jet}	$2.4 - 10.6\%$	5.1%
U_{∞}	3.1%	$2 - 4\%$

which was measured and set using the Stereo PIV set up, was calculated based on the ± 0.1 pixel accuracy of the Gaussian fit in the PIV correlation plane [36].

2.4 Stereoscopic PIV Set-up

2.4.1 Basic Principles

Particle Image Velocimetry (PIV) is a non-intrusive, planar measurement technique. An in depth review of the technique is given by Raffel *et al.* [54], but a summary of the technique is presented here. The current basic setup of PIV, summarised in figure 2.8, is to illuminate a seeded flow field, using a thin monochromatic light sheet, twice in quick succession and record the scattered light from the particles onto an image pair using a single camera, one at time t and the other at time $t^1 = t + dt$ [1]. The displacement of the particles is then extracted by splitting the images into small Interrogation Windows (IWs), containing a small number of particles, and cross-correlating the respective windows. The result in the correlation plane gives a peak at the mean displacement location of the particles within the window. Thus a pixel displacement is obtained in each IW, and by calibrating the cameras this displacement is mapped to the measurement plane. Using the time delay between the image pair dt a velocity is

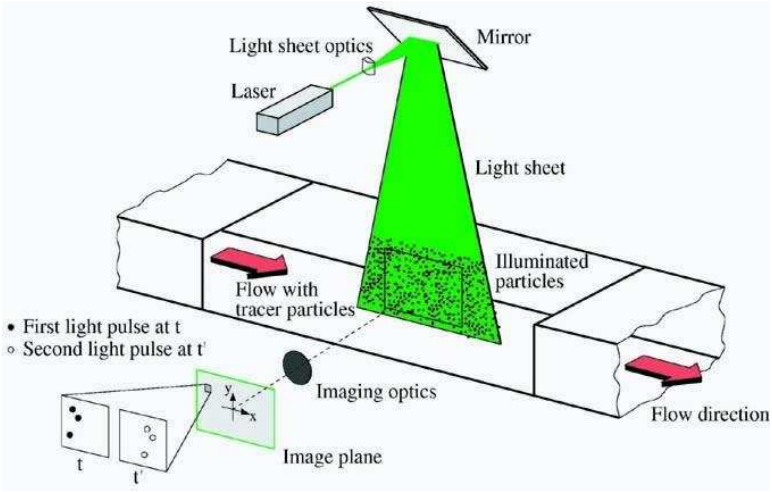

Figure 2.8: Basic principles of PIV. Based on the figure from Raffel *et al.* [54, p. 4].

extracted. Single camera, 2D-PIV described above can therefore extract only the two in-plane velocity components, thus resulting in planar 2-component velocity measurements.

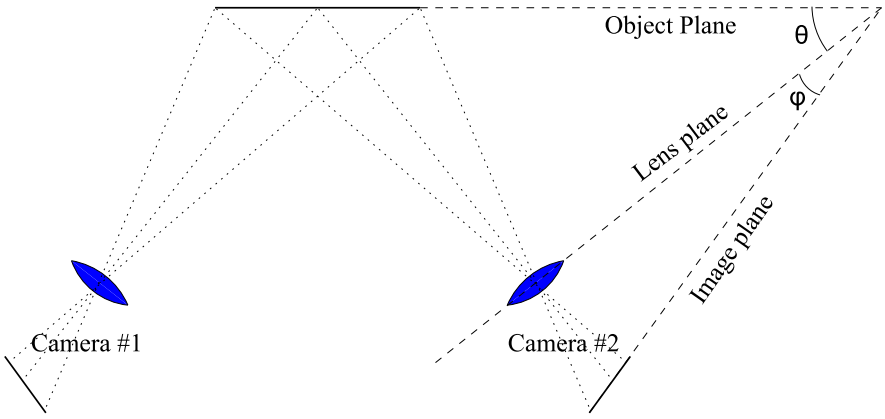

Figure 2.9: Basic configuration for rotational Stereoscopic PIV system. From Willert [66].

The principles of Stereoscopic-PIV (SPIV) is to illuminate the section of the flow to be measured using a thin light sheet and use two cameras to record light scattered off seeding particles present from two different viewing angles.

Figure 2.9 shows a basic rotational stereoscopic imaging configuration, with the measurement plane denoted as the object plane. Using the displacements of the particles in the images from the two different views, additional information about the out-of-plane motion of the particles in the object plane can be extracted. In order to convert the particle position on the image plane (camera CCD) in pixels to a particle position on the object plane (light sheet plane) in meters the two cameras need to be calibrated. Furthermore, in order to be able to extract 3 component vector fields from planar image fields additional information about the camera positions with respect to the object plane is necessary, which requires calibration images of the object plane which are not co-planar. This is done by having the cameras image a multi-level calibration plate, aligned with the light sheet at the measurement plane, containing a fixed grid of dots whose relative positions are known. The velocity measurement, similar to planar 2-component PIV, involves two images being recorded with a small temporal displacement and then cross-correlated to extract the particle displacement, one from each camera. The resulting velocity fields from the two viewing angles are then combined to additionally extract the out of plane velocity component thus resulting in a two dimensional - three component (2D-3C) velocity field.

The relative error in the out-of-plane component to the in-plane component is given by the reciprocal of the tangent of the off-axis half-angle θ in figure 2.9 [52]. Therefore in order for the measurements to have a balanced in-plane and out-of-plane error, an off-axis half angle of $\theta = 45°$ is chosen to be used in the experiments. This angle was also used by Dennis & Nickels [18], van Doorne & Westerweel [65] and Matsuda & Sakakibara [39] who performed Sterescopic-PIV measurements in the cross-plane of a boundary layer, pipe flow and a round free jet respectively. Furthermore, similar to these studies the camera orientation suggested by Willert [66] is used, where the cameras are orientated either side of the object plane. The advantage offered is that both cameras views are identically stretched thus offering a better reconstruction of the out-of-plane component. Furthermore the cameras can be set up in forward scatter mode, thus achieving a better signal to noise ratio in the images, but this was not done due to physical restrictions in the Water Channel and Tow Tank facilities. With the lens plane and the object plane not being parallel, the focal plane of the cameras are not

parallel to the object plane. This can be remedied by enforcing the Scheimpflug condition, which rotates the image plane with respect to the lens plane by an angle ϕ, as shown in figure 2.9. This ensures that the particles are in focus throughout the whole image plane.

2.4.2 Seeding

For all the measurements performed both the jet and the tank/channel were seeded. Since the PIV technique measures the velocity field by measuring the velocity of the particles it is important to check that the particles can accurately follow the flow. A good measure to check this is by calculation of the Stokes number defined as the ratio between the seeding particle response time τ_p and the flow time scale τ_f, which should be much smaller than 1, i.e $St = \frac{\tau_p}{\tau_f} \ll 1$. By use of Stokes drag law [54] an expression for τ_p can be found and is given in equation 2.2. ρ_p is the particle density and μ is the dynamic viscosity of the fluid in which it is suspended. The τ_p response time comes from a balance between the inertia of the seeding particle and the quasi-steady viscous-drag force, and represents a measure of the for the tendency of the seeding particle to attain velocity equilibrium with the fluid in which it is submerged. A small time response therefore, when compare to the flow time scales, would mean that the seeding particles can follow the flow with high fidelity.

$$\tau_p = \frac{d_p^2 \rho_p}{18\mu} \tag{2.2}$$

In the Water Channel experiments the flow was seeded with *Dantec Dynamics* silver-coated hollow glass spheres (*S-HGS*). These are borosilicate glass spherical particles with a density of $\rho_p = 1.4 g/cm^3$ and a size distribution ranging from $2 - 20\mu m$ with mean diameter of $d_p = 10\mu m$. The image size of the seeding particles was between 3-4 pixels which is close to the ideal size of 2-3 pixels [54, pp. 166-169]. Since smallest time-scale in the turbulent flow studied is the Kolmogorov time-scale, this is used as the flow time-scale and is estimated using the Kolmogorov micro-scale equation $\tau_f = \tau_\eta = (\nu/\epsilon)^{1/2}$. The measurements

performed do not resolve the Kolmogorov length scale, so an estimate to the value of ε is made using $\varepsilon = u_{turb}^3/l_{turb}$ [61], where u_{turb} and l_{turb} are characteristic turbulent velocity and length-scale. Calculating Re_Γ at a downstream position of $x/d_j = 30$, using equation 1.27, as the turbulent Reynolds number and the size of the jet $\delta\omega$ (defined later) as a turbulent length-scale, a turbulent velocity u_{turb} can be estimated from $Re_{turb} = (u_{turb}l_{turb})/\nu$. From this an estimate for the dissipation is made which results in a Kolmogorov time-scale estimate of $\tau_\eta = 2.4ms$. Using equation 2.2 the particle response time was calculated to be $\tau_p = 6.82\mu s$ giving a Stokes number $St = 2.84 \times 10^{-3}$ showing that the particles could accurately follow the smallest scales of the turbulent flow.

In the Tow Tank experiments the seeding particles used were *Potters Industries Conduct-O-Fil Spheriglass* spheres (*CoF-S*) with a mean diameter of $d_p = 51.6\mu m$ and a density of $\rho_p = 2.5g/cm^3$. The image size of the seeding particles was between 3-4 pixels which is again close to the ideal size of 2-3 pixels. Similar to the procedure followed above for estimating the Stoke number the fluid turbulent time scale τ_f used is that for small scales, i.e the Kolmogorov time scale. This was estimated using the Kolmogorov equation with $Re_{turb} = Re_\Gamma$ at $x/d_j = 85$, which is the start of the measurement domain. For a Kolmogorov time scale of $\tau_\eta = 9.1ms$ and a particle response time of $\tau_p = 0.32ms$ the resulting Stokes number is $St = 0.035 \ll 1$ which means that these particles could also accurately follow the flow. The properties for both seeding particles used are summarised in table 2.2.

Table 2.2: Summary of seeding particle properties

Property	*S-HGS*	*CoF-S*
Shape	Spherical	Spherical
Material	Borosilicate Glass	Glass
Mean diameter d_p	$10\mu m$	$51.6\mu m$
Diameter Distribution	$2 \leftrightarrow 20$	N/A
Density ρ_p	$1.4g/cm^3$	$2.5g/cm^3$
Stokes number St	2.84×10^{-3}	3.5×10^{-2}

2.4.3 Double Pulsed Lasers

The small seeding particles are illuminated using high power double pulsed laser light source.

For the time resolved measurements in the Tow Tank and Water Channel facilities a *New Wave Pegasus-PIV* laser system is used. This is a water cooled, dual-head, high repetition rate, diode-pumped Nd:YLF laser. At 1kHz the energy per cavity is 10mJ at a wavelength of 527nm, with a pulse width of 180ns and an exit beam diameter of 1.5mm. Since the laser system had a large repetition rate creating a small enough pulse separation that meets the temporal displacement needed between image pairs, both cavities were fired at the same time resulting in an effective energy per pulse of 20mJ.

For the Water Channel mean flow measurements a *New Wave Gemini-PIV* laser system is used. This is a water cooled, dual head, low repetition rate, flash lamp-pumped Nd:YAG laser. At 15Hz (maximum repetition rate) the energy per cavity is 120mJ at a wavelength of 532nm, with a pulse width of 3-5ns. The high power of the laser allowed for each cavity to be fired separately at the small temporal displacement required between image pairs and provide more than enough light to illuminate the particle field.

2.4.4 Laser Light Sheet Formation

The method of Stereoscopic PIV requires a sheet of light to be formed to illuminate the seeding particles. Since the monochromatic light exiting the laser is a beam, it is passed through a series of optics to expand it into a sheet in one direction and control its thickness in the direction perpendicular to the sheet plane.

For the Water Channel statistical measurements the laser was positioned underneath the channel. A standard variable focal length lens assembly, consisting of a negative focal length followed by a positive focal length spherical lens, was used to control the beam thickness by adjusting the relative position of the two lenses and hence the focal point. The beam was expanded into a sheet in the horizontal plane using a negative focal length cylindrical lens. A mirror positioned at 45^0 was used to deflect the expanded sheet upwards into the Water Channel

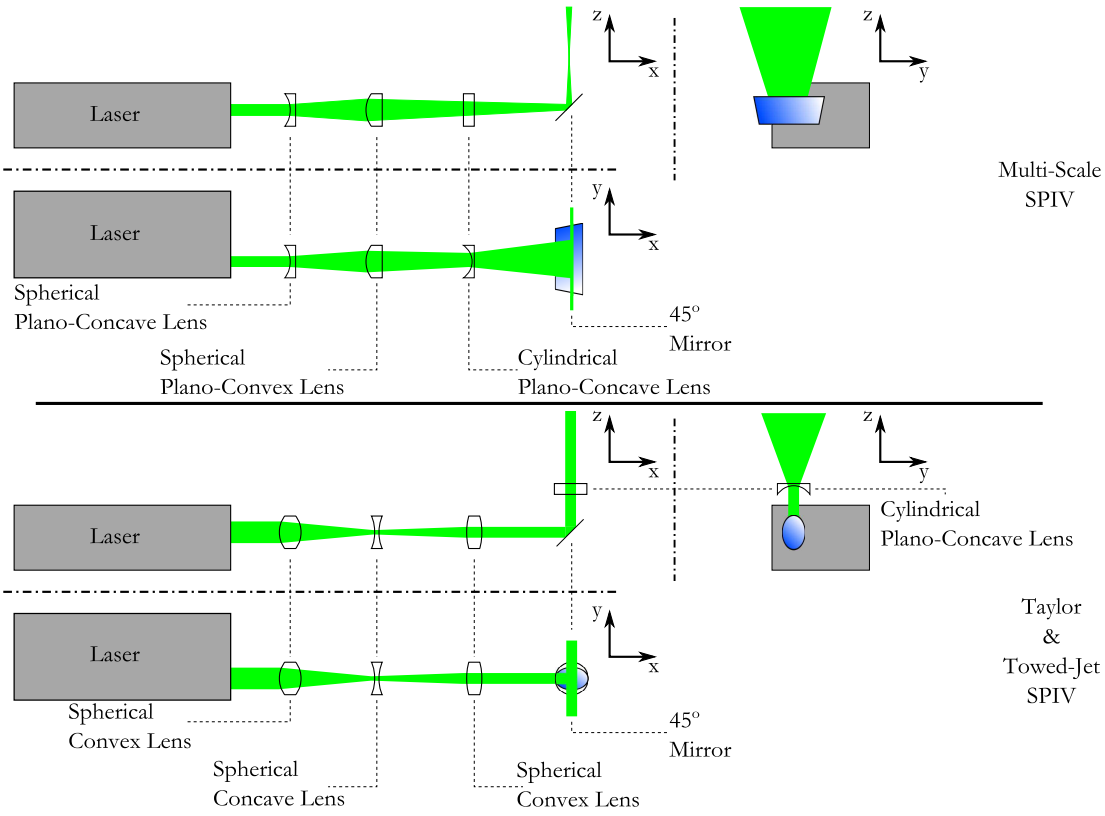

Figure 2.10: Schematic of the laser light sheet formation optics set up

aligned with the span-wise y-z plane. In order to obtain an approximately uniform thickness in the measurement plane with no focal lines, the focal line (or beam waist) was placed before the camera field of view along the path of the laser beam. The top part of figure 2.10 shows a schematic of this set up.

For the time resolved measurements in the Tow Tank and Water Channel facilities the high repetition rate laser was positioned underneath the respective tank. The beam thickness was adjusted by passing it through a *Edmund Optics 64417* beam expander in reverse to collimate it and reduce its width by a factor of 6. It was then turned up using a highly reflective mirror and expanded into a sheet aligned with the span-wise y-z plane using a hyperbolic lens. A schematic of this set up is shown in the bottom part of figure 2.10.

For both set ups the 45^0 mirrors that deflected the beams upward into the channels were mounted on a high precision single-axis manual translation stage. This allowed for the important parallel alignment of the light sheet with the calibration plate to be performed. The thickness of the sheet at the centre of the measurement field of view was not measured rigorously, but estimated to be $3mm$. Although the technique of SPIV does require a slightly thicker light sheet compared to two dimensional digital PIV, the relative orientation of the laser sheet with respect to the cross-flow (x-direction) made this relatively large thickness necessary in order to get a sufficient particle displacement in the recorded images whilst the particles remained inside the laser sheet. Furthermore, this thickness was also chosen so as to be close to the in-plane resolution, defined as the final interrogation window size used for the image cross-correlations.

2.4.5 Camera Set-up

The cameras used for the experiment were Photron Fastcam SA1.1 high speed CMOS cameras with a pixel resolution of 1024×1024, pixel size of $20\mu m$ and a 12-bit dynamic range bit-depth. The cameras had an $8GB$ memory buffer capable of storing a maximum of 5457 images. All cameras were mounted on a *Manfrotto 410 Junior* geared heads which were in turn attached to an optical rail frame built around the facilities. With the axis of the camera and the axis of the measurement plane in Stereoscopic-PIV not aligned (i.e the camera is not perpendicular to the

measurement plane), the lenses used are set at the Scheimpflug condition in order for the imaged particles to be in focus across the whole field of view via the use of Scheimpflug adapters for all camera set ups below.

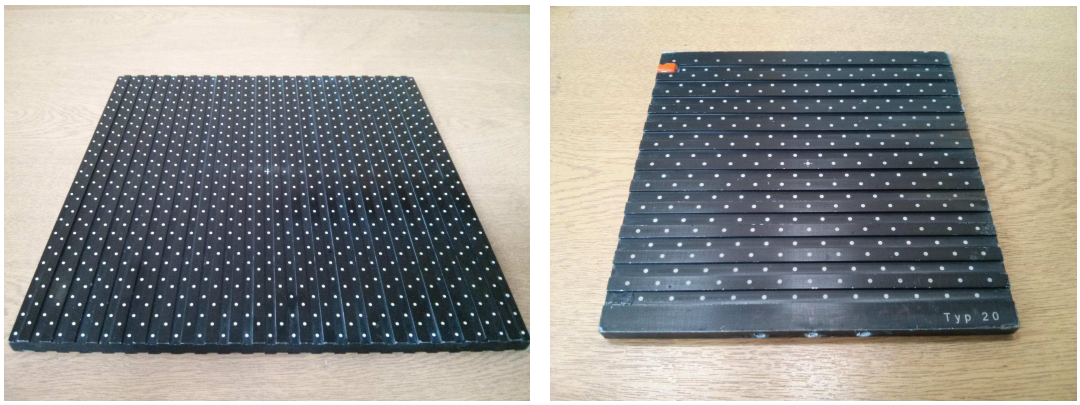

(a) (b)

Figure 2.11: Multi-level calibration plates used to calibrate the two cameras. The plates were made out of black anodised aluminium. The dots were $2mm$ in diameter and had a $15mm$ spacing on each level in both vertical on horizontal directions. Dots between levels were spaced by $7.5mm$in the horizontal direction and offset by $7.5mm$ in the vertical direction.

2.4.6 Triggering System

The signals used to control the various components were mainly 5V TTL signals generated via different means outlined below. The timings of the signals were checked using a *Tektronix* TDS 2002 digital oscilloscope. The cameras were controlled via the *Photron* FASTCAM Viewer software. Additional information, including pulse diagrams and wiring schematics can be found in Appendix A.

For the Water Channel experiments the TTL input signals for the cameras and lasers were created using a *National Instruments* PCI-6602 Counter/Timer connected to a BNC Terminal *BNC-2121*. The various signals were generated via an in house written *Lab-View* code, capable of controlling the various delays between the signals and pulse widths.

As mentioned in section 2.4.4, the orientation the the laser light sheet meant

that the measurement plane was perpendicular to the cross-flow direction. This created a compromise when setting the temporal displacement dt between image pairs, between getting a desirable in-plane particle image displacement (*one-quarter rule* [54, pp. 132-139]), where particles should move a quarter of the interrogation window, or laser sheet thickness in the case of Stereoscopic-PIV [65], and minimising out-of-plane particle pair loss. It should be noted that with the introduction of iterative grid-refining schemes to perform the image cross-correlations (described in section 2.6.1), the *one-quarter rule* for the in-plane particle image displacement is relaxed to the first-pass of the largest interrogation window size only. After various dt's were tested it was found that the limiting factor was the particle pair loss, i.e the value of dt was chosen based on the maximum allowable value before particle pair losses began. A value of $dt = 1ms$ was found to minimise particle pair loss and give a particle image displacement of approximately 3 pixels, except for one measurement case closest to the jet exit where a value of $dt = 0.5ms$ was found necessary.

For the mean flow measurements, vector fields (or image pairs) were acquired at a rate of 1Hz ($DT = 1s$) in order to make sure that the measurements were statistically independent. For the high-speed, time resolved measurements, images were acquired as a time series resulting in a vector field acquisition rate of 1kHz ($DT = 1ms$), with the exception of the case closest to the jet which was 2kHz ($DT = 0.5ms$). For each run performed the camera memory buffer was filled, i.e 5457 images were recorded, which resulted in 2728 vector fields for the mean flow measurements and 5456 vector fields for the high-speed measurements.

The Tow Tank experiments required something a little different. The TTL input signals for the cameras and laser were generated using a *Thurlby TGP110* pulse generator. A TTL signal from the *Compax* controller was used to start recording images when the position of the centre of the carriage (i.e the nozzle) was at the measurement location. This meant that the first recording was at $x = 0m$ consistently for all runs.

The required temporal displacement dt was initially estimated to be approximately $3.3ms$, i.e an acquisition frequency of 300Hz, based on the 1/4 rule of thumb. However by inspecting the particle displacement during measurements a displacement of $dt = 8ms$ gave better results for in plane particle displacement

which was approximately 5 pixels. As a result the data was recorded as a time series with $f = 125Hz$ ($DT = 8ms$) for all velocity ratios studied. Additional measurements at a frequency of 250Hz were taken only for a velocity ratio of 10.

2.4.7 SPIV Set-up in Water Channel Experiments

For the Multi-Scale measurements the camera set up is shown in figure 2.12. The aim of set up employed was to increase the measurements dynamic range by using a technique that was already well established. This would allow both large scale and small scale flow features to be analysed at the same time. A total of 4 camera were used in two Stereoscopic PIV set-ups, one in which the field of view captured the whole of the CVP, the Large-scale Field of View (LFoV), and the second which zoomed in on one of the vortex cores, the Small-scale Field of View (SFoV). Thus simultaneous overlapping measurements are obtained, each covering a different range of scales. The two cameras of each stereoscopic set up were positioned on one side of the channel at an angle of 45^o to the measurement plane, thus creating a 90^o angle between them. For the LFoV the viewing axis of the lenses intersected at the jet centreline whereas for the SFoV the intersection was offset to the left at the CVP core position. Both stereoscopic systems were simultaneously calibrated using a two-level *LaVision Type 20* calibration plate (figure 2.11b). This allowed for relative position between the centre of the two field of views to be easily set. The light sheet was carefully aligned parallel to the calibration plate by aligning the centre of the light sheet, in the direction of its thickness, with the top level of the plate on one side.

The change in medium across the channel wall introduces a significant optical distortion when an oblique viewing angle is in place as the light is refracted through the water-perspex-air interface. To minimise this distortion 45^o prisms, filled with distilled water, were mounted flash to the tunnel wall with the camera lens viewing axis perpendicular to the prism face. Furthermore distilled water was added between the prism and the tunnel wall to eliminate the possibility of an air pocket.

One of the main issues with multi-scale PIV measurements is the particle images themselves. Since the same particles are imaged in the two FoVs their

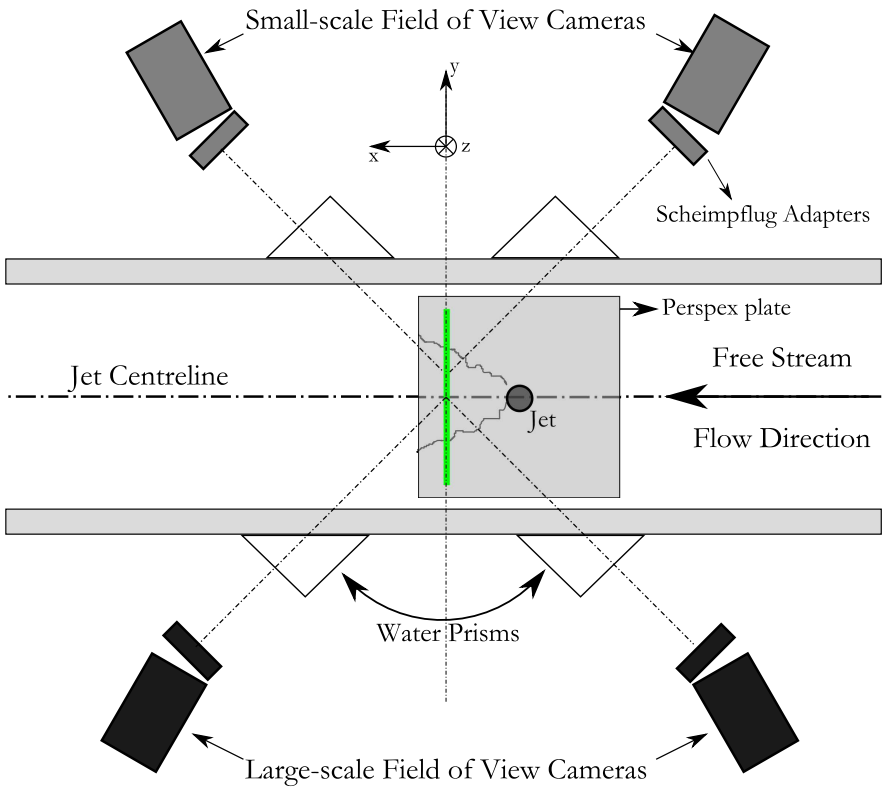

Figure 2.12: Schematic of the Multi-Scale SPIV camera set up. The camera set up for the Taylor SPIV is identical to that of the Multi-Scale SPIV with the Small-Scale Field of View stereoscopic set up removed.

size and density will be different. Specifically the particles in the small-scale FOV will have larger diameter and the seeding density will be lower for a given large-sale FoV. As a result the relative sizes of the two FoVs were chosen by finding a balance between the seeding density and the particle size so that image correlations can be performed with a window size of 32×32 pixels in the SFoV measurements and avoid peak-locking in the LFoV measurements. Increasing the ratio between the two FoVs would then introduce problems such as over seeding the flow or having particles which are less than a pixel in size. The best balance was found after testing various lenses and FoVs, resulting in the configuration summarised in table 2.3. A similar multi-scale PIV measurement was performed by Buxton [10] who measured the interaction between the large and small scales in the self similar region of a planar mixing layer. PIV measurements at two different resolutions were performed by having one camera on one side of the laser sheet capturing low resolution (large FoV) vector fields, and 3 cameras on the other side capturing high resolution (small FoV) vector fields at three different locations within the large FoV. All camera FoVs were illuminated by the same laser thus obtaining simultaneous overlapping measurements. Another example involves multi-scale measurements in a turbulent boundary layer by Phillip *et al.* [50] who study the energy fluxes across the turbulent/non-turbulent interface. An array of 8 cameras was used positioned in two rows, each one containing 4 cameras, with the bottom row of cameras having a higher resolution (small FoV) than the top row (large FoV). The FoVs in this case only had a small overlap between them and were stitched together to provide a single two dimensional velocity field.

Table 2.3: Multi-Scale and Taylor SPIV camera configuration

	LFoV	SFoV
Lenses	*Nikkor* 105mm	*Nikkor* 200mm
Aperture	$f/8$	$f/4$
FoV (mm^2)	158×124	55×50
Resolution (pix/mm)	8.9	17.6

The time resolved measurements used the same set-up, with the difference

that the high repetition rate laser was used to produce the light sheet and only the LFoV stereoscopic camera configuration was used. An attempt was made to perform time resolved multi-scale measurements but it was found that the laser was not powerful enough to produce satisfactory particle images for the SFoV. Three-dimensional flow structures can be extracted from the measurements by performing a 'Taylor' reconstruction of the data. A similar technique was used by Ganapathisubramani *et al.* [24] who measured the fine scales in a turbulent jet. This is done by taking the measurements in the single plane perpendicular to the cross-flow, analogous to the jets axis in Ganapathisubramani *et al.* [24], with the mean flow passing through it, and performing the reconstruction by 'artificially' translating measurements downstream using Taylor's Hypothesis. Other examples include the turbulent boundary layer reconstruction by Dennis & Nickels [18], the round free jet reconstruction by Matsuda & Sakakibara [39] and the pipe flow reconstruction by van Doorne & Westerweel [65]. Details of the reconstruction are discussed in section 2.6.2.

2.4.8 SPIV Set-up in Tow Tank Experiment

A schematic of the camera set up is shown in figure 2.13. The cameras were positioned at an angle of 45^o to the measurement plane, creating a 90^o angle between them. The cameras were fitted with *Nikkor* 105mm lenses, with an aperture setting of f/5.6, which resulted in a FoV size of $280mm \times 210mm$ and a resolution of $5.2pix/mm$. The calibration of the cameras was performed using a two level calibration plate, similar to the *LaVision Type 20* used in the Water Channel set-up (figure 2.11a), with the two cameras facing opposite sides of the plate. The light sheet was aligned with the calibration plate in the same way as for the Water Channel experiments.

The novel feature of this set up is that it allows the downstream evolution of the CVP to be measured without having to move the optical (camera + laser) set up. As the carriage moves across and away the from the measuring plane (i.e the laser sheet) the downstream position of the jet with respect to the laser sheet increases. Therefore the successive velocity fields extracted from the PIV measurements correspond to different downstream positions. This allows for 3D flow

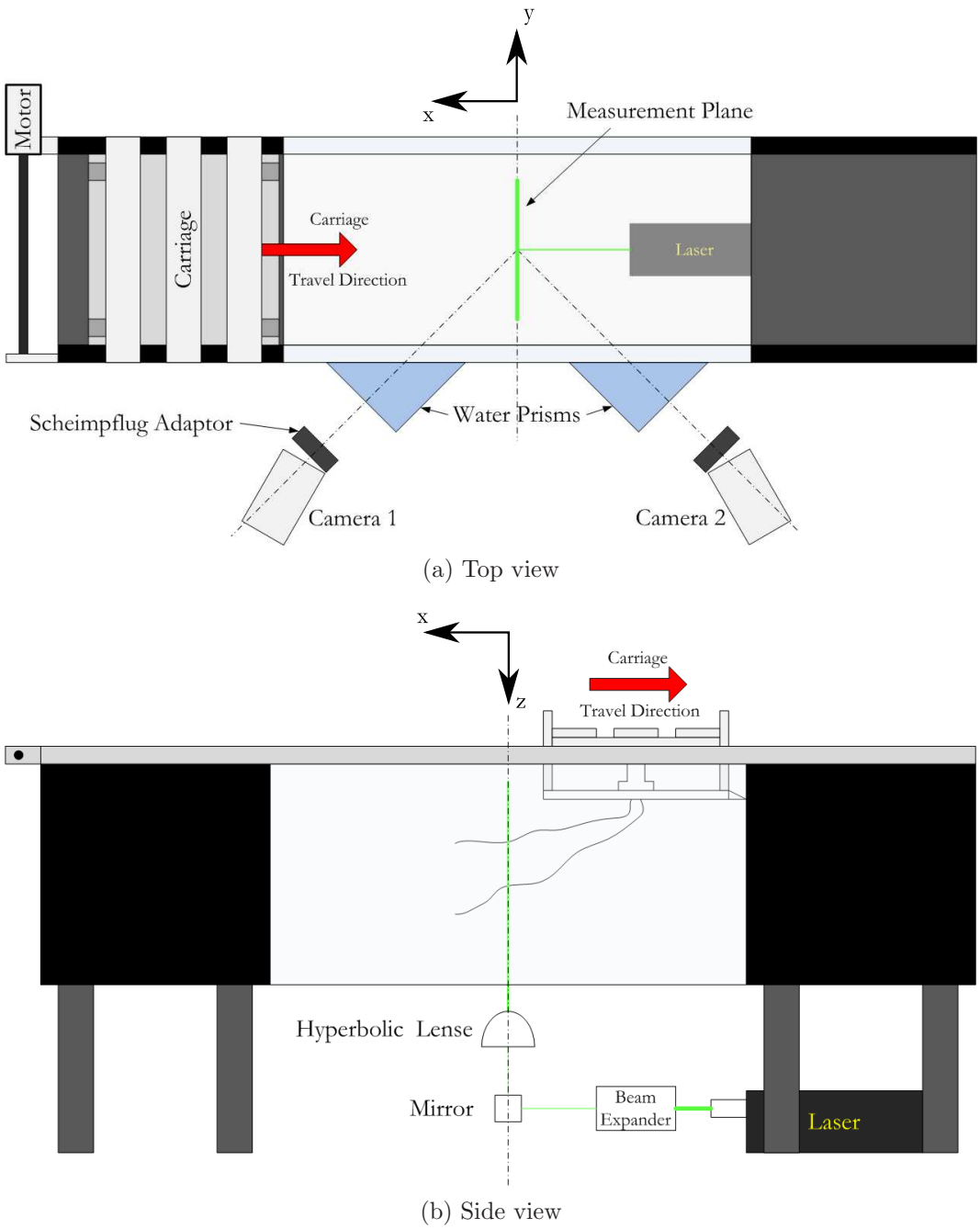

(a) Top view

(b) Side view

Figure 2.13: Schematic of the CVP cross-plane Stereoscopic experimental set up

structures to be extracted by performing a cinematographic reconstruction of the data. This is again similar to the 'Taylor' technique used by Ganapathisubramani *et al.* [24], however in the experiment preformed here, Taylor's Hypothesis is not strictly used as the reconstruction is performed from 'physical' downstream measurements. The technique is therefore more similar to a Scanning-PIV measurement, with the scanning speed being equal to the speed at which the jet is towed U_t, i.e the cross-flow velocity. Towing the jet through a quiescent flow effectively changes the frame of reference to that of moving with the cross-flow and therefore effectively removing the cross-flow velocity. As a result the difficulties of having the mean flow being perpendicular to the measurement plane are removed. The limits on the size of the reconstructed volume will be discussed in chapter 4.

A step by step account of the procedure followed to perform these measurements is outlined below.

- Before any measurements were taken the tank was stirred in order to ensure a uniform and appropriate seeding density. The tank was then allowed to settle for approximately 10 minutes, making sure that the tank was quiescent with no background motion.
- Recording of the voltage signals of the pressure transducer and optical switch was commenced
- The jet was turned on before the carriage moved and was allowed to settle for approximately 30 seconds.
- The laser was turned on and the cameras were set to wait for the trigger to start recording
- The carriage program was run. After the carriage stopped the cameras would continue to record until the camera buffer was full. Once the buffers were full the jet was turned off
- Recording of the voltage signals was stopped and the laser was turned off
- The tank was allowed to settle for 10 minutes before the process was repeated

To ensure consistency 5 runs for each V_r setting were performed. The aim was not to extract an average velocity field as this would require more runs.

2.5 PIV Uncertainties

Raffel *et al.* [54] classify the absolute measurement error ϵ_{tot} in the estimation of the displacement vectors as being made up of two types of error:

$$\epsilon_{tot} = \epsilon_{bias} + \epsilon_{rms} \tag{2.3}$$

The bias error ϵ_{bias} is associated with a bias introduced into the measurement which leads to a degree of over or under-estimation of the displacement vectors in all measurements. The rms error ϵ_{rms} is associated with random errors or measurement uncertainties and thus takes the form $\pm\epsilon_{rms}$. Sources for these errors include:

- Particle image diameter d_τ: For $d_\tau \leq 1$ pixel, the displacements tend to be biased towards integral values of pixels. This effect is known as peak locking and increases with decreasing d_τ. For single exposure image, such as those taken in the current experiment, a d_τ of approximately 2-3 pixels gives minimum error estimated as an rms-uncertainty of $0.02 - 0.04$ pixels [54, pp. 166-169]. Size of particle images for this experiment was on average between 2-4 pixels and peak locking did not occur.

- Particle Density: Low levels of particle density can increase the rms error due to the fact that there are less particle image pairs to correlate. Furthermore non-uniform particle density also introduces local errors in the vector field. For single exposure double frame PIV the rms-uncertainty decreases from 0.04 pixels to 0.015 pixels by increasing the particle image pair density within a 32×32 pixel interrogation window from 5.2 to 32 [54, pp. 170-172]. Increasing the seeding density increases the probability of matching particle image pairs and thus reduces the error. However if the density is too high then the laser light is scattered to such a degree before it reaches the measurement location that the resulting images are too dark.

A balance between the two is required for optimal results. A rule of thumb is for at least 3 to 4 particles to be present in both interrogation areas to be correlated [54, pp. 170-172].

- Regions of intense gradients and 3D flow: Large gradients can lead to loss of particle image pairs and thus bias the data towards smaller displacement vectors.

- Non-uniform laser illumination of particles: Particles have different contribution to the correlation function with the effect of introducing a bias based on the laser profile. The use of optics to produce an uniform laser sheet and image preprocessing ensured that the bias was removed.

- Camera Noise: Background noise in the images can introduce errors estimated as an rms-uncertainty ranging from $0.025-0.04$ pixels for noise levels between $5\% - 20\%$ [54, p. 174]. This was overcome by 'black correcting' the cameras before each set of measurements with the lights turned off and the laser turned off within the enclosure.

2.6 Data Processing

All of the acquired images were pre-processed and cross-correlated using the software program *Davis 7.2* by *LaVision GmbH*. The resulting vector fields were then exported and post-processed in the software program *MATLAB*.

2.6.1 Image Cross-Correlation

Using the captured calibration images, the cameras were calibrated using a 3rd order polynomial calibration function for all three camera set ups, except for the SFoV cameras of the Multi-Scale SPIV set up which were calibrated using the pinhole model. The results of the calibration were confirmed to be satisfactory as the calibration plate dots in the sum of the two de-warped images were perfectly coincident, for the appropriate level. Additionally an rms fit error below 0.3 pixels was achieved for all three set ups which is deemed to be very good. A common issue with Stereoscopic PIV is that a misalignment of the laser sheet with

the calibration plate during the calibration procedure would create a disparity between the imaged particle positions in the two cameras images (recorded at the same time). To correct for this a self-calibration procedure was applied which involves cross-correlating the images from the two cameras to extract a 'disparity map', which is used to adjust the calibration and remove the disparity between the two camera views.

The seeding particles used covered a range of particle diameter and thus resulted in particle images with high intensity fluctuation. To remove this fluctuations and make the particle intensities more uniform, the particle images were pre-processed using the *min/max filter* which involved passing them through a high-pass filter, to remove the local minimum background intensity, and then performing a local intensity normalisation. For the computation of the vector fields a multi-pass interrogation scheme with decreasing interrogation window size was used. In this scheme, after the first pass is performed, subsequent interrogation windows are offset and deformed based on information from the previous pass greatly increasing the fraction of matched particle pair images and hence the signal-to-noise ratio (strength of the correlation peak), thus reducing the rms uncertainty in the displacement vector to a minimum. A high accuracy Whittaker reconstruction technique was used to interpolate the the image intensity during the multi-pass vector calculation, and finally a normalised cross-correlation scheme was selected for the final cross-correlation. The location of the peak is measured by employing a Gaussian peak fit. The software used to perform the PIV processing fits two independent Gaussian functions to the correlation peak in the two directions, which provides an accuracy of the order of 0.1 pixels [36]. Details of the schemes and resulting in plane resolutions for the three set ups, based on the final interrogation window size, can be found in tables 2.4 and 2.5. A final interrogation window size of 32×32 pixels (px) was used for all measurements, with a 50% overlap for the time resolved measurements and a 75% overlap for the Multi-Scale mean flow measurement.

A vector validation algorithm was then applied to the resulting 2D-3C vector fields in order to remove any false vectors using a Q-factor thresholding and a 3×3 regional median filter. The resulting empty spaces are then filled with interpolated vectors, calculated as local mean of all non-zero neighbouring vectors.

Table 2.4: Multi-Scale (MS) and Taylor (T) SPIV processing parameters

	MS-SPIV		T-SPIV
	LFoV	SFoV	
Calibration rms error fit (px)	0.1	0.267	0.12
FOV (mm^2)	158×124	55×50	158×124
Initial Iterogation Window Size (px)	64×64	64×64	64×64
Final Interogation Window Size (px)	32×32	32×32	32×32
Overlap	75%	75%	50%
Resolution $\lambda_p(mm)$	3.6	1.8	3.6
Time between frames $dt(ms)$	1	1	1
Time between vector fields $DT = 1/f_s(ms)$	1000	1000	1

Table 2.5: Towed-Jet SPIV processing parameters

V_r	10	20	25
Calibration rms error fit (px)	0.247	0.267	0.175
FOV (mm^2)	280×210		
Initial Iterogation Window Size (px)	128×128		
Final Interogation Window Size (px)	32×32		
Overlap	50%		
Resolution $\lambda_p(mm)$	6.15		
Time between frames $dt(ms)$	8		
Time between vector fields $DT = 1/f_s(ms)$	8		

It must be noted that although the images for the Multi-Scale measurements were processed with a 75% overlap in order for the multi-pass interrogation scheme to be fully effective [54, pp. 146-158], the resulting vector fields were downsampled to a 50% overlap grid for post-processing. This was done because the central differencing scheme was used to estimate velocity gradients (section 2.7.2) which, with a 50% overlap, produces estimates that do not rely on velocity vectors that share image particles (i.e the velocity estimates used are independent), thus avoiding neighbouring gradient estimations from being locally biased (for example due to local low seeding density or high velocity gradient). To estimate velocity gradients using 75% overlap a different scheme would have to be used which takes into account that the two additional vectors due to the 75% overlap share particle images, and are thus correlated, into consideration. Lastly, a single pass 3×3 Gaussian smoothing filter is applied to the Multi-Scale SPIV data and a single pass 3×3×3 Gaussian smoothing filter is applied to the 3D reconstructed velocity fields of the Tow Tank and time resolved Water Channel SPIV data.

2.6.2 Volume Reconstruction

Details of how three-dimensional velocity fields are reconstructed from the time resolved Stereoscopic-PIV measurements are outlined here. As mentioned earlier, although both two-dimensional Towed Jet and high-speed, time resolved Water Channel SPIV measurements are converted to three-dimensional measurements, the different experimental set ups require a different approach to the reconstruction method.

In the Water Channel experiment, as mentioned in section 2.4.7, measurements were taken at various single downstream positions. Figure 2.14 shows a sequence of 4 velocity vector fields from the measurements at $x/d_j = 85$ separated in time by 3ms, which corresponds to the matched grid resolution in the streamwise x-direction of 1.8mm. The 4 vector fields show a strong resemblance to each other indicating a slow change with time, i.e the flow is very well temporally resolved. Furthermore given that there is also a predominant flow direction, that being the cross-flow (streamwise) direction, this suggest that Taylor's hypothesis or the 'frozen turbulence approximation' [60] can be applied in order to recon-

struct a quasi-instantaneous three dimensional velocity field from the temporally resolved data.

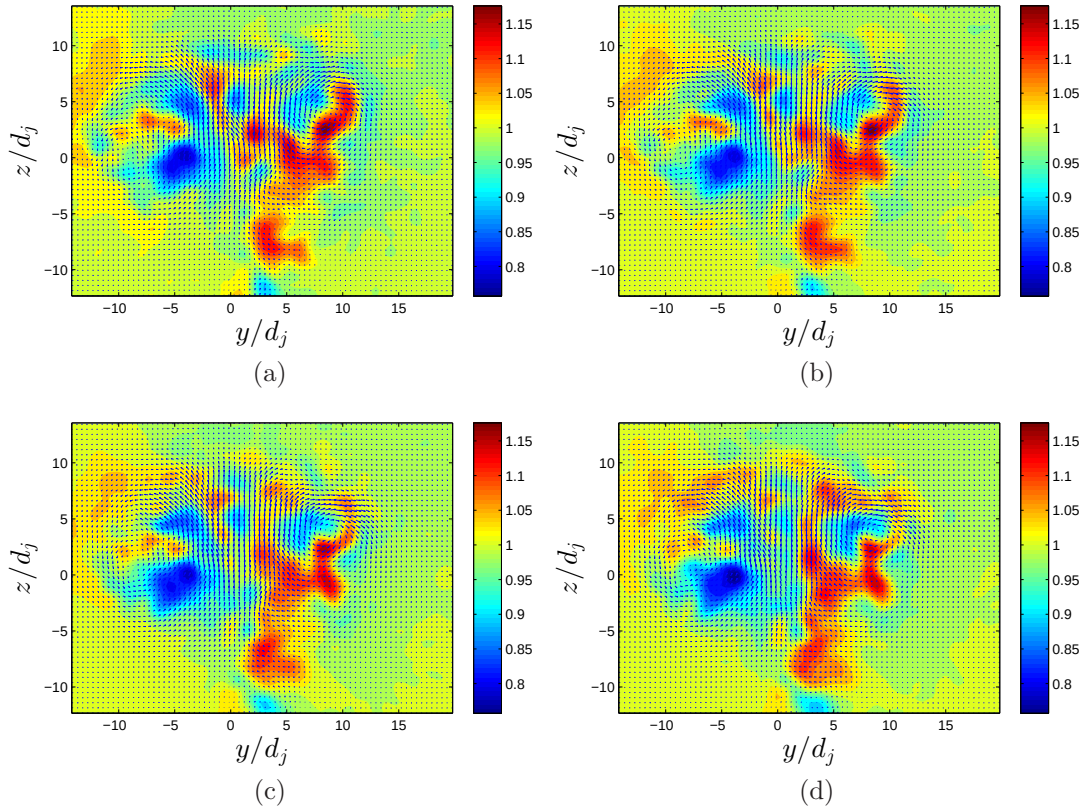

Figure 2.14: Sequence of four consecutive velocity vector fields, separated in time by 3ms. Vector arrows represent the in-plane velocity components V/U_∞ and W/U_∞, with the out of plane component U/U_∞ represented by the background colour contours.

Taylor's hypothesis was initially introduced in order to approximate spatial correlation from temporal correlations from a single hot-wire probe in flows having a predominant flow direction and low turbulence intensity level. This can be extended to PIV measurements if each final interrogation window is though of as a single measurement probe whose measurements are convected downstream by a convection velocity U_c. Given that with PIV measurements there exists a grid of 'probes', a quasi-instantaneous three dimensional velocity field can be reconstructed. Therefore Taylor's hypothesis can be used to estimate spatial

gradients from time derivatives as shown in equation 2.4.

$$\frac{\partial \mathbf{u}}{\partial x} = \frac{-1}{U_c}\frac{\partial \mathbf{u}}{\partial t} \tag{2.4}$$

$$x(q\Delta t, y, z) = (N - q)\Delta t U_c(y, z) \tag{2.5}$$

A spatially uniform convection velocity was utilised to convect the measurements downstream which was equal to the cross-flow velocity, $U_c(y, z) = U_{cf}$, thus resulting in a uniform, regular grid in the cross-flow x-direction. The downstream location of the convected measurements was calculated using equation 2.5, where the first recorded vector field, $q = 1$, in the time series measurement of N samples is convected furthest downstream. All successive recorded vector fields, $q = 2, 3, 4..., N$, separated in time by $q\Delta t$ are stacked behind this first vector field, with the last sample in the time series being furthest upstream. The aim of the reconstruction was also to match the spacing of the vectors in the x-direction with the in plane vector spacing, including the overlap vectors, as closely as possible. This is controlled via the quantity Δt which is the time difference between vector fields chosen from the time-series to be used to reconstruct the three dimensional velocity field. This is not the time difference between successive sampled vector fields from the PIV measurements DT, but is equal to an integer multiple of it.

Given the above, it is clear that the convection velocity chosen is important for the reconstruction process and the resulting pseudo three-dimensional volume, and it is a topic of much debate in the literature. A correct convection velocity would have to be calculated by additional measurements made in a plane containing the streamwise component x. From these measurements space-time correlations of the streamwise velocity component at two points separated by a distance δx for various time delays δt would need to be performed, as shown in equation 2.6.

$$R_{uu}(\delta x, \delta t) = \frac{\overline{u(x, y, z, t)u(x + \delta x, y, z, t + \delta t)}}{\sqrt{\overline{u^2}}\sqrt{\overline{u^2}}} \tag{2.6}$$

The convection velocity is then given by $U_c = \delta x/\delta t$, where δx and δt are the

values which maximise the correlation [25]. Such an analysis was performed by Dennis & Nickels [17] in a turbulent boundary layer using 2D-PIV measurements parallel to the wall to extract a correlation map and find U_c, and by Matsuda & Sakakibara [39] in a round jet using again 2D-PIV measurements in the streamwise-radial plane. Both showed that the local mean is the suitable convection velocity. Ganapathisubramani *et al.* [24] also used the local mean as the convection velocity when investigating the fine scale structures in a turbulent jet. Given that the mean velocity profile of U for the cross-flow jet is not one dimensional, as it is for the boundary layer with distance from the wall and for the round jet with distance from the jet axis, performing such an analysis would require measurements in multiple planes spanning the whole width and height of the CVP which would very difficult and time consuming. Alamo & Jimenez [3] introduced a new technique of calculating the convection velocity using spectral information in only one plane (space or time), and local derivatives in the remaining plane. The technique, summarised by Moin [41], involved finding the frame of reference (i.e a convection velocity) in which the variance of total derivative of a propagating wave is minimised. For a propagating wave proportional to $exp[i\kappa(x - ct)]$ (with wave number κ and phase velocity c), moving in a frame of reference with speed c would freeze the wave, meaning Taylor's approximation applies exactly and the variance of the total derivative would be zero. Application of their technique, which included the dependence on wavelength and wall distance, on data from numerical simulation of a turbulent channel flow showed that, away from the wall, small scales move with the local mean velocity, whereas the larger scales are convected with an almost uniform velocity which is close to the bulk flow velocity. Elsinga *et al.* [21] showed, using Tomographic-PIV, that vortical structures in a turbulent boundary layer are passively convected by the external velocity field, without them undergoing a significant change in topology over a time-scale of the order of a large-scale eddy turn-over time (taken as the boundary layer thickness over the free stream velocity). Since Taylors Hypothesis is applied here with the large-scale structures in mind, were it works best [17], it is reasonable to assume that they are convected by the cross-flow. Furthermore considering that in the far field, where the CVP is fully developed and the velocity magnitudes within the CVP are comparable to the cross-flow velocity, a

constant convection velocity equal to the cross-flow is a good approximation. A constant convection velocity was eventually used by Matsuda & Sakakibara [39], given a small variation in the mean velocity in their area of interest, and by van Doorne & Westerweel [65] to reconstruct the transitional flow in a pipe, both of which provided good results.

In chapter 4 an assessment of Taylor's Hypothesis will be carried out by looking at various properties of the resulting 3D volume reconstructed, such as divergence etc.

In the towed jet measurements, as mentioned in section 2.4.8, the experimental set up allowed for the downstream evolution of the CVP to be measured without moving the laser and cameras. The measurement volume was simply reconstructed by 'stacking' vector fields in the $y-z$ plane side by side with the distance x between them decided by the velocity of the carriage and the time between pulses dt, i.e the vector field sampling rate. The velocity of the carriage can therefore be considered as the 'scanning speed' and dt can be seen as the quantity controlling the resolution in the x-direction. The x location of the stacked vector fields is calculated using equation 2.7.

$$x(q\Delta t, y, z) = (q-1)\Delta t U_t \tag{2.7}$$

Similar to the equation used for the Water Channel reconstruction (equation 2.5), q represents successive vector fields ($q = 1, 2, 3, ...N$), in the order the were recorded, and Δt the time separation between them. However by comparing the two equations, the vector fields here are stacked in reverse order here due to the fact that as time progresses during data acquisition, the jet moves further away from the measurement plane as explained in section 2.4.8. Therefore in this case the last recorded vector field in the recorded time series is translated furthest downstream.

2.7 Post Processing

2.7.1 Reynolds Decomposition

A Reynolds decomposition is carried out in order to split the velocity into a mean and fluctuating component as follows:

$$U_i(\mathbf{x}, t) = \overline{U}_i(\mathbf{x}) + u_i'(\mathbf{x}, t) \tag{2.8}$$

where the $\mathbf{x}$ is the position vector $\mathbf{x} = (x, y, z)$. For statistically stationary turbulence the time average $\overline{U}$ is given by

$$\overline{U} = \frac{1}{T}\int_0^T U(t)\,\mathrm{d}t, \tag{2.9}$$

for large enough sampling time T. For discrete data, a temporal mean of an ensemble of any quantity $\overline{\psi}$ acquired over time is calculated using equation 2.10, where m denotes the sample index within the ensemble and N the total number of samples. The same equation can be used to calculate spatial means as well.

$$\overline{\psi} = \frac{1}{N}\sum_{m=1}^{N}\psi_m(t) \tag{2.10}$$

2.7.2 Gradients

The velocity gradients were calculated using a central differencing scheme, which is second order accurate. The equations for the calculation of the gradients in the y and z direction for the streamwise component U are given below.

$$\left(\frac{\partial U}{\partial y}\right)_{i,j} = \frac{U_{i+1,j} - U_{i-1,j}}{2 \times \delta y} \qquad \left(\frac{\partial U}{\partial z}\right)_{i,j} = \frac{U_{i,j+1} - U_{i,j-1}}{2 \times \delta z} \tag{2.11}$$

$$\left(\frac{\partial U}{\partial y}\right)_{i,j} = \frac{U_{i+1,j} - U_{i,j}}{\delta y} \qquad \left(\frac{\partial U}{\partial z}\right)_{i,j} = \frac{U_{i,j+1} - U_{i,j}}{\delta z} \tag{2.12}$$

$$\left(\frac{\partial U}{\partial y}\right)_{i,j} = \frac{U_{i,j} - U_{i-1,j}}{\delta y} \qquad \left(\frac{\partial U}{\partial z}\right)_{i,j} = \frac{U_{i,j} - U_{i,j-1}}{\delta z} \tag{2.13}$$

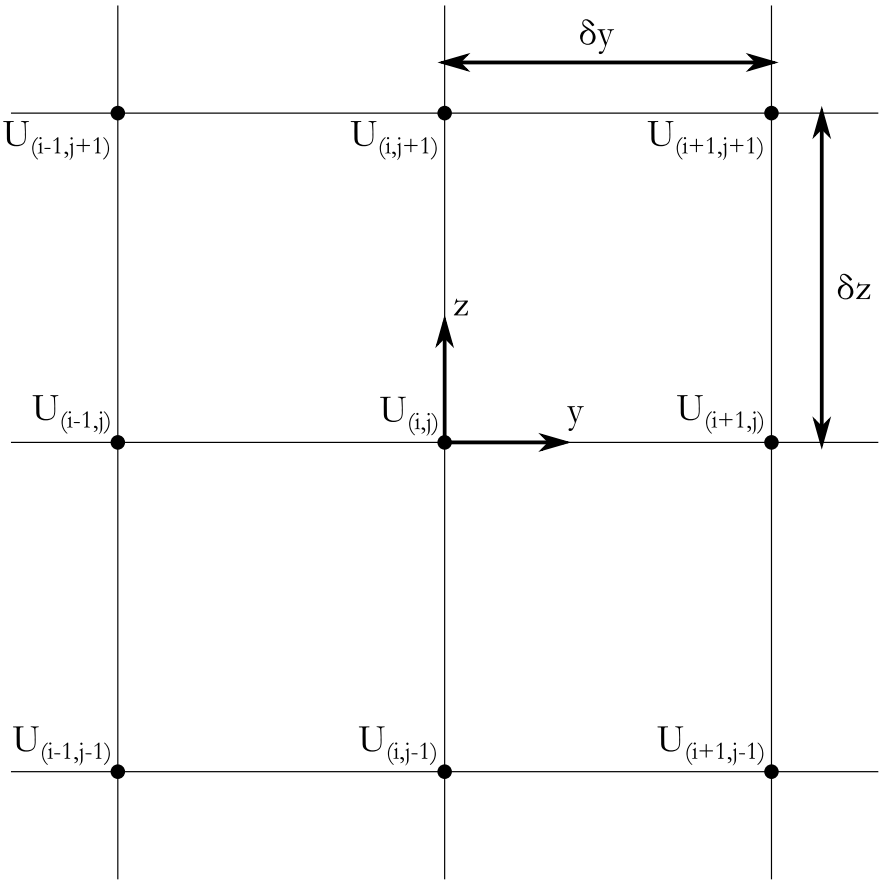

Figure 2.15: Discretised velocity field

Equation 2.11 is the second order central differencing scheme which is used in the centre of the data domain. At the edges of the data domain forward and backward differencing schemes, equations 2.12 and 2.13 respectively, are used which are first order accurate. The same equations are applied similarly for all components of $\mathbf{U}$ where $\mathbf{U} = (U, V, W)$. Furthermore the same schemes are applied in the x-direction for the case of the 3D measurements.

The three components of vorticity are calculated by taking the curl of the velocity field, $\omega = \nabla \times \mathbf{U}$ as follows.

$$\omega_x = \frac{\partial W}{\partial y} - \frac{\partial V}{\partial z} \tag{2.14a}$$

$$\omega_y = \frac{\partial U}{\partial z} - \frac{\partial W}{\partial x} \tag{2.14b}$$

$$\omega_z = \frac{\partial V}{\partial x} - \frac{\partial U}{\partial y} \tag{2.14c}$$

The vorticity vector is then given by $\boldsymbol{\omega} = \omega_x \hat{\mathbf{e}}_\mathbf{x} + \omega_y \hat{\mathbf{e}}_\mathbf{y} + \omega_z \hat{\mathbf{e}}_\mathbf{z}$ with magnitude $\omega = \sqrt{\omega_x^2 + \omega_y^2 + \omega_z^2}$, where $\hat{\mathbf{e}}_\mathbf{x}, \hat{\mathbf{e}}_\mathbf{y}$ and $\hat{\mathbf{e}}_\mathbf{z}$ are unit vectors in the x, y and z directions respectively.

Enstrophy is a scalar measure of the vorticity magnitude, defined by equation 2.15 in tensor notation, similar to how kinetic energy can be considered as a scalar measure to velocity.

$$\Omega = \frac{1}{2}\omega_i \omega_i \tag{2.15}$$

Circulation is defined as the line integral of velocity along a closed loop C. Using Stokes theorem this can be converted to a calculation of the vorticity flux through the surface S enclosed by C, as shown in equation 2.16.

$$\Gamma = \oint_C \mathbf{u} \cdot \mathrm{d}\mathbf{l} = \iint_S \nabla \times \mathbf{u} \, \mathrm{d}\mathbf{S} = \iint_S \boldsymbol{\omega} \, \mathrm{d}\mathbf{S} \tag{2.16}$$

The circulation is calculated using the planar Multi-Scale SPIV measurements from which only the out-of-plane, i.e streamwise, vorticity component is available. The equation is discretised for the discrete vorticity field (resulting from the PIV data) as in equation 2.17, where δy and δz being the separation between each data point in the y and z direction respectively and $n \times m$ is the number of data

points used for the calculation.

$$\Gamma = \sum_{j=1}^{j=m} \sum_{k=1}^{k=n} \omega_{x,ijk} \delta y \delta z \tag{2.17}$$

The circulation calculation needs a boundary to be defined around which the calculation is performed. Normally this would be the largest iso-vorticity contour defining the boundary. However the presence of noise in the data can influence the circulation value calculated and thus a threshold is defined around an appropriate iso-contour level. A sensitivity analysis showed that the circulation increased linearly with decreasing threshold level defined as a fraction of peak value ω/ω_0. A 5% threshold was found to define a appropriate iso-contour, separating the two cores in the mean field clearly and removing background noise giving a good estimate to the circulation.

In the two dimensional Multi-Scale SPIV measurements the location of the cores of the CVP can be found by choosing a certain quantity to track. For the mean profile tracking the location of the peak vorticity magnitude would be a suitable choice, but this would prove to be a problem for tracking the core location from instantaneous (not averaged) measurements given its turbulent nature. To overcome this problem the vorticity centroid is used, which is analogous to the centre of mass of a body. In the $y-z$ plane the coordinates of the vorticity centroid are defined in equation 2.18, calculated using the vorticity normal to the measurement plane ω_x, i.e the streamwise vorticity component.

$$y_c = \frac{\iint y\omega_x \, \mathrm{d}y\mathrm{d}z}{\iint \omega_x \, \mathrm{d}y\mathrm{d}z} \qquad \text{and} \qquad z_c = \frac{\iint z\omega_x \, \mathrm{d}y\mathrm{d}z}{\iint \omega_x \, \mathrm{d}y\mathrm{d}z} \tag{2.18}$$

2.7.3 Vortex Detection

As mentioned in section 1.6, the cross-flow jet is composed of many coherent structures. Therefore identifying them and distinguishing their geometry, in both 2D and 3D measurements, is very important in understanding the structure of the cross-flow jet. Enstrophy, which is simply the square of the vorticity magnitude (equation 2.15), is one of the parameters used to visualize the vorticity field. A topological analysis using Critical Point Theory can be used to identify salient

flow features and thus better characterise the flow.

The topological methodology of using Critical Point Theory and the velocity gradient tensor has been used as a means of identifying structures within a flow. It was initially meant as a framework to better visualize and understand complex three-dimensional flow fields. The concept of this method is to split up the field in question into salient features, namely nodes, saddles and foci. This therefore allows the topological structure of an average or instantaneous velocity to be studied. Perry & Chong [47] initially performed a classification of critical points in two-dimensional planes and was later extended to be applicable to general three-dimensional flows by Chong *et al.* [13]. In short the full velocity gradient tensor in the case of a fluid flow contains all of the information about the flow field around the critical point. This is defined as 'points in the flow field where the streamline slope is indeterminate and the velocity is zero relative to an appropriate observer'. The critical point can then be classified as either a node saddle or focus through the analysis of the VGT which in three-dimensions is given by:

$$\mathbf{A} = \begin{bmatrix} \frac{\partial U}{\partial x} & \frac{\partial U}{\partial y} & \frac{\partial U}{\partial z} \\ \frac{\partial V}{\partial x} & \frac{\partial V}{\partial y} & \frac{\partial V}{\partial z} \\ \frac{\partial W}{\partial x} & \frac{\partial W}{\partial y} & \frac{\partial W}{\partial z} \end{bmatrix} \tag{2.19}$$

The analysis is based on the eigenvalues,with corresponding eigenvectors, and the three invariants of a 3×3 Jacobian matrix which are capable of completely classifying the topology of the three-dimensional flow pattern.

A comprehensive background of analysis is presented by Perry & Chong [47] and Chong *et al.* [13] and a summary of that is only presented here. The eigenvalues of the velocity gradient tensor can be found by solving $det[A - \lambda I] = 0$ which results in the characteristic equation

$$\lambda^3 + P\lambda^2 + Q\lambda + R = 0 \tag{2.20}$$

where λ are the eigenvalues and P, Q and R are the first, second and third invariants respectively. The eigenvalues of the 3×3 velocity gradient tensor, can

either be (i) all real, (ii) all real with a double root or (iii) one real root and complex conjugate pair. The distinction between (i) or (ii) and (iii) is important as it separates the classification of critical points to saddles and nodes (case (i) and (ii)) and foci/vortices (case (iii)). In case (iii) the eigenvector corresponding to the real eigenvalue represents the direction of the axis of the vortex.

The imaginary part of the complex conjugate pair eigenvalue, λ_{ci}, can therefore be used as vortex identifier. The quantity represents the strength of the rotating motion in the plane spanned by the two eigenvectors corresponding to the imaginary eigenvalue pair. Zhou *et al.* [69] named this the *swirling strength* of the vortex. Its advantage is that it does not include the contribution of vorticity from non-spiralling motion, such as shear layers, thus allowing for a clearer detection, and visualisation, of the core of vortex tubes. λ_{ci} has units of s^{-1} and is therefore analogous to vorticity. This can be extended to be analogous to enstrophy by plotting λ_{ci}^2.

The calculation of swirl shown above therefore requires 3D measurements to be performed in order to be calculated. The streamwise-x, spanwise-y and wall-normal-z components of swirl can also be calculated by using the same method as above but on the reduced 2D VGT. It can therefore be calculated for 2D planar measurements by performing the same analysis on the reduced VGT (equation 2.21), giving a measure for the in-plane swirl motion.

$$\mathbf{A_r} = \begin{bmatrix} \dfrac{\partial V}{\partial y} & \dfrac{\partial V}{\partial z} \\ \dfrac{\partial W}{\partial y} & \dfrac{\partial W}{\partial z} \end{bmatrix} \tag{2.21}$$

The swirling strength λ_{ci} does not have a sign since it is the imaginary part of the complex conjugate pair eigenvalue. Therefore the sense of rotation, clockwise or counter-clockwise is not retained. Given that it is very similar to vorticity, it is reasonable to assign a sign equal to the local sign of a chosen vorticity component, $\omega_i / \mid \omega_i \mid$. This technique has been used by other researchers in previous studies [18, 31].

2.8 Turbulent Length-Scales

Since the measurements performed are mainly to study the large scale features of the flow the resolution requirement is set by the viscous length scale λ_ν. The viscous length scale is the length scale at which viscosity begins to have an effect on the turbulent flow. This can be taken as the scale at which the turbulent power spectra begins to deviate from the -5/3 power law behaviour (inertial range) at high wavenumbers. It should be noted that two-point correlations are performed in the next chapter, allowing for the calculation of the integral length scale from equations 1.14 or 1.16. However due to inhomogeneity in the turbulent velocity field (as will be observed later), the viscous length scale is chosen as the characteristic turbulent length scale, as it is also the most frequently used one in the JICF literature involving PIV measurements [27, 57, 58, 59]. The Kolmogorov length scale λ_κ can be calculated from Kolmogorov's equation

$$\lambda_\kappa = \left(\frac{\nu^3}{\varepsilon}\right)^{1/4}. \tag{2.22}$$

Since dissipation measurements are not available, ε can be estimated from $\varepsilon = u_{turb}^3/l_{turb}$ [61], where u_{turb} is a characteristic turbulent velocity and l_{turb} a characteristic turbulent length scale. Substituting this into equation 2.22 an alternative equation is derived give by

$$\lambda_\kappa = \Lambda l_{turb} Re_{turb}^{-3/4} \tag{2.23}$$

where $Re_{l_{turb}}$ is a characteristic turbulent Reynolds number. The characteristic turbulent length scales most often used in these calculations is the size of the flow δ, examples being the jet half-width for a free or co-flowing jet and the size of a boundary layer, with an equivalent Reynolds number Re_δ for the characteristic turbulent Reynolds number, based on a mean local velocity.

The value of Λ is of the order of unity when estimating the Kolmogorov lengthscale. The viscous length scale λ_ν is a multiple of λ_κ and so equation 2.23 can be used to estimate it with $\Lambda = \lambda_\nu/\lambda_\kappa > 1$. Different authors use different values of Λ for different applications, but the values used for the cases of a jet in cross-flow are shown in table 2.6. As a conservative estimate a value

Table 2.6: Summary of quantity $\Lambda = \lambda_\nu/\lambda_\kappa$ used in the literature

Authors	Measurement Technique	Λ
Shan & Dimotakis [57]	PLIF	50
Su & Mungal [59]	PIV & PLIF	15
Hasselbrink & Mungal [27]	PIV & PLIF	O(10)
Smith & Mungal [58]	PLIF	25

of 15 will be used as suggested by Su & Mungal [59]. The characteristic length scale δ_ω used will be the jet width defined as the distance between the 5% peak vorticity points along the profile through the cores of the mean vorticity field in the spanwise y-direction. Furthermore for the crossflow jet a suitable Reynolds number to be used is the circulation Reynolds number Re_Γ as given by Broadwell & Breidenthal [9]. This is reproduced below for clarity together with the equation used to estimate λ_ν.

$$Re_\Gamma = \left(\frac{x}{V_r d_j}\right)^{\frac{-1}{3}} Re_j \tag{2.24}$$

$$\lambda_\nu = 15\delta Re_\Gamma^{-3/4} \tag{2.25}$$

Chapter 3

Mean Flow Properties in the Far-Field

Using the data from the MS-SPIV measurements the flow is characterised by investigating mean flow and statistical turbulent properties in the far field of the cross-flow jet for the various flow conditions studied. Before this however, it is important to make an assessment of the measurements by quantifying the resolution for the various conditions and the level of statistical convergence.

The chapter begins with an assessment of the PIV measurements by looking at the experimental resolution and the resulting dynamic range of scales covered, the statistical convergence of the data which will be used as a measure of measurement accuracy and a look at the effect of decreasing the interrogation window size versus decreasing field of view size i.e an assessment of the Multi-Scale SPIV technique. With the assessment complete the jet trajectory and mean vorticity field will be examined to characterise the flow. After that the instantaneous vorticity structure of the CVP will be examined by looking at pdfs of various quantities, such as vorticity and the position of maxima and minima. The effect of this structure will then be examined by firstly looking at the mean velocity profiles and resulting strain fields. Finally the underlying turbulent field will be examined by looking at the rms velocity and Reynolds stress profiles and by using the results from all the mean profiles the presence of structures will be investigated from the 2D measurements by looking at various spatial correlation profiles.

Table 3.1: Flow conditions for MS-SPIV Experiment. The jet diameter for all conditions was $d_j = 4mm$.

V_r	x/d_j	x_{bp}/d_j	U_{jet} m/s	U_∞ m/s	Re_{jet}	Re_Γ	No of Samples
	30					1.39×10^4	5456
10	55	20	5.7	0.57	2×10^4	1.13×10^4	5456
	85					9.80×10^3	8184
15	85	45	5.7	0.38	2×10^4	1.12×10^4	2728
20	85	80	5.7	0.285	2×10^4	1.23×10^4	5456

3.1 Measurement Assessment

The flow conditions studied are detailed in table 3.1. Since the measurements were performed at specific downstream positions, the Circulation Reynolds number Re_Γ, estimated using equation 1.27, is included in the table.

3.1.1 Data Resolution

Using the analysis outlined in section 2.8, the Kolmogorov length-scale η and viscous length-scale λ_ν are estimated for each downstream location and velocity ratio studied and summarised in table 3.2. Both length-scales increase with downstream distance for a fixed velocity ratio of $V_r = 10$, and also increase with increasing velocity ratio at a fixed downstream location of $x/d_j = 85$.

By performing simultaneous measurements with two different FoV sizes the dynamic range of the measurements, and hence the range of turbulent structures that can be resolved, is increased. So for example for the measurements performed at $x/d_j = 85$ for $V_r = 20$, the range of scales that can be Nyquist resolved in the Large FoV is $1162\eta - 53\eta$. Similarly for the Small FoV the range is $404\eta - 26.2\eta$. Combining the range covered by the two field of views approximately doubles the dynamic range of the measurement to $1162\eta - 26.2\eta$.

Since it is the large-scale structures which are of interest, which contain most of the turbulent energy, the fact that the viscous lengthscales are not fully resolved should pose a problem to the analysis performed here. Hasselbrink & Mungal

Table 3.2: Experimental resolution for a jet Reynolds number of $Re_{jet} = 2 \times 10^4$. The jet diameter for all conditions was $d_j = 4mm$.

	V_r	10	10	10	15	20
	x/d_j	30	55	85	85	85
	δ_ω	$18.1 \times d_j$	$20.3 \times d_j$	$22.1 \times d_j$	$34.3 \times d_j$	$39.7 \times d_j$
	$\lambda_\kappa(mm)$	$0.06mm$	$0.07mm$	$0.09mm$	$0.126mm$	$0.136mm$
Large-Scale	FoV $(158\times124mm^2)$	$2633\lambda_\kappa \times 2066\lambda_\kappa$	$2257\lambda_\kappa \times 1771\lambda_\kappa$	$1755\lambda_\kappa \times 1377\lambda_\kappa$	$1254\lambda_\kappa \times 984\lambda_\kappa$	$1162\lambda_\kappa \times 912\lambda_\kappa$
	Resolution $(\lambda_{p_L} = 3.6mm)$	$60\lambda_\kappa$ $4\lambda_\nu$	$51.4\lambda_\kappa$ $3.4\lambda_\nu$	$40\lambda_\kappa$ $2.7\lambda_\nu$	$29\lambda_\kappa$ $1.93\lambda_\nu$	$26.5\lambda_\kappa$ $1.77\lambda_\nu$
Small-Scale	FoV $55 \times 50mm^2$	$917\lambda_\kappa \times 833\lambda_\kappa$	$785\lambda_\kappa \times 714\lambda_\kappa$	$611\lambda_\kappa \times 556\lambda_\kappa$	$437\lambda_\kappa \times 397\lambda_\kappa$	$404\lambda_\kappa \times 368\lambda_\kappa$
	Resolution $(\lambda_{p_S} = 1.8mm)$	$30\lambda_\kappa$ $2\lambda_\nu$	$25.7\lambda_\kappa$ $1.71\lambda_\nu$	$20\lambda_\kappa$ $1.3\lambda_\nu$	$14.3\lambda_\kappa$ $0.95\lambda_\nu$	$13.2\lambda_\kappa$ $0.88\lambda_\nu$

[27] quantified the error associated with the finite resolution by thinking of it as a filtering of the energy containing scales for wave numbers above $k > 1/2\lambda_p$ by the final Interrogation window in the PIV process. To makes this estimation the energy spectrum is assumed to follow the $-5/3$ power-law throughout the scales in question and that the Interrogation window represents a top-hat profile filter in wavenumber space with a cut-off at $\kappa = 1/2\lambda_p$. The percentage of the total turbulent energy measured is then estimated using the following ratio.

$$\frac{E_{measured}}{E_{total}} \approx \frac{\int_{1/\delta}^{1/2\lambda_p} \kappa^{-5/3} d\kappa}{\int_{1/\delta}^{1/\lambda_\nu} \kappa^{-5/3} d\kappa} = \frac{1 - (2\lambda_p/\delta)^{2/3}}{1 - (\lambda_\nu/\delta)^{2/3}} \tag{3.1}$$

The ratio λ_p/δ and λ_ν/δ as well as the estimated ratio of measured to total energy for all conditions are summarised in table 3.3. The large-scale measurements keep

Table 3.3: Estimate of measured percentage of total fluctuating energy for Large FoV data

V_r		10		15	20
x/d_j	30	55	85	85	85
δ/λ_ν	80.4	77.3	65.5	72.6	77.8
δ/λ_p	20.1	22.6	24.6	38.1	44.1
E_{meas}/E_{total}	82.0%	84.8%	86.6%	91.2%	92.3%
$\sqrt{\overline{u_i'u_i'}}_{meas}$	90.6%	92.1%	93.1%	95.5%	96.1%

$\delta/\lambda_p > 20$. This translates into a minimum percentage of the total fluctuating energy measured to be approximately 82%, meaning that the measured $\sqrt{\overline{u_i'u_i'}}$ velocities represent, approximately, a minimum of 91% of the true value.

3.1.2 Statistical Convergence

Given that a finite number of samples are taken in order to calculate various turbulence statistics (see table 3.1), it is important to assess their accuracy by quantifying the uncertainty involved in calculating the 'sample' mean, rather than the true mean. Benedict & Gould [5] present a method of calculating this

uncertainty for a number of turbulent statistics commonly used, which is briefly summarised here. In general for a large number of uncorrelated samples, $N > 30$, the statistic z in equation 3.2 has a standardised normal distribution regardless of the distribution of x, which has a true mean mean equal to μ_x, sample mean equal to $\overline{x}$ and a variance of s_x^2.

$$z = \frac{\overline{x} - \mu_x}{[s_x^2/N]^{\frac{1}{2}}} \tag{3.2}$$

Therefore the estimated statistic $\overline{x}$ has a true mean μ_x and a variance equal to s_x^2/N. We can therefore say that, with a 95% confidence interval, the true mean μ_x lies in the range $\overline{x} \pm 1.96\sqrt{\frac{s_x^2}{N}}$.

The variable x above can be any statistic of the measured velocity components, for example the variance of the streamwise velocity $\overline{u'^2}$. Applying the above gives the following equation for the error in the estimated statistic.

$$\mu_{u'^2} = \overline{u'^2} \pm \overbrace{1.96\sqrt{\frac{s^2_{u'^2}}{N}}}^{\text{uncertainty}} \tag{3.3}$$

Benedict & Gould [5] provide a method for calculating the highlighted uncertainty in the equation above, for any statistic, as well as a table with formulas for some commonly used turbulent statistics.

Figure 3.1 shows convergence plots for the three rms velocity components, that is how the mean converges to the final calculated mean with an increasing number of samples, at the position where each component has a maximum value. The rms velocities converge relatively quickly, as the measurements are made in the far field of the cross-flow jet, with all three components showing equal levels of convergence to approximately ±5% after 1000 samples and to ±1% after 3000 samples.

The uncertainty in the sample mean w.r.t the true mean is shown as a ratio of the uncertainty highlighted in equation 3.3 to the calculated sample mean as a function of N in figure 3.2, again at the position where each component has a maximum value. The figure shows that the uncertainty decreases with a rate

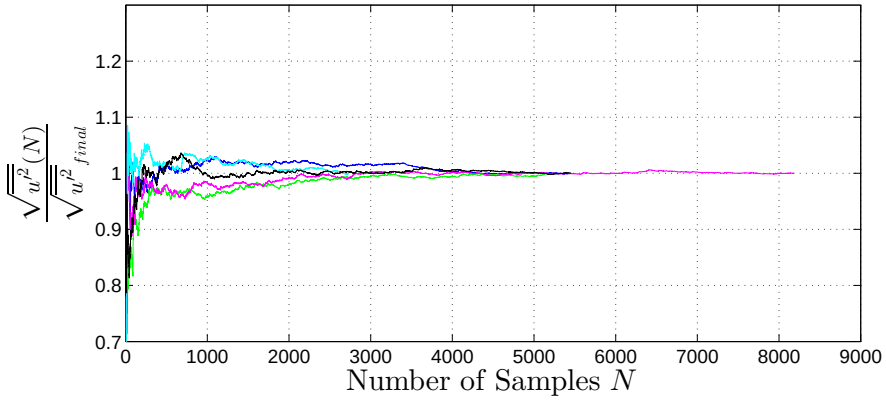

(a) $\sqrt{\overline{u'^2}}$ convergence.

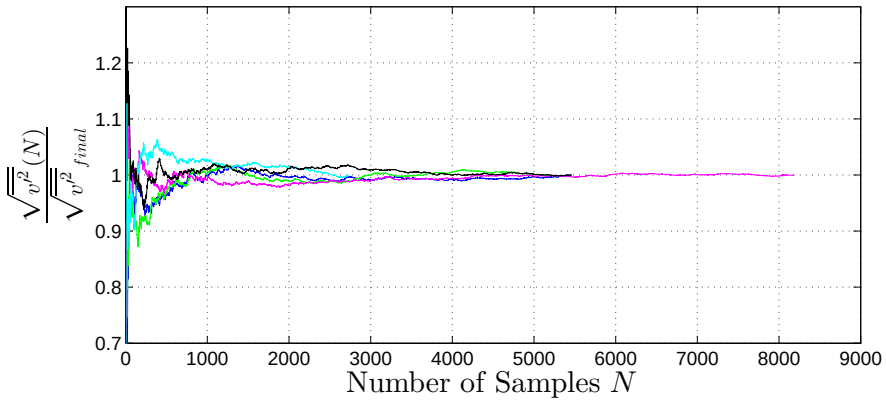

(b) $\sqrt{\overline{v'^2}}$ convergence.

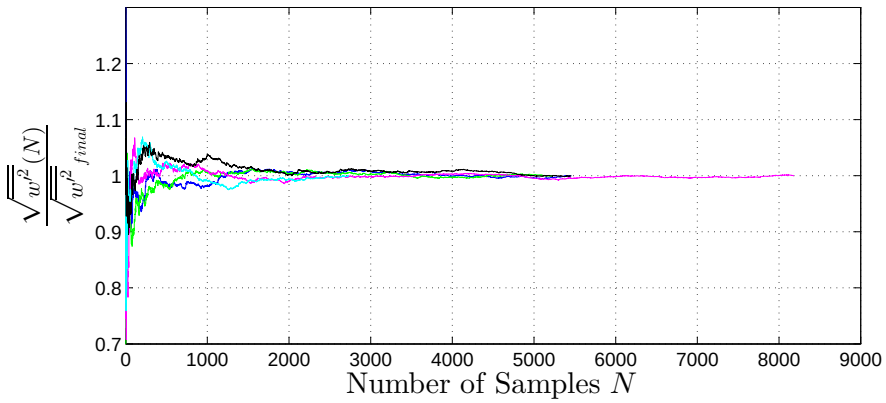

(c) $\sqrt{\overline{w'^2}}$ convergence.

Figure 3.1: Convergence plots of the rms velocity components for all flow conditions. For color coding refer to the caption of figure 3.2.

of $N^{-1/2}$, which is shown by the slope of the red solid line in each plot. All rms velocity components for all conditions reach final 95% confidence interval of less than $\approx 2\%$, with the exception of the measurements for $V_r = 15$ at $x/d_j = 85$ which is slightly higher at $\approx \pm 2.5\%$ due to the lower number of samples recorded. Figure 3.3 shows a profile of $\sqrt{\overline{u'^2}}$, $\sqrt{\overline{v'^2}}$ and $\sqrt{\overline{w'^2}}$ components across the cores of the CVP along the spanwise y-direction, together with error-bars representing the uncertainty calculated with equation 3.3, for the case of $V_r = 10$ at $x/dj = 85$. The plot shows that the confidence level in the sample mean is small enough to accurately represent the spatial variation of the rms velocities in the FoV, with similar results observed for profiles in the wall-normal z-direction.

3.1.3 Interrogation Window vs Field of View Size

As mentioned in section 2.4.7, the ratio of the size of the two FoVs was limited by the quality of resulting images themselves, with an upper limit on the size of the Large-Scale FoV set by largest possible size of the jet in the far field measurement position. Given that the size of the jet δ_ω scales with $V_r d_j$ as does the jet trajectory, this was thus limited by the depth of the Water Channel. One way the resolution can be increased is by reducing the Interrogation Window (IW) size. However if there aren't a sufficient number of particles in the window this has the effect of increasing noise. The increase in the measurement resolution between the Large-Scale FoV and Small-Scale FoV can also be achieved by performing the image cross-correlation with a final IW size of 16×16, rather than 32×32, for the Large-Scale FoV measurements. This therefore presented the opportunity of studying the effect of increasing the measurement resolution by decreasing the final interrogation window size compared to decreasing the size of the FoV. The seeding density of the Large-Scale FoV was large enough to allow for the decrease in interrogation window size.

Results from the two inlet conditions of $V_r = 10$ at $x/d_j = 55$ and $V_r = 20$ at $x/d_j = 85$ will be used for the analysis to assess different measurement resolutions. Results from three different data sets for a given inlet condition, the Large-Scale and Small-Scale field of view data, together with data from the Large-Scale FoV processed with a final Interrogation Window size of 16×16 are

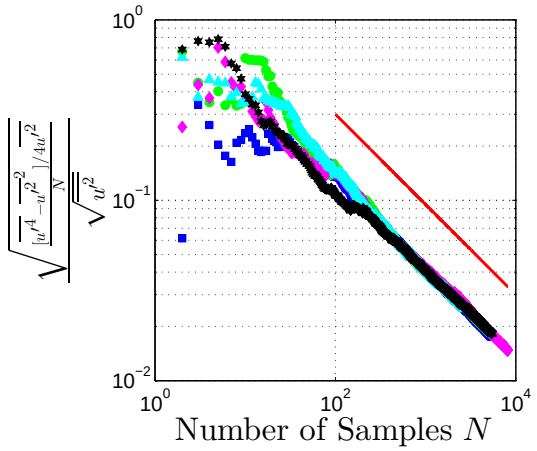

(a) $\sqrt{\overline{u'^2}}$ confidence.

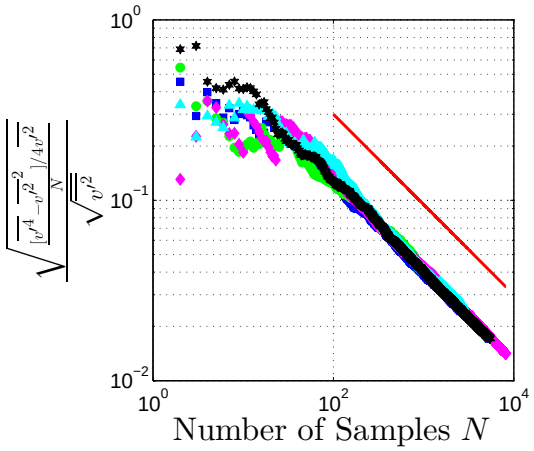

(b) $\sqrt{\overline{v'^2}}$ confidence.

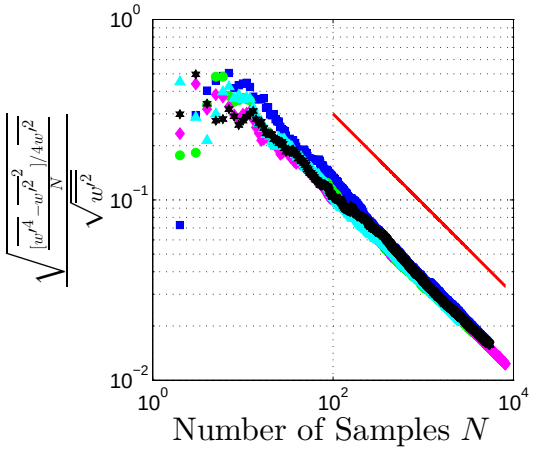

(c) $\sqrt{\overline{w'^2}}$ confidence.

Figure 3.2: Confidence plots of the rms velocity components for all flow conditions. The different symbols represent the different inlet parameters and measurement locations. ■ : $V_r = 10$ at $x/d_j = 30$, ● : $V_r = 10$ at $x/d_j = 55$, ♦ : $V_r = 10$ at $x/d_j = 85$, ▲ : $V_r = 15$ at $x/d_j = 85$, ★ : $V_r = 20$ at $x/d_j = 85$. — : $N^{-1/2}$ power law.

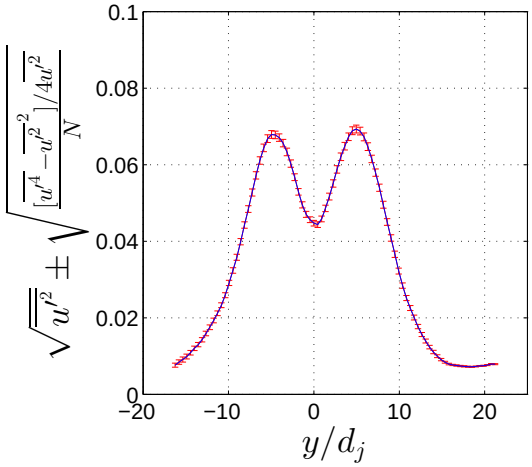

(a) $\sqrt{\overline{u'^2}}$(m/s) profile.

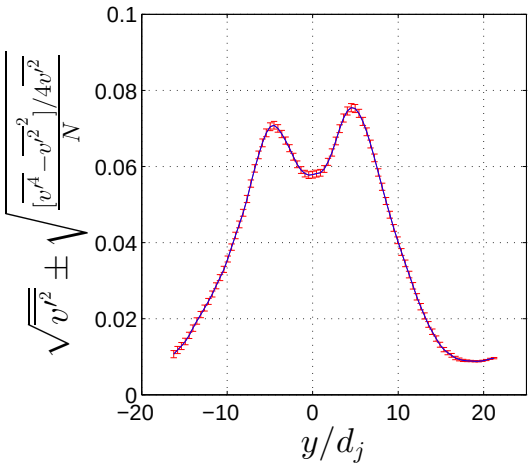

(b) $\sqrt{\overline{v'^2}}$(m/s) profile.

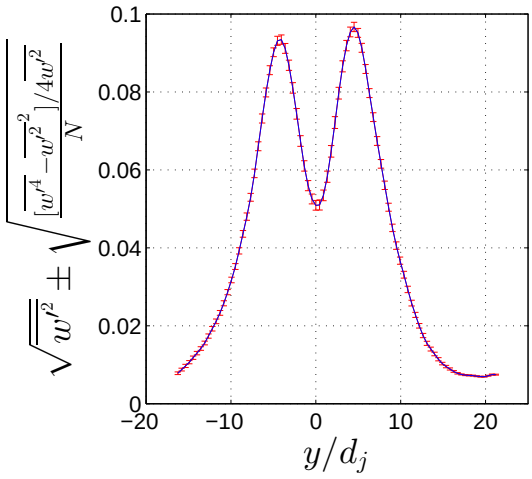

(c) $\sqrt{\overline{w'^2}}$(m/s) profile.

Figure 3.3: Profiles of rms velocity for all three components with errorbars of $\pm 1.96\sqrt{\frac{s^2_{u'^2}}{N}}$

compared. Figure 3.4 shows profiles of mean vorticity and all three rms velocity

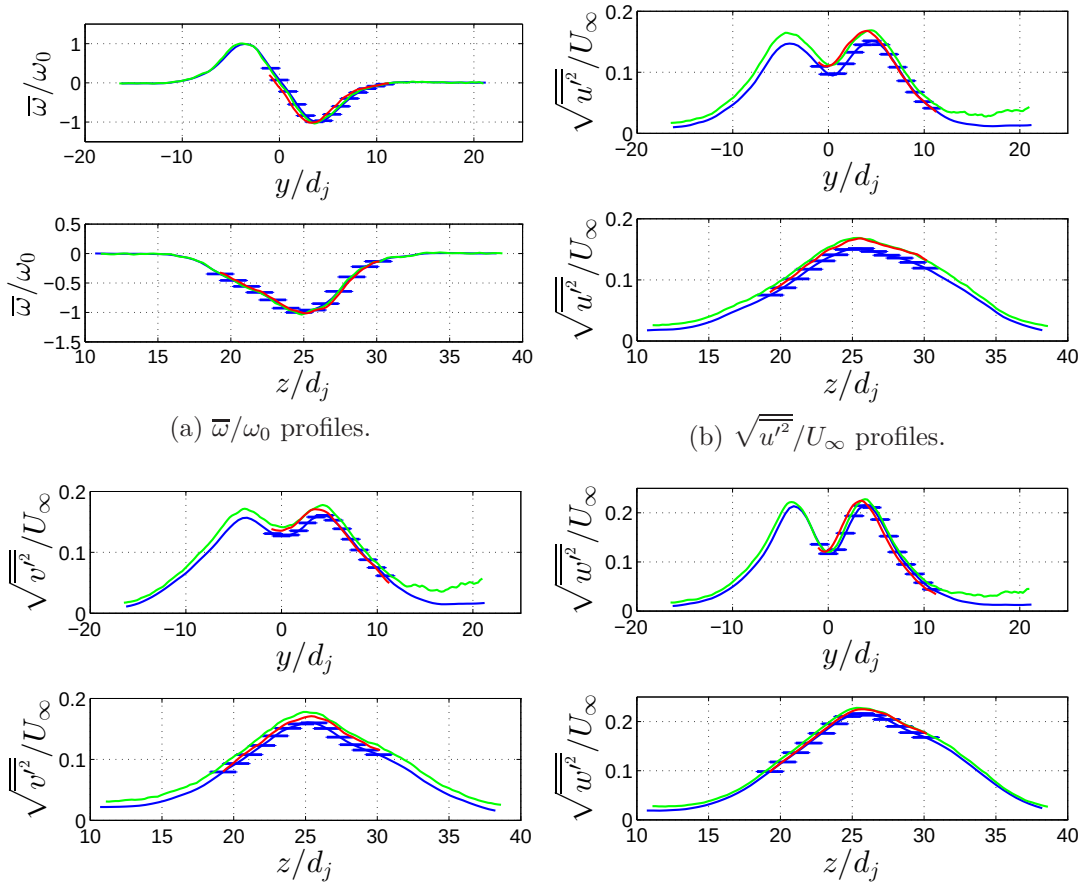

(a) $\overline{\omega}/\omega_0$ profiles.

(b) $\sqrt{\overline{u'^2}}/U_\infty$ profiles.

(c) $\sqrt{\overline{v'^2}}/U_\infty$ profiles.

(d) $\sqrt{\overline{w'^2}}/U_\infty$ profiles.

Figure 3.4: Profiles along the y and z direction of vorticity and all three rms velocity components across the position of maximum respective magnitude for the case where $V_r = 10$ at $x/d_j = 55$. Errorbars represent the resolution of the Large-Scale FoV measurements $\pm\lambda_{p_L}$. — : Large-Scale FoV data, — : Large-Scale FoV $16 \times 16 FIW$ data, — : Small-Scale $32 \times 32 FIW$ data

components across the position where their respective magnitudes are maximum for a $V_r = 10$ at $x/d_j = 55$. The vorticity profiles (figure 3.4a) shows good agreement between the Large-Scale and Small-Scale FoV measurements in terms of vorticity magnitude. However a small shift in the position of vorticity peaks (i.e position of CVP), between the two field of views is observed but this lies

within the resolution of the Large-Scale FoV measurements, indicated by the blue error bars, suggesting that the offset is due to the more limited resolution of the Large-Scale FoV measurements.

The rms velocity profiles show a good agreement but, in general, the Small-Scale FoV and the higher resolution Large-Scale FoV data predict larger magnitudes. This is not a surprise since the vorticity and rms have energy containing motions at the small scale and therefore, as shown in section 3.1.1, the higher resolution means more of the total turbulent energy is measured. The percentage difference between the Large-Scale 32×32 IW and Large-Scale 16×16 IW rms velocities is approximately 10.5% for the $V_r = 10$ at $x/d_j = 55$ case, which is higher that the difference to the Small-Scale data of approximately 4.5%. The same pattern is observed for the $V_r = 20$ at $x/d_j = 85$ case, with a difference of 4.4% to the 16×16 IW Large-Scale data, larger than the difference of 2.6% to the Small-Scale data. Applying a similar analysis to that performed in section 3.1.1 results in equation 3.4 which gives a prediction to the percentage difference of measured rms velocity between the higher and lower resolution data of approximately 4.3% for the $V_r = 10$ at $x/d_j = 55$ case and 2.6% for $V_r = 20$ at $x/d_j = 85$ case.

$$\frac{E_{\lambda_{p_S}}}{E_{\lambda_{p_L}}} \approx \frac{\int_{1/\delta}^{1/2\lambda_{p_S}} \kappa^{-5/3} d\kappa}{\int_{1/\delta}^{1/2\lambda_{p_L}} \kappa^{-5/3} d\kappa} = \frac{1 - (2\lambda_{p_S}/\delta)^{2/3}}{1 - (2\lambda_{p_L}/\delta)^{2/3}} \tag{3.4}$$

The difference in measured rms velocities can therefore be accounted for by the difference in measurement resolution for the Small-Scale FoV data, but a larger difference is observed for the Large-Scale 16×16 IW data. This suggests that reducing the IW size has introduced noise.

Noise is difficult to quantify, but a more rigorous approach is to test the resolution without resolving to estimates based on scaling, as in the example above. A way to do so is to look at the shape of the pdf of the invariants of the Velocity Gradient Tensor [11]. The effect of IW vs FoV will be further examined here by looking at the invariants of the reduced Velocity Gradient Tensor (VGT),

$\mathbf{A_r}$.

$$\mathbf{A_r} = \begin{bmatrix} \frac{\partial v'}{\partial y} & \frac{\partial v'}{\partial z} \\ \frac{\partial w'}{\partial y} & \frac{\partial w'}{\partial z} \end{bmatrix} \tag{3.5}$$

Once again a comprehensive background of the analysis of the full VGT is presented by Perry & Chong [47]. Here we consider an analysis on the reduced Velocity Gradient Tensor shown by Cardesa *et al.* [12], but in summary similar to the analysis performed on the full Velocity Gradient Tensor (see section2.7.3), the eigenvalues of $\mathbf{A_r}$ can be found by solving $|\mathbf{A_r} - \lambda\mathbf{I}| = 0$ which results in its characteristic equation

$$\lambda^2 + p\lambda + q = 0 \tag{3.6}$$

where p and q are the invariants and equal to

$$p = -\left(\frac{\partial v'}{\partial y} + \frac{\partial w'}{\partial z}\right) = -tr\left[\mathbf{A_r}\right] \tag{3.7}$$

$$q = \frac{\partial v'}{\partial y}\frac{\partial w'}{\partial z} - \frac{\partial w'}{\partial y}\frac{\partial v'}{\partial z} = det\left[\mathbf{A_r}\right] \tag{3.8}$$

Cardesa *et al.* [12] plotted joint pdfs of p and q for a variety of different flows: DNS of channel flow, isotropic turbulence in a periodic cube, 2D PIV data of a turbulent round jet and isotropic turbulence generated in a mixing tank. The resulting pdfs showed a striking similarity between the turbulent flows. Importantly they showed similar asymmetry, as shown in the joint pdf contours of p and q in figure 3.5a. This assymetry in $p-q$ space was demonstrated to be due to vortex stretching which occurs at the small scales [6]. When the flow is not well resolved or noisy distributions tend to a more symmetrical shape (i.e showing a Gaussian behaviour) which is unphysical. Examining the degree of asymmetry is a strict test of measurement noise and poor resolution. For the present measurements the data case where $V_r = 20$ at $x/d_j = 85$ has the highest resolution of 13η, and is thus used for the analysis. Figures 3.5b, (c) and (d) show the joint pdfs of p and q for the cross-flow jet data which were produced using the same number of data points for consistency.

Figure 3.5b shows the results produced using data from the Small-Scale FoV

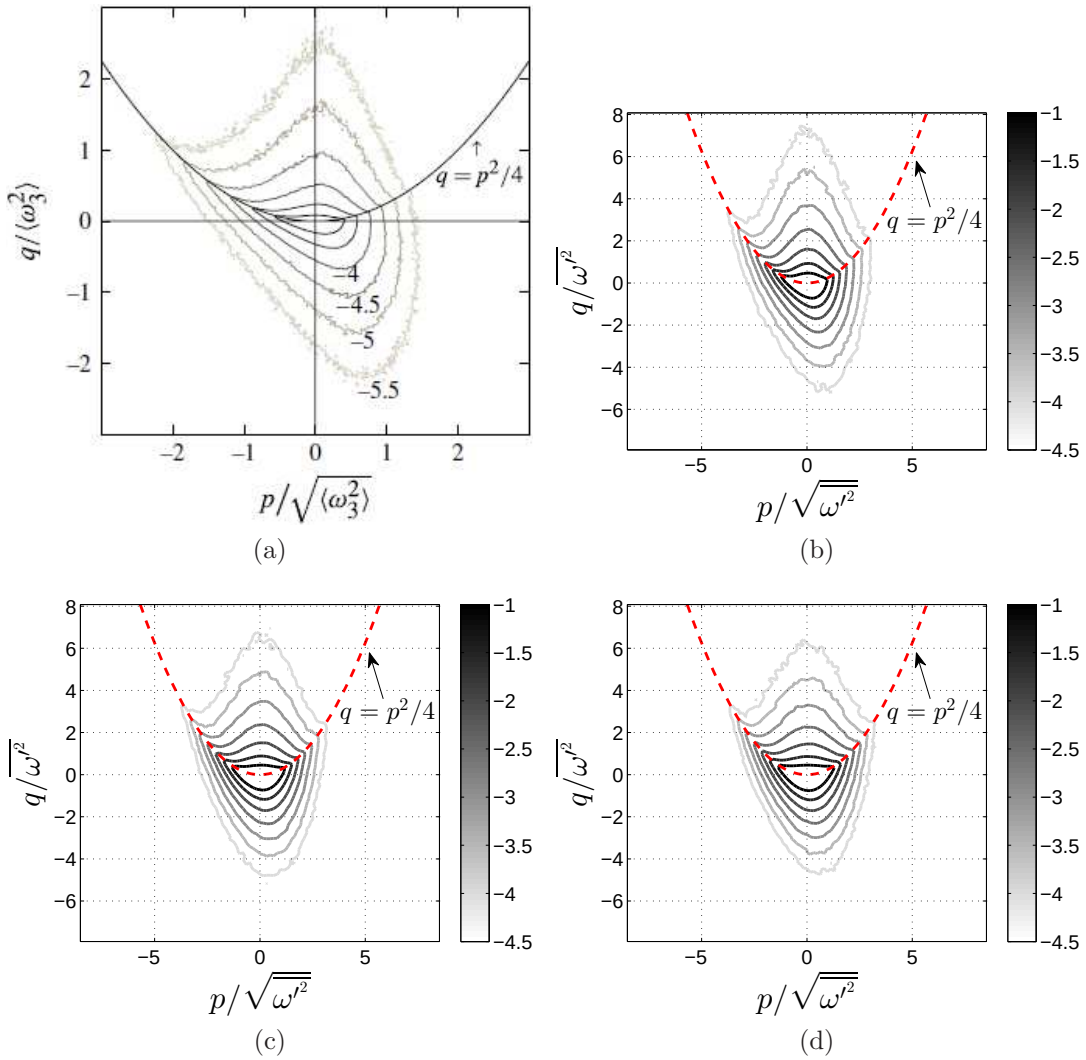

Figure 3.5: Joint pdf of the p and q invariants of the reduced Velocity Gradient Tensor. (a) DNS data of water channel at $y^+ = 120$ with $Re_t = 934$ reproduced here from Cardesa *et al.* [12] . (b) Data from Small-Scale FoV measurements for $V_r = 20$ at $x/d_j = 85$. (c) Data from Large-Scale FoV measurements processed with a $16 \times 16px$ final interrogation window size. (d) Data from Small-Scale FoV measurements with added Gaussian noise.

measurements. The shape shows similar attributes as for the results of the DNS data, specifically the influence of the $q = p^2/4$ parabola, representing the boundary between the real and imaginary roots of the characteristic equation 3.6, on the shape of the pdf, and its asymmetry, showing a skewness towards a negative value of $\overline{pq}$. However the pdf is not identical to that from the DNS data, both in terms of its shape and the magnitude of p and q. The smaller degree of asymmetry observed indicates that the vortex stretching scales are not resolved in the current measurement, as would be expected form the measurement resolution of 13η. Figure 3.5c is produced using the data from the higher resolution Large-Scale FoV measurements. The pdf is more symmetric when compared to that produced using the Small-Sacle FoV data. Reducing the IW size therefore makes the $p - q$ plot visibly more symmetric, meaning that noise is added to the data. To show that this is an artefact of noise present in the data, random Gaussian noise was added to each velocity component of Small-Scale FoV data. The noise added had a mean of zero and a standard deviation equal to 15% of the standard deviation of the components velocity distribution to which it was added. The results are shown in figure 3.5d. The results are now similar to those in figure 3.5c illustrating that it is the presence of noise that changes the shape of the pdf of the Small-Scale FoV data towards the shape of the Large-Scale FoV data.

3.2 Jet Trajectory and Mean Vorticity Distribution

The jet trajectory was one of the first properties of the cross-flow jet to be measured, and is the most frequently quoted property in the literature. Using the scaling law suggested by Pratte & Baines [53] to collapse the trajectories from visualizations of oil aerosol jets, the trajectory was estimated by tracking the position of maximum/minimum vorticity and fitting the data with a least squares method to equation 1.28 reproduced below:

$$\frac{z}{V_r d_j} = A \left(\frac{x}{V_r d_j} \right)^m . \tag{3.9}$$

The values of A and m reported in the literature range from $1.2 < A < 2.6$ and $0.28 < m < 0.38$ [26]. The values of A and m from this study obtained by a curve fit as shown by the red line in figure 3.6a, were found to be $A = 1.58$ and $m = 0.28$.

The far field of the cross-flow jet is dominated, in the mean, by a counter-rotating vortex pair. Figure 3.6b shows the mean vorticity field at the three downstream measurement locations for the cases where $V_r = 10$. The figure illustrates where the measurement planes where positioned with respect to the jet trajectory. The dominant presence of the CVP is clearly illustrated, together with its increasing distance from the bottom wall and its decay in vorticity magnitude with downstream distance. Figure 3.7 looks at the CVP for each of the conditions studied by plotting the mean vorticity field extracted from the Large-Scale FoV data. Furthermore each figure indicates the position of the Small-Scale of view within the Large-Scale FoV showing that it enhances the right, negative, core of the CVP. The mean shape of the cores looks elliptical, rather than circular, with the cores being elongated in the wall-normal z direction. In addition, at the furthest downstream position of $x/d_j = 85$ the cores become slightly asymmetrical, as it can be seen in figures 3.7c, d and e. Smith & Mungal [58] also found their concentration fields for high velocity ratio ($V_r > 10$) at large downstream positions ($x > V_r d_j$) to be asymmetrical. They also discuss that asymmetry in the scalar field has also been observed elsewhere in the literature. Given that PIV velocity measurements in the CVP plane are very scarce the asymmetry in the velocity field cannot be checked with other results. However, it should be mentioned that the nozzles were manufactured to high machine accuracy, and were rotated between the various runs performed. The results from the various runs for each condition were checked and found to show the same asymmetry.

Broadwell & Breidenthal [9] modelled the average far field of a high velocity ratio ($V_r > 10$) cross-flow jet as a pair of counter-rotating vortex lines. Their analysis suggest that the global length-scale in the far-field, l scales with $V_r d_j$ and that the spacing between the vortex lines R is proportional to the distance from the wall z, based on dimensional reasoning. The jet trajectory that comes out of this model has the same $V_r d_j$ scaling of equation 1.28, but with the constant $m = \frac{1}{3}$. Figure 3.6a shows that the data here agrees with the scaling suggested

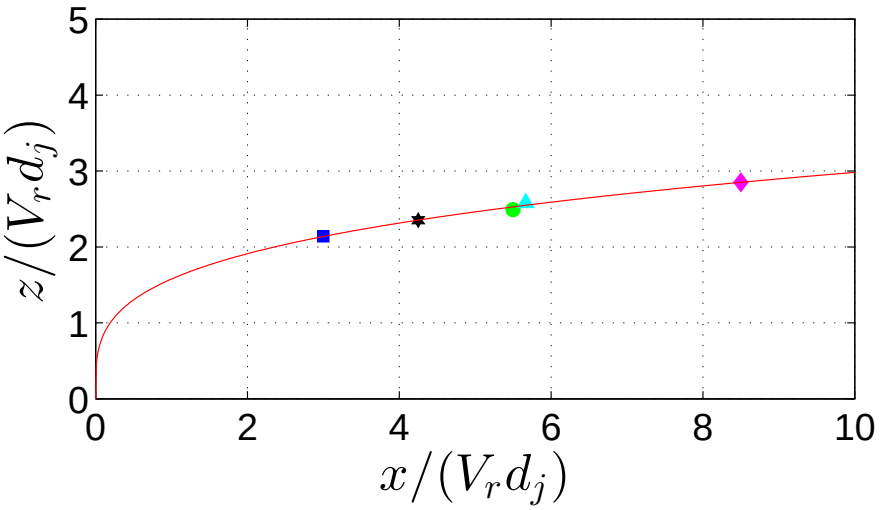

(a)

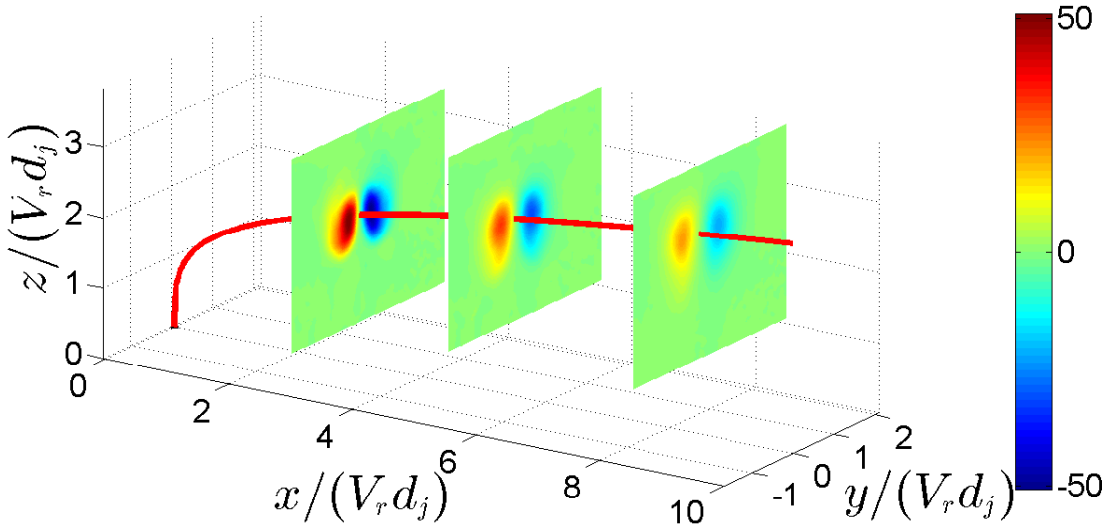

(b)

Figure 3.6: (a) Plot of the normalised jet trajectory. The solid red line represents equation 1.28 with $A = 1.58$ and $m = 0.28$. The symbols used follow the same notation as those in figure 3.2. (b) Downstream evolution of the mean vorticity field $\overline{\omega}(\mathrm{s}^{-1})$ using the case where $V_r = 10$. Red solid line represents the jet trajectory, as estimated from the curve fit in figure (a).

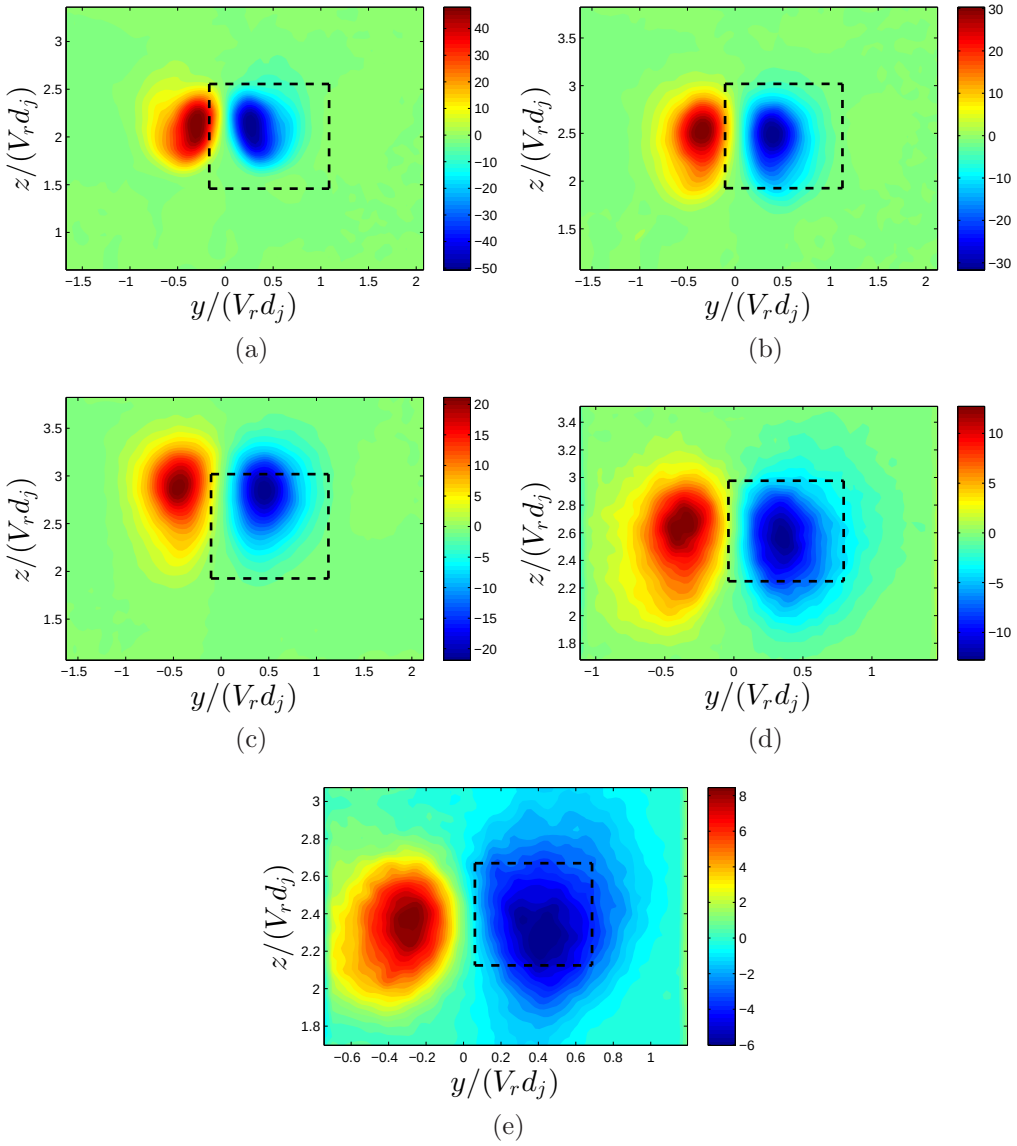

Figure 3.7: Mean vorticity field for all the inlet conditions studied. The dotted black line indicates the position of the Small-Scale FoV. (a) $V_r = 10$ at $x/dj = 30$. (b) $V_r = 10$ at $x/dj = 55$. (c) $V_r = 10$ at $x/dj = 85$. (d) $V_r = 15$ at $x/dj = 85$. (e) $V_r = 20$ at $x/dj = 85$.

by the model but has a different value for the constant m. The scaling can be further tested by looking at the analogous spacing between the vortex lines, taken as the spacing between the centroids of vorticity of each core R_c.

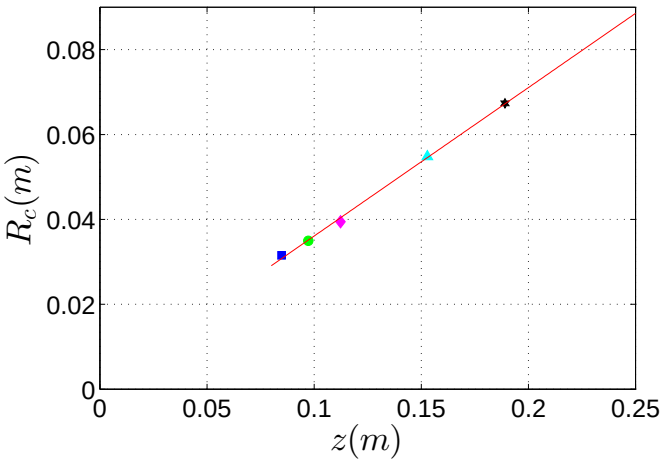

(a)

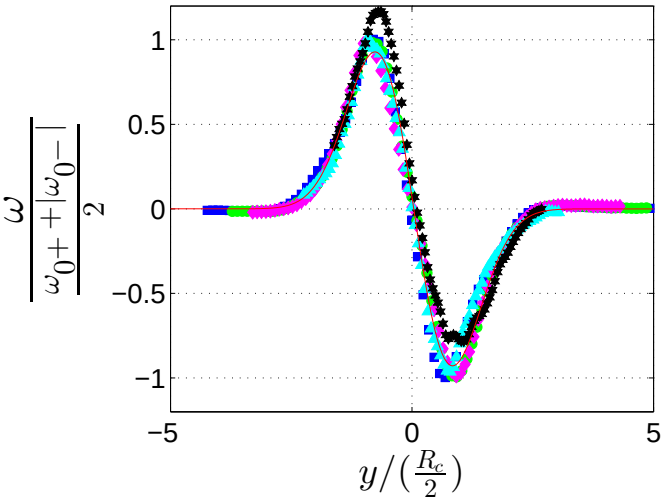

(b)

Figure 3.8: Scaling properties for the CVP when using the vorticity centroid spacing as the controlling parameter. The symbols used indicating the different inlet parameters and measurement locations follow the same notation as those in figure 3.2. (a) Change in core spacing with wall normal distance z. The red line represents the curve fit $R_c = c_0 z$ with $c_0 = 0.31$. (b) Normalised vorticity profiles across the cores of the CVP.

Figure 3.8a shows that the data agrees with the assumption of a similarity solution where the vortex spacing R is proportional to z as seen by the straight red line fit. This would therefore suggest that the half-width distance of the core separation can be used to collapse the profiles of various quantities across the cores of the CVP. Figure 3.8b shows that this is indeed the case for the vorticity profile across the cores for all cases studied. It should be noted however that for a proper complete similarity solution, the Reynolds stresses and rms velocity fields need to collapse as well.

Using this similarity solution the model by Broadwell & Breidenthal [9] predicts an expression for R and Γ as a function of x given in equations 3.10 and 3.11. Substituting for l above and rearranging results in the power law expressions given on the right.

$$\frac{R}{l} = c_1 \left(\frac{x}{l}\right)^{\frac{1}{3}} \rightarrow \quad \frac{R}{V_r d_j} = c_3 \left(\frac{x}{V_r d_j}\right)^{\frac{1}{3}} \tag{3.10}$$

$$\frac{\Gamma}{U_\infty l} = c_2 \left(\frac{x}{l}\right)^{\frac{-1}{3}} \rightarrow \quad Re_\Gamma = c_4 \left(\frac{x}{V_r d_j}\right)^{\frac{-1}{3}} Re_{jet} \tag{3.11}$$

These scaling laws can be tested against the data presented here by fitting curves through the data, allowing for both constants c and s to be estimated. Figure 3.9 show the plots of normalised core separation and circulation Reynolds number against normalised downstream distance and the respective curve fits, with the resulting expressions given in equation 3.12 and 3.13.

$$\frac{R}{V_r d_j} = c_3 \left(\frac{x}{V_r d_j}\right)^{s_1} \qquad c_3 = 0.58, s_1 = 0.23 \tag{3.12}$$

$$Re_\Gamma = c_4 \left(\frac{x}{V_r d_j}\right)^{s_2} Re_{jet} \quad c_4 = 1.77, s_2 = -0.4 \tag{3.13}$$

The suggested $V_r d_j$ scaling seems to collapse the data very well, although the value of the constant s is different that that predicted by the model of 1/3 as is for the case of the trajectory scaling. Interestingly the model predicts an inverse relationship between the core spacing and circulation power law (one being 1/3 and the other $-1/3$) and this does not appear to be the case when using the vorticity centroid spacing as the distance R The distance between the vorticity

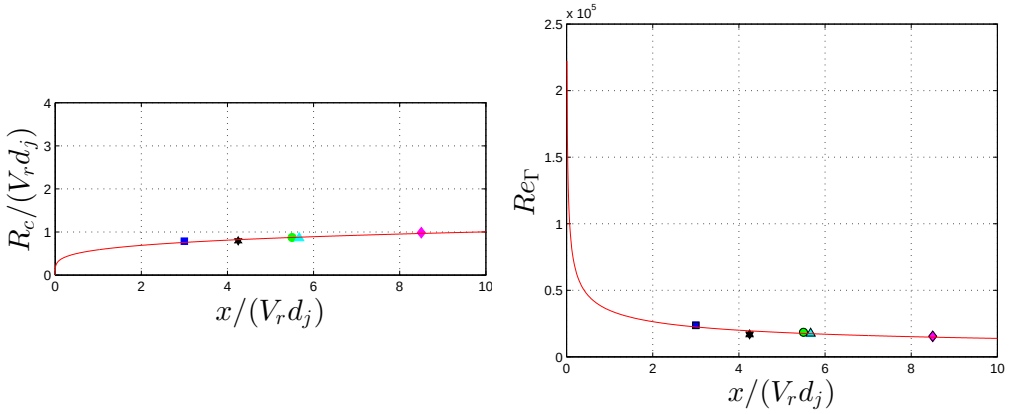

(a) (b)

Figure 3.9: Scaling of the core spacing R_c and circulation Γ as a function of downstream distance x. (a) Change in core spacing with downstream distance x. Red line represent the curve fit $\frac{R}{V_r d_j} = c_3 \left(\frac{x}{V_r d_j}\right)^{s_1}$ to the data with $c_3 = 0.39$ and $s_1 = 0.4$. (b) Circulation scaling with downstream distance x. Red line represent the curve fit $Re_\Gamma = c_4 \left(\frac{x}{V_r d_j}\right)^{s_2} Re_{jet}$ to the data with $c_4 = 1.77$ and $s_2 = -0.4$

centroids was chosen to perform the above analysis as it best collapsed the data, especially in figures 3.8a and 3.8b. However, with regards to the vortex line model and the curve fit in figure 3.9a, choosing the spacing between the vorticity maximum and vorticity minimum of the two cores might be more appropriate. Doing so gives a value of $c_3 = 0.39$ and $s_1 = 0.4$, agreeing with the inverse relationship between R and Γ but with a power value of 0.4(2/5). Therefore figures 3.6, 3.8 and 3.9 show that the model predicts the correct scaling in the far field with a slightly different power law exponent. This does not come as a surprise as the $V_r d_j$ scaling comes from purely a non-dimensional reasoning of the global length scale in the far field. However the 1/3 power law for the jet trajectory and core spacing, and the $-1/3$ power law of the circulation come from the modelling of the CVP as two vortex lines. As is reported in the literature, and as will be shown in later sections, the CVP has a characteristic 'kidney' shape, and would therefore expect the vortex lines model to be limited in its prediction of the value of the constants.

3.3 The CVP

The mean vorticity field at all measurement positions and conditions shows that the CVP is made up of two vortex cores. However, the cross-flow jet is a turbulent flow and in order to better understand its structure the instantaneous field needs to be looked at. Figure 3.10 shows a contour plot example of the instantaneous

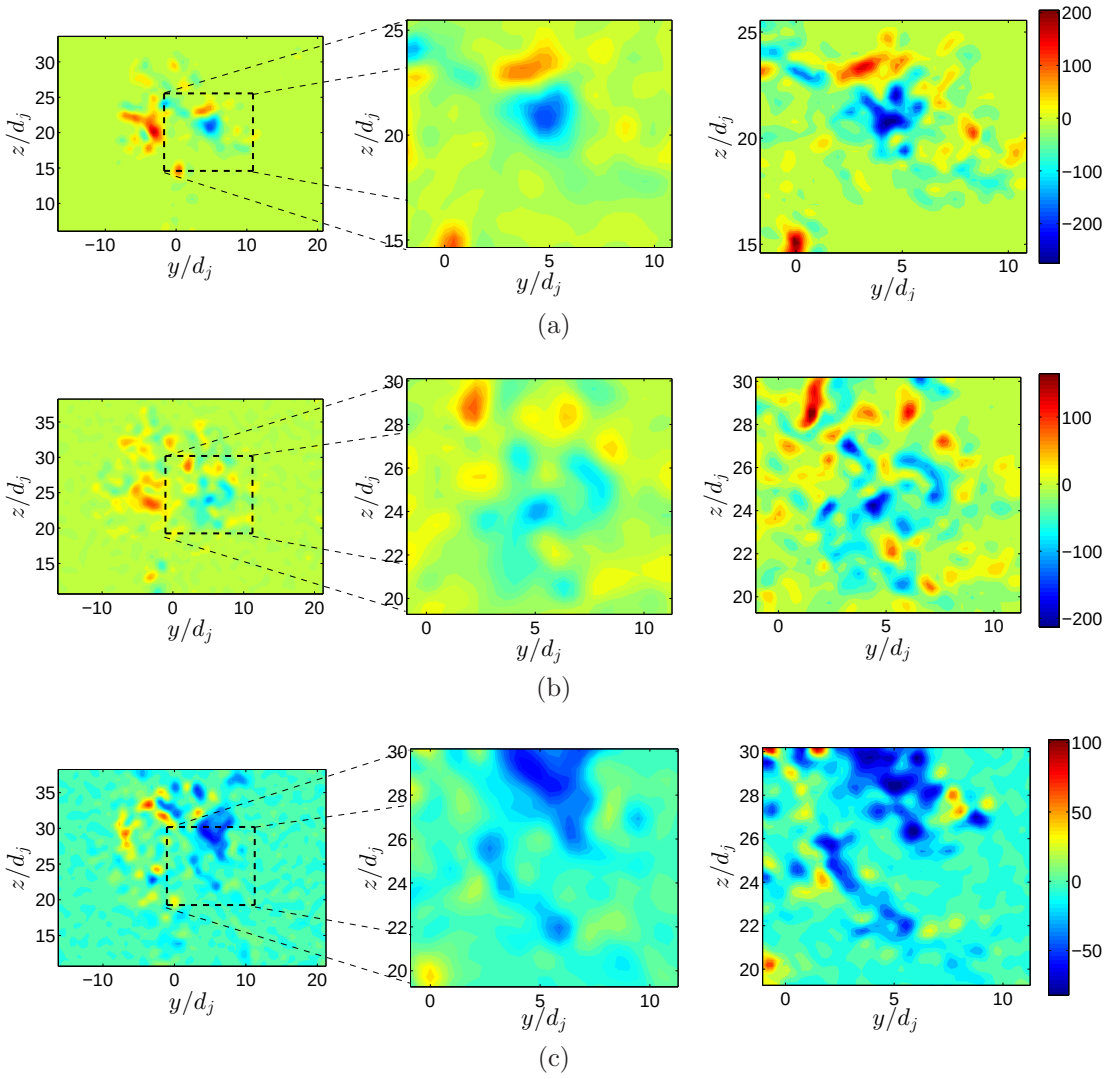

Figure 3.10 (a-c): For caption see following page.

vorticity field for all conditions studied. The plots in the first column show the

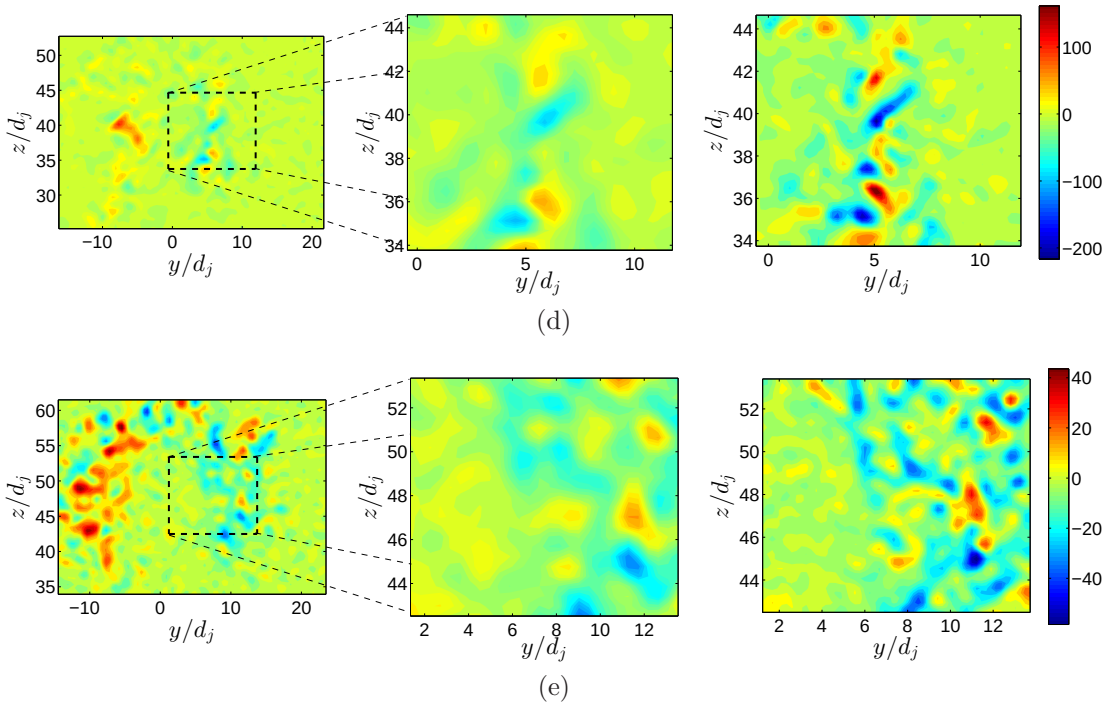

Figure 3.10: Instantaneous vorticity field ($\omega(\mathrm{s}^{-1})$) contour plots. First column shows data from the LFOV measurements. The second/middle column is an extract of the LFoV data from the dashed square area which indicates the SFoV position. Third column shows data from the SFoV measurements. Each row represents data for a given case: (a) $V_r = 10$ at $x/dj = 30$. (b) $V_r = 10$ at $x/dj = 55$. (c) $V_r = 10$ at $x/dj = 85$, (d) $V_r = 15$ at $x/dj = 85$. (e) $V_r = 20$ at $x/dj = 85$.

results from the Large-Scale FoV measurements, the second column is a zoomed in view equal to the Small-Scale FoV and the third column shows the results from the Small-Scale FoV. Looking at the position of strong vorticity events in the Large-Scale FoV measurements, the two FoVs show a good agreement. The lack of spatial resolution in the Large-Scale FoV results appear to smooth out vorticity shown in the the Small-Scale FoV measurements. The Small-Scale FoV measurement manages to resolve smaller vortices within the CVP which are not present in the Large-Scale FoV results. This illustrates the advantage of performing multi-scale measurements to capture a larger range of scales of the flow.

Both the Large-Scale and Small-Scale FoVs shows that instantaneously the flow is made up of a number of small structures with high vorticity ω. This is not totally surprising since the flow is highly turbulent, but when considering the mean vorticity field of the CVP is made up of 2 distinct cores, this suggests that the CVP might be instantaneously made up of a number of small vortex cores bundled together, rather than a single core. In order to further investigate this, the CVP is studied in more detail by looking at the instantaneous distribution of vorticity in the next section.

3.3.1 Probability Density Distribution

The structure of the CVP is examined by producing probability density functions (pdf) of the instantaneous vorticity distribution, both for the CVP as a whole and each core individually. This is done by detecting peak vorticity events (both maxima and minima) in each instantaneous vector field/sample and recording their strength and location. The location and strength recorded are of the peak/trough vorticity. The analysis was performed with the aim of detecting strong events only, and a threshold of 50% of the events magnitude detected in each sample was used, below which detected peaks were rejected.

In the analysis to follow the number of events detected in each core was found to depend on the measurement resolution. However, the Small-Scale FoV data was found to give similar distribution shapes to the Large-Scale FoV data, with the difference that a larger number of events were detected. However since we

are interested in the large scale events, results from the Large-Scale FoV are only considered here for the pdfs.

Looking at the Small-Scale FoV data in figure 3.10 which is zoomed in on the right/negative core of the CVP, distinct negative events and, perhaps unexpectedly, positive events of vorticity are present. Although only a few snapshots are shown this was observed in all instantaneous vorticity fields. Figure 3.11 shows pdfs of the number, and strength, of positive and negative vorticity events detected on each side of the CVP, i.e in the positive and negative CVP core, for all inlet conditions. The pdfs in the left column show the number of distinct

Table 3.4: Average number of tubes detected in the CVP plane

V_r		10		15	20
x/d_j	30	55	85	85	85
Same sign	4.6	5	5.5	7.5	6.6
Opposite sign	1.2	1	1.28	2.6	3.1
Ratio	3.8	5	4.3	2.9	2.1

vorticity peaks in both the right and left cores according to their sign. The solid lines correspond to the left/positive core of the CVP and the dashed lines to the right/negative core. Positive and negative events are detected in both cores, with each core containing events of the same sign. Table 3.4 shows that the average number of distinct vorticity peaks is greater than 1. In addition to a larger number of smaller scale vorticity events, the distribution of their magnitudes detected, shown in the pdfs in the right column, shows that stronger events are detected in the cores of the same sign. The same analysis was conducted using the swirl field (see section 2.7.3) and produced almost identical results. This gives new and important insight into the structure of the CVP. There is strong evidence to suggest that it is made up of strong swirling structures, instead of shear layer structures, one possible interpretation being that the CVP is made up by multiple vortex tubes of the same sign.

The spatial distribution of these vortex tubes is examined by first looking at the joints pdfs of their strength and relative y and z location in figure 3.12. The pdfs present similar information as figure 3.11 but show that tubes with large

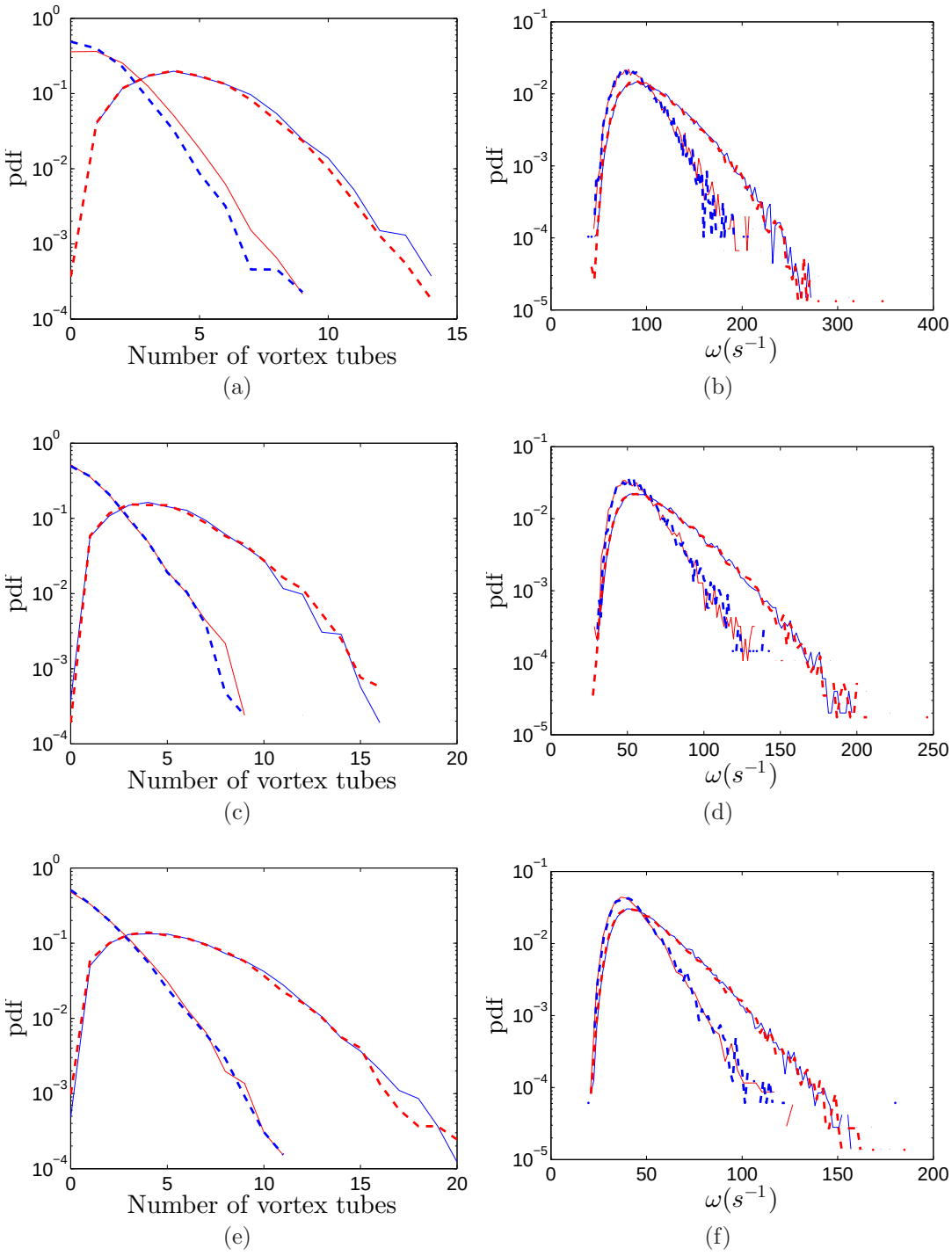

Figure 3.11 (a-f): For caption see following page.

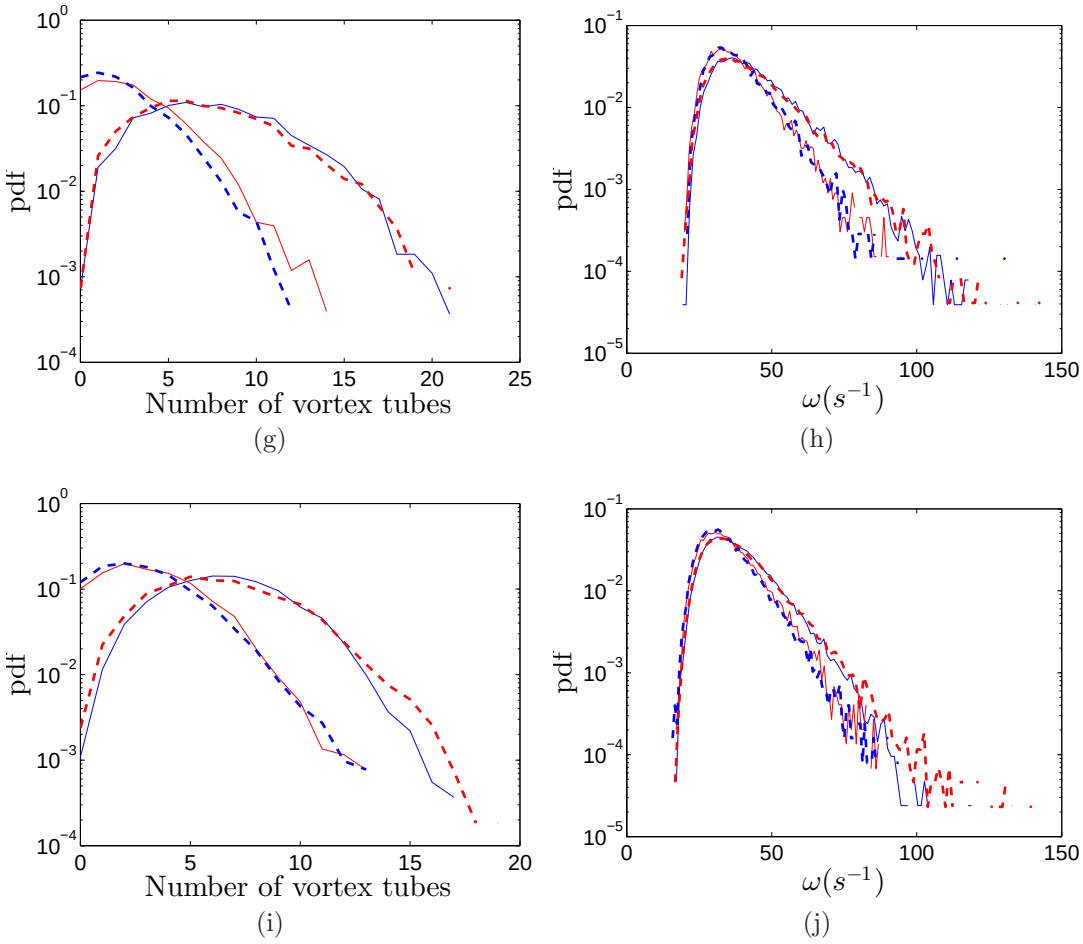

Figure 3.11: Pdfs of the number (left column) and strength (right column) of detected tubes. Solid lines are for the left/positive core and the dashed lines are for the right/negative core. Blue lines represent positive vorticity and the red lines negative vorticity. Each row represents data for a given case: (a) → (b) $V_r = 10$ at $x/dj = 30$, (c) → (d) $V_r = 10$ at $x/dj = 55$, (e) → (f) $V_r = 10$ at $x/dj = 85$, (g) → (h) $V_r = 15$ at $x/dj = 85$, (i) → (j) $V_r = 20$ at $x/dj = 85$.

vorticity magnitude are concentrated around the cores of the CVP, defined here as the position of peak magnitude of the respective core. This is indicated by the peaky shape of the contours around the position of the CVP cores, shown by the dashed lines. The black and white dashed lines in the left and right column figures indicate the respective coordinate position (y-position for the pdfs on the left and z position ofr the pdfs on the right) of the positive and negative CVP core respectively. With increasing downstream distance and velocity ratio the distribution become less peaky, and more flat, around the position of the CVP cores as in figures 3.12i and j, indicating that the large vorticity magnitude tubes are spread more evenly throughout the cores.

Figure 3.13 plots joint pdfs of the detected vortex tube locations. As expected a greater number of positive vortex tubes cluster around the mean peak vorticity region of the positive core (indicated by the intersection of the black and white dashed lines) and visa versa, as seen in the left and middle columns of the figure. Furthermore the vortex tube clusters around the core location show a similar structure to the mean vorticity in figure 3.7. A smaller number of tubes also appear in the core of opposite sign, as was concluded in figure 3.11, located in an arc on the top side of the CVP extending from the core with the same sign to the core of opposite sign. This number increases with increasing downstream distance and velocity ratio. This reveals an additional interesting result for the instantaneous structure of the CVP. Although in the mean vorticity field in figure 3.7 the two cores are independent, the joint pdf of all detected tube locations shown in the right column of figure 3.13 shows that they are actually connected via an arc, something that results in the CVP having the characteristic kidney shape as reported in the literature. One reason this arc does not appear in the mean vorticity field may be that an equal number of positive and negative stream-wise vorticity exists at this location.

3.4 Mean Velocity Field

Before examining the mean velocity profiles, a comment about the relative position of the measurement location should be made. In section 1.3.3 and 3.2 it was shown that the global length scale in the far field l, based purely on

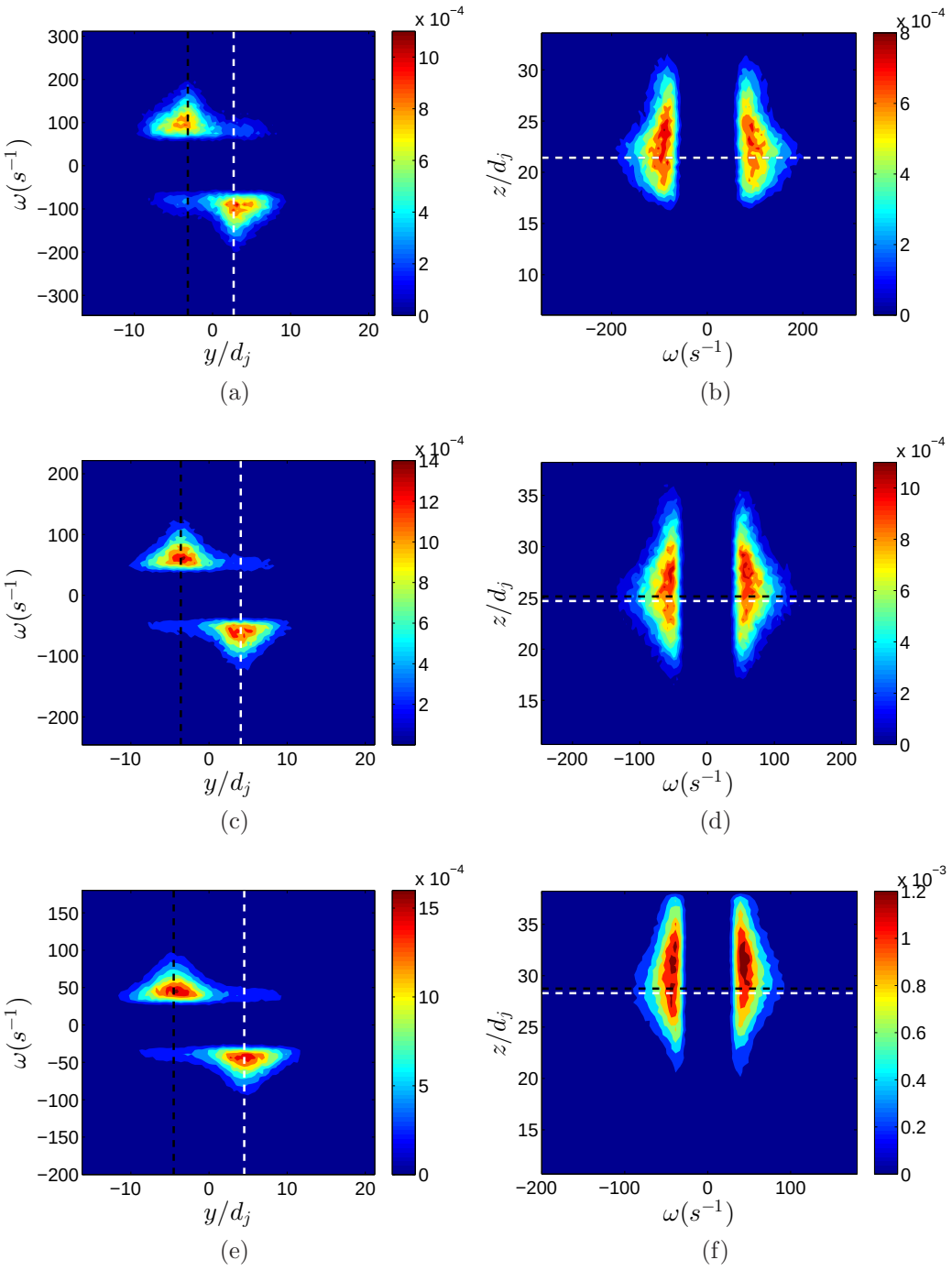

Figure 3.12 (a-f): For caption see following page.

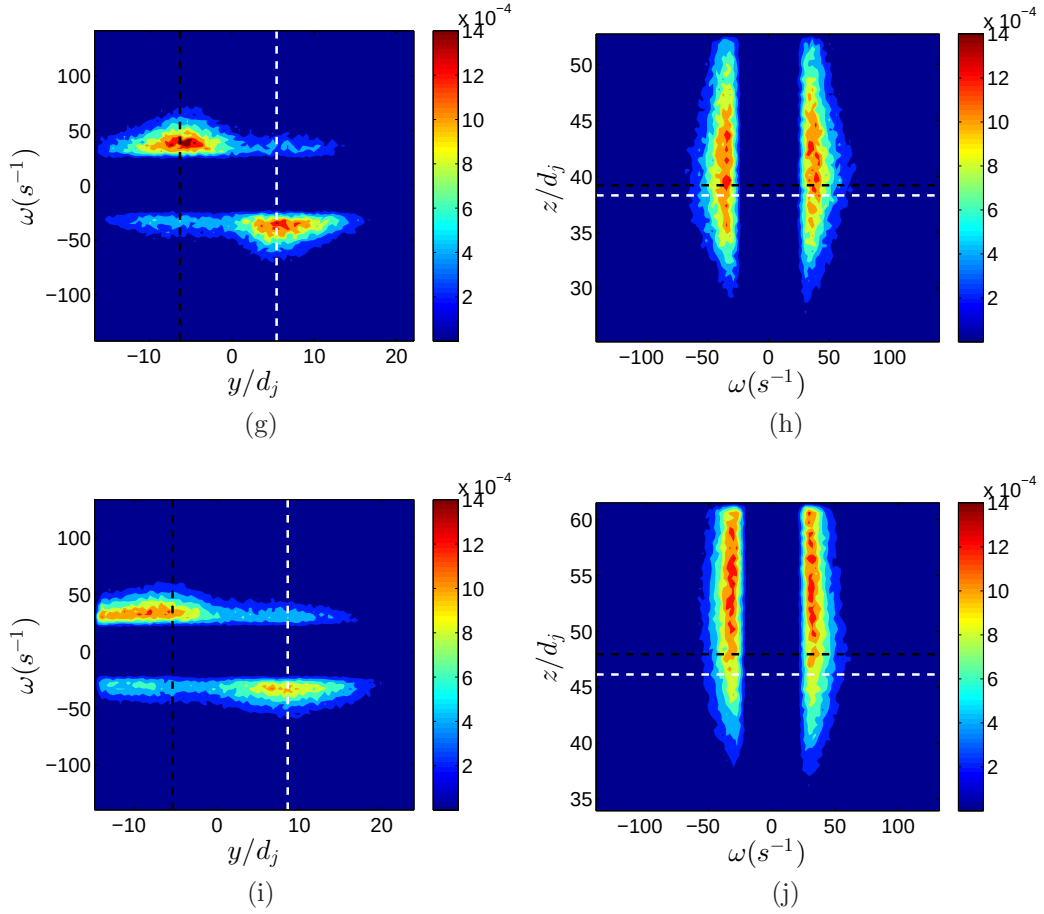

Figure 3.12: Distribution of the detected vortex tube strength and relative position. The left column plots the joint pdfs of strength vs y-position and the right column plots joint pdfs of strength and z-position. The black and white dashed lines in the left and right column figures indicate the position of the positive and negative CVP core respectively. Each row represents data for a given case: (a) → (b) $V_r = 10$ at $x/dj = 30$, (c) → (d) $V_r = 10$ at $x/dj = 55$, (e) → (f) $V_r = 10$ at $x/dj = 85$, (g) → (h) $V_r = 15$ at $x/dj = 85$, (i) → (j) $V_r = 20$ at $x/dj = 85$.

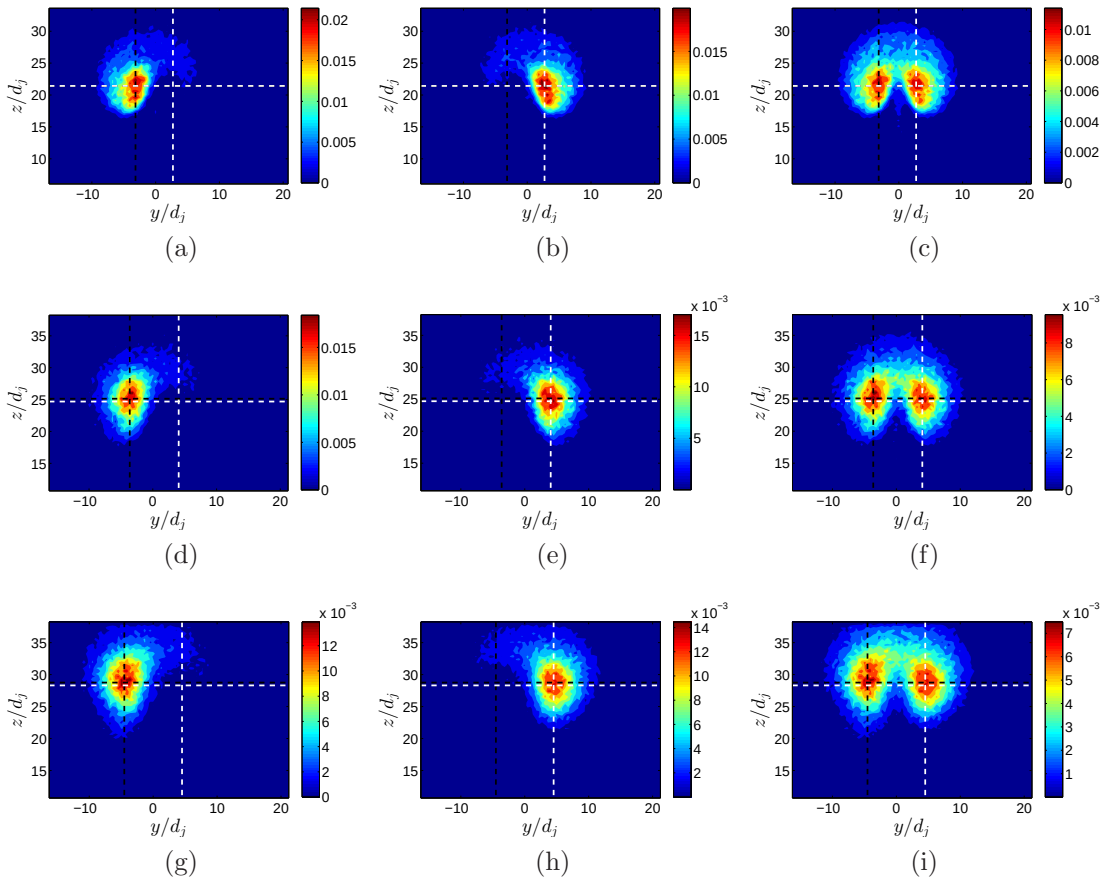

Figure 3.13 (a-i): For caption see following page.

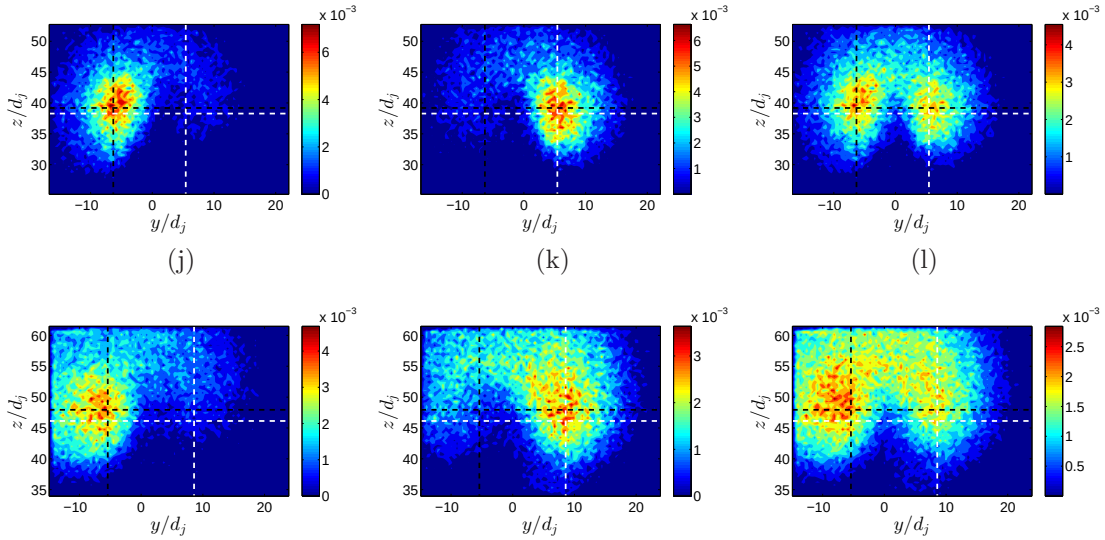

Figure 3.13: Joint pdf of the vortex tube detected y and z position. Left column is the pdf of the positive tubes, middle column the negative tubes and right column is for all (both positive and negative) tubes detected. Intersection of black dashed lines and white dashed lines indicates position of positive and negative CVP core. Each row represents data for a given case: (a) $\rightarrow$ (c) $V_r = 10$ at $x/dj = 30$, (d) $\rightarrow$ (f) $V_r = 10$ at $x/dj = 55$, (g) $\rightarrow$ (i) $V_r = 10$ at $x/dj = 85$, (j) $\rightarrow$ (l) $V_r = 15$ at $x/dj = 85$, (m) $\rightarrow$ (o) $V_r = 20$ at $x/dj = 85$.

non-dimensional reasoning, scales with $l \propto V_r d_j$. Furthermore the jet trajectory collapses when normalised by $V_r d_j$ as initially suggested by Pratte & Baines [53] and was shown in section 3.2. However since the measurements were performed at various velocity ratios and downstream positions, the measurement locations in $V_r d_j$ space, $x/(V_r d_j)$, are different. The non-dimensional measurement locations based on $V_r d_j$ scaling are shown in table 3.5. So in order to examine the evolution of the mean properties, with the aim of collapsing the data, the results are presented in order of increasing $x/V_r d_j$. This scaling, relative to a fixed FoV of the measurements means the flow is more zoomed in for the higher V_r cases.

Table 3.5: Downstream measurement location in $V_r d_j$

V_r	10	20	10	15	10
x/d_j	30	85	55	85	85
$x/(V_r d_j)$	3	4.25	5.5	5.67	8.5

Figure 3.14 shows contour plots of all three components of the mean velocity normalised by the cross-flow velocity. The results of the $\overline{V}$ and $\overline{W}$ velocity fields are what is expected from a CVP, with 4 segments of alternating sign for $\overline{V}$ and a large positive upwash between the cores for $\overline{W}$, with their profile shape being retained with increasing $x/(V_r d_j)$. The $\overline{U}$ contour plots show a profile which is more similar to a wake, with a velocity deficit in the y = 0 centre plane and a surplus on either side, at the position of each vortex core. In contrast to the $\overline{V}$ and $\overline{W}$ components however, an evolving velocity field profile is observed. For the two measurement locations where $x/(V_r d_j) \leq 4.25$ the two high momentum cores on each side of the wake are connected to each other by an arch similar to that observed in figure 3.13. It should be noted that figure 3.13 shows the location of streamwise vorticity, ω_x, which can only induce a velocity in the y and z direction i.e V and W components only. This arch therefore in the $\overline{U}$ field must be induced by a different mechanism. For the two measurement locations at approximately $x/(V_r d_j) = 5.6$ a similar profile is observe but with the arch being absent. Finally at the furthest $x/(V_r d_j)$ position the streamwise velocity field is almost uniform with a variation of less than 4%. Furthermore, as it was the case in the mean

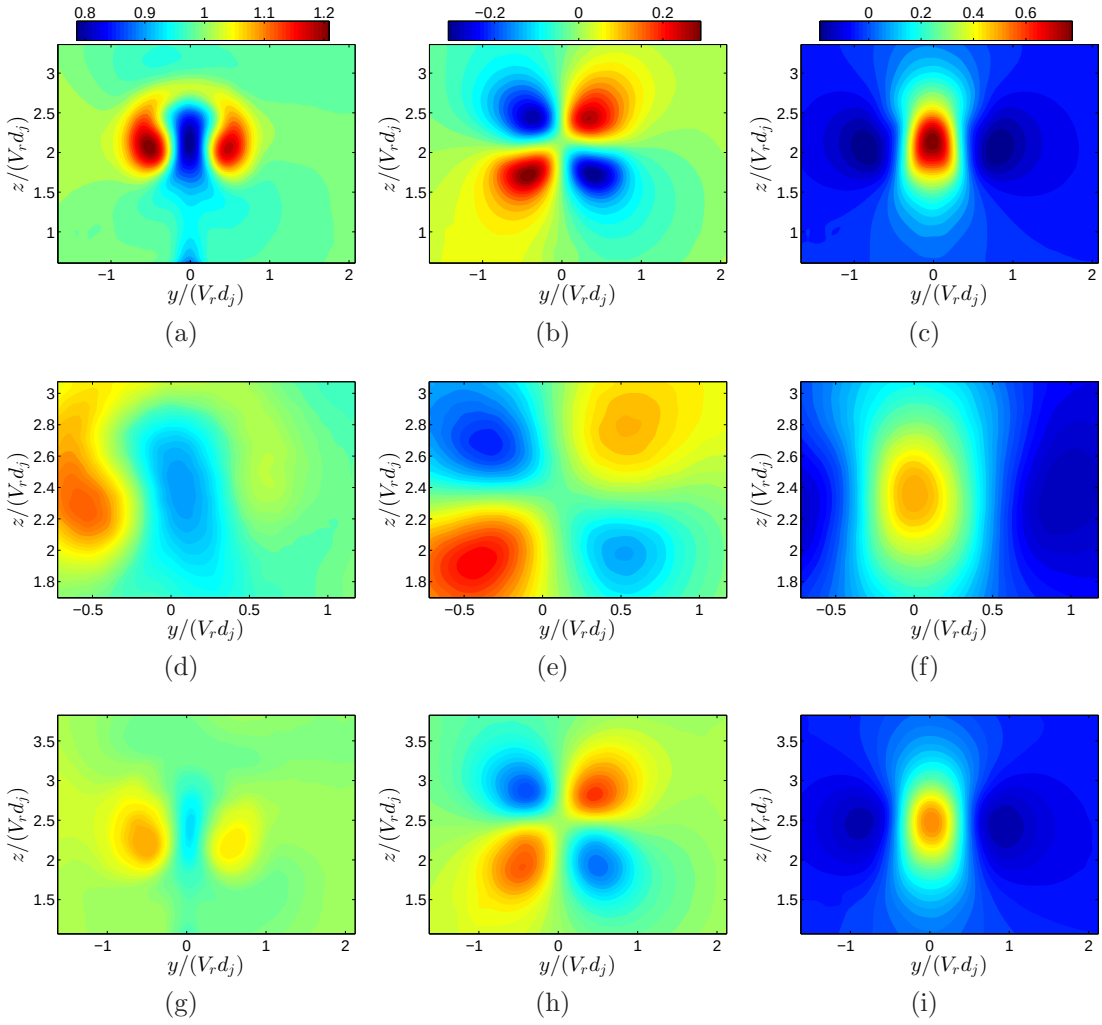

Figure 3.14 (a-i): For caption see following page.

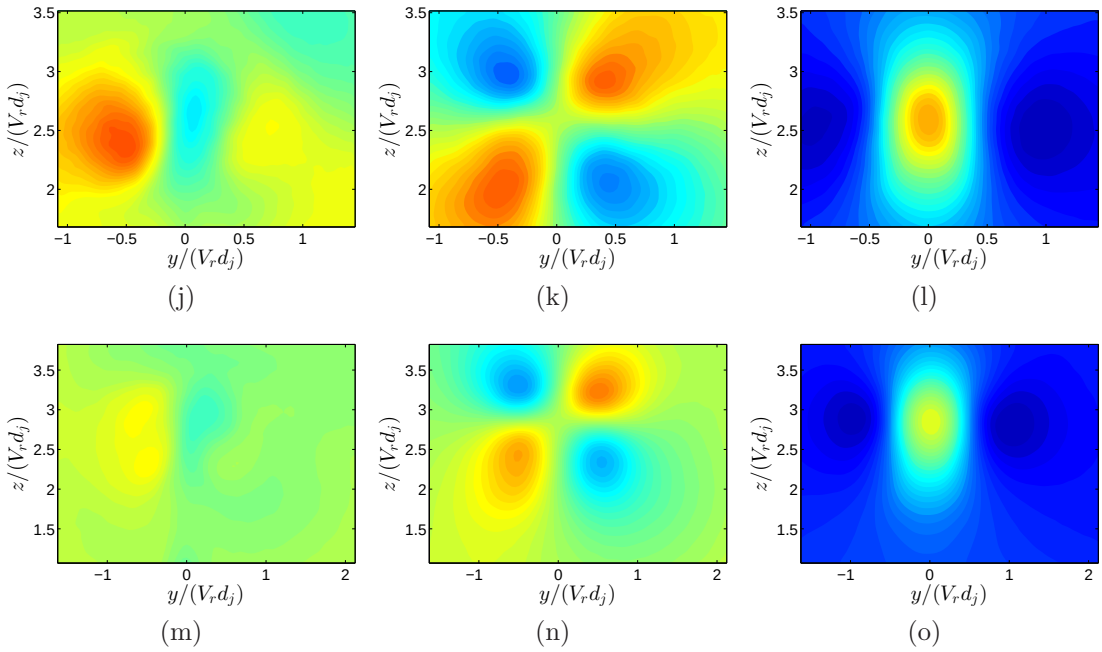

Figure 3.14: Mean velocity field for all inlet conditions. First column shows contour plots of $\overline{U}/U_\infty$, second column of $\overline{V}/U_\infty$ and third column of $\overline{W}/U_\infty$. Each row is for a given case: (a) $\rightarrow$ (c): $V_r = 10$ at $x/dj = 30$, (d) $\rightarrow$ (f): $V_r = 20$ at $x/dj = 85$, (g) $\rightarrow$ (i): $V_r = 10$ at $x/dj = 55$, (j) $\rightarrow$ (l): $V_r = 15$ at $x/dj = 85$, (m) $\rightarrow$ (o): $V_r = 10$ at $x/dj = 85$.

vorticity fields (section 3.2), asymmetries in the velocity fields are also observed, specifically for measurements further downstream in x.

Normalising all three component velocity profiles by the free stream velocity results in a gradual decay in magnitude with increasing $x/(V_r d_j)$. This is be expected when the results from the vortex line model of Broadwell & Breidenthal [9] are considered. The circulation was shown to decay with $(x/V_r d_j)^{-1/3}$ in equation 3.11. With the assumption that the cores of the CVP are represented by vortex lines, the induced velocity magnitude U_Γ from each core in the y-z plane is simply calculated using the inviscid relation 3.14, where r_c is the modulus of the position vector with the position of the line vortex, i.e CVP core, as the origin.

$$U_\Gamma = \frac{\Gamma}{2\pi r_c} \qquad \rightarrow \qquad \Gamma = 2\pi U_\Gamma r_c \tag{3.14}$$

$$\frac{\Gamma}{U_\infty l} = c_2 \left(\frac{x}{l}\right)^{\frac{-1}{3}} \quad \rightarrow \quad \frac{U_\Gamma}{U_\infty} = c_5 \left(\frac{x}{V_r d_j}\right)^{\frac{-1}{3}} \frac{V_r d_j}{r_c} \tag{3.15}$$

Substituting the expression for Γ into the expression on the left hand side of equation 3.11 (reproduced here again on the left) gives the result shown in equation 3.15. The resulting expression shows that the induced velocity magnitude decays with $x/V_r d_j$ for a given $r/V_r d_j$ position. The results of the mean velocity profiles gives weight to the idea that the velocity field of a cross-flow jet with different inlet conditions can be collapsed using the global length scale of $V_r d_j$. However, only 5 measurements conditions at different $x/V_r d_j$ locations are presented here so there is not enough evidence to substantially support this claim. Furthermore asymmetries in the velocity fields make comparisons even harder.

3.5 The Underlying Turbulent Field

The mean turbulent properties of the CVP plane of the cross-flow jet are presented in this section. Once again the data is presented in order of increasing $x/(V_r d_j)$ to examine if the turbulent field follows the same scaling as the mean velocity field and can hence be collapsed to a single case using the $V_r d_j$ global length scale.

3.5.1 RMS Velocity Field

Figure 3.15 shows contours of the rms component velocities. Streamlines of the mean velocity field are added as conceptual aids. All figures are normalised by the free stream velocity, and therefore correspond to the component turbulence intensities. The results show a clear distinguishable shape to the contours, for all downstream positions. They clearly demonstrate the characteristic kidney shape of the CVP reported in the literature. The left and right columns show contours of the streamwise $\sqrt{\overline{u'^2}}/U_\infty$ and wall-normal component $\sqrt{\overline{w'^2}}/U_\infty$ are similar in shape and exhibit the kidney shape. The streamlines show that two peaks in the rms velocity observed near the cores of the CVP are connected together via an arch of strong turbulence intensity on the top/windward side. Contours of the spanwise component $\sqrt{\overline{v'^2}}/U_\infty$ don't show the same kidney shape but appears two have two peaks which are connected by a region of high turbulence intensity, this time on the bottom/wake side of the CVP. Furthermore the $\sqrt{\overline{u'^2}}/U_\infty$ and $\sqrt{\overline{v'^2}}/U_\infty$ profiles seem to have distinct but low level fluctuations extending from the CVP into the wake towards the wall. This is more apparent for measurements in the near field. This may be a result of the wake structures observed by Smith & Mungal [58] in their scalar measurements for $V_r > 10$ (reproduced here in figure 1.7). Furthermore it is interesting to note the large turbulence intensities are observed to persist far downstream, a value of 10% being observed in the cores even at $85d_j$ downstream for the case where $V_r = 10$. From the overlayed streamlines, the peaks in the rms velocity fields for all three components appear close to the cores of the CVP. This is examined further by plotting spanwise and wall-normal profiles of each rms velocity component through the peaks and profiles of vorticity through the CVP cores in figure 3.16. The data from the Small-Scale FoV data is also plotted to see if the change in resolution affects the results. Profiles in the y-direction from the first three $x/(V_r d_j)$ locations only are presented here, but results form the remaining two cases (as well as profiles in the z-direction) show the same results. The profiles from both LFoV and SFoV data sets show that the maximum rms velocity occurs, for all three components, at the position of maximum vorticity i.e the core of the CVP. As a consequence this also mean that the maximum of the rms velocity for all three components

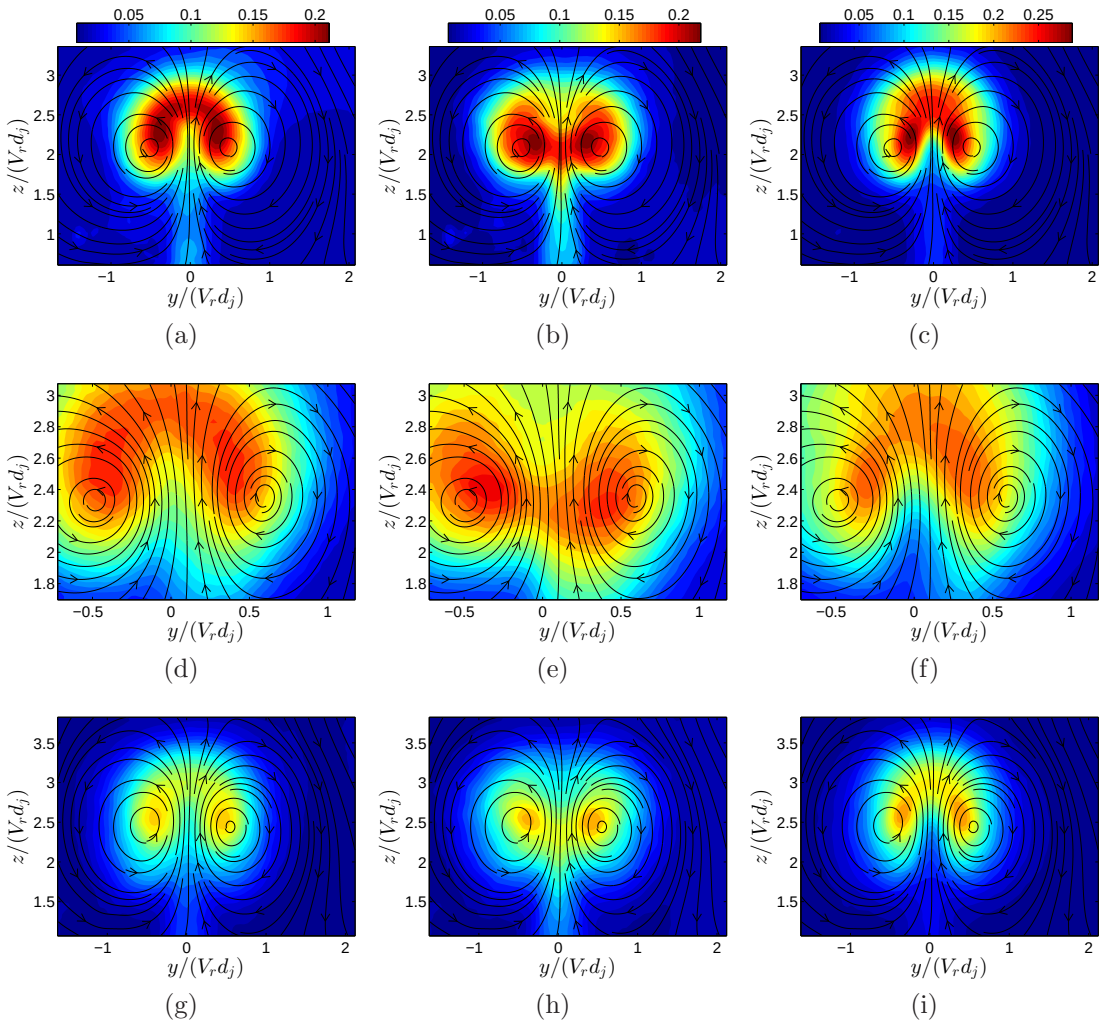

Figure 3.15 (a-i): For caption see following page.

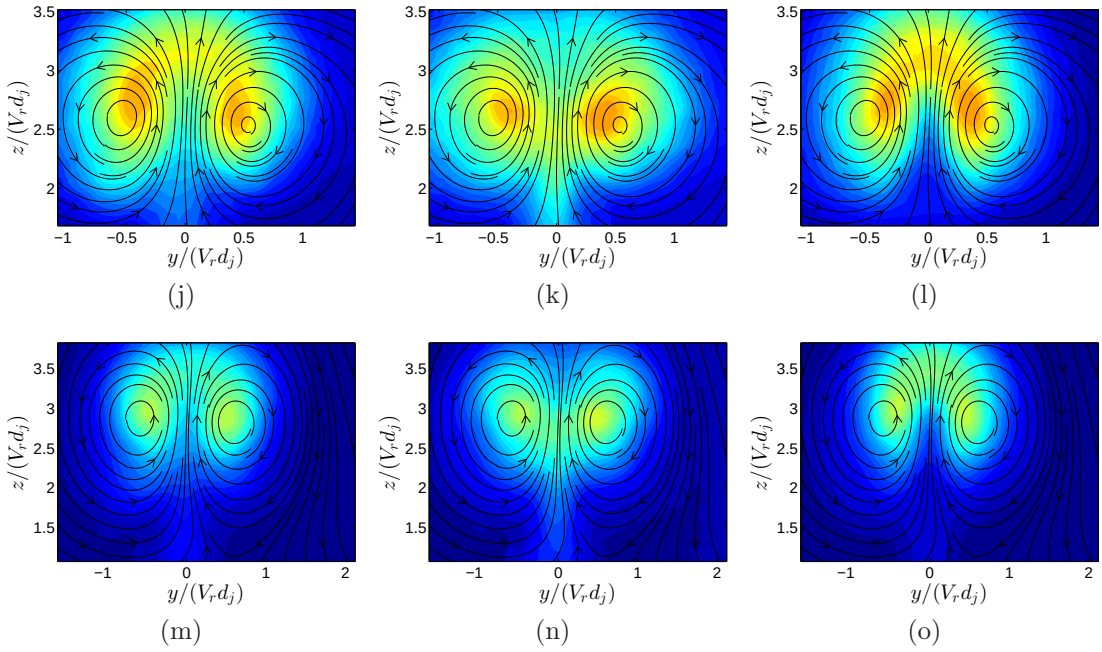

Figure 3.15: RMS velocity fields for all conditions. First column is $\sqrt{\overline{u'^2}}/U_\infty$, second column is $\sqrt{\overline{v'^2}}/U_\infty$ and third column is $\sqrt{\overline{w'^2}}/U_\infty$. Each row is for a given case: (a) → (c): $V_r = 10$ at $x/dj = 30$, (d) → (f): $V_r = 20$ at $x/dj = 85$, (g) → (i): $V_r = 10$ at $x/dj = 55$, (j) → (l): $V_r = 15$ at $x/dj = 85$, (m) → (o): $V_r = 10$ at $x/dj = 85$.

occurs at the same location. Furthermore the position of minimum rms velocity along the profile for all components within the CVP occurs at the position of minimum vorticity, the midpoint between the cores.

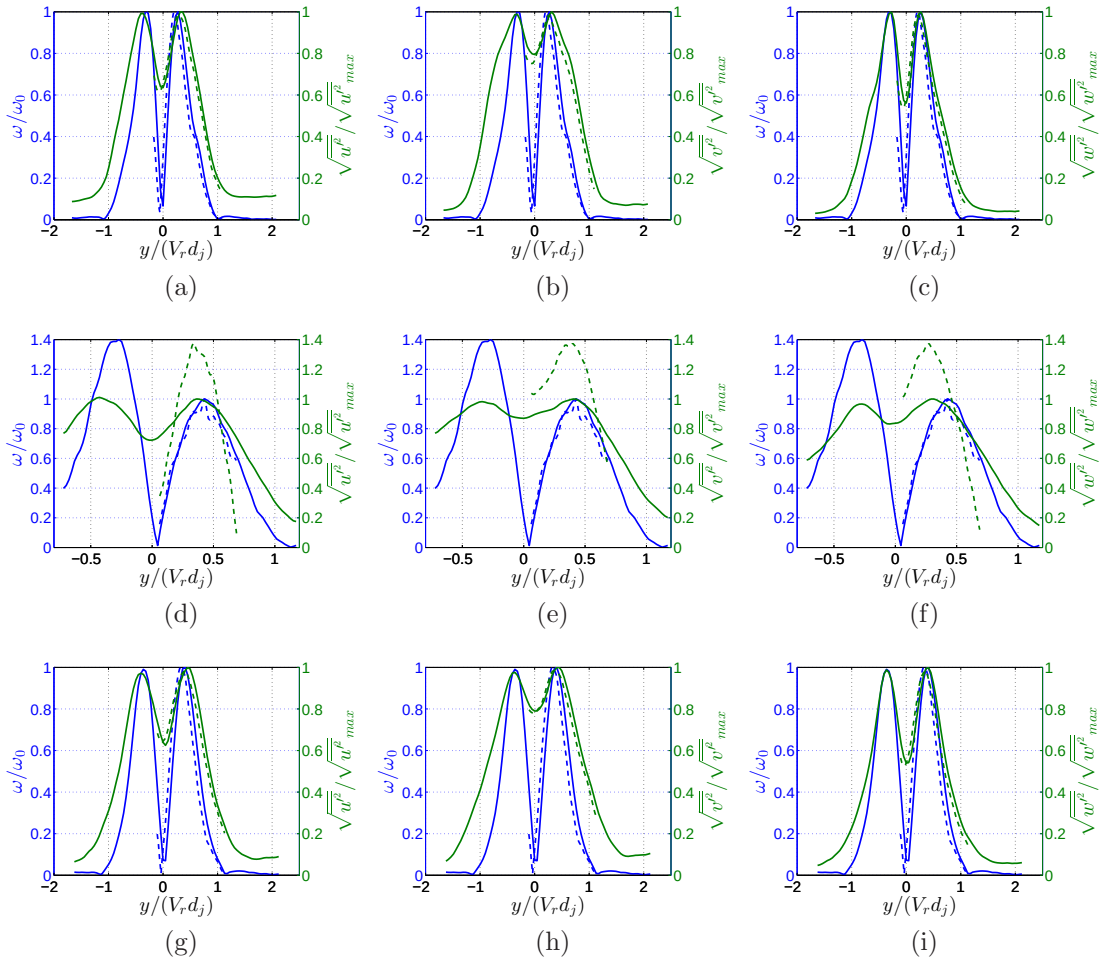

Figure 3.16: Spanwise rms and vorticity profiles through peaks and CVP cores respectively. Left column is profiles of $\sqrt{\overline{u'^2}}$, middle column is profiles of $\sqrt{\overline{v'^2}}$ and right column is profiles $\sqrt{\overline{w'^2}}$. Each row is for a given case. (a) $\rightarrow$ (c): $V_r = 10$ at $x/dj = 30$, (d) $\rightarrow$ (f): $V_r = 20$ at $x/dj = 85$, (g) $\rightarrow$ (i): $V_r = 10$ at $x/dj = 55$.

With the knowledge of the position of the streamwise vortex tubes, as shown in figure 3.12 and 3.13, a few comments can be made about the rms velocity

profiles. First, the two peaks in rms velocity field can be explained for the $\sqrt{\overline{v'^2}}$ and $\sqrt{\overline{w'^2}}$ components by the high concentration of strong vortex tubes around the cores. Since, similar to the mean streamwise velocity field $\overline{U}$, the streamwise vortex tubes cannot induce a streamwise velocity u' (in the x-direction), the peaks in $\sqrt{\overline{u'^2}}$ must originate from a different mechanism. Second, the presence of a large rms contour in the $\sqrt{\overline{v'^2}}$ field at the midpoint between the cores through the wake, where streamwise vortex tubes are absent, also means that there is another mechanism creating this. Given the fluctuations are observed to stretch into the wake, this may be a result of the wake structures present which can induce a spanwise velocity v' (in the y-direction). Finally, and most interestingly, the absence of the top/windward arch in the $\sqrt{\overline{v'^2}}$ profiles, appear to contradict the presence of streamwise vortex tubes at this position as detected in figure 3.13. This indicates that only part of the flow can be explained by vorticity structures aligned in the streamwise direction.

3.5.2 Reynolds Stresses

The Reynolds stresses in the CVP plane $\overline{u_i' u_j'}$ are plotted in figure 3.17. Different colormaps are used for each plot due to the change in value of an order of magnitude between the various inlet conditions where blue to red represents negative to positive values of Reynolds stress respectively, and white being $\overline{u_i' u_j'} = 0$.

Once again, although not as much as the rms velocities in figure 3.15, a high level of organisation/coherency is observed. The third column of contour plots of the $\overline{v'w'}/U_\infty^2$ component, i.e the components in the CVP plane, shows a very distinct symmetric in shape and antisymmetric in sign structure about the centre plane which remains the same for all inlet conditions and downstream positions (ear shaped opposite signed stresses either side of the jet centreline). Each side of this shape shows a peak just to the inside of the position of CVP core (towards the centre plane) with a second peak just above CVP core. It should be noted that since the Reynolds stress is calculated from the prime velocity fields, the mean flow is subtracted and the CVP is therefore removed. The remaining two components show an evolving shape with increasing $x/V_r d_j$ position. The $\overline{u'v'}/U_\infty^2$ profiles show again an antisymmetric structure. For $x/(V_r d_j) < 4.25$ the profile

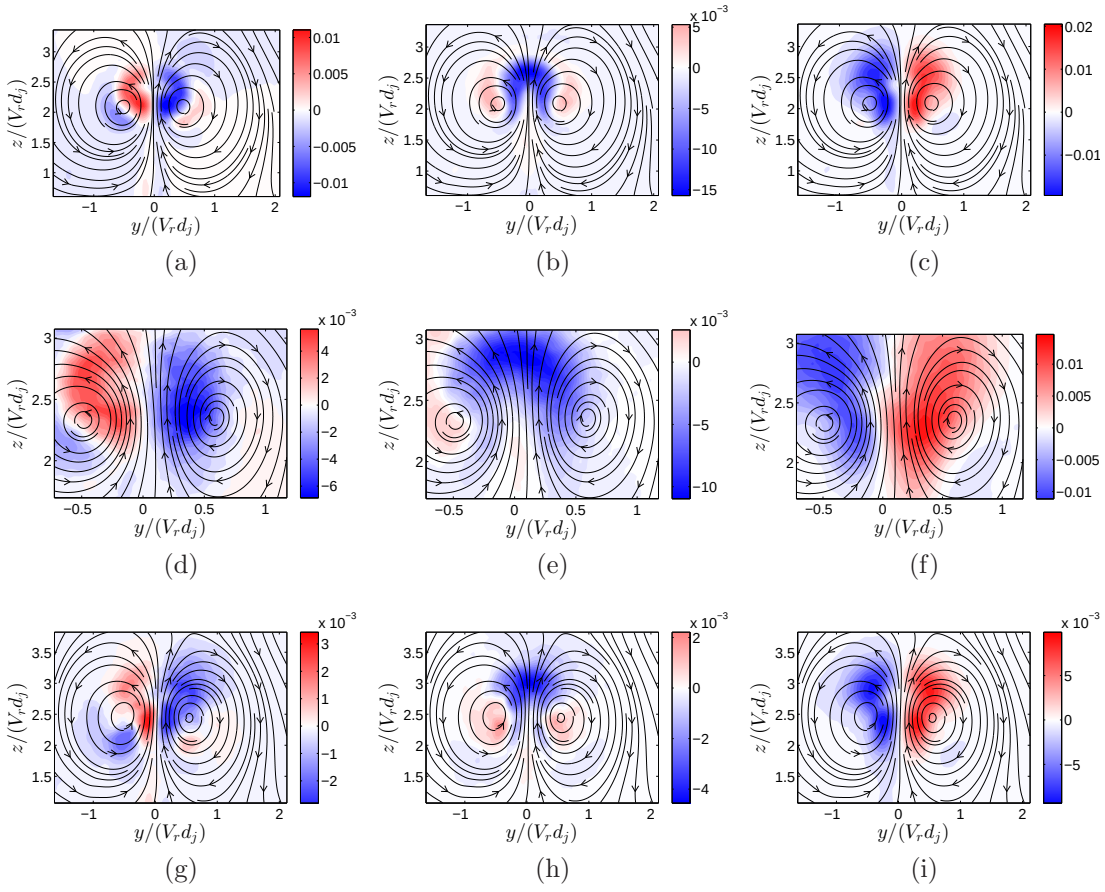

Figure 3.17 (a-i): For caption see following page.

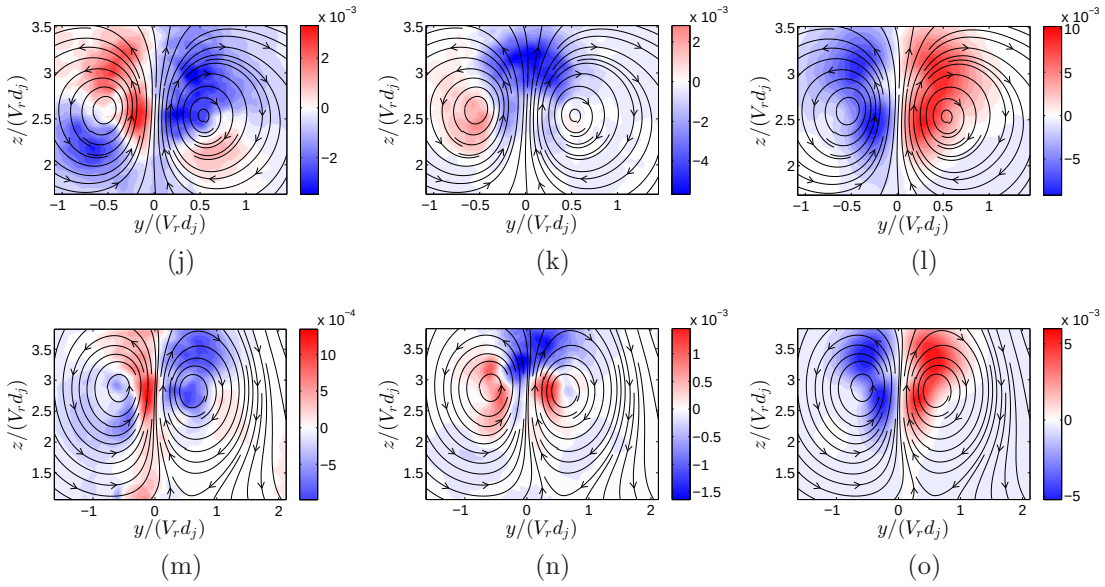

Figure 3.17: Reynolds stress fields. Left column is contour plots of $\overline{u'v'}/U_\infty^2$, middle column of $\overline{u'w'}/U_\infty^2$ and right column of $\overline{v'w'}/U_\infty^2$. Each row is for a given case: (a) $\rightarrow$ (c): $V_r = 10$ at $x/dj = 30$, (d) $\rightarrow$ (f): $V_r = 20$ at $x/dj = 85$, (g) $\rightarrow$ (i): $V_r = 10$ at $x/dj = 55$, (j) $\rightarrow$ (l): $V_r = 15$ at $x/dj = 85$, (m) $\rightarrow$ (o): $V_r = 10$ at $x/dj = 85$.

shows two kidney shaped contours of opposite sign, being positive on the left hand side and negative on the right hand side of the centre plane. A contour of the opposite sign to these kidney shapes is observed diagonally downwards towards the wall for each side. The two contours of opposite sign on each side of the centre plane seem to be located diagonally about the position of the CVP core when observing the streamlines. Further downstream in $x/(V_r d_j)$ the high level of organisation is lost but the main shape is retained, with the main difference that the top/windward side of the kidney shaped contours expanding outwards away from the wall. The $\overline{u'w'}/U_\infty^2$ shows a more symmetric shape, with the centre plane dominated by a negative contour with two positive contours either side of which, for low values of $x/(V_r d_j)$, wrap around this negative contour on the top/windward side. Furthermore two 'legs' of the negative contour appear on the bottom/wake side extending into either side of the CVP. The saddle shape between these two legs of zero $\overline{u'w'}/U_\infty^2$ reflects the low values of both $\sqrt{\overline{u'^2}}$ and $\sqrt{\overline{w'^2}}$ observed in the same region in figure 3.15. Further downstream this region around the centre plane is still dominated by a negative contour but the two positive contours move down and towards the centre plane.

3.5.3 TKE Production

Given that the LFOV measurements mainly resolve the large scale structures, which are associated with the production of Turbulent Kinetic Energy (TKE) passed down to the smaller scales via the cascade effect, it is worth examining how the mean flow gradients of the CVP interact with the Reynolds stresses to identify where the TKE production originates from. The mechanism for TKE production is expected to come from the shear between the jet and the cross-flow on the windward side. The expression for the production of TKE production is composed of 9 terms when equation 3.16 is expanded:

$$\mathcal{P} = -\overline{u_i' u_j'} \frac{\partial \overline{U_i}}{\partial x_j} \tag{3.16}$$

Stereoscopic PIV measurement gives access to the first two columns, i.e 6 components, of the velocity gradient tensor (equation 2.19). Furthermore using con-

tinuity the out of plain gradient of the U component can be estimated as shown below.

$$\nabla \cdot \mathbf{U} = \frac{\partial U}{\partial x} + \frac{\partial V}{\partial y} + \frac{\partial W}{\partial z} = 0 \rightarrow \frac{\partial U}{\partial x} = -\left(\frac{\partial V}{\partial y} + \frac{\partial W}{\partial z}\right) \tag{3.17}$$

Therefore 7 of 9 components are available, leading to a two dimensional-three component estimate $\mathcal{P}_{2D3C}$ given by:

$$\begin{aligned} -\mathcal{P}_{2D3C} = \overline{u'^2}\frac{\partial \overline{U}}{\partial x} + \overline{v'^2}\frac{\partial \overline{V}}{\partial y} + \overline{w'^2}\frac{\partial \overline{W}}{\partial z} \\ + \overline{v'w'}\frac{\partial \overline{V}}{\partial z} + \overline{v'w'}\frac{\partial \overline{W}}{\partial y} + \overline{u'v'}\frac{\partial \overline{U}}{\partial y} + \overline{u'w'}\frac{\partial \overline{U}}{\partial z} \end{aligned} \tag{3.18}$$

Figure 3.18 shows contour plots of $\mathcal{P}_{2D3C}$ for all conditions studied. In all cases TKE is predominantly produced on the top/windward side of the CVP between the two cores, as expected. The distribution of the TKE is symmetrical about the centre plane with a distinct 'hole' in the wake of the jet where there is no production. To identify the largest contribution to the total mean TKE production, each

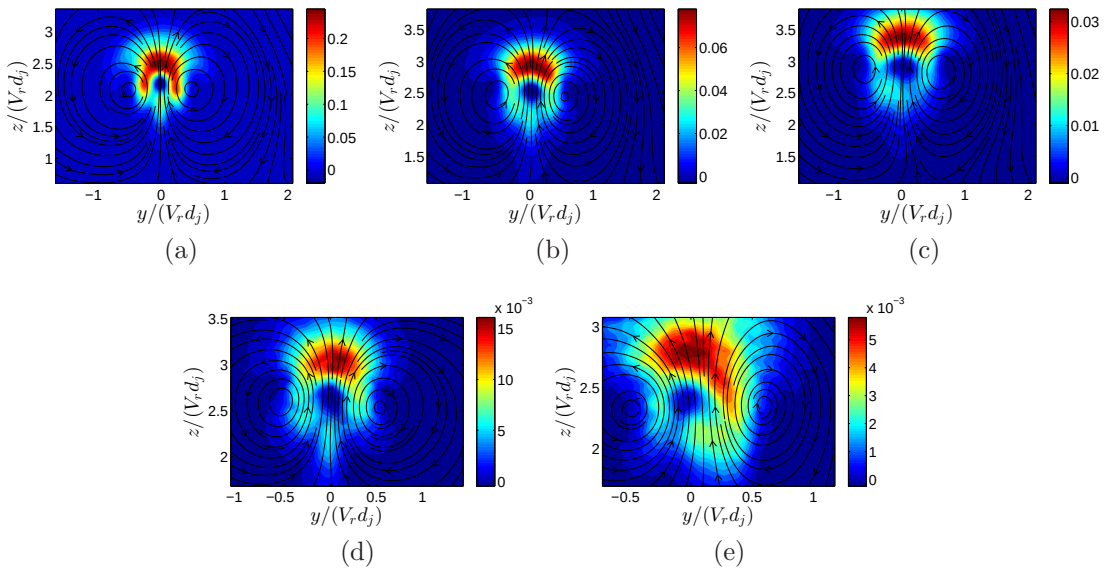

Figure 3.18: Contour plots of part of the mean turbulent kinetic energy production $\mathcal{P}_{2D3C}(m^2/s^3)$. (a) $V_r = 10$ at $x/d_j = 30$, (b) $V_r = 10$ at $x/d_j = 55$, (c) $V_r = 10$ at $x/d_j = 85$, (d) $V_r = 15$ at $x/d_j = 85$, (e), $V_r = 20$ at $x/d_j = 85$

component is plotted individually. The individual components for the case where $V_r = 10$ at $x/d_j = 55$ are plotted in figure 3.19. The figure shows that three

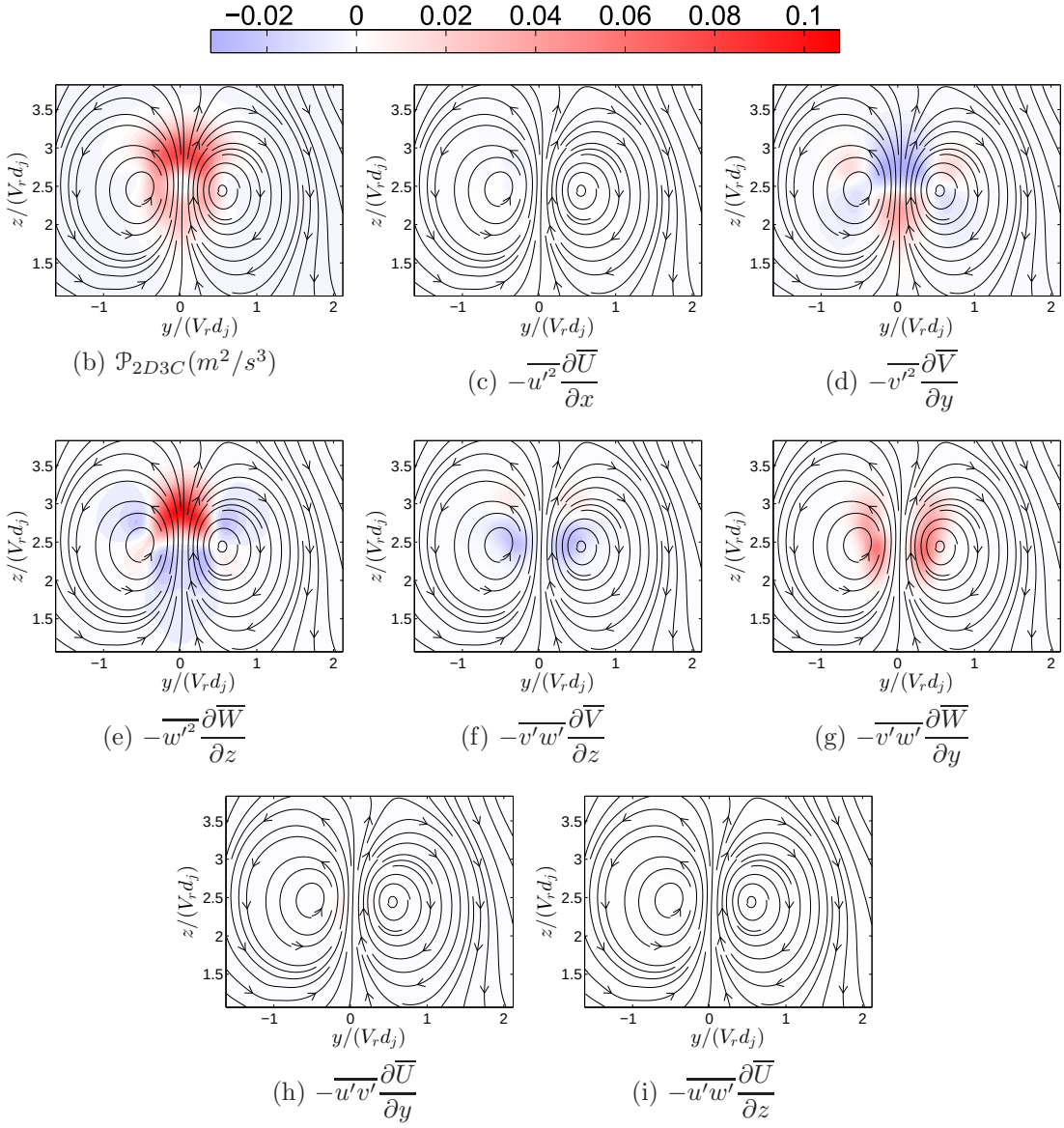

(b) $\mathcal{P}_{2D3C}(m^2/s^3)$ (c) $-\overline{u'^2}\frac{\partial \overline{U}}{\partial x}$ (d) $-\overline{v'^2}\frac{\partial \overline{V}}{\partial y}$

(e) $-\overline{w'^2}\frac{\partial \overline{W}}{\partial z}$ (f) $-\overline{v'w'}\frac{\partial \overline{V}}{\partial z}$ (g) $-\overline{v'w'}\frac{\partial \overline{W}}{\partial y}$

(h) $-\overline{u'v'}\frac{\partial \overline{U}}{\partial y}$ (i) $-\overline{u'w'}\frac{\partial \overline{U}}{\partial z}$

Figure 3.19: Contour plots of all the individual components of $\mathcal{P}_{2D3C}(m^2/s^3)$. Results are from the case where $V_r = 10$ at $x/d_j = 55$. The colour map at the top applies for all contour plots.

components provide most of the source of TKE production, the $\overline{w'^2}\left(\partial \overline{W}/\partial z\right)$,

the $\overline{v'w'}\left(\partial\overline{W}/\partial y\right)$ and the $\overline{v'^2}\left(\partial\overline{V}/\partial y\right)$ component in order of decreasing magnitude. From the figures, the different contributions of each component is evident. The $\overline{w'^2}\left(\partial\overline{W}/\partial z\right)$ component contributes most to $\mathcal{P}_{2D3C}$ around the centre plane above the CVP cores and this is expected to be due to the shear generation between the jet and cross-flow. The $\overline{v'w'}\left(\partial\overline{W}/\partial y\right)$ contributes to the part of $\mathcal{P}_{2D3C}$ which extends from the windward side down to the wake side and this is a reflection of the shape of $\overline{v'w'}$ shown in figure 3.17. The components that include the streamwise velocity component provide little contribution to momentum transfer.

3.5.4 Two-Point Spatial Correlations

The unique features of the rms velocity, Reynolds stresses and TKE production fields of the CVP plane, which persist far downstream for different velocity ratios, begs the question of what comprises the structure of the cross-flow jet in the far field. An initial way to assess any underlying structure is to look at correlation maps calculated using equation 3.19:

$$R_{u_iu_j}(y_0, z_0, \delta y, \delta z) = \frac{\overline{u_i'(y_0, z_0)u_j'(y_0 + \delta y, z_0 + \delta z)}}{\sqrt{\overline{u_i'^2}}\sqrt{\overline{u_j'^2}}} \tag{3.19}$$

For a given origin (y_0, z_0) in the CVP plane two dimensional correlations can be calculated.

One of the most striking features of the rms velocity fields is the kidney shape [22, 31, 32, 37, 38, 58], and specifically the arc connecting the two peaks as shown in the left and right column contour plots of figure 3.15. To gain a better understanding of why this shape appears correlations are taken about the point in the centre plane at the height of the top of the arch, i.e on the windward side of the CVP(denoted by the intersection of the dashed lines in the contour plots on the left in figure 3.20). The middle and right columns plots in figure 3.20 shows the results of $R_{uu}(y_0, z_0, \delta y, \delta z)$ and $R_{wu}(y_0, z_0, \delta y, \delta z)$ respectively. Note that the results of $R_{wu}(y_0, z_0, \delta y, \delta z)$ and $R_{uw}(y_0, z_0, \delta y, \delta z)$ are not the same, with the latter calculating the correlation coefficient of the u' component at (y_0, z_0) with the w' component throughout the field. The results of $R_{uu}(y_0, z_0, \delta y, \delta z)$ in the

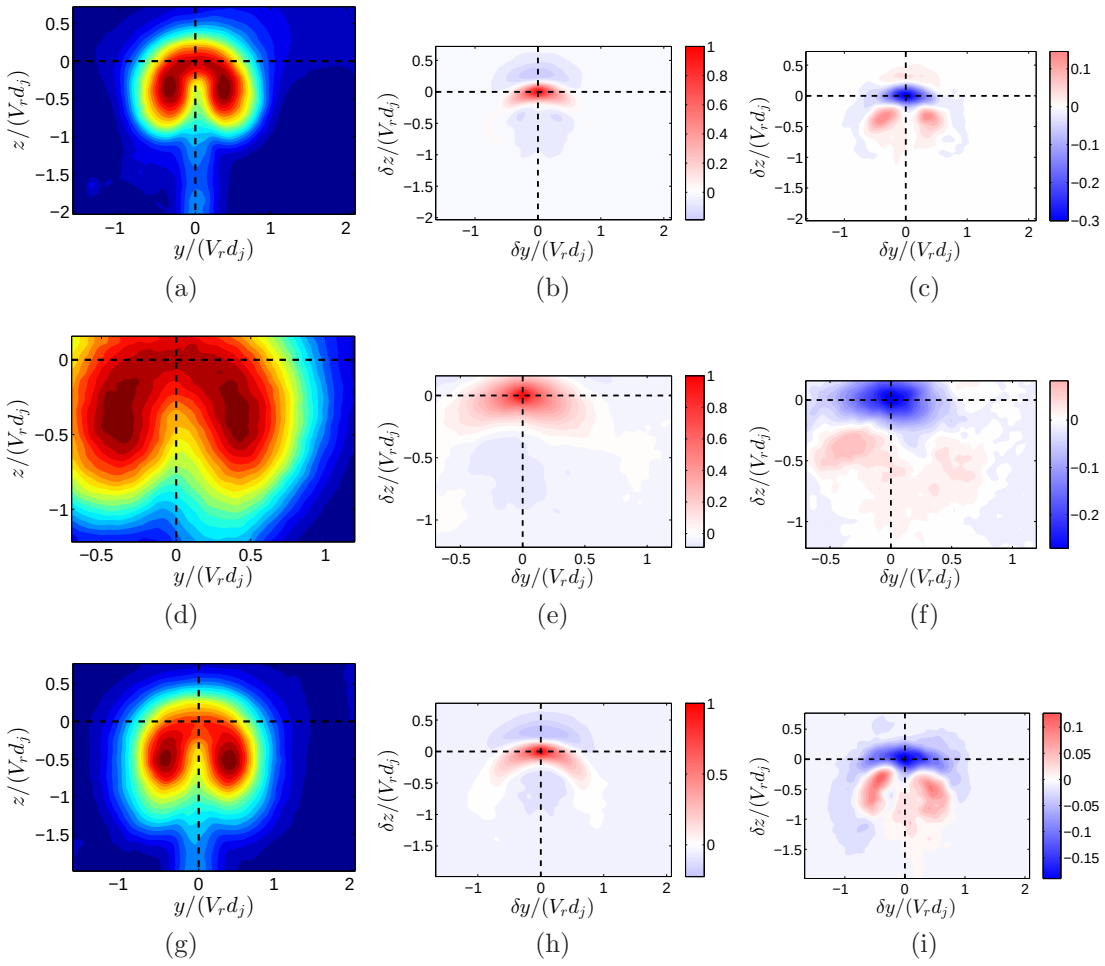

Figure 3.20 (a-i): For caption see following page.

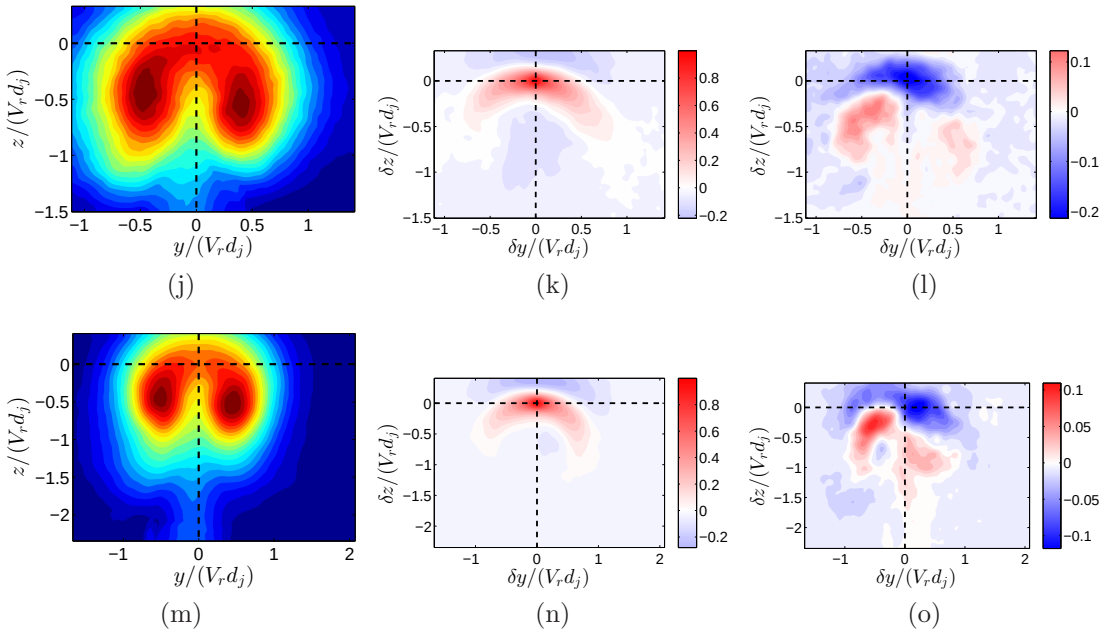

Figure 3.20: Correlation maps for windward side of the CVP plane. Intersection of dotted lines in left column show location of (y_0, z_0) in the $\sqrt{\overline{u'^2}}$ field. Middle column shows $R_{uu}(y_0, z_0, \delta y, \delta z)$. Right column shows $R_{wu}(y_0, z_0, \delta y, \delta z)$. Each row is for a given case: (a) → (c): $V_r = 10$ at $x/dj = 30$, (d) → (f): $V_r = 20$ at $x/dj = 85$, (g) → (i): $V_r = 10$ at $x/dj = 55$, (j) → (l): $V_r = 15$ at $x/dj = 85$, (m) → (o): $V_r = 10$ at $x/dj = 85$.

middle column shows that the u' component remains correlated along an arc shape similar to that in the $\sqrt{\overline{u'^2}}$ field. This could indicate the existence of a persistent eddy structure in the shape of an arched roller or a hairpin head, extending from the windward side down to the cores of the CVP. The top of such a structure would be aligned in the spanwise y-direction and would thus be expected to also result in the strong correlation between the u' and w' components at and around the centre position (y_0, z_0), which can be seen by the negative contours in the plots of R_{wu} in the right column. Furthermore, the positive contour either side of the centre plane at the core locations shows that the flow is correlated downwards towards the cores of the CVP from the windward side.

All this information points to a structure, whose mean shape generates the kidney shape observed in the rms profiles in figure 3.15. A cartoon of a possible interpretation of this structure this is shown in figure 3.21. The sketch illustrates the hairpin by drawing a vortex line which represents the spine of the structure. This structure would also explain the low value of $\sqrt{\overline{v'^2}}$ velocity at the location of the top of the arch, and the high value in both $\sqrt{\overline{u'^2}}$ and $\sqrt{\overline{w'^2}}$ velocity fields, as this structure would only induce a u' and w' component. The existence of such a structure would also explain the presence of streamwise vorticity in the area around the top of the arch in the pdfs of vortex tubes shown in figure 3.13. Since this structure would, on average, be aligned in the spanwise y-direction, streamwise vorticity would appear instantaneously but on average would be zero, as is observed in the mean vorticity fields in figure 3.7.

An additional characteristic of this hypothetical eddy structure can be postulated by looking at the profiles of the principal correlation functions i.e R_{uu}, R_{vv} and R_{ww}, in the z directions, shown in figure 3.22. The profiles are taken with centre (y_0, z_0) at the position of maximum rms velocity in the left/negative CVP core. Furthermore data from the SFOV measurements is also shown to ensure that the LFOV data resolution is high enough to correctly represent the correlations. Concentrating on the right hand side of the plots i.e for $\delta z > 0$ going upwards away from the wall, the transverse correlation (velocity component at right angle to separation) $R_{uu}(y_0, z_0, 0, \delta z)$ profile becomes negative before approaching zero. This would be expected for a structure which was inclined in the $y - z$ plane consistent with the arch shape in figure 3.20. The longitudinal correlation

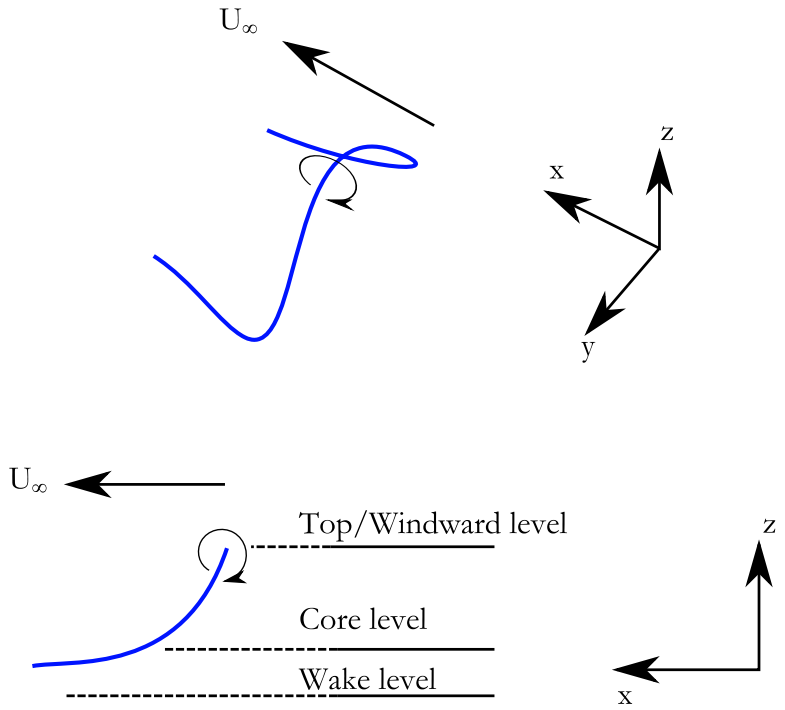

Figure 3.21: A cartoon of an inclined hairpin structure. Top part shows a 3D view. Bottom part shows a side view together with the z-level of each part relative to the CVP.

(velocity component parallel to separation) $R_{ww}(y_0, z_0, 0, \delta z)$ does not become negative and also persists for larger δz separations for all cases. This could indicate a structure which is preferentially oriented in the z-direction. Finally, the remaining transverse correlation $R_{vv}(y_0, z_0, 0, \delta z)$, similarly to $R_{uu}(y_0, z_0, 0, \delta z)$, also becomes negative resulting from an inclination of the structure in the $x - z$ plane. Therefore a clearer picture of the arch shaped structure is emerging which could be one of an inclined hairpin head in the streamwise direction, as shown in figure 3.21.

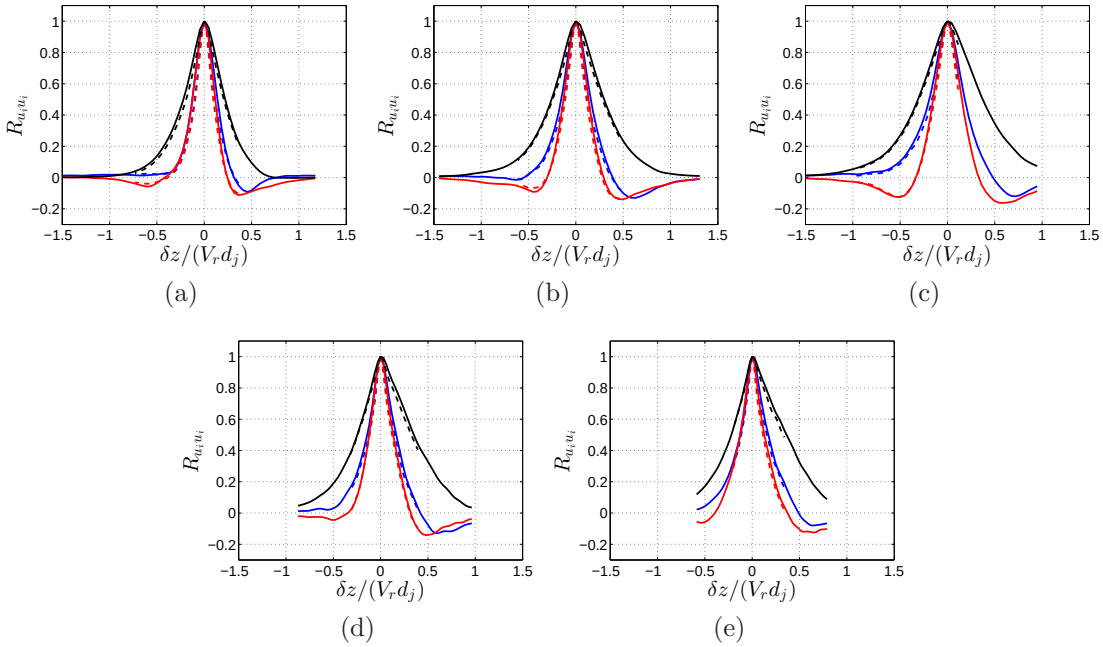

Figure 3.22: Profiles of the principal correlations functions along the z-direction. Centre (y_0, z_0) is taken as the position of maximum rms velocity in the negative/left core. Blue lines show $R_{uu}(y_0, z_0, 0, \delta z)$ component, red lines show $R_{vv}(y_0, z_0, 0, \delta z)$ components and black lines are for $R_{ww}(y_0, z_0, 0, \delta z)$ component. Dashed lines are from the SFoV data.

Another important feature of the CVP is the wake. Wake structures have been examined in the literature numerous times (as summarised in section 1.3.2), but most studies consider $V_r < 10$ where a strong interaction with the wall is observed (see section 1.3.2). However, evidence of their presence also appears

here, specifically in the rms velocity profiles presented in figure 3.15. A better test however for their presence here is to look at correlation maps with centre (y_0, z_0) in the centre plane on the wake side of the CVP. Figure 3.23 shows the results of $R_{uu}(y_0, z_0, \delta y, \delta z)$ and $R_{vu}(y_0, z_0, \delta y, \delta z)$. The results of R_{uu} in the middle column show that the u' velocity component stays correlated along a thin upright shape, where the wake structures occur. If we consider the simple case where the wake structure is a vortex tube aligned normal to the wall along $y = 0$ in the figures, then the v' component on the centre plane to be strongly correlated to the u' component on either side of the centre plane. This is evident in the plots of R_{vu} in the right column.

As expected the correlations extend downwards but interestingly they also extend upwards into the CVP, suggesting that these structures are somehow connected to it. Rivero *et al.* [55] and Eiff & Keffer [19] have also observed and studied the link between the wake structures and CVP using hot wire measurements together with a pattern recognition technique for low velocity ratios of $V_r = 3.8$ and $V_r = 3$ respectively. This is much lower than the velocity ratios studied here and in a different flow regime of $V_r < 10$ [58]. Another interesting feature is the presence of a weaker negative correlation in the R_{uu} map in the shape of an arch on top of the wake structure (positive correlation), on the windward side of the CVP. This arch has the same shape and position as that observed in the second column in figure 3.20, suggesting that these two structures may be linked.

The $2D-3C$ PIV data reveal a number of interesting results, especially when looking at the spatial correlations above, regarding the coherent structure of the cross-flow jet but are limited in the conclusions that can be drawn. This is due to the fact that the flow is a very complex three dimensional flow with various flow structures interacting with each other. However an important conclusion that can be drawn is that the correlation maps and profiles are very similar for all cases studied. This suggests that the structure of the CVP is common for all V_r investigated and persists into the far field. Smith & Mungal [58] however have noticed differences in the scalar structure for increasing velocity ratios above $V_r = 10$, where more jet fluid has been observed in the wake area (see figure 1.7) indicating a cross-flow Reynolds number dependence. The highly dynamic

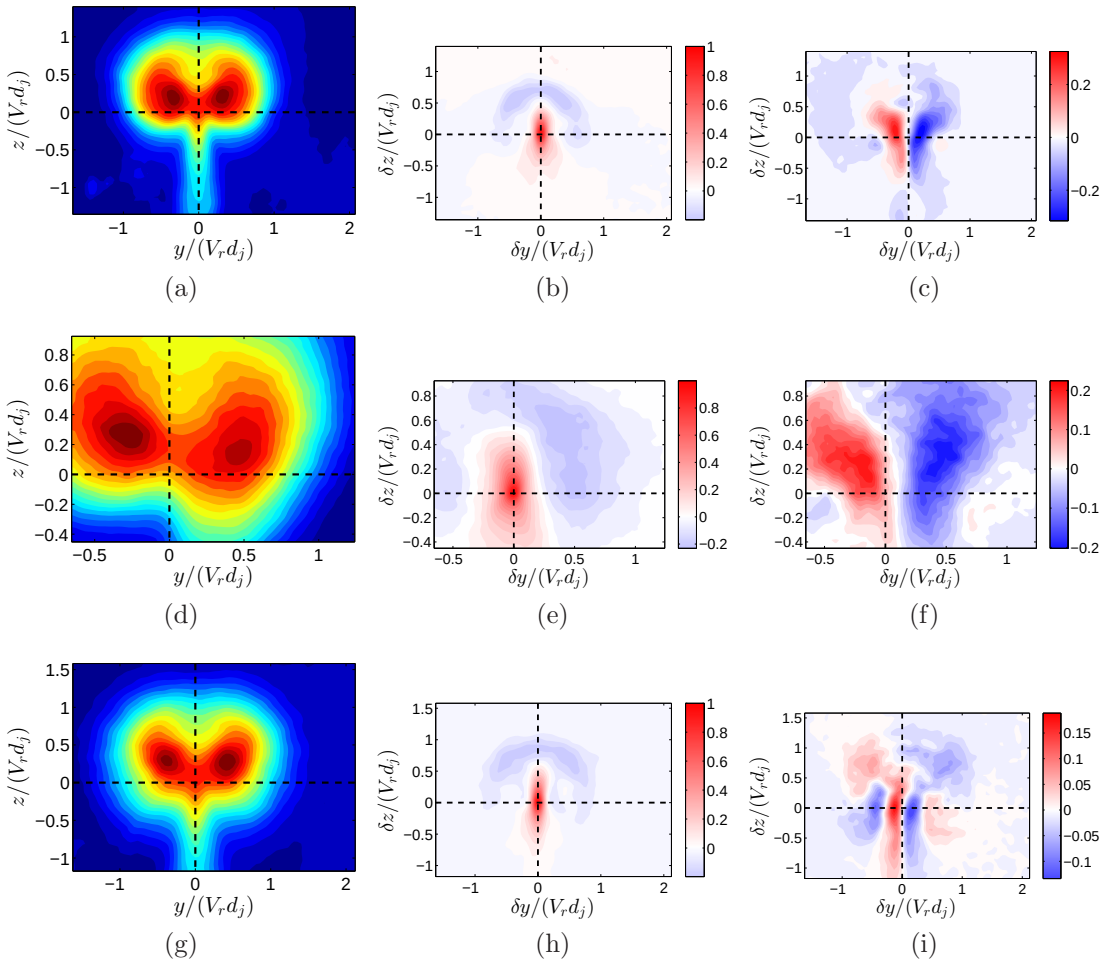

Figure 3.23 (a-i): For caption see following page.

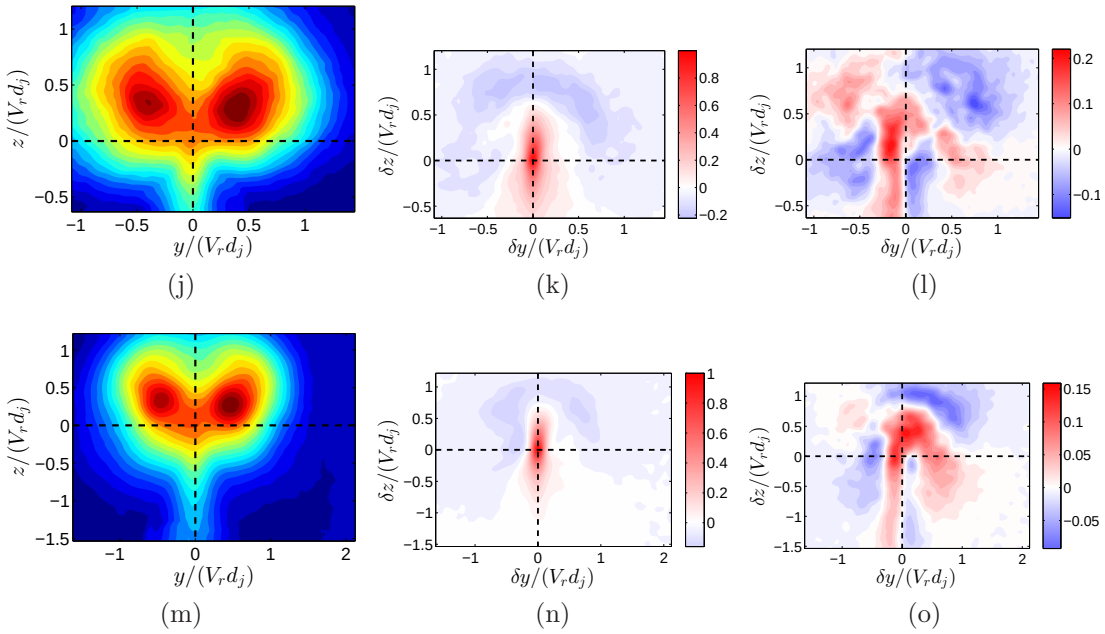

Figure 3.23: Correlation maps for wake side of the CVP plane. Intersection of dotted lines in left column show location of (y_0, z_0) in the $\sqrt{\overline{v'^2}}$ field. Middle column shows $R_{uu}(y_0, z_0, \delta y, \delta z)$. Right column shows $R_{vu}(y_0, z_0, \delta y, \delta z)$. Each row is for a given case: (a) → (c) $V_r = 10$ at $x/dj = 30$, (d) → (f) $V_r = 20$ at $x/dj = 85$, (g) → (i) $V_r = 10$ at $x/dj = 55$, (j) → (l) $V_r = 15$ at $x/dj = 85$, (m) → (o) $V_r = 10$ at $x/dj = 85$.

nature of the cross-flow jet means that 3D data is necessary to develop a better understanding of the $3D$ coherent structures. This is the focus of the next chapter.

Chapter 4

3D Structure of the CVP

In this Chapter the 3D structure of the CVP is investigated using Taylor's Hypothesis applied to high-speed data at various downstream locations. The downstream evolution of the CVP plane is also investigated using the volume reconstructions from the Towed Jet experiment. Combining the results together with the mean properties examined in the previous chapter gives a fuller understanding of the instantaneous turbulent structure of the far field of a cross-flow jet. However, it is important to assess limitations of the measurements by quantifying resolution and level of divergence.

The chapter begins with an assessment of the PIV measurements by looking at the experimental resolution and the resulting scales of structures that can be detected, how divergence free the resulting 3D reconstructed volumes are, which is used as a measure of the accuracy of the reconstruction, and finally the size of the reconstructed volumes which can be considered valid for quasi-instantaneous information. The downstream evolution of the CVP is firstly examined using the Tow-Tank SPIV data which allows for a general characterisation of the instantaneous vorticity structure. After that the instantaneous eddy structures present, and their relative orientation, at the downstream positions where the measurements were performed are investigated using the Taylor reconstructed data. Finally using conditionally averaging methods, the dominant eddy structures are extracted and their average shape analysed, allowing for a classification of the structures present in the far field of a cross-flow jet and how they generate the mean turbulent properties.

4.1 Outline of Measurement Assessment

An outline of the various properties of the Towed Jet and Taylor SPIV experimental measurements and the resulting vector fields used to assess them are outlined below. Details for each one are given in their respective sections 4.2 and 4.3.

4.1.1 Data Resolution

The aim of the high-speed measurements was to examine the eddy structures responsible for the resulting characteristic mean velocity profiles and turbulent features of the whole CVP, as examined in the previous chapter. Therefore the experimental resolution was selected so as to resolve the large scales, i.e. to cover the inertial range of length-scales, and not the Kolmogorov length-scale. Using the analysis outlined in section 2.8 the viscous length-scale λ_ν, defined as the length-scale at which the turbulent power-spectra begins to deviate from the -5/3 power law behaviour (inertial range) at high wavenumbers, is estimated for each velocity ratio studied for both Towed-Jet and High-Speed SPIV measurements.

4.1.2 Size of Reconstructed Volumes

For every run performed data was recorded for the maximum amount of time possible, as determined by the camera memory and frame rate. Additionally, from the experimental method of forming the 3D measurement volumes for both experiments described in section 2.6.2, the resulting velocity field cannot be considered as being instantaneously frozen, but instead is quasi-instantaneous [17]. The size of the volume in the reconstructed x-direction is thus a question of to what extent can the flow be considered quasi-instantaneous, i.e where the large-scale structures remain correlated. This should be based on some property of the turbulent flow and a good limit would be for the volumes to cover approximately one large-scale eddy turnover time, which can be estimated using the equation below:

$$t_{turb} = \frac{l_{turb}}{u_{turb}}, \tag{4.1}$$

where l_{turb} is a characteristic turbulent length-scale and u_{turb} is a characteristic velocity. The jet width can be used as a characteristic length-scale. For

the characteristic velocity the difference between the maximum and minimum $\overline{U}$ component, i.e difference in velocity surplus in the cores and deficit in the wake $\overline{U}_{core} - \overline{U}_{wake}$, is used. This is equivalent to the centreline velocity being used for a normal jet flow or the centreline velocity deficit for a wake flow.

4.1.3 Reconstruction Validation

In order to assess if the application of Taylor's hypothesis is valid, the spatial gradients derived from its application on temporal measurements (denoted with subscript 't'):

$$\left(\frac{\partial \mathbf{u}}{\partial x}\right)_t = \frac{-1}{U_c}\frac{\partial \mathbf{u}}{\partial t}, \tag{4.2}$$

would need to be checked against direct spatial gradient measurements. This would require time resolved measurements in a plane containing the streamwise x-direction. However this data is not available here. However the application of Taylor's hypothesis results in the availability of the full 9-component Velocity Gradient Tensor (VGT). This therefore allows for the divergence of the velocity fields $\nabla \cdot \mathbf{U}$ to be computed, shown in equation 4.3, which is used instead to assess the accuracy of the full 9-component VGT extracted and the robustness of the reconstructions.

$$\nabla \cdot \mathbf{U} = \frac{\partial U_i}{\partial x_i} = \frac{\partial U}{\partial x} + \frac{\partial V}{\partial y} + \frac{\partial W}{\partial z} \tag{4.3}$$

Since the flow is incompressible the resulting velocity fields should be divergence free, i.e $\nabla \cdot \mathbf{U} = 0$. Averaging both sides of the equation also gives the result that $\nabla \cdot \overline{\mathbf{U}} = 0$. Using this result together with a Reynolds decomposition of $\mathbf{U}$ gives the additional result that $\nabla \cdot \mathbf{u}' = 0$. The amount therefore by which the data deviates from this is a measure of the divergence error. The divergence error is therefore an indicator which quantifies how accurate the reconstructed volume is. Apart from the method of the reconstruction, e.g the use of Taylor's Hypothesis and choice of Taylor convection velocity (see section 2.6.2), errors in the divergence of the data can also be attributed to the intrinsic measurement uncertainty associated with the method of PIV (see section 2.5) and specifically Stereoscopic PIV. This uncertainty would arise from a misalignment of the laser sheet with the calibration plate, large amounts of optical distortion resulting in

bad quality images, error in the peak detection in the image cross-correlation plane, and a recombination error in the extraction of the out-of-plane velocity component. Furthermore errors in the divergence would arise from the noise associated with the calculation of the spatial gradients from discrete data using the second order central differencing scheme utilised here. The divergence was checked using a number of measures for each experiment, which are detailed below in sections 4.2.3 and 4.3.3.

4.2 Towed Jet Results

The flow parameters examined and the relative settings for the Tow Jet-SPIV measurements are summarised in table 4.1. The table also shows the initially chosen control values for V_r and Re_{jet} in brackets as well as the measured values. Unfortunately, due to time constraints, the data for the velocity of the carriage

Table 4.1: Flow conditions for the Towed Jet-SPIV experiment

V_r	d_j mm	U_{jet} m/s	$U_\infty = U_t$ m/s	Re_{jet}
9.1 (10)	10	2.17 (2.28)	0.24 (0.228)	19000 (20000)
17 (20)	5	4.11 (4.56)	0.24 (0.228)	18000 (20000)
23.5 (25)	5	4.5 (4.56)	0.19 (0.182)	19700 (20000)

and jet were processed after the experiment was completed, which explains why a V_r below 10 was recorded. The towing speed of the carriage is the cross flow velocity that the jet experiences. As mentioned in section 2.4.8, 5 runs were performed for each velocity ratio with the aim to ensure consistency rather than try to extract an average field, which would require a much larger number of runs. Images were sampled at a rate of $f_s = 125Hz$.

As mentioned in section 2.4.8 the towed jet experiment has a frame of reference of moving with the cross-flow, and therefore removes the cross-flow velocity. Applying a transformation back to a stationary frame a reference of means that the measurement is effectively akin to a scanning-PIV measurement with the

scanning speed being equal to the cross-flow velocity and the scanning direction in the cross-flow direction.

4.2.1 Data Resolution

The results for the Towed Jet measurements are summarised below in table 4.2. The FoV for all cases was $280 \times 210mm^2$. The table shows the resolution in all

Table 4.2: Resolution for Towed Jet experiments

V_r	9.1	17	23.5
x/d_j	$20 - 120$	$100 - 200$	$100 - 200$
d_j	$10mm$	$5mm$	$5mm$
δ_{ω_c}	$3.8 \times d_j$	$6.7 \times d_j$	$8.2 \times d_j$
Re_Γ	1.27×10^4	0.99×10^4	1.22×10^4
λ_ν	$0.48mm$	$0.51mm$	$0.525mm$
FoV	$28d_j \times 21d_j$ $583\lambda_\nu \times 438\lambda_\nu$	$56d_j \times 42d_j$ $549\lambda_\nu \times 412\lambda_\nu$	$56d_j \times 42d_j$ $533\lambda_\nu \times 400\lambda_\nu$
Resolution $(\lambda_{p_x} \times \lambda_{p_y} \times \lambda_{p_z})$	$15\lambda_\nu \times 13\lambda_\nu \times 13\lambda_\nu$	$14\lambda_\nu \times 12\lambda_\nu \times 12\lambda_\nu$	$11\lambda_\nu \times 12\lambda_\nu \times 12\lambda_\nu$

three directions, in terms of the viscous length-scale. The out-of-plane reconstructed resolution λ_{p_x} for the velocity ratios of $V_r = 9.1\,\&\,17$ is $7.3mm$, and $5.8mm$ for the case where $V_r = 23.5$. The in plane measurement resolution, $\lambda_{p_y}\&\lambda_{p_z}$, is $6.15mm$. Successive vectors are separated by half of the quoted values in the respective directions as a result of the 50% overlap with which the images were processed (this was also implemented in the out-of-plane direction). Since instantaneous velocity data is available the distance between the centroids of positive and negative vorticity, δ_{ω_c} averaged over the downstream positions shown in table 4.2, is used as an estimate for the jet width in the spanwise y-direction. The circulation Reynolds number is then calculated at the start of the range shown in the table. With the drop in the circulation Reynolds number with increasing x/d_j, the turbulent length scales increase and the estimated resolution is only a minimum resolution which improves with downstream distance.

Furthermore the jet width based on the centroids of vorticity δ_{ω_c} is significantly smaller compared to the jet width δ_{ω}, defined as the distance between the points where the vorticity drops to 5% of its maximum value along the y-axis through the cores, and therefore the resolution estimates are very conservative estimates.

4.2.2 Size of Reconstructed Volumes

In addition to the requirement of covering a maximum of one turbulent time-scale t_{turb}, two more factors were also considered, summarised below.

- The turbulent time scale of the large scale flow t_{turb}: The volume created should span a maximum of one turbulent time scale (eddy turnover time).
- The extent of correlation of the velocity data in the x-direction: The size of the volume should not be so large that the velocity field becomes decorrelated from the first vector field in the volume.
- The tow tank carriage should be in motion. This factor places a limit on the last vector field that can be used.

This was done due to the fact that mean properties are not available from the Towed Jet measurements, as only 5 runs were performed for each velocity ratio (total of 15 runs). The large scale turbulent time scale t_{turb} is estimated using equation 4.1 with δ_{ω_c}, given in table 4.2, taken as the characteristic length scale l_{turb}. Since the the cross flow is removed by the experimental set up the resulting measured U-component velocity field is a cross flow-subtracted velocity field. Since mean values are not available an estimate to u_{turb} can be found by taking $\sqrt{\overline{u'^2 + v'^2 + w'^2}}$ velocity, i.e the rms velocity magnitude, across the whole field at a given downstream location. This gives a measure of the fluctuation about the cross-flow speed, equivalent to the definition given for u_{turb} above.

The velocity field at the start of the volume from which the resolution parameters are calculated (table 4.2) is selected with the criteria that the cores of the CVP are in the field of view. For a run with velocity ratio of 9.1 the characteristic turbulent velocity is $u_{turb} = u_{rms} = 0.015m/s.$ which equates to a turbulence intensity of $u_{rms}/U_{cf} = 6.6\%$, using the cross flow speed as the mean velocity for

normalisation. The turbulent time scale is therefore $t_{turb} = 2.47s$. The distance travelled by the carriage at $0.228m/s$, and hence the estimated size of the volume, is $0.56m$ or $56 \times d_j$. The same analysis is carried out for the remaining two velocity ratios and the results are summarised in table 4.3 below.

Table 4.3: Size of reconstructed volumes in the streamwise x-direction based on 1 large eddy time scale for the Towed Jet-SPIV measurements.

V_r	d_j mm	U_{tow} m/s	t_{turb} s	Volume Size
9.1	10	0.24	2.47	$56 \times d_j$ $(14.7\delta_{c_\omega})$
17	5	0.24	1.98	$90 \times d_j$ $(13.4\delta_{c_\omega})$
23.5	5	0.19	2.25	$82 \times d_j$ $(10\delta_{c_\omega})$

The correlation criteria is examined by plotting a normalised correlation plot for the wall-normal velocity component W in the x-z centre-plane (i.e spanwise reference position is $y_0 = 0$), shown in figure 4.1. The correlation coefficients are calculated using equation 4.4 below.

$$C_{U_iU_j}(y_0, \delta x, \delta z) = \frac{\sum_{x=x_{min}}^{x_{max}} \sum_{z=z_{min}}^{z_{max}} U_i(x,z)U_j(x+\delta x, z+\delta z)}{\sum_{x=x_{min}}^{x_{max}} \sum_{z=z_{min}}^{z_{max}} U_i(x,z)U_j(x,z)} \tag{4.4}$$

The calculation is similar to the one in section 3.5.4, except in this case the results come from spatially averaging the correlation across the whole x-z plane, rather than averaging over all the observations/samples recorded at a given spatial location. As a result $C_{U_iU_j}$ is only a function of $(y_0, \delta x, \delta z)$. The angle of the contours with respect to the streamwise x-direction in the figures reflects the trajectory of the CVP with downstream distance. The plot shows that the W velocities are correlated with a correlation coefficient C above 0.5 up to a distance of approximately $50d_j$ for the case where $V_r = 9.1$ (figure 4.1a), and $80d_j$ for the case where $V_r = 17$ and 23.5 (figures 4.1b and 4.1c), which agrees with the turbulent time scale calculation in table 4.3.

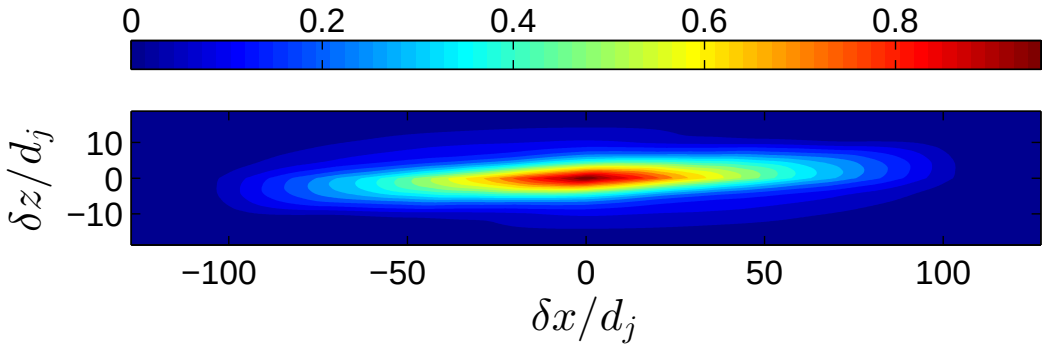

(a)

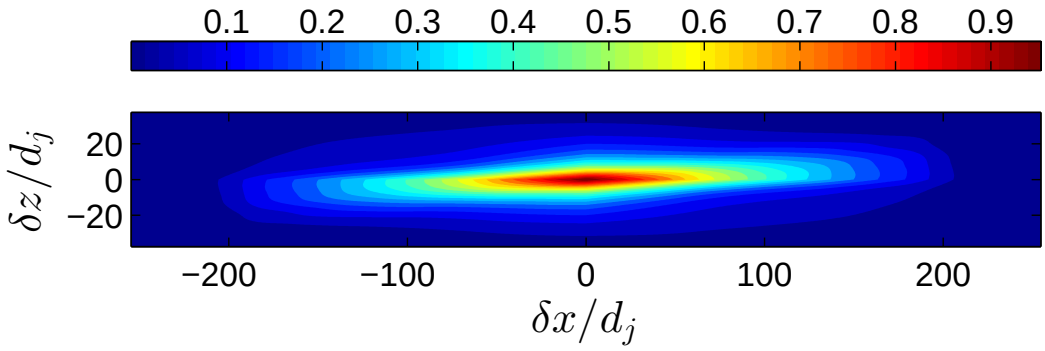

(b)

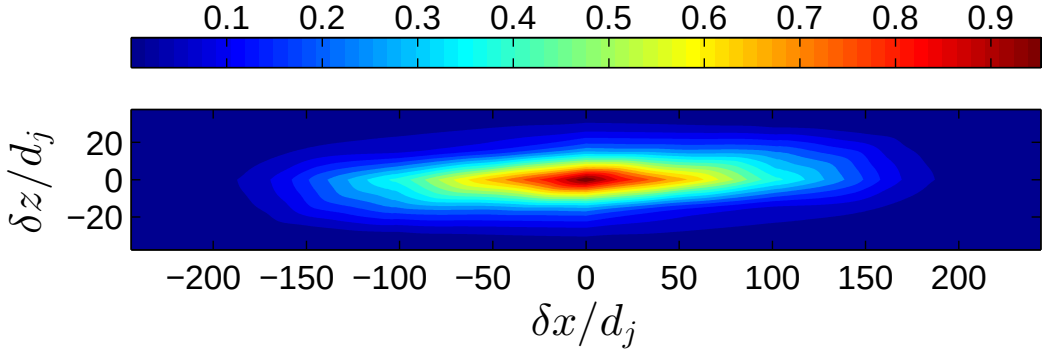

(c)

Figure 4.1: Two dimensional correlation coefficient of the wall normal velocity component C_{WW} in the $x-z$ centre-plane ($y_0 = 0$) for (a) $V_r = 9.1$, (b) $V_r = 17$ and (c) $V_r = 23.5$.

4.2.3 Volume Reconstruction Validation

In order to check the validity of the volume reconstruction, and how accurate the full 9-component velocity gradient tensor is, the divergence of the velocity fields $\nabla \cdot \mathbf{U}$, shown in equation below.

$$\nabla \cdot \mathbf{U} = \frac{\partial U_i}{\partial x_i} = \frac{\partial U}{\partial x} + \frac{\partial V}{\partial y} + \frac{\partial W}{\partial z} \tag{4.5}$$

Since the flow is incompressible the resulting velocity fields should be divergence free, i.e $\nabla \cdot \mathbf{U} = 0$. As was highlighted in section 4.1.3, the divergence error is an indicator which shows how accurate the reconstruction is. With the intrinsic uncertainties associated with Stereoscopic PIV it would be unreasonable to expect the measurements to be fully divergence free. The extracted velocity gradient tensor would therefore be valid if small deviation from zero divergence are observed and invalid for significant large deviations.

Figure 4.2 shows the joint pdf $\partial u/\partial x$ and $-(\partial v/\partial y + \partial w/\partial z)$. A single pass Gaussian smoothing filter has been applied to the data shown in the figure. According to equation 4.5 the two quantities should be equal. Therefore divergence free data should lie on the 45° straight line, shown as a solid black line in the figures, and the amount of data off this line indicates the extend of the divergence error in the measurements. Strikingly the contours do not seem to align with the 45° solid line, indicating a large divergence error. This error is quantified by calculating the correlation coefficient between the two quantities $\mathcal{Q}$. The value of $\mathcal{Q}$ for each velocity ratio is shown in their respective figures and is as expected very low. Upon a closer inspection the contours are actually alinged in the vertical direction, meaning that on average the streamwise velocity gradient $\partial U/\partial x$ is approximately zero. This therefore indicates that the measurement technique, and by extension the reconstructed velocity field, fails to capture gradients in the streamwise direction.

The reason for this can be explained when the question of what is the measuring technique recording is asked. As mentioned above the measurements are akin to a scanning PIV measurement, following the free-stream direction at the cross-flow speed slicing through the jet in the CVP plane. With the assumption

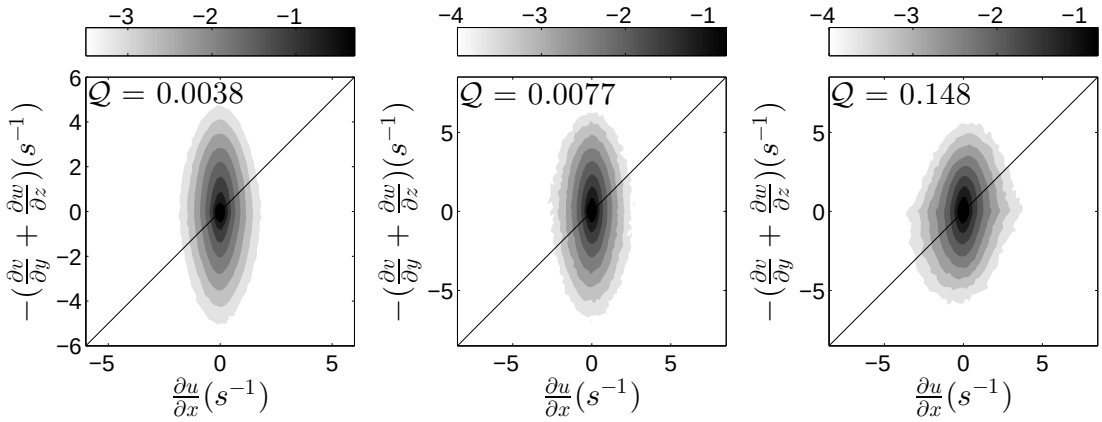

(a) $V_r = 9.1$ (b) $V_r = 17$ (c) $V_r = 23.5$

Figure 4.2: Joint pdf of $\partial u/\partial x$ and $-(\partial v/\partial y + \partial w/\partial z)$, shown by contours of base 10 exponentials. Each figure is for a different velocity ratio.

that, in the far field, the turbulent eddy structures are convected downstream with an average speed equal to the cross-flow speed, the measurements here only track a slice through these structures. Since the jet is in the moving frame of reference the flow structures move within the measurement plane but do not advect, preventing the quantification of the out-of-plane gradients. However, the results do allow us to study of the downstream evolution of the CVP plane of the cross-flow jet, although this is clearly only part of the picture.

4.2.4 Velocity Field

Figure 4.3 shows streamlines in the spanwise-wall normal (y-z) plane at different downstream positions. The figure clearly shows the CVP entering from the bottom of the measurement plane and moving upwards in the z-direction with downstream distance x. This illustrates how the measurements performed track the path and evolution of the CVP plane.

4.2.5 Vorticity Field: Braid structure

In section 3.3 the structure of the CVP plane was investigated by looking at pdfs of the distribution of vorticity. From this data one possible explanation for the

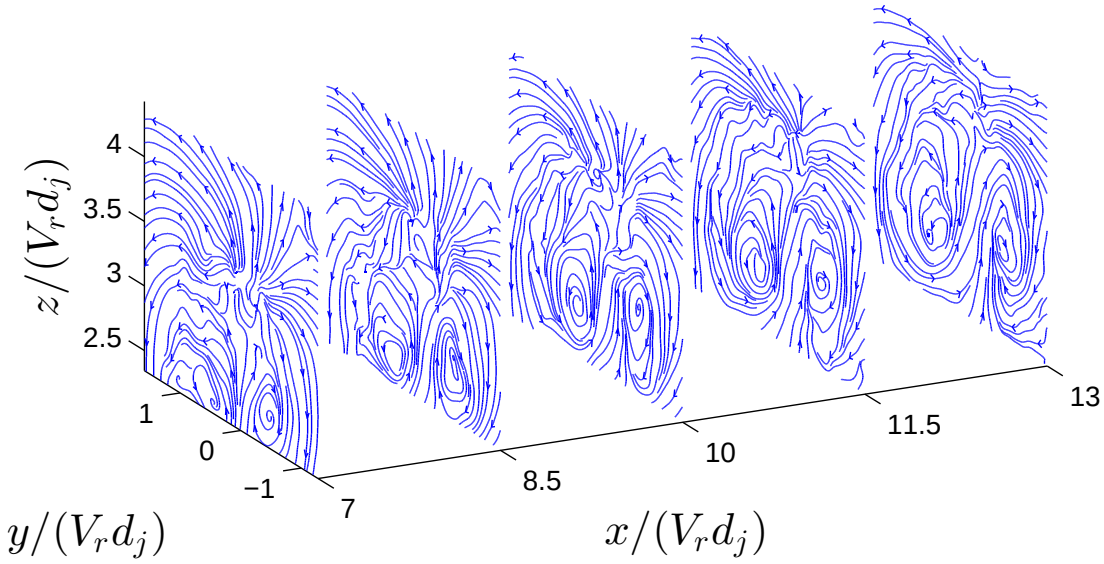

Figure 4.3: Streamline patterns in the y-z plane for different downstream positions for a $V_r = 9.1$

structure of the CVP is that it is made of a collection of vortex tubes concentrated around the core position, rather than the large single core of the mean field. To best visualize the vorticity field isosurface contours of swirl λ_{ci} (imaginary part of the complex eigenvalue of the velocity gradient tensor) are plotted. As is normally the case a threshold is required to be able to provide good visualisation of the flow. The choice of a minimum threshold needs to highlight significant areas of swirl, but at the same time limit the effect of background noise. It was found that a range of isosurfaces from $0.25\lambda_{ci,max}0.15\lambda_{ci,max}$ gave the best results of representing the vorticity field. Solid isosurfaces of $0.25\lambda_{ci,max}$ together with transparent isosurfaces of $0.15\lambda_{ci,max}$ are used to plot the 3D votricity field. Higher threshold values were found to produce only small regions of intense swirl, but were not large enough to be able to identify any characteristic structures. Lower threshold values were found to produce more regions of swirl, but in a very complex mix of interconnected structures which made studying the instantaneous field extremely difficult.

Three dimensional isosurface contours of swirl λ_{ci} for $V_r = 9.1$ are plotted in figure 4.4. Figure 4.4a shows a side-view (x-z plane) of the jet where the positive

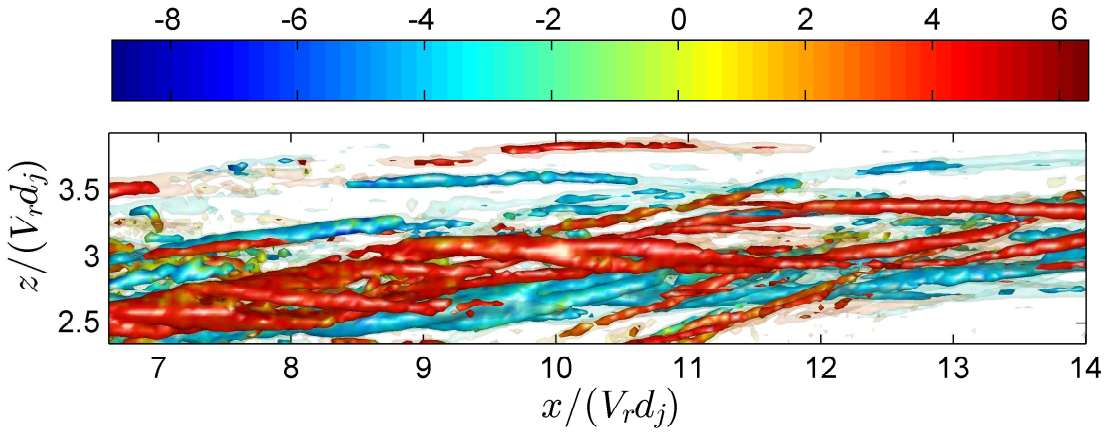

(a)

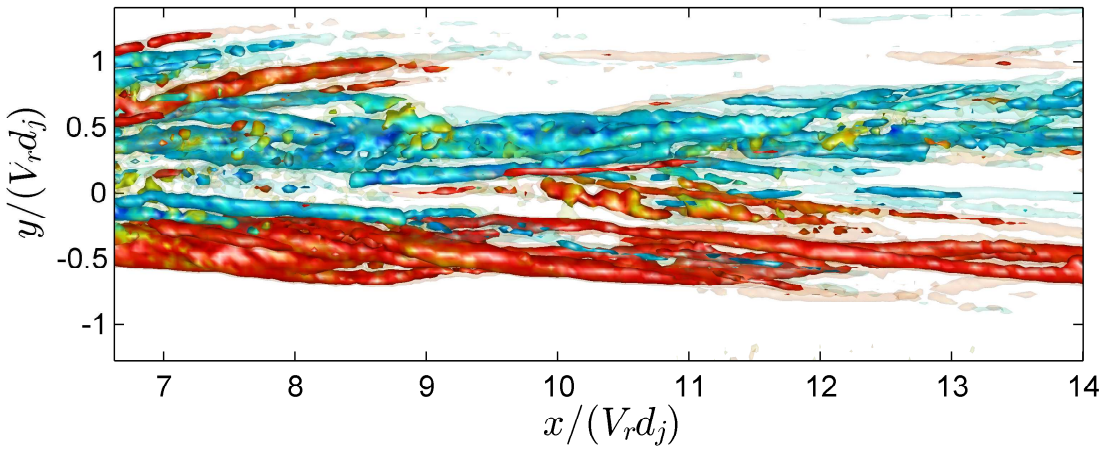

(b)

Figure 4.4 (a-b): For caption see following page.

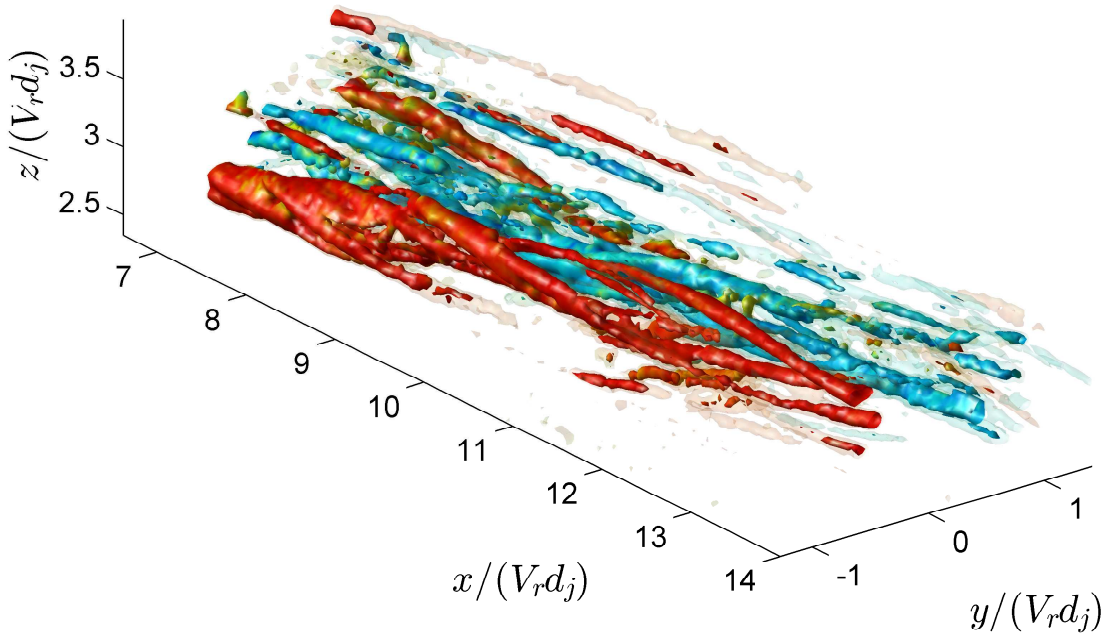

(c)

Figure 4.4: Iso-contours of $\lambda_{ci,iso} = 0.25\lambda_{ci,max}$ (solid) and $\lambda_{ci,iso} = 0.15\lambda_{ci,max}$ (transparent) for $V_r = 9.1$. Surface is coloured by the local value of $\lambda_{ci,x}(\mathrm{s}^{-1})$. (a) Side view (x-z plane). (b) Top view (x-y plane). (c) 3D view.

angle of the isosurfaces, with respect to the x-axis, reflect the jets trajectory moving away from the wall ($z = 0$) with downstream distance. Figure 4.4b is a top-view (x-y plane) of the jet, showing the two cores about the $y = 0$ line and how the distance between them, i.e the jet width, increases with downstream distance. The two views show that the vorticity in the core of the CVP seems to be organised in a cluster of small vortex tubes, and not one single vortex and that tubes of opposite sign of vorticity appear on both sides of the CVP, as shown by the pdfs in section 3.3. The clustered structure can be seen better in figure 4.4c, which shows a 3D view of the jet looking upstream from a downstream position. The tubes appear to rotate with the mean rotation of the respective core of the CVP with downstream distance resulting in a rope like structure. This kind of structure is expected when a collection of vortex tubes of the same sign, i.e co-rotating vortex pairs (figure 4.5b), are in close enough proximity for their induced velocities to interact with each other, much like the mean cores of the CVP induce an upward velocity on each other resulting in the jets trajectory 4.5a. Additional figures of different runs for the same conditions can be found in appendix showing similar results.

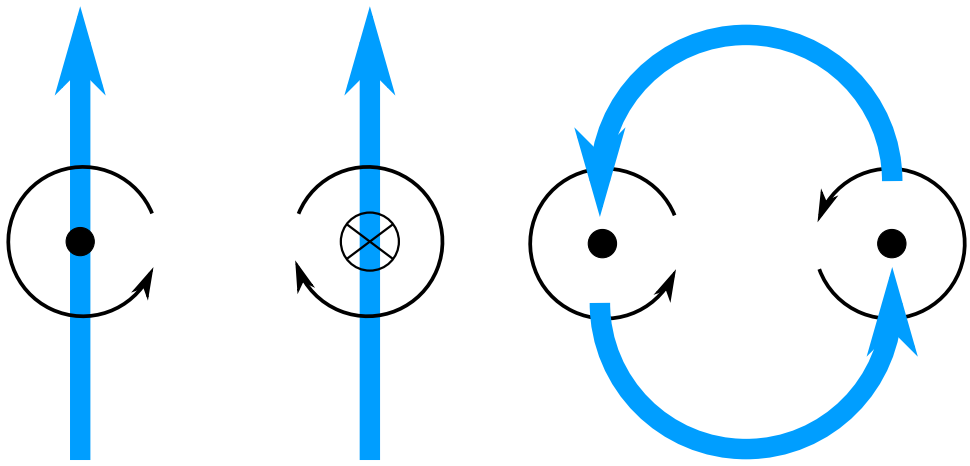

(a) (b)

Figure 4.5: Schematic of interaction between vortex tubes. (a) Counter-rotating vortex pair. (b) Co-rotating vortex pair.

Figure 4.6 shows the isosurface contours for the case where $V_r = 17$. The

results are similar to those for $V_r = 9.1$ above, with the difference that, by visual inspection, a larger number of individual tubes are observed. Furthermore the tubes are spread out over a larger area, compared to the case of $V_r = 9.1$ where the tubes are more concentrated around the position of the core. This again agrees with the results of section 3.3. The number of detected tubes was found to increase with velocity ratio (table 3.4) and the joint p.d.f of the y and z location of the detected tubes (figure 3.13) for $V_r = 15$ and 20 showed a much flatter peak when compared to the results of $V_r = 10$. Similar observations appear for velocity ratios above 20, as shown in figure 4.7. A larger number of individual tubes is observed which also appear more spread out.

The tube structures for all velocity ratios appear to stay intact along the whole measurement volume. Given that the measurements capture the downstream evolution of a slice through any of the large scale turbulent structures present, this might have been expected for volumes that cover one large eddy turnover time, which is the case here. With the assumption that the turbulent eddy structures are convected downstream with an average speed equal to the cross-flow speed, the measurements here track a slice through these structures. It is important to point out that this data cannot offer any information about the structures which advect with the mean flow.

4.3 Water Channel Results

To investigate the structure of the CVP, this section focuses on the High-Speed Stereoscopic PIV measurements and the application of Taylor's hypothesis to reconstruct 3D structures. The $V_r = 10$ jet will be the main focus and the inlet conditions are in table 4.4. Furthermore since the measurements were performed at specific downstream positions the Circulation Reynolds number Re_Γ, estimated using equation 1.27, is included in the table. Based on the definition of the far field by Smith & Mungal [58] as the 'branch point' at $x_{bp} = 0.2V_r^2 d_j$, the measurement at $x/d_j = 15$ is just before the branch point at $x_{bp}/d_j = 20$ (for $V_r = 10$) but the estimate is still shown as it is used for the calculation of the measurement resolution in the following section. Five runs were performed for each of the downstream locations at $x/d_j = 30$ and 85, each one recording 5.457 seconds of

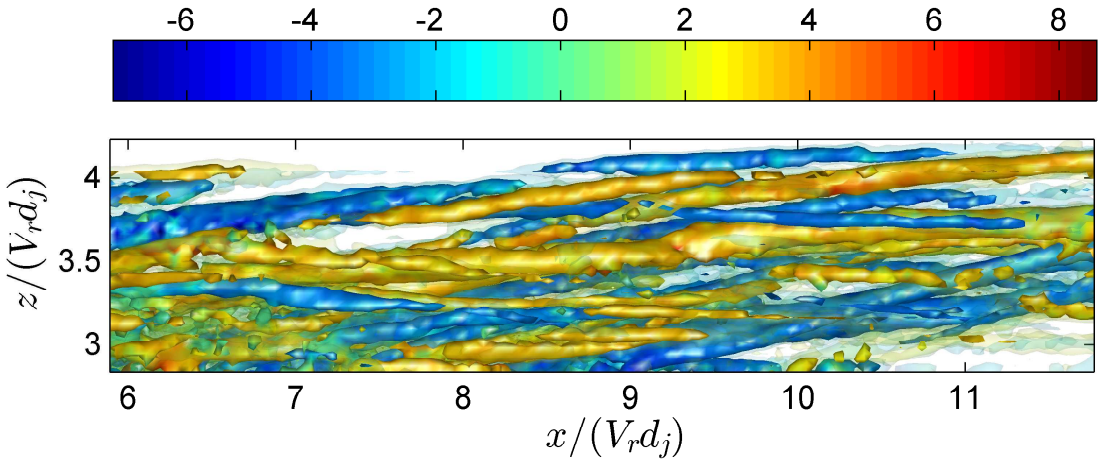

(a)

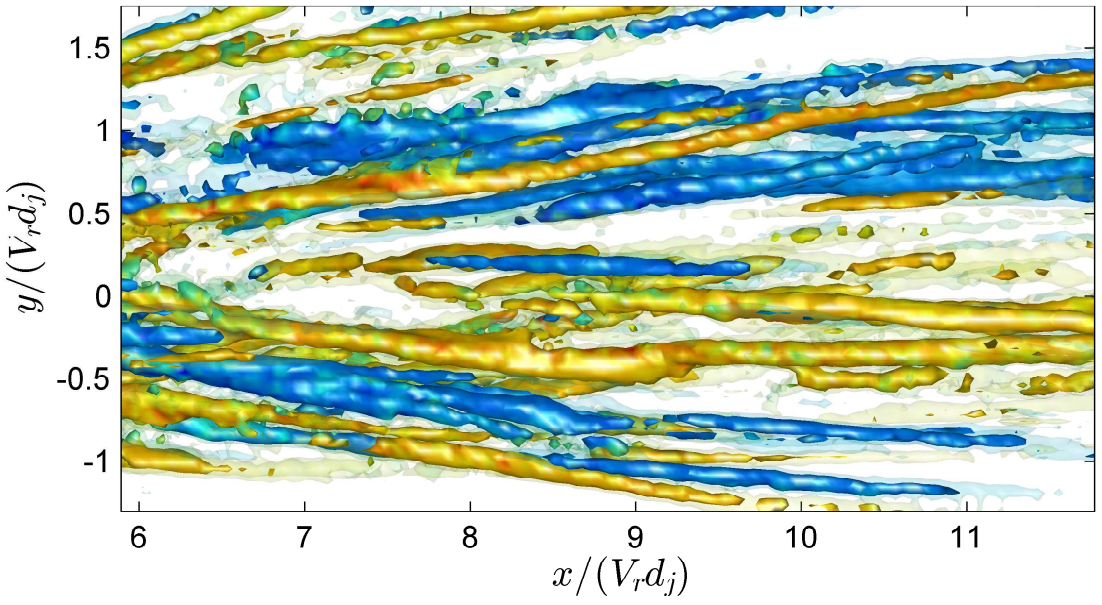

(b)

Figure 4.6 (a-b): For caption see following page.

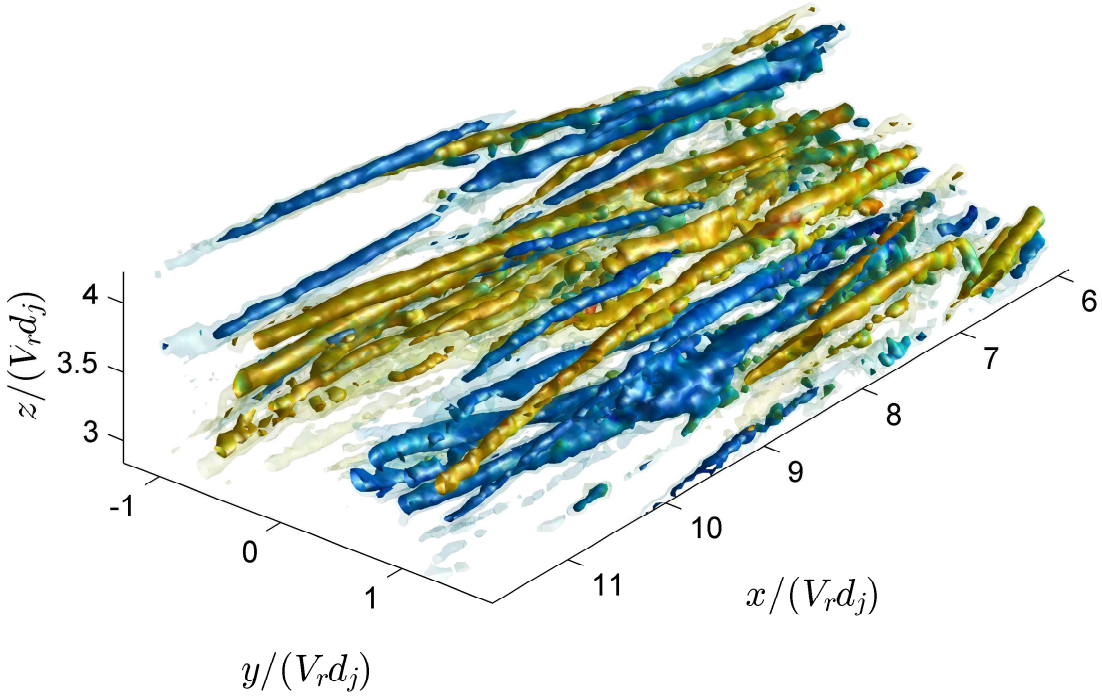

(c)

Figure 4.6: Iso-contours of $\lambda_{ci,iso} = 0.25\lambda_{ci,max}$ (solid) and $\lambda_{ci,iso} = 0.15\lambda_{ci,max}$ (transparent) for $V_r = 17$. Surface is coloured by the local value of $\lambda_{ci,x}(\mathrm{s}^{-1})$. (a) Side view (x-z plane). (b) Top view (x-y plane). (c) 3D view.

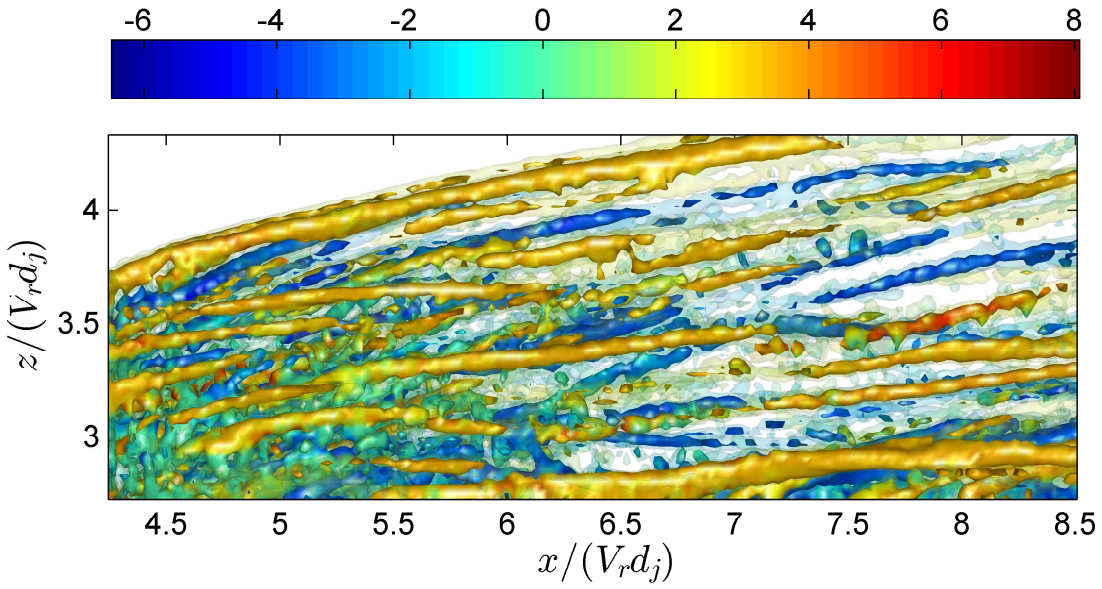

(a)

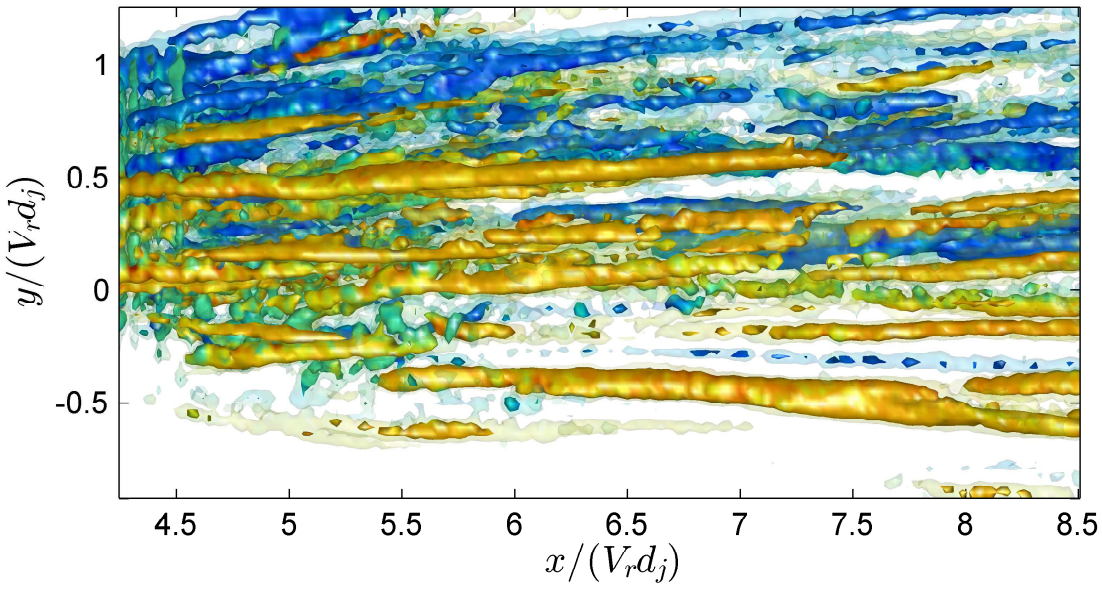

(b)

Figure 4.7 (a-b): For caption see following page.

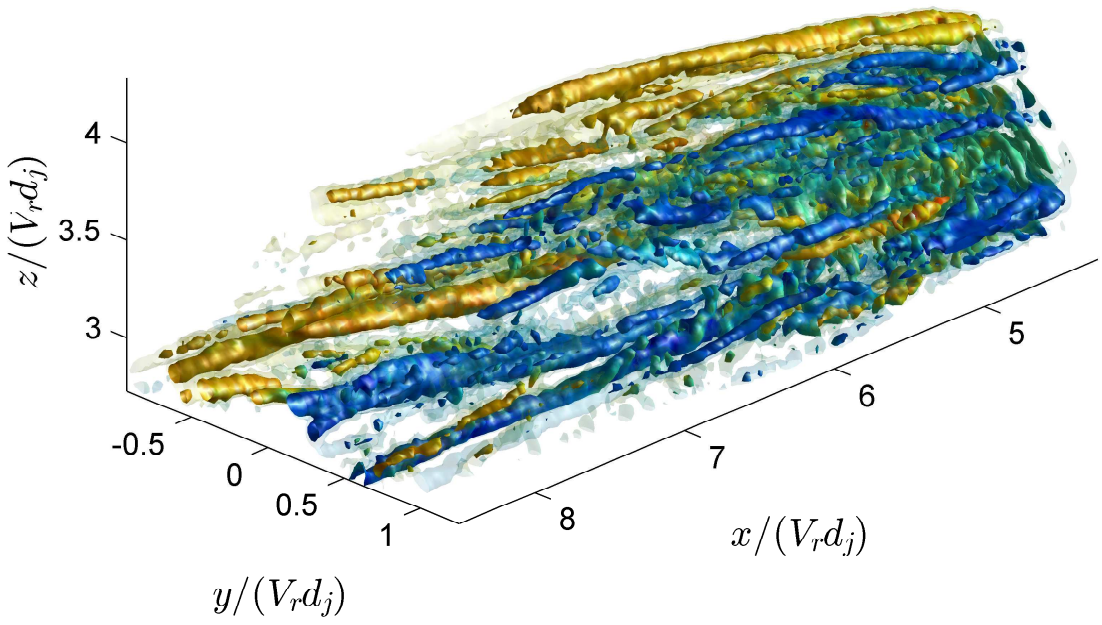

(c)

Figure 4.7: Iso-contours of $\lambda_{ci,iso} = 0.25\lambda_{ci,max}$ (solid) and $\lambda_{ci,iso} = 0.15\lambda_{ci,max}$ (transparent) for $V_r = 23.5$. Surface is coloured by the local value of $\lambda_{ci,x}(\mathrm{s}^{-1})$. (a) Side view (x-z plane). (b) Top view (x-y plane). (c) 3D view.

data at sampling rate of $f_s = 1kHz$, resulting in 5456 vector fields per run. Three runs were performed for the measurements at $x/d_j = 15$ each one recording 2.728 seconds of data, this time though at a sampling rate of $f_s = 2kHz$, resulting again in 5456 vector fields per run.

Table 4.4: Flow Conditions for the Taylor-SPIV experiment. The jet diameter for all conditions was $d_j = 4mm$.

V_r	x/d_j	x_{bp}/d_j	U_{jet} m/s	U_∞ m/s	Re_{jet}	Re_Γ
	15					1.75×10^4
10	30	20	5.7	0.57	2×10^4	1.39×10^4
	85					9.80×10^3

Before the results are studied a few definitions are made in order to aid with the analysis of 3D data. A turbulent 'eddy', or structure, is considered here as a region of concentrated vorticity of a given spatial extent and shape, enclosed by a vorticity iso-surface of a given threshold level (the choice of this is discussed later). The vorticity field can therefore be used as an identifier for a structure present in the turbulent field. Furthermore the structures to be analysed here refer to large-scale structures. Using this definition the structure of the cross-flow jet can be studied [29]. The difference between the terms 'structure' and 'coherent structure' is discussed. A structure can be defined as an observable flow event (i.e an instantaneous observation). A 'coherent structure' however is usually referred to a clearly repeatable regular structure as defined by the word coherent. This sometimes is a result of an ensemble average of structures of similar shape, size and strength making it a statistical entity. However here, the term structures and coherent structures are used in conjunction since, as will be clearly seen in the results, they appear clearly and consistently in the resulting reconstructions. The averaged structures, which are extracted at the end from the conditional averaging procedure in section 4.4, are clearly labelled as conditionally averaged structures.

It is important to note that experimental work concentrating on examining coherent structures present in the CVP of the far field of the cross-flow jet is very

limited. As a result an appropriate complete paradigm does not exist to use as framework to analyse the data to be presented. Therefore structures from other paradigms are borrowed here, the main one being the hairpin vortex from the hairpin vortex-packet model in turbulent boundary layers. This together with the wake structures describing the wake of the cross-flow jet are used as a way to interpret the data presented. It is possible to interpret the results using different paradigms but it was felt that the hairpin model was the most appropriate one.

4.3.1 Data Resolution

For the high-speed measurements the results are summarised in table 4.5. The field of view is $158 \times 124 mm^2$, which is equivalent to $39.5 d_j \times 31 d_j$ for a jet diameter of $d_j = 4mm$, for all conditions studied. Given that two of the measurements locations are the same as for the Multi Scale-SPIV measurements, at $x/dj = 30 \,\&\, 85$ for $V_r = 10$, the same results apply here and are repeated in the table below. The length-scales at $x/d_j = 15$ are estimated using the width of the jet extracted from the actual high-speed measurements and the circulation Reynolds number in table 4.4. The table again shows the resolution in all three directions in terms of the viscous length-scale, with the out-of-plane resolution being equal to $3.4mm$, and the in plane resolution being equal to $3.6mm$. Once again successive vectors are separated by half of these values in the respective directions as a result of the 50% overlap.

Table 4.5: Resolution for the Water Channel High-Speed measurements. The jet diameter for all conditions was $d_j = 4mm$.

V_r	10	10	10
x/d_j	15	30	85
δ_ω	$13.3 \times d_j$	$18 \times d_j$	$22.1 \times d_j$
λ_ν	$0.53mm$	$0.9mm$	$1.35mm$
FoV	$300\lambda_\nu \times 236\lambda_\nu$	$176\lambda_\nu \times 138\lambda_\nu$	$117\lambda_\nu \times 92\lambda_\nu$
Resolution $(\lambda_{p_x} \times \lambda_{p_y} \times \lambda_{p_z})$	$6.5\lambda_\nu \times 6.8\lambda_\nu \times 6.8\lambda_\nu$	$3.8\lambda_\nu \times 4\lambda_\nu \times 4\lambda_\nu$	$2.5 \times 2.7\lambda_\nu \times 2.7\lambda_\nu$

4.3.2 Size of Reconstructed Volumes

For the high-speed Stereoscopic PIV measurements l_{turb} is taken as the jet width δ_ω, defined as the distance between the points where the vorticity drops to 5% of its maximum value along the y-axis through the cores. u_{turb} is taken as the difference between the maximum and minimum mean streamwise velocity component, i.e difference in velocity surplus in the cores and deficit in the wake $\overline{U_{core}} - \overline{U_{wake}}$, in the measurement plane. Similarly to the method described for the towed jet experiment, the volume sizes were calculated by using the large-scale eddy turnover time t_{turb} and the Taylor convection speed U_c at which the temporal measurements where convected downstream, chosen to be the the cross-flow velocity U_∞ (see section 2.6.2). The results are summarised in table 4.6. As expected t_{turb}, and hence the size of the reconstructed volumes, increases with downstream distance.

Table 4.6: Size of reconstructed volumes in the streamwise x-direction based on 1 large eddy time scale for the high-speed Taylor-SPIV measurements. Jet diameter is $d_j = 4mm$ for all cases.

V_r	x/d_j mm	U_t m/s	t_{turb} s	Volume Size
10	15	0.57	0.11	$16\times d_j$ $(1.2\delta_\omega)$
10	30	0.57	0.29	$41\times d_j$ $(2.3\delta_\omega)$
10	85	0.57	1.83	$260\times d_j$ $(11.8\delta_\omega)$

4.3.3 Taylor Reconstruction Validation

In order to check if the Taylor reconstruction is valid, and specifically how accurate the full 9-component velocity gradient tensor that can be extracted is, the data is used to compute the divergence of the velocity fields $\nabla \cdot \mathbf{U}$, as before. It must be noted that the analysis hereafter only uses data within a rectangular section of the FoV which includes the CVP, i,e the ambient cross flow is excluded. This section was selected based on the rms velocity fields, excluding areas where the rms velocity drops below the free stream rms velocity value.

Figure 4.8 shows the joint pdf of $\partial u'/\partial x$ and $-(\partial v'/\partial y + \partial w'/\partial z)$, which according to equation 4.3 should be equal and lie on a 45° straight line, shown as a solid black line in the pdfs. Deviations from this line indicate the extent of the divergence error. Each row in the figure corresponds to a single downstream measurement location, with each column showing the joint pdf after $\mathcal{S}$ passes of a 3×3×3 Gaussian smoothing filter. The first column has no smoothing, the second has 1 pass applied, and the third column has 2 passes applied. The extend of the divergence error can be quantified by calculating the correlation coefficient between the two values, $\mathcal{Q}$ using the general equation for the correlation coefficient , $\rho_{A,B} = cov(A,B)/(\sigma_A \sigma_B)$. Applying this to the quantities used in the joint pdf gives:

$$\mathcal{Q} = \frac{\overline{\left(\frac{\partial u'}{\partial x}\right)\left(-\left(\frac{\partial v'}{\partial y}+\frac{\partial w'}{\partial z}\right)\right)}}{\sqrt{\overline{\left(\frac{\partial u'}{\partial x}\right)^2}}\sqrt{\overline{\left(-\left(\frac{\partial v'}{\partial y}+\frac{\partial w'}{\partial z}\right)\right)^2}}} \tag{4.6}$$

The resulting values of $\mathcal{Q}$ are summarised in table 4.7. The figures show that by smoothing the data the divergence error decreases, with the contours stretching more along the 45° black solid line, this being reflected in the increasing value of $\mathcal{Q}$. Furthermore for increasing spatial resolution the divergence is observed to improve. Tsinober *et al.* [64] calculated a value of 0.7 from multi-probe hot wire measurements and Ganapathisubramani *et al.* [24] a value of approximately 0.82 from the Cinematographic Stereo PIV jet measurements after a Gaussian smoothing filter was applied (single pass). This are similar to the present values observed after a single pass of the Gaussian smoothing filter for all measurement locations.

A second quantitative estimate of the divergence error can be made by calculating the ratio ξ given below.

$$\xi = \frac{\left(\frac{\partial u'}{\partial x}+\frac{\partial v'}{\partial y}+\frac{\partial w'}{\partial z}\right)^2}{\left(\frac{\partial u'}{\partial x}\right)^2+\left(\frac{\partial v'}{\partial y}\right)^2+\left(\frac{\partial w'}{\partial z}\right)^2} \tag{4.7}$$

This quantity was first introduced by Zhang *et al.* [68], who used this value to

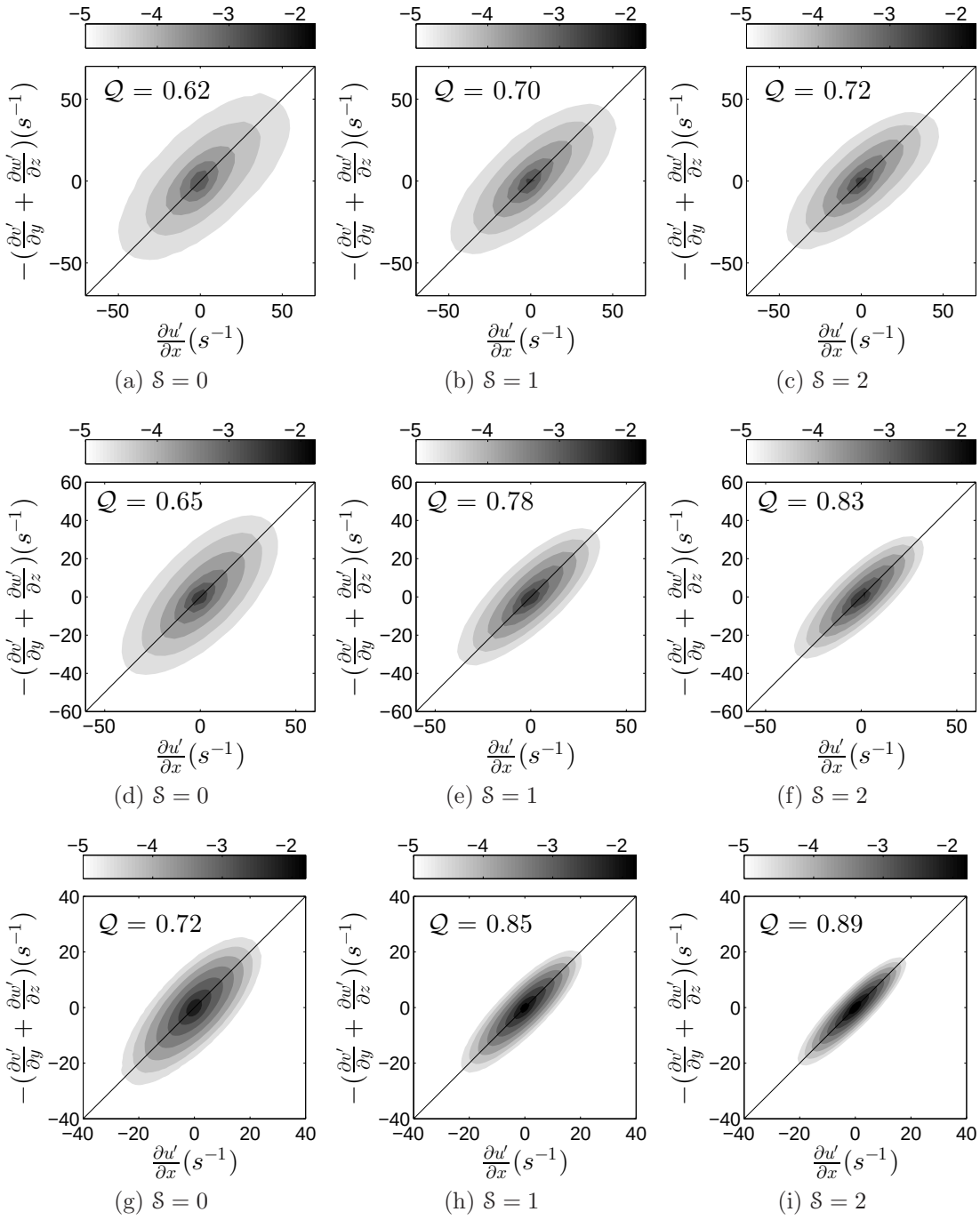

(a) $\mathcal{S} = 0$ (b) $\mathcal{S} = 1$ (c) $\mathcal{S} = 2$

(d) $\mathcal{S} = 0$ (e) $\mathcal{S} = 1$ (f) $\mathcal{S} = 2$

(g) $\mathcal{S} = 0$ (h) $\mathcal{S} = 1$ (i) $\mathcal{S} = 2$

Figure 4.8: Joint pdf of $\partial u'/\partial x$ and $-(\partial v'/\partial y + \partial w'/\partial z)$, shown by contours of base 10 exponentials. Each row is for a given downstream measurement location. (a) → (c): $x/dj = 15$, (d) → (f): $x/dj = 30$, (g) → (i): $x/dj = 85$. $\mathcal{S}$ represent the number of Gaussian smoothing passes has been applied.

Table 4.7: Quantification of divergence error for all downstream measurement location for $V_r = 10$.

Position	Quantity	Gaussian Smoothing Passes $\mathcal{S} = 0$	$\mathcal{S} = 1$	$\mathcal{S} = 2$
$x/d_j = 15$	$\mathcal{Q}$	0.62	0.70	0.72
	ξ	0.44	0.34	0.30
	σ	0.30	0.24	0.22
$x/d_j = 30$	$\mathcal{Q}$	0.65	0.78	0.83
	ξ	0.41	0.29	0.23
	σ	0.28	0.21	0.18
$x/d_j = 85$	$\mathcal{Q}$	0.72	0.85	0.89
	ξ	0.41	0.26	0.19
	σ	0.29	0.21	0.17

provide a quantitative estimate of how well their holographic PIV measurements satisfied continuity, and then also used by Ganapathisubramani *et al.* [24] for their Cinematographic PIV jet measurements. Given that the numerator is the divergence of the velocity field, the value of ξ should be zero to satisfy continuity. For statistically independent data, i.e zero correlation between $\partial u'/\partial x$, $\partial v'/\partial y$ and $\partial w'/\partial z$, the value of ξ is on average equal to unity. Therefore for data which includes measurement and discretisation errors it is expected to vary between zero and unity, where a value closer to zero indicates a smaller divergence error. Zhang *et al.* [68] found that the value of ξ decreased rapidly with increasing interrogation volume size and when the data is smoothed using a spatial filter. For a comparable physical interrogation window size, of 6.72mm, the mean value of ξ was found to be 0.12 with no filter applied, and 0.072 with Gaussian smoothing applied (single pass). Ganapathisubramani *et al.* [24] found a mean value equal to $\overline{\xi} = 0.18$. Figure 4.9 shows the distribution of ξ for all three downstream positions. Each plot shows the effect of applying Gaussian smoothing to the data, for zero to two passes. The mean value of ξ for each distribution, at all downstream locations, is summarised in table 4.7. The plots show that the distribution reaches a maximum at zero and has tail extending to $\xi = 1$. Similar to the observations of Zhang

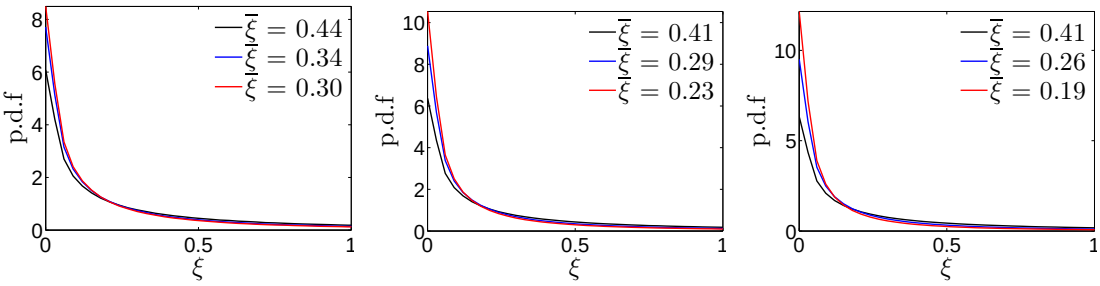

(a) $x/d_j = 15$ (b) $x/d_j = 30$ (c) $x/d_j = 85$

Figure 4.9: P.D.F of ξ. $\mathcal{S}$ represent the number of passes of Gaussian smoothing that have been applied. Black lines are for $\mathcal{S} = 0$, blue lines are for $\mathcal{S} = 1$ and red lines are for $\mathcal{S} = 2$.

et al. [68], smoothing the data reduces the value of ξ towards the ideal value of zero. For a single pass of the Gaussian smoothing filter the smallest value of ξ is 0.26 at $x/d_j = 85$ and largest with a value of 0.34 at $x/d_j = 15$, both of which are larger than the values quoted above from Zhang *et al.* [68] and Ganapathisubramani *et al.* [24]. However it should be noted that these studies focused on the turbulent fine-scales, whereas here the large scales are measured. The calculations of ξ depends on the estimation of second order gradients (velocity gradients squared), and therefore any small errors present are greatly amplified, evidence of which is in the significant reduction of the value of ξ after a single pass Gaussian smoothing is applied. The effect of noise on second order gradients was also shown in the loss of asymmetry in the $p - q$ plots (invariants of the reduced Velocity Gradient Tensor) in section 3.1.3.

A final test is done by plotting the distribution of the local divergence $\nabla \cdot \mathbf{u}'$ normalised by the local norm of the velocity gradient tensor $(\nabla \mathbf{u}' : \nabla \mathbf{u}')^{\frac{1}{2}}$, i.e the magnitude of the velocity gradient tensor. This quantity was first used by Mullin & Dahm [43] when assessing the accuracy of measuring the full velocity gradient tensor using the dual-plane stereo PIV technique in the self-similar far field of an axisymmetric coflowing turbulent jet. The resulting distribution had a mean of zero and an rms value of 0.35, which is used as a measure of the relative (to the local norm) divergence error. The authors note that this error is consistent with the rms uncertainty of the velocity-difference distribution between two coincident

measurement planes, of 9% for the in plane components and 16% for the out-of-plane stereo component. Ganapathisubramani *et al.* [24] also calculated this distribution which had a mean value of zero and an rms value of 0.25. The

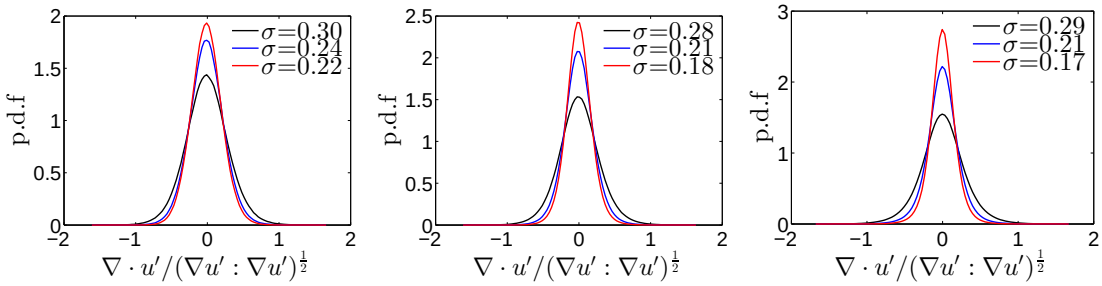

(a) $x/d_j = 15$ (b) $x/d_j = 30$ (c) $x/d_j = 85$

Figure 4.10: P.D.F of $\nabla \cdot \mathbf{u}'/(\nabla \mathbf{u}' : \nabla \mathbf{u}')^{\frac{1}{2}}$. $\mathcal{S}$ represent the number of Gaussian smoothing passes that have been applied. Black lines is for $\mathcal{S} = 0$, blue lines is for $\mathcal{S} = 1$ and red lines is for $\mathcal{S} = 2$.

normalised local divergence for the present data, shown in figure 4.10, also follow a normal distribution with a mean of zero and an rms value σ summarised in table 4.7. Smoothing the data decreases the rms value, and hence the divergence error, and make the distributions peakier. For a single pass Gaussian smoothing filter applied the rms value is similar to that of the Taylor reconstructed fields of Ganapathisubramani *et al.* [24] and the dual-plane stereo PIV measurements of Mullin & Dahm [43].

Since PIV errors do not tend to vary with velocity magnitude, high magnitude gradients are expected to be more accurate than small magnitude gradients. This can be investigated by plotting the joint p.d.f of the normalised local divergence ($\nabla \cdot \mathbf{u}'/(\nabla \mathbf{u}' : \nabla \mathbf{u}')^{\frac{1}{2}}$) and the velocity gradient magnitude ($(\nabla \mathbf{u}' : \nabla \mathbf{u}')^{\frac{1}{2}}$) to observe how the accuracy of the divergence (and hence of the velocity gradients) correlates to the magnitude of the gradients. The joint pdfs are shown in figure 4.11 at all three measurement positions. The triangular shape of the contours shows that the divergence error is larger for smaller magnitude gradients, and very importantly smaller for large magnitude gradients. Similar distributions were observed in the Cinematographic PIV data of Ganapathisubramani *et al.* [24]. This suggests that large-scale eddy structures, which create regions of high

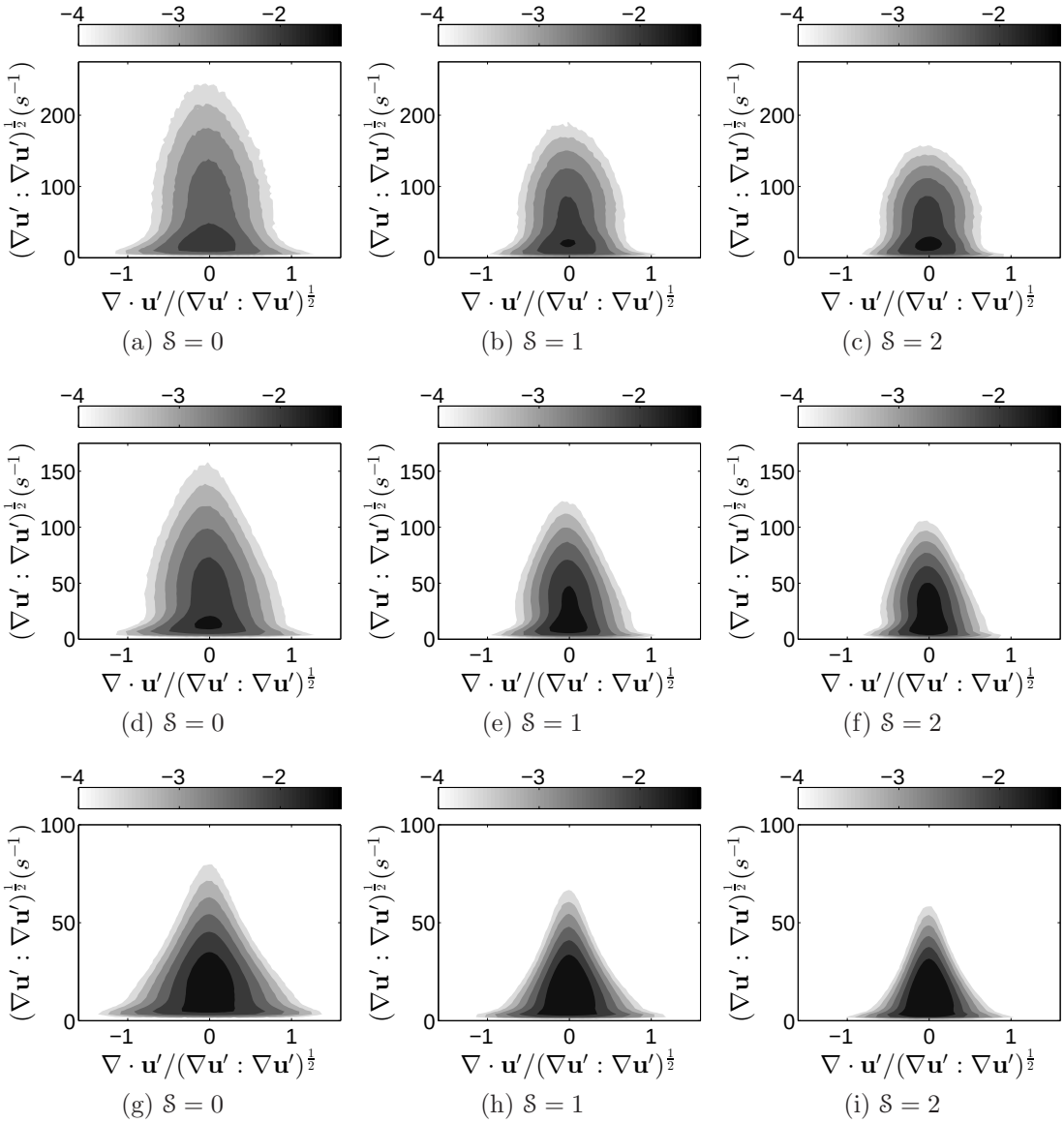

Figure 4.11: Joint pdf of normalised local divergence and velocity gradient magnitude, shown by contours of base 10 exponentials. Each row is for a given downstream measurement location. (a) → (c): $x/dj = 15$, (d) → (f): $x/dj = 30$, (g) → (i): $x/dj = 85$. $\mathcal{S}$ represent the number of Gaussian smoothing passes has been applied.

velocity gradient magnitude will be reconstructed more accurately than regions with low velocity gradient magnitude, which is what the aim of the measurement is.

4.3.4 Velocity Field

Figure 4.12 shows streamlines in the spanwise-wall normal (y-z) CVP plane at different downstream positions. These were obtained from the reconstructions of the measurements at the three measurement locations and cover approximately 1 large-scale eddy turnover time. The figures show that, unlike the streamline pattern from the Towed-Jet experiment, the CVP is at a constant height from the wall for all downstream positions within the reconstructed volume and has a constant core spacing. This is the same, and even more clear, when volumes that cover more than one larger-scale eddy turnover time are formed. This demonstrates a limitation of Taylor's Hypothesis, whereby the trajectory and large scale evolution of the CVP is not captured by the measurement, and by extension is not present in the reconstructions. This goes back to some points made in section 1.6 and 4.2.5 that although these measurements are suitable for identifying the flow structures and their relative orientation at the measurement location, they cannot accurately track the evolution of the CVP. In effect they provide short volume snapshots.

4.3.5 Coherent Eddy Structures

To best visualise the coherent structures present at the three downstream positions, iso-surfaces of enstrophy Ω are plotted. A small threshold is required to provide a good visualisation of the flow, and similar to the procedure followed in section 4.2.5 for its selection, a value of $0.1\Omega_{max}$ was used.

The first set of results presented are from the measurements at $x/d_j = 15$ in figure 4.13 showing a domain covering approximately 5 large-scale eddy turnover times. This location is upstream of the 'branch point' of $x/d_j = 20$ as proposed by Smith & Mungal [58] and therefore can be considered in the near field. The presence of coherent structures in the near field (close to the jet exit) is well documented in the literature, see [14, 15, 19, 33, 37, 56]. However only few

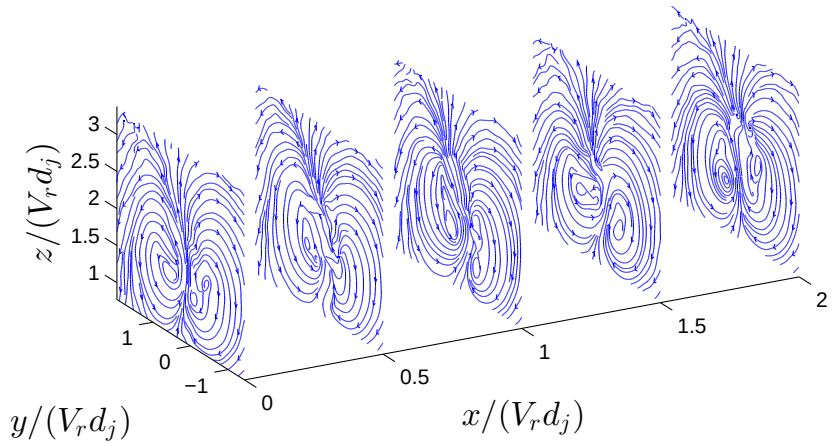

(a)

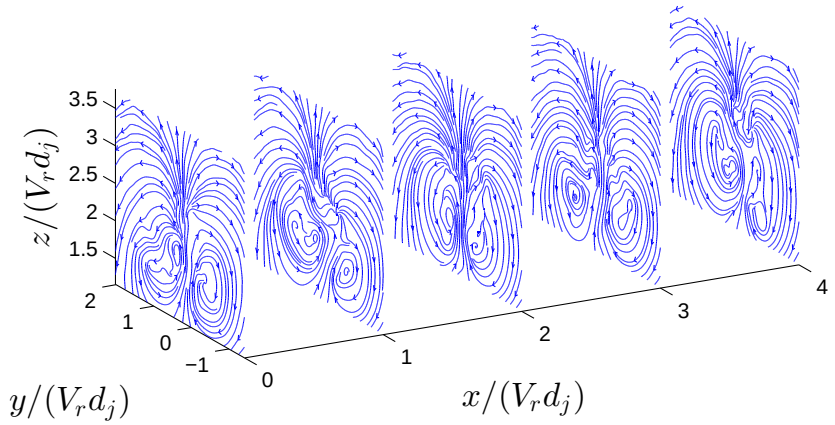

(b)

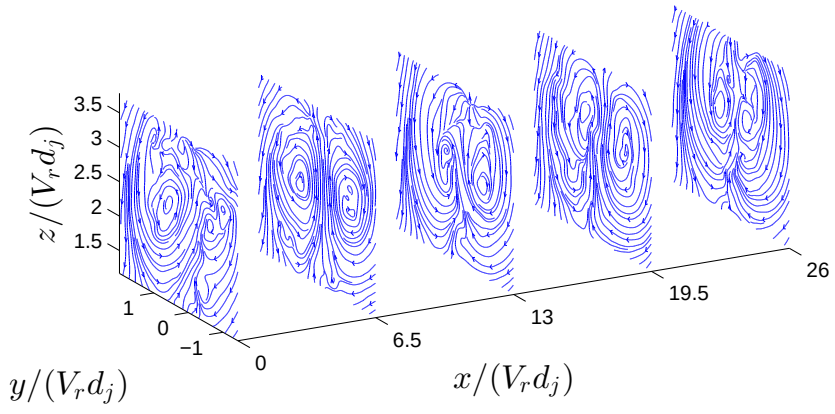

(c)

Figure 4.12: Two dimensional streamline pattern of reconstructed volumes in the y-z plane. Reconstruction from measurements at: (a) $x/dj = 15$, (b) $x/d_j = 30$ and (c) $x/d_j = 85$.

studies at $V_r > 10$ have been reported. The reconstructions allow the CVP structure in the near field to be examined first, which in turn will create a better understanding of the resulting far field structures. The enstrophy field shows iso-surfaces coloured by the local value of the streamwise vorticity. This allows for the direction of the vorticity vector to be interpreted. This technique is also used in other figures below to help better understand the orientation and direction of rotation of the coherent structures. So in the figure the negative core of the CVP is clearly visible as dark blue (negative streamwise vorticity) iso-surfaces, with dark red corresponding to the positive core (positive streamwise vorticity) of the CVP. Figure 4.14 shows a side and bottom view with the cross-flow direction from right to left. The bottom view (figure 4.14b) clearly shows both positive and negative cores of the CVP. On average one can envisage these as two vortex lines of opposite circulation. A striking feature of these figures is the presence of a significant number of structures that appear on the top (windward) side of the CVP. These are arched shaped, inclined against the flow direction and show some periodicity.

A more detailed, view of these structures is shown in figure 4.15 by plotting a top view (x-y plane) of a section of the figure covering approximately one large-scale eddy turnover time. The section plotted is between $x = 4.2$ and $6V_r d_j$, indicated between the two dotted lines in figure 4.13. Furthermore a colour-map is used which highlights only strong positive and negative local values of vorticity component used to colour the iso-surfaces. The two cores of the CVP are shown by dark red and blue isosurfaces. Several arched shaped windward side structures appear can be seen extending across the cores, connecting them together. The top the arch is predominantly aligned in the spanwise direction. To be able to further understand how they interact with the cores iso-surface contours coloured by the local spanwise vorticity ω_y are shown in figure 4.15b. Iso-surfaces with both positive (red) and negative (blue) ω_y component are observed. This means that structures aligned in the spanwise direction with both a clockwise and anti-clockwise rotational direction appear on the windward side of the CVP.

To better observe this behaviour a longer volume (covering approximately 5 large-scale eddy turnover time) is plotted in figure 4.16 with the iso-surfaces coloured by the local value of the spanwise ω_y component. This reveals that

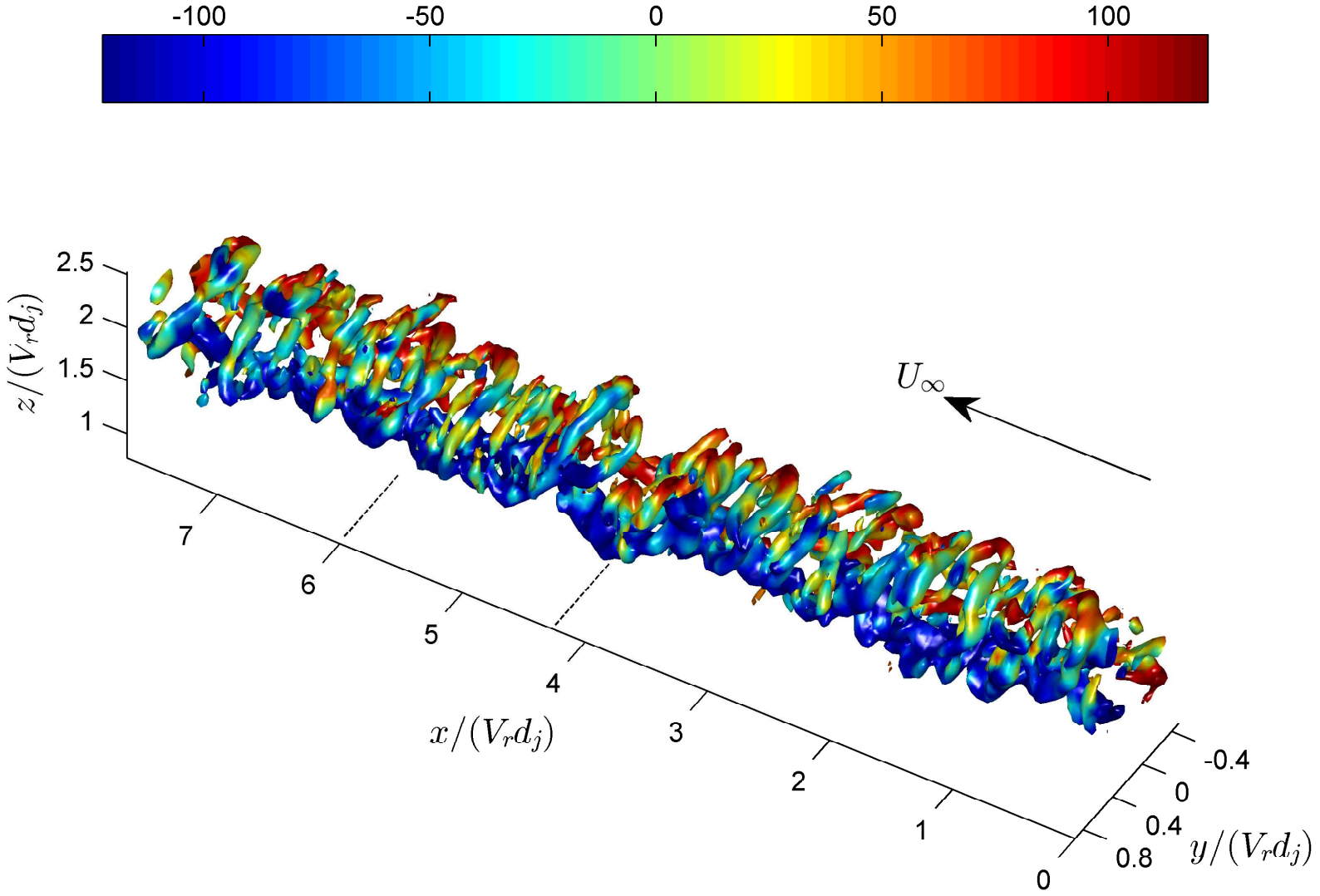

Figure 4.13: Volume 1 at $x/d_j = 15$: Enstrophy field structures over a long volume. Iso-surfaces of $\Omega_{iso} = 0.12\Omega_{max}$. Surface is coloured by the local value of streamwise vorticity $\omega_x(\mathrm{s}^{-1})$.

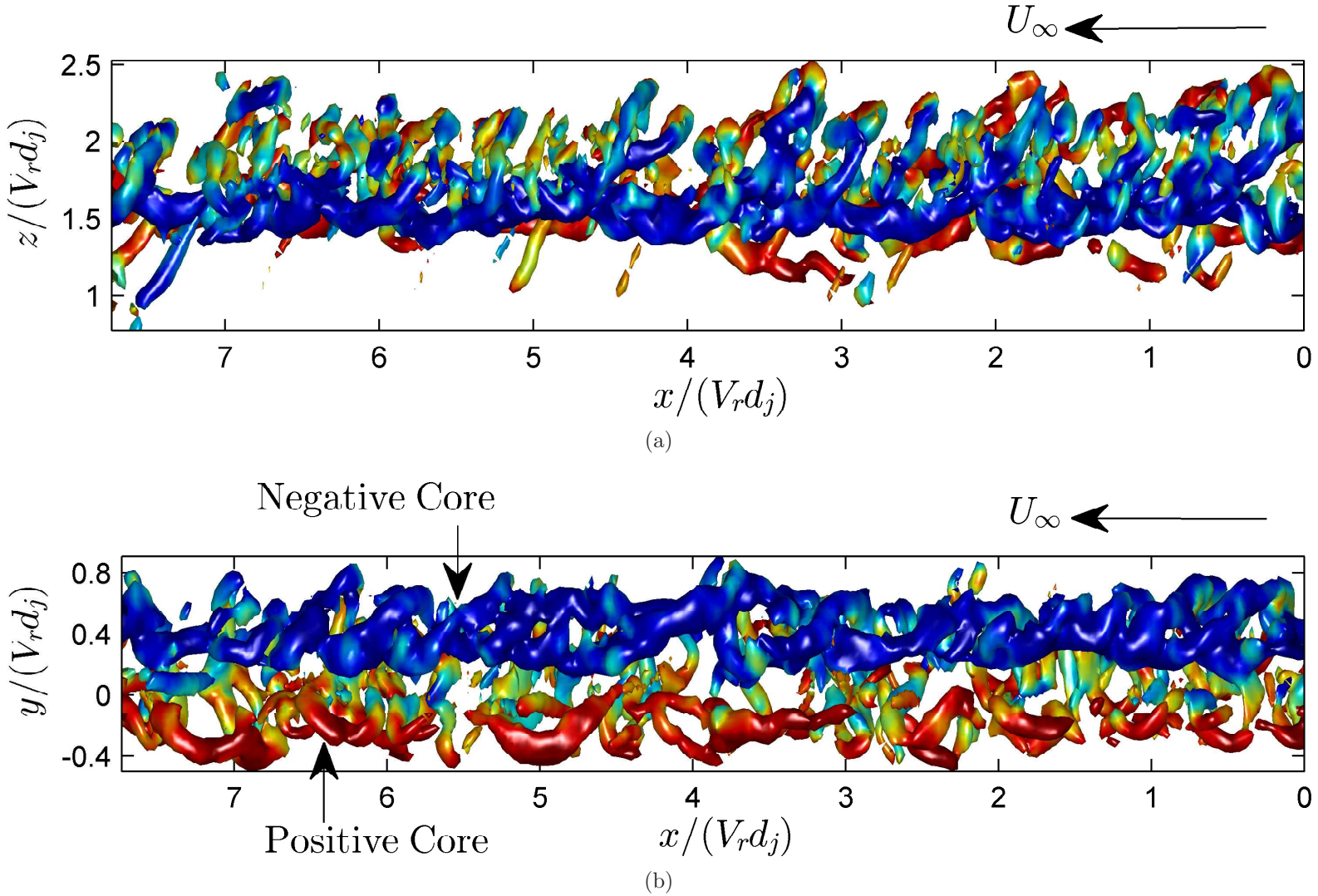

Figure 4.14: Volume 1 at $x/d_j = 15$: (a) Side view and (b) Bottom view of the jet structure. Iso-surfaces of $\Omega_{iso} = 0.12\Omega_{max}$. Surface is coloured by the local value of $\omega_x(\mathrm{s}^{-1})$.

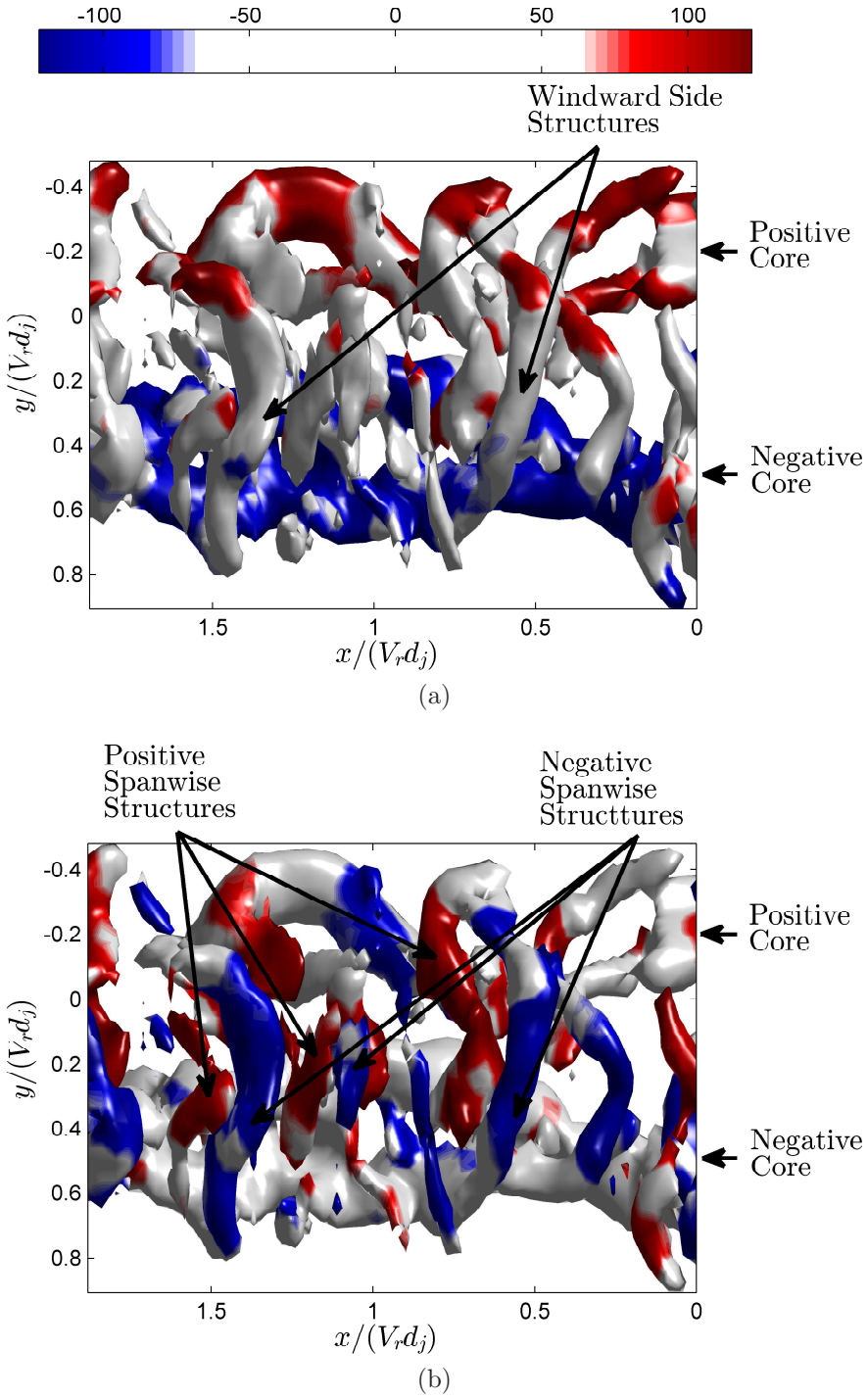

Figure 4.15: Volume 1 at $x/d_j = 15$: Top view of section between $x/(V_r d_j) = 4.2 - 6$ of figure 4.13. Iso-surfaces of $\Omega_{iso} = 0.12\Omega_{max}$. Surface is coloured by the local value of (a) streamwise vorticity $\omega_x(\mathrm{s}^{-1})$ and (b) spanwise vorticity $\omega_y(\mathrm{s}^{-1})$. Colour-map used highlights only strong positive and negative local values of the vorticity component.

these structures, with both positive and negative ω_y component, appear with some consistency and exhibit ordered behaviour on the windward side of the cross-flow jet. A cut through the centre-plane (mid point between the two cores in the y-direction) is shown in figure 4.17 with contours of the spanwise ω_y component within the cut iso-surfaces. A series of these structures is observed to appear almost in a quasi-periodic fashion with their rotational direction alternating with downstream distance based on the change of sign of the ω_y component. Furthermore the structures with positive spanwise vorticity are positioned just in front and slightly below the negative ones. The degree of order in which these windward side structures appear suggests that they may have their origin in the roll-up of the upstream/windward side of the jet shear layer near the jet exit, like a Kelvin Helmholtz instability but 3D. This is shown in figure 1.4 as postulated by Lim *et al.* [37] and in the computational results of Cortelezzi & Karagozian [15] and Schlegel *et al.* [56] in figures 1.3 and 1.5 where the rolled up upstream side of the jet shear layer follows the mean curvature of the cross-flow jet. Frequency spectra of the velocity signals were examined at the position of these structures but did not result in a dominant frequency to compare against results from the literature. This could possibly be because the measurements are too far downstream to be able to do so. From the orientation of the jet and the coordinate system used here, the roll-up of the upstream side of the jet shear layer would result in only the negative windward structures. The positive "roller like" structures therefore must originate from somewhere else, possibly arriving from the downstream/lee side of the jet shear layer to the windward side via the folding of the sides of the cylindrical shear layer as shown by the the proposed mechanism of Lim *et al.* [37] in figure 1.4.

Upon closer observation in figure 4.16, the top part of the arched negative windward structures, aligned in the spanwise direction, appear to extend downwards on either side and connect to the cores of the CVP. Figure 4.18 shows another example of a volume (similar to figure 4.13) covering more than one large-scale eddy turnover time where this is more clear, with a view of looking downstream from upstream and the isosurfaces coloured by the local value of streamwise vorticity ω_x. A series of these 'legs' can be observed, which extend from the arch downwards inclined in the downstream direction eventually align-

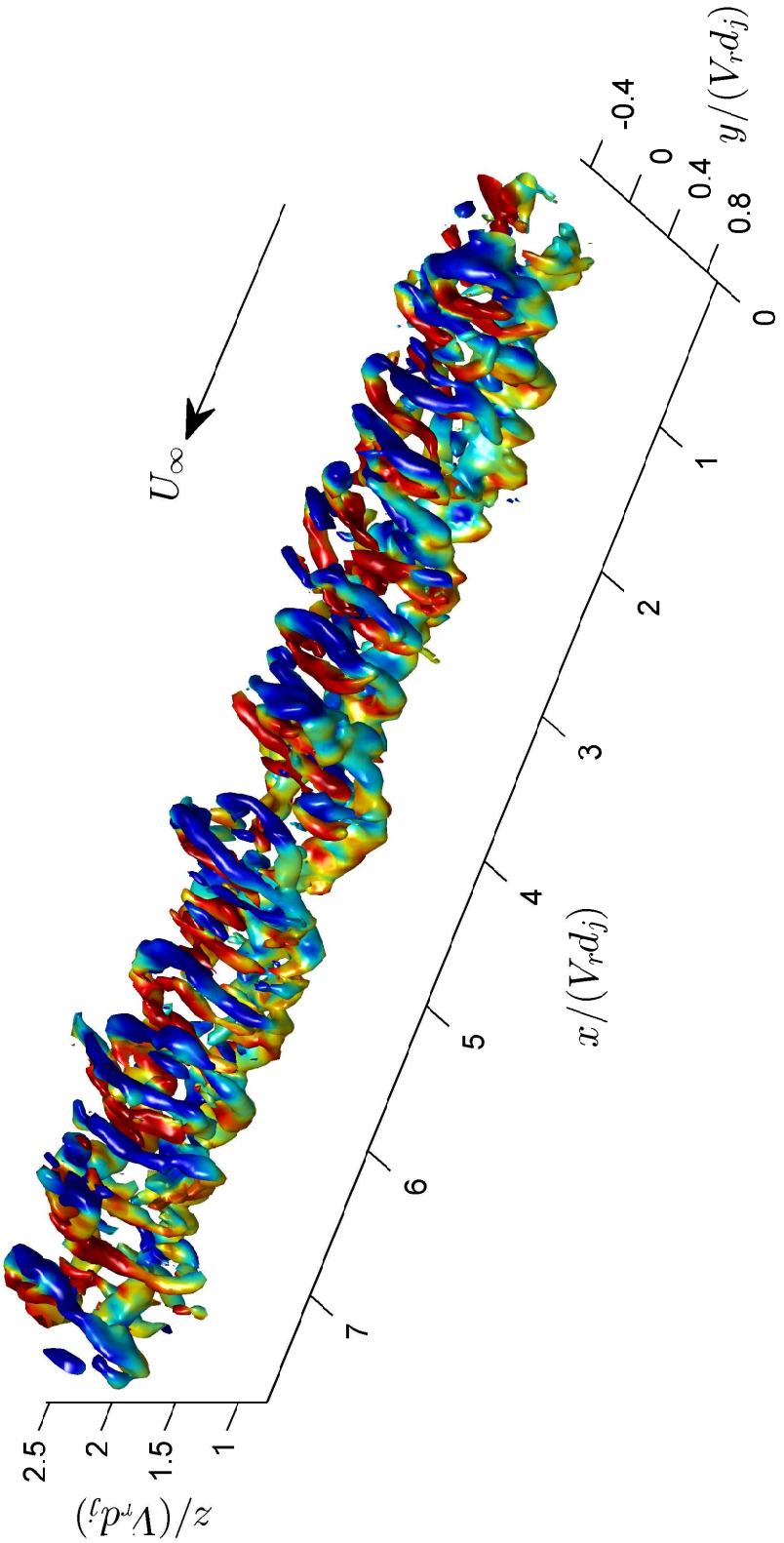

Figure 4.16: Volume 1 at $x/d_j = 15$: Iso-surface contours of figure 4.13 ($\Omega_{iso} = 0.12\Omega_{max}$) coloured by the local value of spanwise vorticity $\omega_y(\mathrm{s}^{-1})$. Colormap is the same as that in figure 4.13.

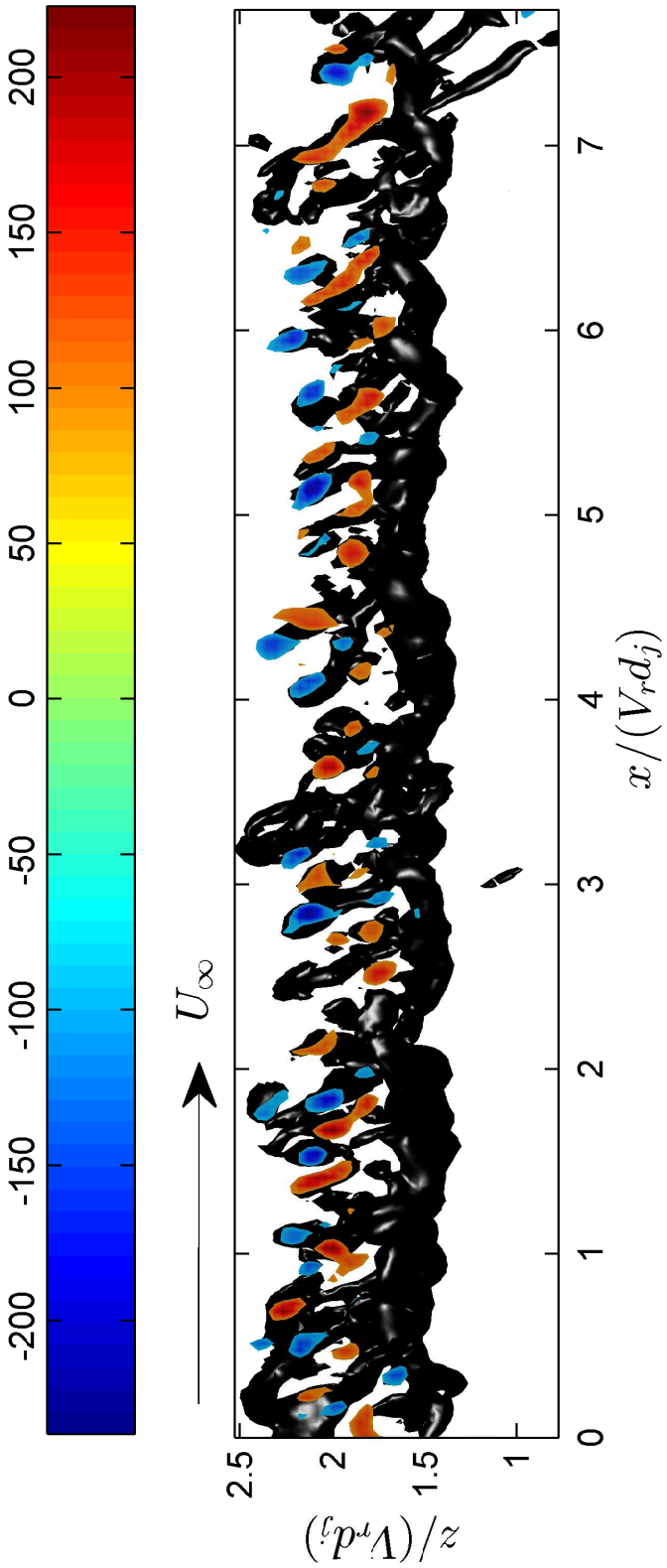

Figure 4.17: Volume 1 at $x/d_j = 15$: Cut through the centre-plane of the iso-surface contours of figure 4.16 highlighting the local value of spanwise vorticity $\omega_y(\mathrm{s}^{-1})$.

ing with the cross-flow direction around the position of the cores of the CVP in one continuous structure.

There are obvious similarities to hairpin structures found in turbulent boundary layers [2, 18, 20, 30, 62, 69] which are used as possible representative eddies to model the flow [46, 48, 49] using the ideas of Townsend's attached eddy hypothesis which describes the flow as a distribution of geometrically similar eddies of different size which scales with wall distance [63]. For the purposes of discussion a cartoon of a hairpin structure is shown in 4.19. Figure 4.19a shows the decomposition of the hairpin in three parts, the head, legs and tails. Figure 4.19b shows a train of these structures and how they might link together. These terms will be used to help in interpreting the various observations made in the 3D reconstructions. It is important to state that instantaneously these structures do not exist everywhere but are rather a mean/idealised building block of the CVP which, as will be demonstrated, can explain the turbulent structure. Figure 4.20 shows a side and bottom view of a section of figure 4.18, from $x/(V_r d_j) = 0-3.86$, that show 4 instances of these structures and are denoted by arrows. Due to the repeatable pattern, the section highlighted covers more than one large-scale eddy turnover time as it offers more insight into the overall structure. The part of the structures extending downwards towards the core show a consistent inclination forwards, in the downstream direction. These structures show a strong resemblance to hairpins, with the windward side negative structures representing the head of the hairpin, and the part extending downwards towards the CVP the legs of the hairpin. The bottom view reveals an interesting aspect of these structures. As the legs bend and become aligned with the cross-flow direction, they continue to extend downstream and interact with the legs of the hairpin structure in front of them. These parts of the hairpin, referred to here as the 'tails', extend downstream and inwards towards the centre plane (y = 0), before wrapping around the inside of the tails of the hairpin in front as shown in the cartoon in figure 4.19b. The tails therefore are not attaching to the cores, but actually form the cores of the CVP. A similar pattern is observed for the positive core, albeit a bit more broken up, but becomes more clear when a lower threshold is used. The tails have a helical shape in the streamwise direction. This is consistent with the fact that the Multi-Scale SPIV results show clusters of streamwise vorticity in

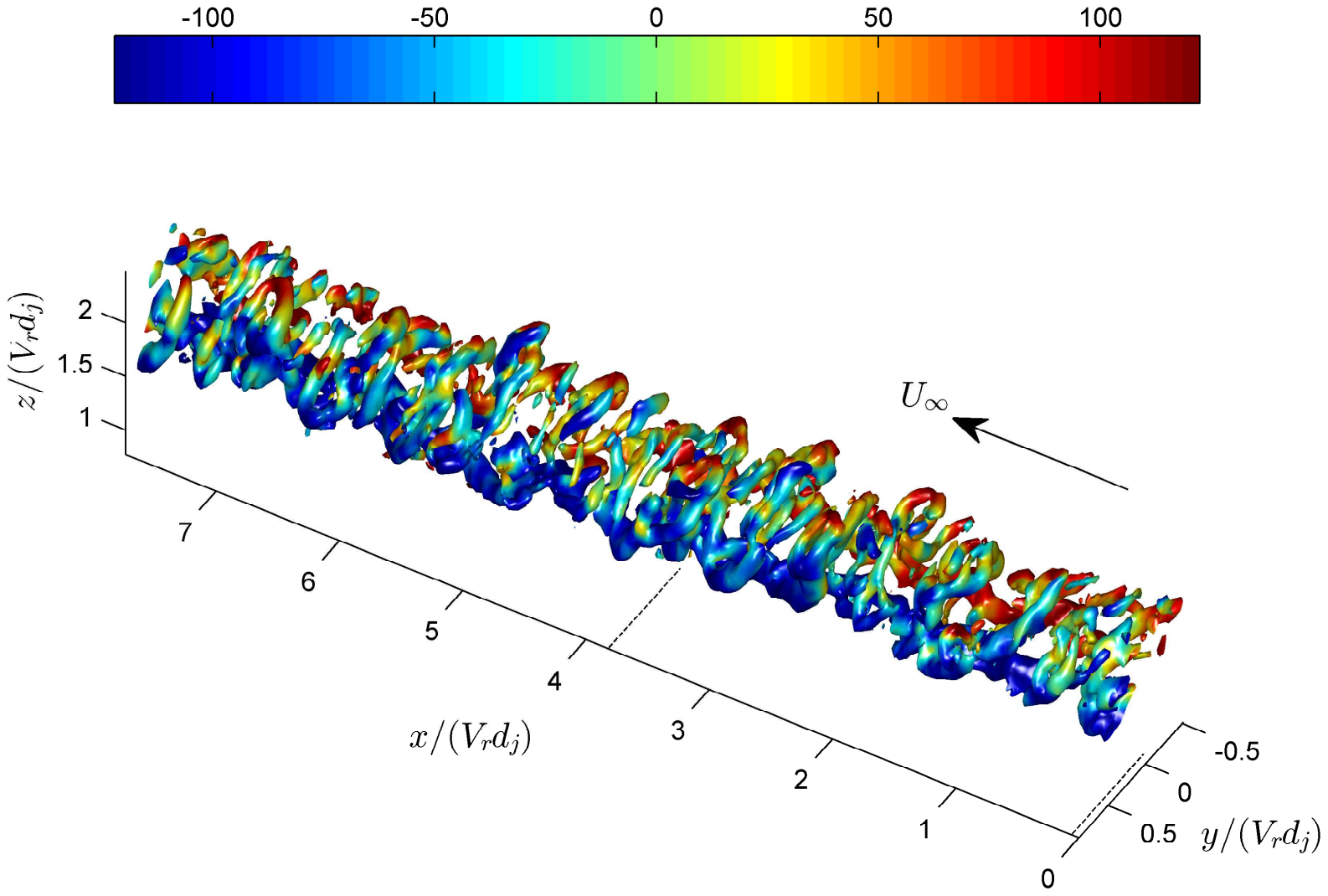

Figure 4.18: Volume 2 at $x/d_j = 15$: Visualisation of linking of structures from measurements at $x/d_j = 15$ over a long volume. Iso-surfaces of $\Omega_{iso} = 0.12\Omega_{max}$. Surface is coloured by the local value of $\omega_x(\mathrm{s}^{-1})$.

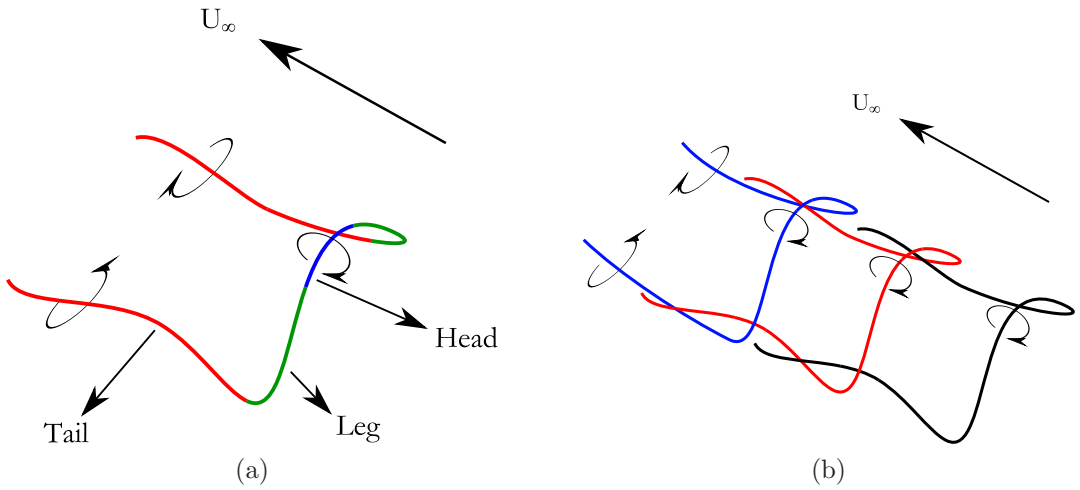

Figure 4.19: Cartoon of the hairpin structures. (a) Decomposition of the various parts of the hairpin. Blue part is the head, green parts are the legs and red parts are the tails. (b) Train of three hairpins, each one indicated by a different colour.

instantaneous realisations of the CVP (section 3.3).

A closer look at figure 4.20a shows another structure of what appears to be upright vortices extending from the area between the cores downwards. A lower threshold is needed to visualize them better and this is shown in figure 4.21a, which is the same view and iso-surface contour value as figure 4.20a, but with a second lower iso-surface contour added and the surfaces coloured by the local value of the wall normal vorticity component ω_z. The lower threshold makes these structures appear more prominently, extending well into the wake from the position of the cores. These wake vortices, have been observed by a variety of authors [19, 23, 33, 55, 58] but few velocity measurement exist. An alternating series of both positive and negative vorticity wake structures are observed. Their origin is not well understood with one postulation being that they lifted from the boundary layer from both sides of the jet and appearing in the wake similar to a von Karman vortex street. The wake vortices appear to be titled slightly forwards, at angles similar to the angle observed of the jet fluid streaks appearing in the wake of the cross-flow jet. There are many similarities to the results of Smith & Mungal [58] (figure 1.7).

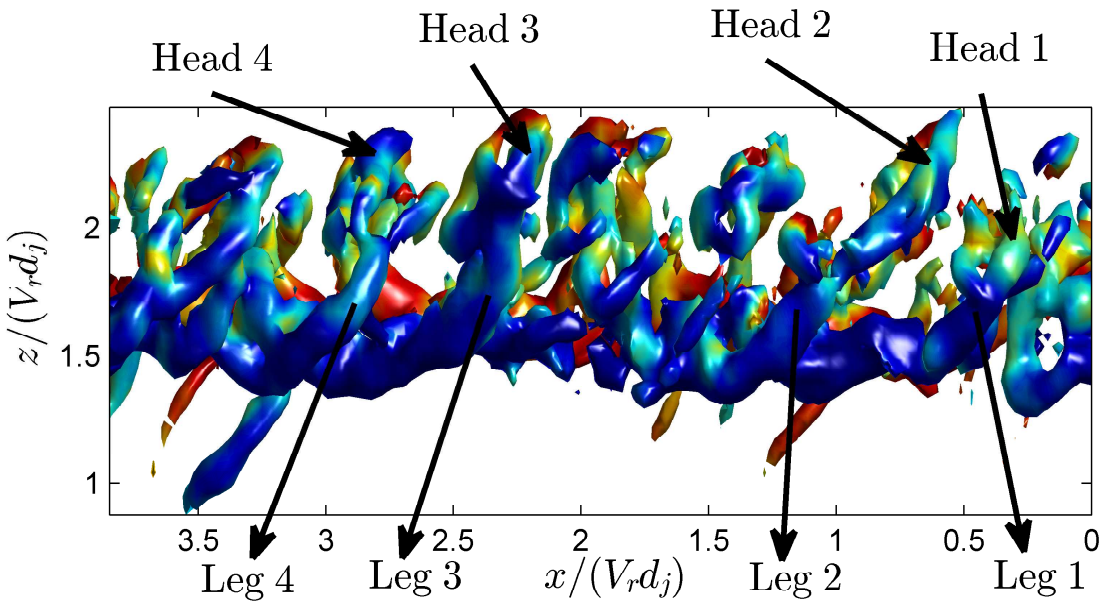

(a)

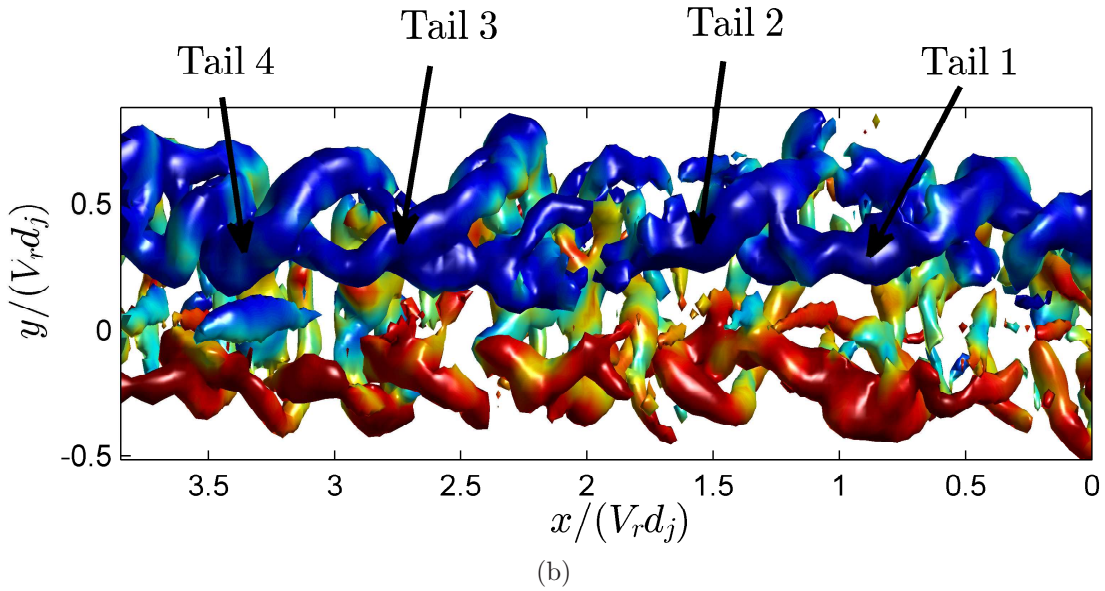

(b)

Figure 4.20: Volume 2 at $x/d_j = 15$: (a) Side view and (b) Bottom view of figure 4.18. Iso-surfaces of $\Omega_{iso} = 0.12\Omega_{max}$. Surface is coloured by the local value of $\omega_x(\mathrm{s}^{-1})$. Colormap is the same as that in figure 4.18.

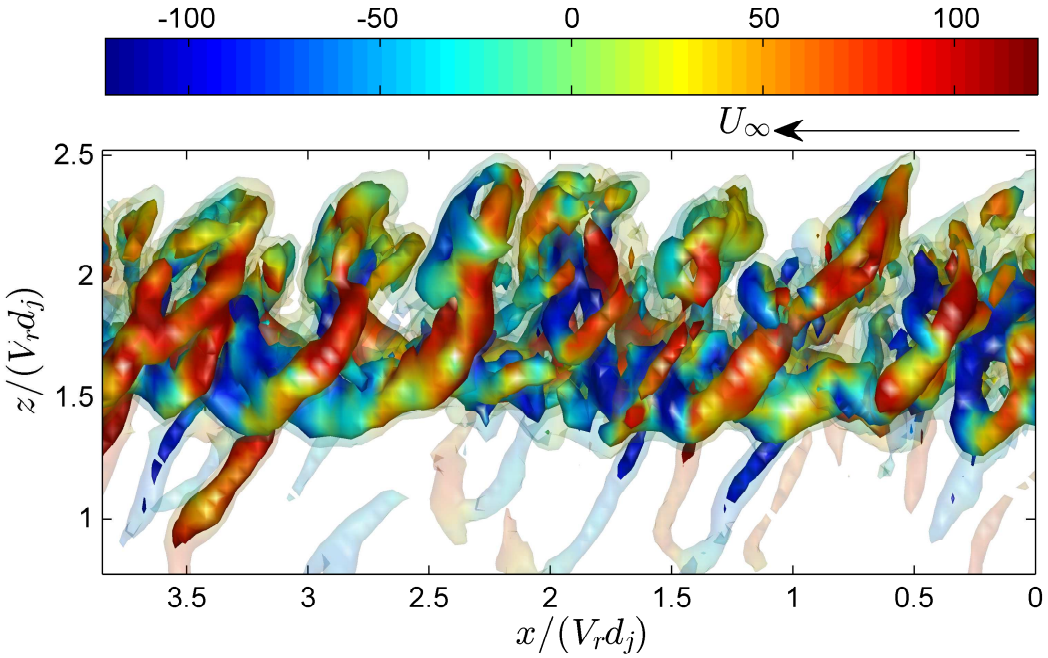

(a)

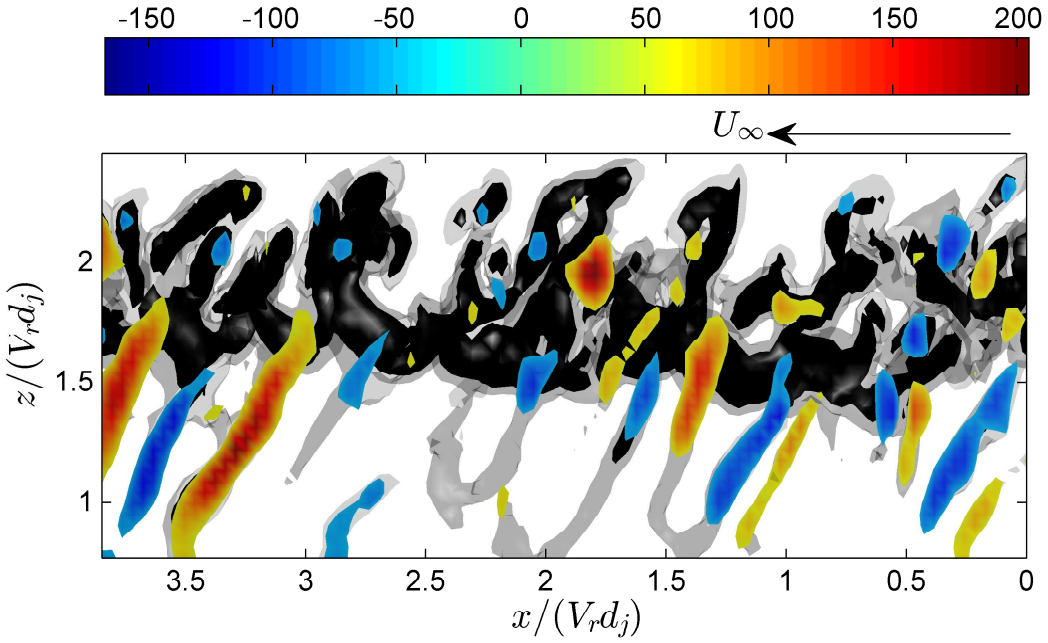

(b)

Figure 4.21: Volume 2 at $x/d_j = 15$: Visualisation of upright wake vortices from measurements at $x/d_j = 15$. (a) Iso-surfaces of $\Omega_{iso} = 0.12\Omega_{max}$ (solid) and $\Omega_{iso} = 0.05\Omega_{max}$ (transparent). Surface is coloured by the local value of $\omega_z(\mathrm{s}^{-1})$. (b) Cut through centre-plane of figure (a) showing contours of $\omega_z(\mathrm{s}^{-1})$ within the cut iso-surfaces (which are coloured black for clarity).

The velocity distribution with respect to the structures identified can be studied by looking at iso-surface contours of streamwise high-momentum and low momentum fluid, relative to the cross-flow velocity. Recall that in the mean the jet is actually more like a wake flow with 2 high momentum cores either side of a low momentum wake (section 3.4). Figure 4.22 shows these iso-surfaces together with an iso-surface of the enstrophy, showing the vortex structures. High momentum

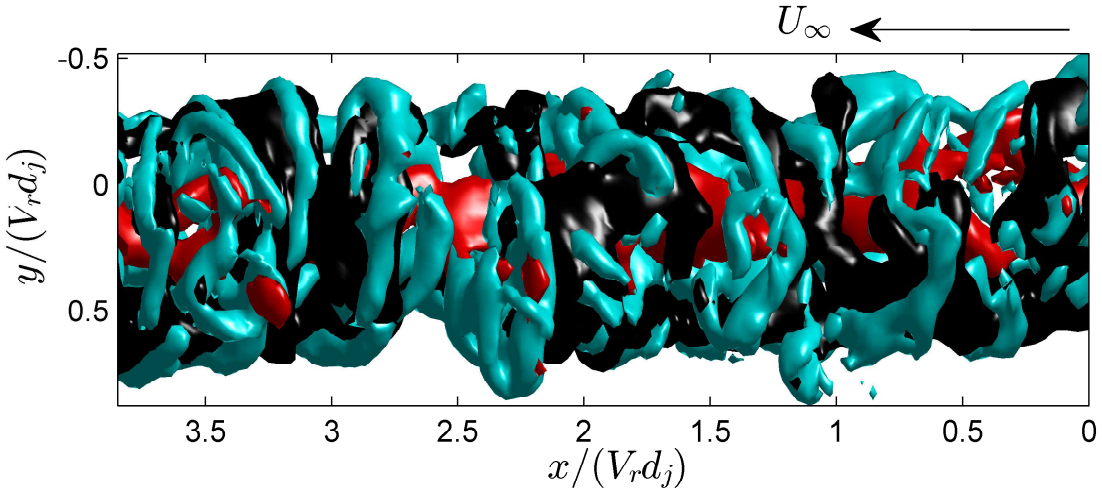

Figure 4.22: Volume 2 at $x/d_j = 15$: Top view visualisation of high and low momentum regions. Cyan iso-surfaces: $\Omega_{iso} = 0.12\Omega_{max}$. Red iso-surface: $U_{iso} = 0.7U_\infty$. Black iso-surface: $U_{iso} = 1.3U_\infty$.

fluid (black iso-surfaces) sits underneath the negative windward structures (i.e the heads of the hairpins) and above the positive windward structures, as well as on the inside of the side arms extending downwards to the cores of the CVP forming an arch shape on top of the cores. This high momentum fluid in an arch connecting the cores was observed in the mean streamwise velocity profile of the measurements at $x/d_j = 30$ in the previous chapter (figure 3.14). The flow structures responsible for the mean profile can be attributed to the heads and legs of the hairpins structures inducing this high momentum fluid. Side and bottom views of figure 4.22 help make this more clear. The bottom view in figure 4.23b shows the tails of the interacting hairpins being wrapped around a region of high momentum fluid (core). This is fully consistent with the mean velocity profiles where high momentum regions occur at the core locations. The low momentum

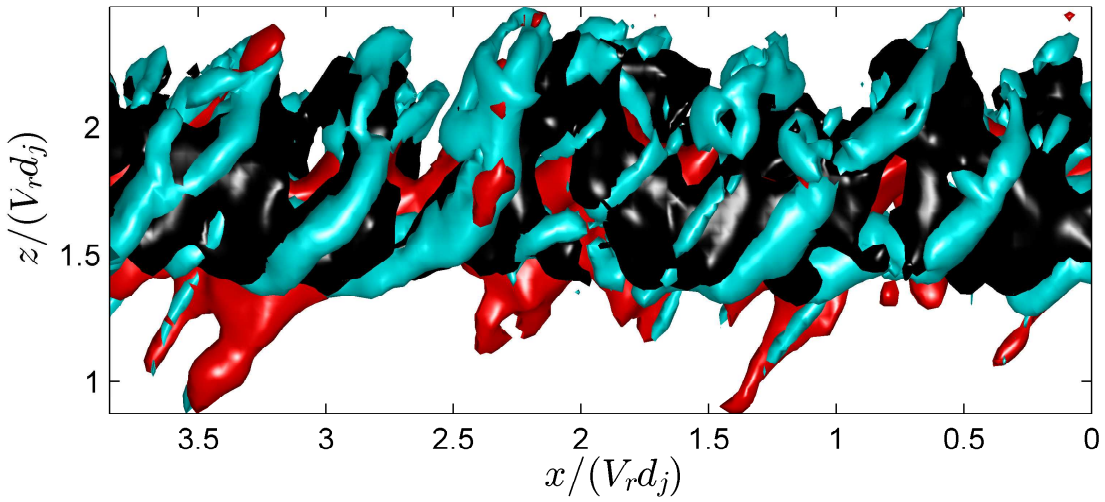

(a)

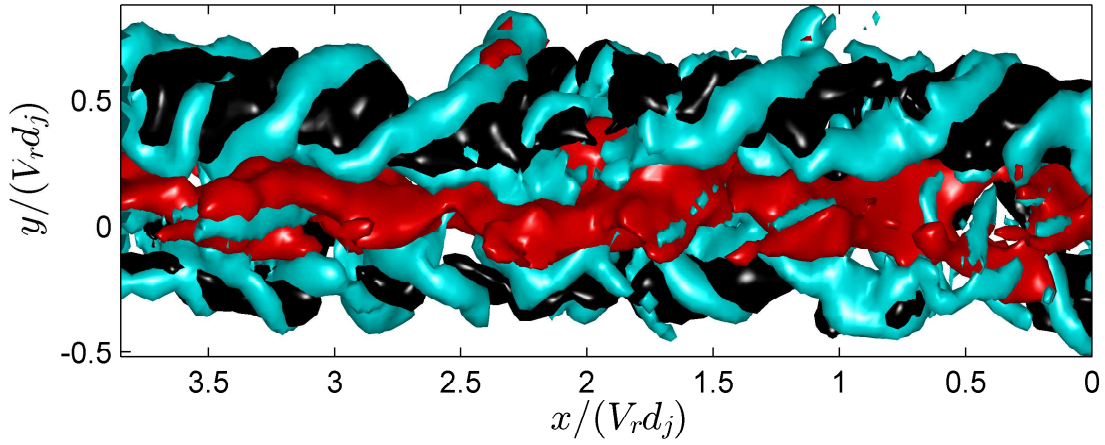

(b)

Figure 4.23: Volume 2 at $x/d_j = 15$: (a) Side view and (b) Bottom view of figure 4.22. Cyan iso-surfaces: $\Omega_{iso} = 0.12\Omega_{max}$ show the legs of the hairpin like structures and their interlinking. Red iso-surface: $U_{iso} = 0.7U_\infty$ indicates the low momentum 'wake' region. Black iso-surface: $U_{iso} = 1.3U_\infty$ indicates the high momentum region.

region (red iso-surfaces), can be observed on the lee side of the jet sitting in between the two cores. Some wake structures can be seen extending down into the wake towards the wall in figure 4.23a. Again this is in agreement with the mean velocity profiles. The degree of order in the flow structure is most likely due to the fact that the data was take in the near field at $x/d_j = 15$. What is of interest is whether any trace of this observed structure persists into the far field.

Figure 4.24 shows the enstrophy field of a volume covering approximately 2 large-scale eddy turnover time-scales at $x/d_j = 30$. The two cores are visible with a number of windward structures, as observed in the results at $x/d_j = 15$, on the windward side. Figure 4.25 shows a side and bottom view of figure 4.24, with the bottom view clearly showing the two cores of the CVP. The side view shows more clearly the windward structures and although there are similarities to the ones at $x/d_j = 15$, where a high degree of coherency was observed, the results here are somewhat less coherent in the sense that the structures are visibly less regular. This becomes more obvious when the iso-surface contours are coloured by the local value of the spanwise vorticity ω_y to better visualise the hairpin heads in figure 4.26.

A similar but more turbulent structure compared with the near field at $x/d_j = 15$ is observed. Regularly spaced structures aligned in the spanwise direction having both positive and negative component of spanwise vorticity ω_y, alternate with downstream distance. This indicates that the flow structures from $x/d_j = 15$ persist into the far field at least until $x/d_j = 30$. The top view in figure 4.27a shows these structures span over the two cores and although they may on average align in the spanwise y-direction, instantaneously individual hairpin heads and rollers are orientated at a small angles to the y-axis. In the previous chapter it was observed that the distribution of vortex tubes of streamwise vorticity ω_x in the CVP plane formed a horseshoe on the windward side whose feet were connected to the two cores. Such structures are not obviously inferred from the mean vorticity field $\overline{\omega_x}$ in figure 3.7. This can be explained by the observed varying orientation of the hairpin heads and rollers at small angles to the y-axis, thus instantaneously having a small component in the streamwise direction agreeing with the joint pdfs of figure 3.13. However on average, across the whole volume, they are aligned along the y-axis resulting in a negligible streamwise vorticity component ω_x, as

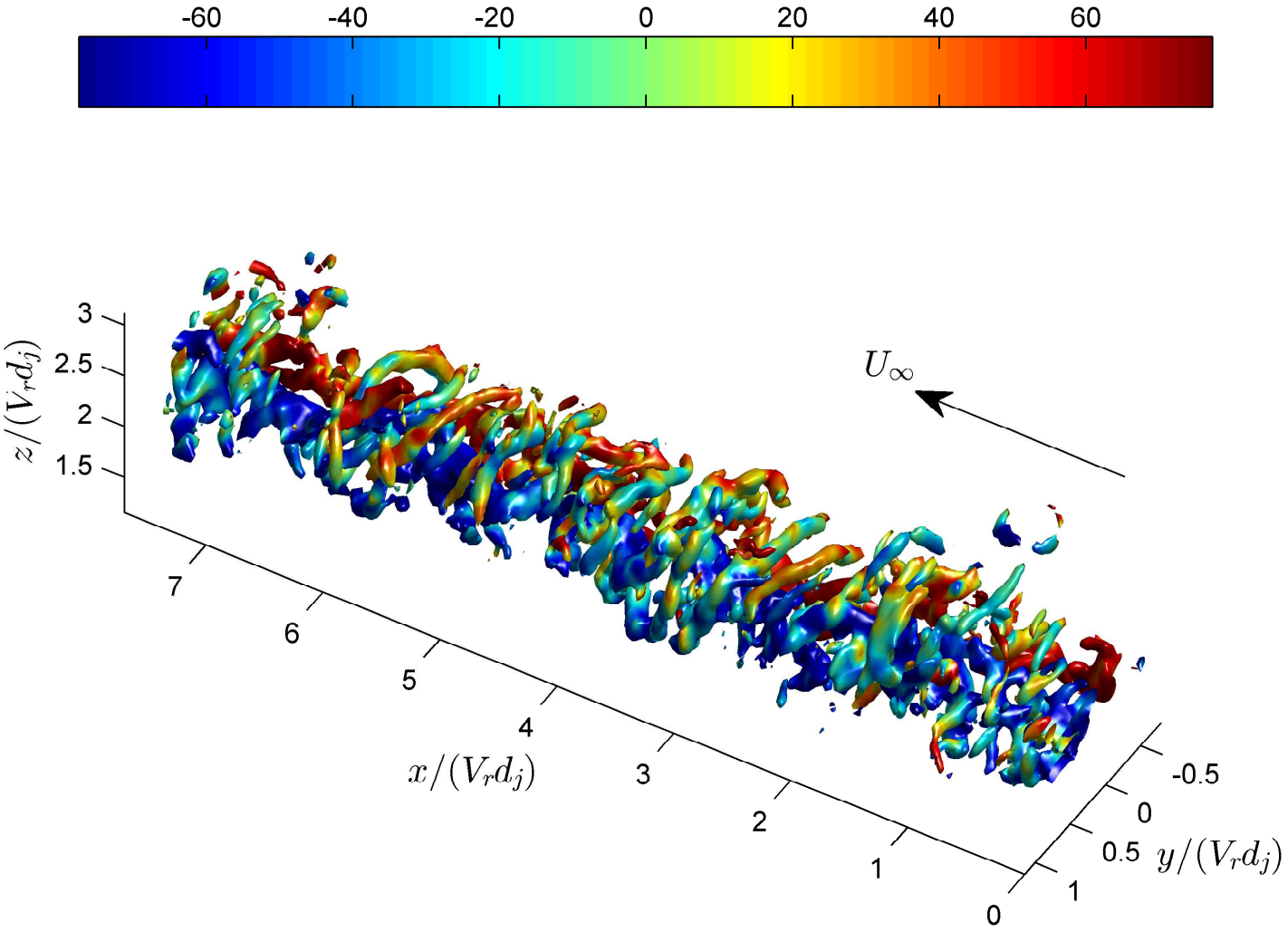

Figure 4.24: Volume 1 at $x/d_j = 30$: Enstrophy field structures. Iso-surfaces of $\Omega_{iso} = 0.1\Omega_{max}$. Surface is coloured by the local value of streamwise vorticity $\omega_x(\mathrm{s}^{-1})$.

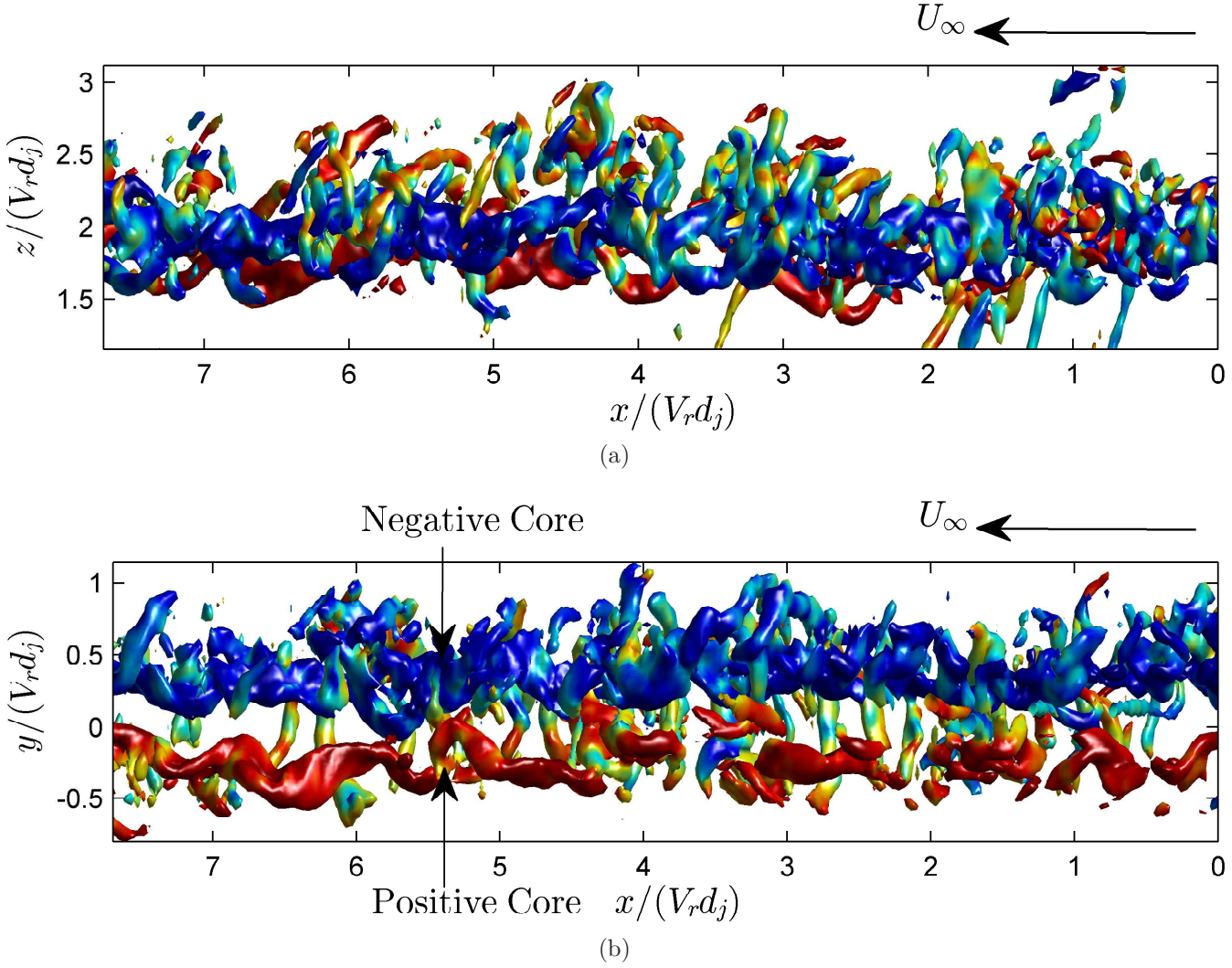

Figure 4.25: Volume 1 at $x/d_j = 30$: (a) Side and (b) Bottom view of figure 4.24. Iso-surfaces of $\Omega_{iso} = 0.1\Omega_{max}$. Surface is coloured by the local value of $\omega_x(\mathrm{s}^{-1})$.

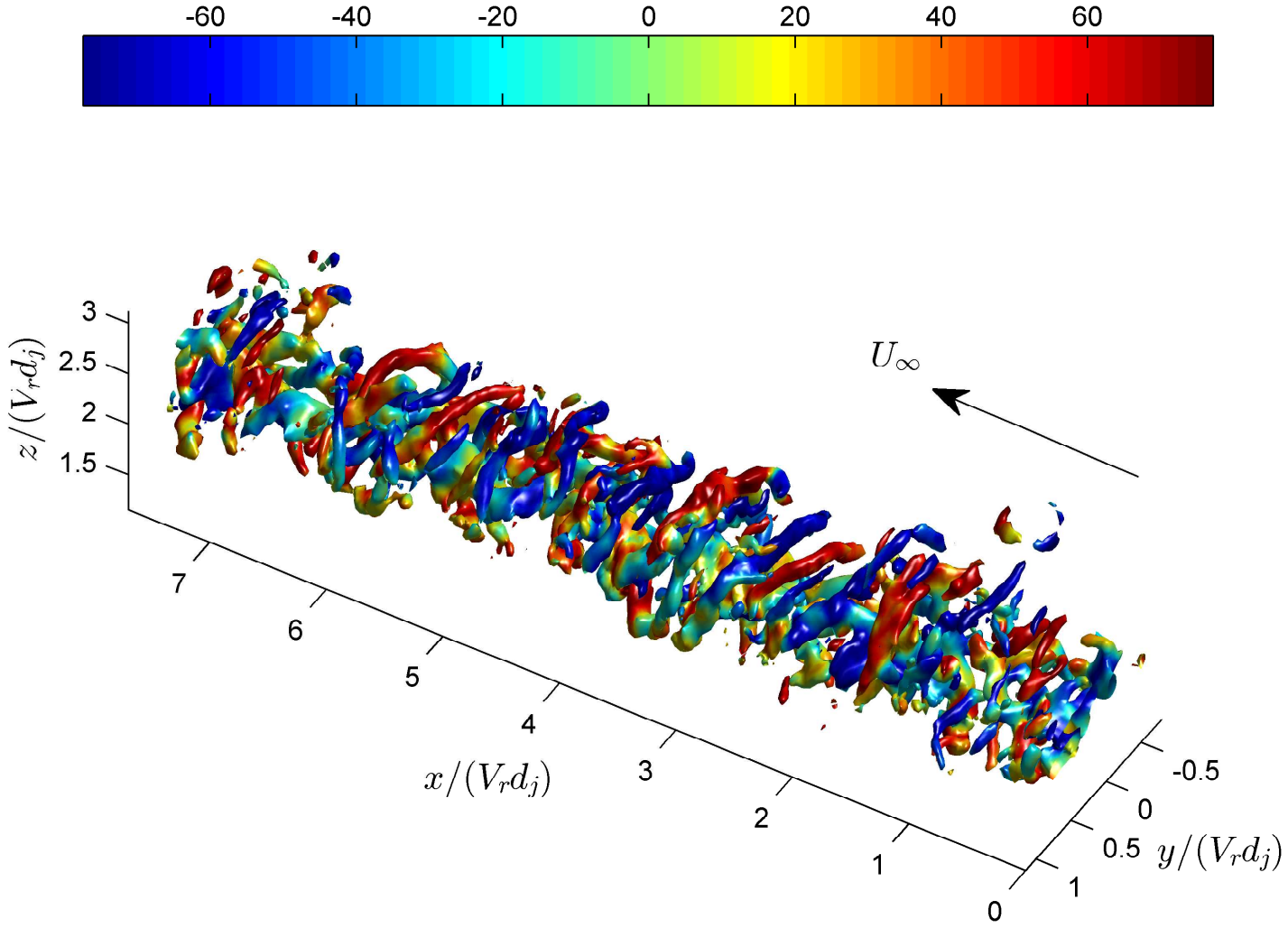

Figure 4.26: Volume 1 at $x/d_j = 30$: Enstrophy field structures. Iso-surfaces of $\Omega_{iso} = 0.1\Omega_{max}$. Surface is coloured by the local value of spanwise vorticity $\omega_y(\mathrm{s}^{-1})$.

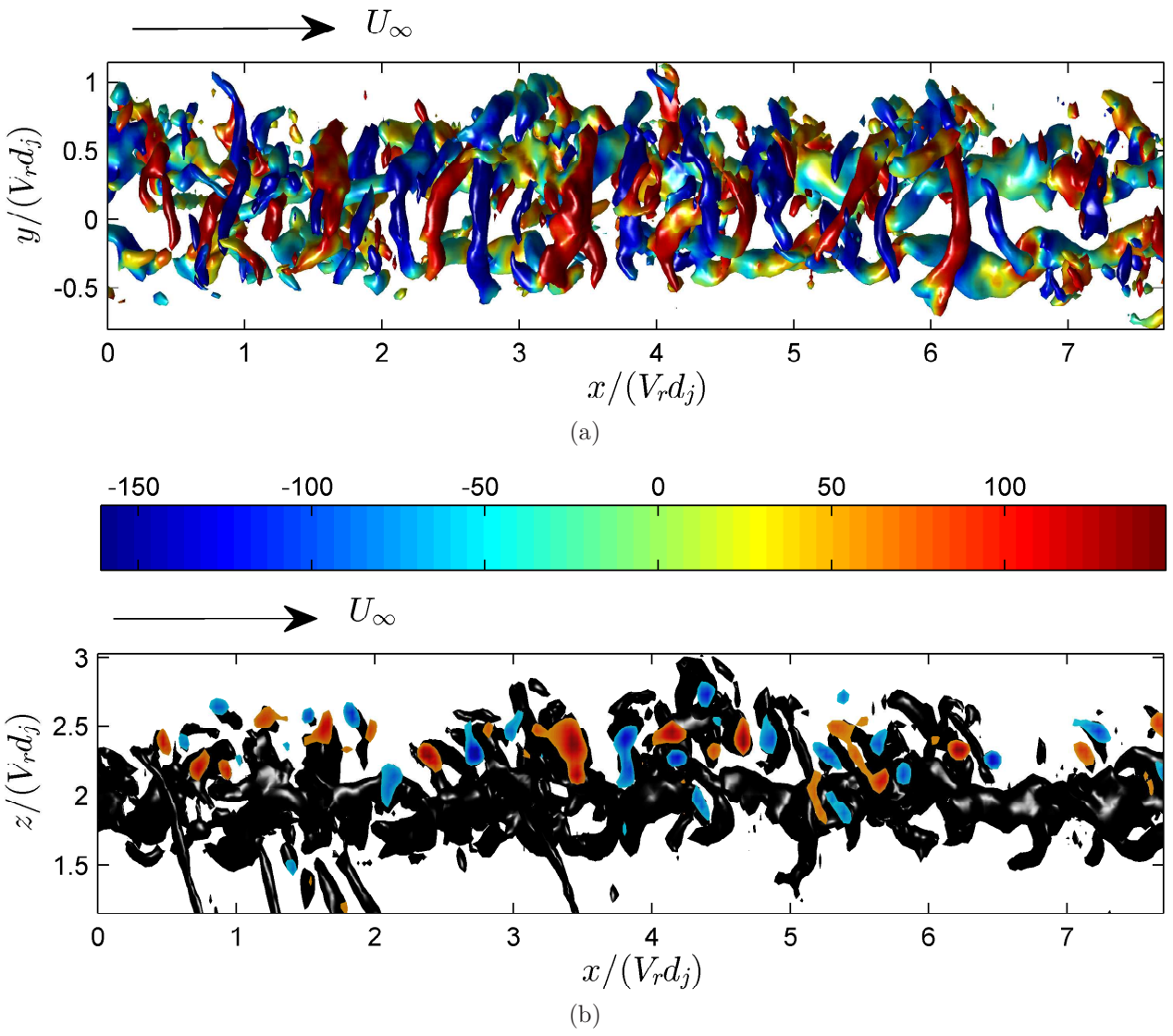

Figure 4.27: Volume 1 at $x/d_j = 30$: (a) Top view of figure 4.26 ($\Omega_{iso} = 0.1\Omega_{max}$). (b) Cut through centre-plane ($y = 0$) of figure (a) showing contours of $\omega_y(\mathrm{s}^{-1})$ within the cut iso-surfaces (coloured black for clarity).

shown in figure 3.7 and other studies [22, 31, 34]. It should be noted that very few velocity measurements have been carried out in the CVP plane in the literature , so it's not very surprising that these structures have not seen before. This view, together with the side view of figure 4.25a shows how a smaller degree of coherency exists in the far field regarding the organisation of the hairpins heads (negative structures) and rollers (positive structures). A cut at the centre-plane ($y = 0$) through the iso-surfaces in figure 4.27b shows that their relative positioning also changes when compared to that at $x/d_j = 15$. The positive and negative contours now appear to be, on average, at similar wall-normal heights above the cores.

Smith & Mungal [58] observed events in their scalar measurements on the windward side of the jet where areas with zero jet fluid concentration and areas of intense jet fluid concentration would appear (their figure 12). The areas of zero jet fluid concentration would extend down to the centreline of the jet. The relative positioning of the negative hairpin heads and positive rollers provides a mechanism to explain these observations. The alternating sign of the ω_y component creates regions of large positive wall-normal velocity between the heads of the hairpins and the rollers resulting in an upwash, as is the case between the two cores of the CVP. These ejection regions are shown in figure 4.28, which highlights iso-surfaces of large positive wall-normal velocity, W. These isosurfaces, coloured black, appear between the spanwise oriented positive roller (red) and negative hairpin head (blue) structures corresponding to regions of upwash extending beyond the area between the cores of the CVP and into the windward side of the jet. This would transfer jet fluid upwards, creating areas where jet fluid is ejected on the windward side of the jet into the cross-flow. Given the repeatable nature of the hairpin heads and rollers, areas of negative wall-normal velocity can be created between these structures. This is illustrated by the contour plot of the wall-normal velocity component W along the centreline of the jet ($y = 0$) in figure 4.29. The contour plot shows the positive upwash between the cores and on the windward side together regions of negative W component, which appear to be weaker in strength. These negative regions appear to extend down to the CVP cores. These negative regions may entrain fluid from the free-stream creating the regions of zero jet fluid concentrations observed by Smith & Mungal [58]. Indeed, this may be one contributing factor as to why the jet is such an

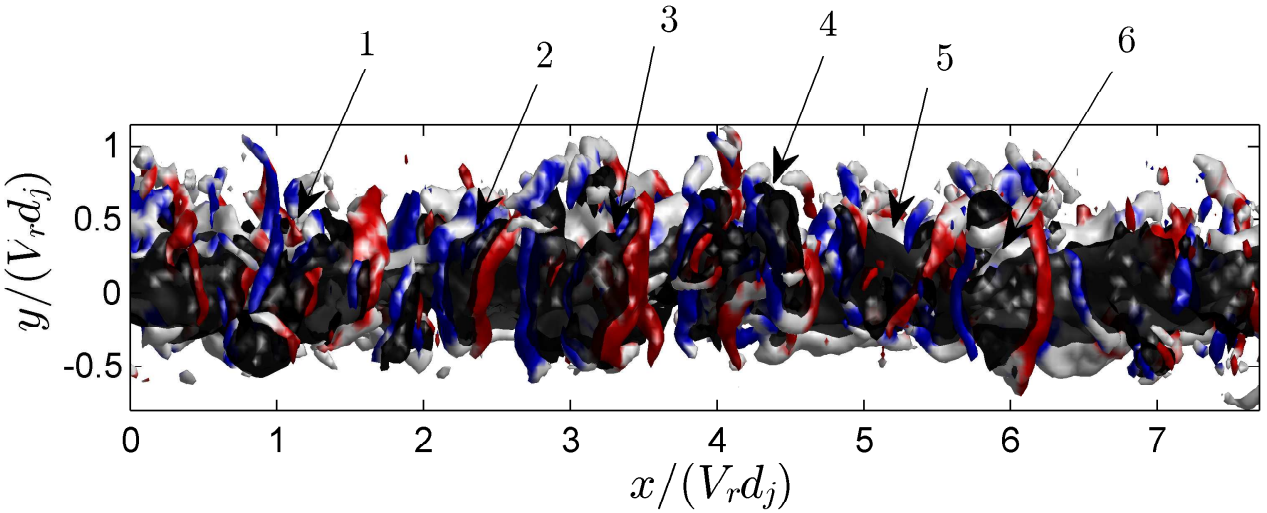

(a)

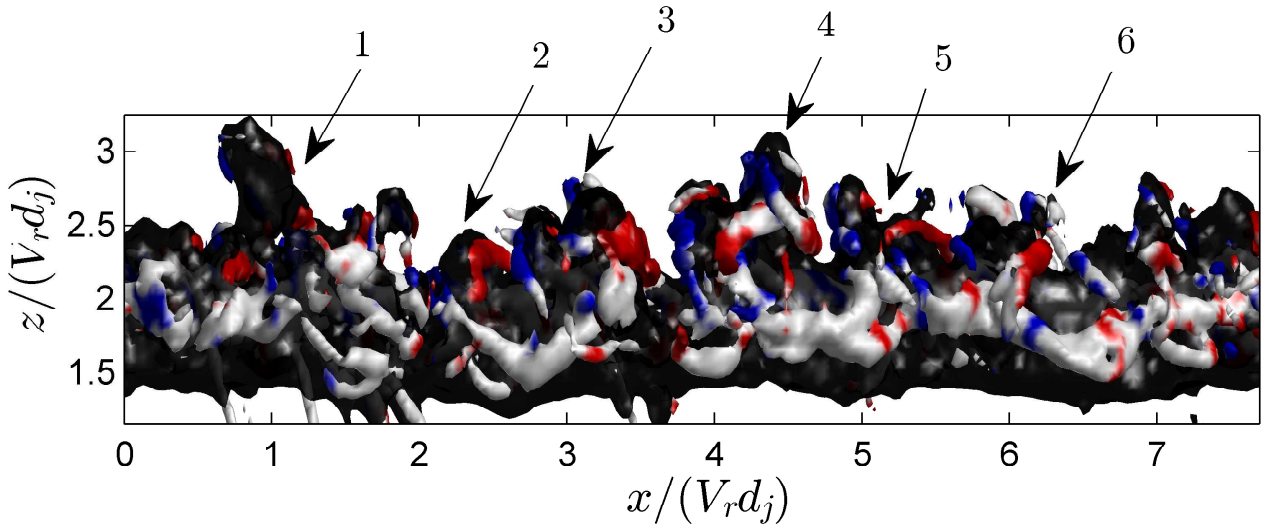

(b)

Figure 4.28: Volume 1 at $x/d_j = 30$: (a) Top and (b) Side view of jet fluid ejection. Red, white and blue coloured iso-surface: $\Omega_{iso} = 0.1\Omega_{max}$. Black iso-surface: $W_{iso} = 0.44\overline{W}_{max}$.

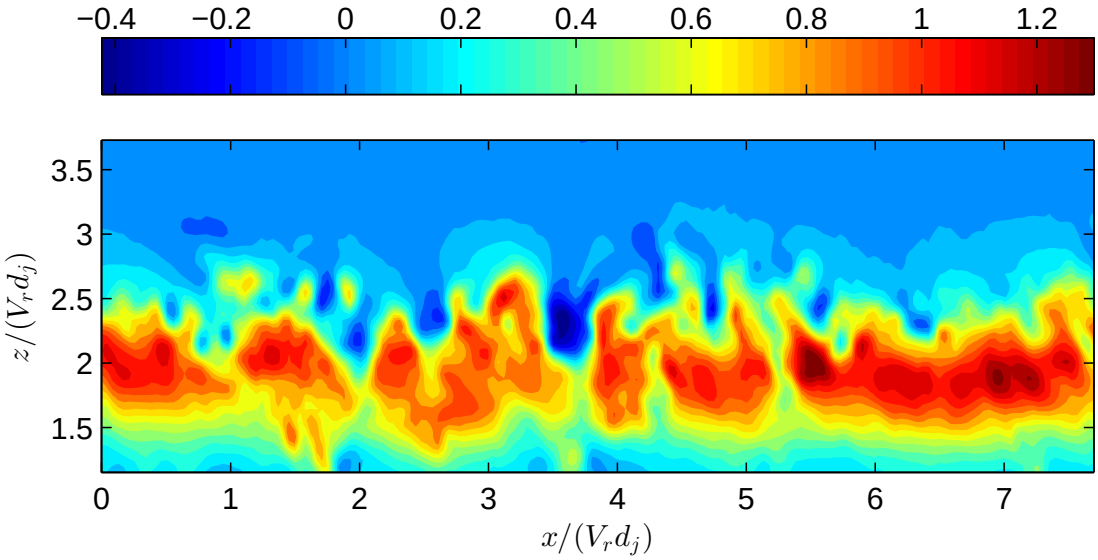

Figure 4.29: Contour plot of wall-normal velocity component W(m/s) at the centreplane $y = 0$ normalised by $\overline{W}_{max}$(m/s)

efficient mixer, with the spanwise rollers and hairpins entraining free-stream fluid and ejecting jet fluid, mixing the two together.

From the side and bottom view of the long volumes above in figure 4.25 there are no clear observations of the hairpin legs or their interaction with each other as was seen at $x/d_j = 15$ in figure 4.20. However figure 4.27a shows that the hairpin heads and rollers are still present. This would suggest that further into the far field the hairpin structures break up, but a footprint of them remains. Although fewer in number there are instances where the hairpins remain intact as is shown in figures 4.30 and 4.31. Figure 4.30 shows the top view of a volume which shows a similar structure to the previous figures. The heads of intact hairpins are annotated together with a hairpin head which is detached from the CVP core. This becomes clear in the side and bottom view of figure 4.31 where the legs and tails of the attached hairpins are visible but not so for the detached example. Furthermore, a number of other hairpins heads shown by negative iso-surfaces which are slightly broken up, can be seen in the top view which are not attached to the cores of the CVP. Different thresholds were checked and did not change the observations. The legs of the attached hairpins are inclined against the flow

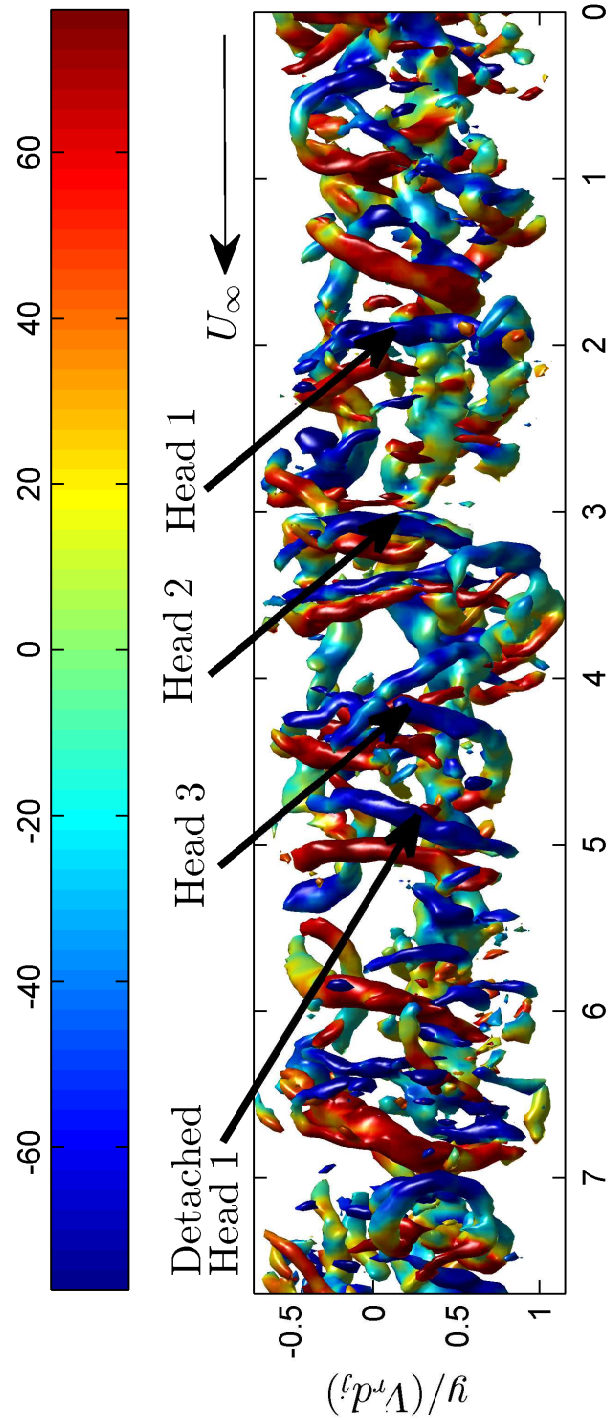

Figure 4.30: Volume 2 at $x/d_j = 30$: Top view of the jet. Taylor's reconstructions showing footprints of hairpin structures. Iso-surfaces of $\Omega_{iso} = 0.1\Omega_{max}$. Surface is coloured by the local value of spanwise vorticity $\omega_y(\mathrm{s}^{-1})$.

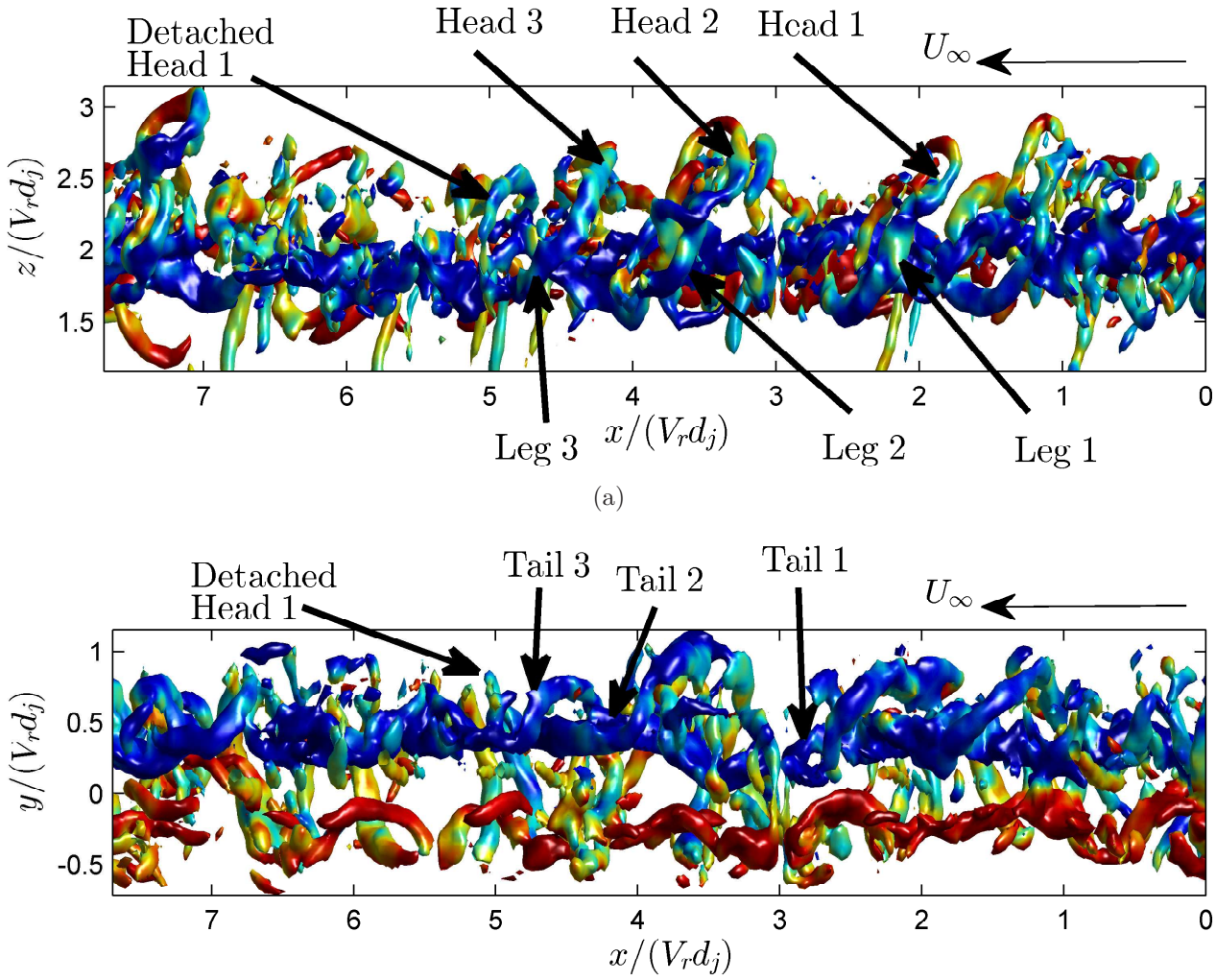

Figure 4.31: Volume 2 at $x/d_j = 30$: (a) Side and (b) Bottom view of figure 4.30 ($\Omega_{iso} = 0.1\Omega_{max}$) Surfaces are now coloured by the local value of streamwise vorticity $\omega_x(\mathrm{s}^{-1})$. Colormap is the same as that in figure 4.30.

direction as observed for the hairpins at $x/d_j = 15$. Both attached and detached hairpins are observed throughout the data set showing how the eddy structure of the cross-flow jet at the start of the far field is a footprint of the near field eddies being formed as the jet interacts with the cross-flow.

The side view of the volume in figure 4.31a shows a number of wake vortices, similar to those observed in the reconstructions at $x/d_j = 15$. Figure 4.32a shows the same side view with the iso-surfaces coloured by the local value of wall-normal vorticity ω_z together with transparent iso-surfaces of a lower contour threshold revealing more wake vortices. The wake vortices therefore persist in the far field in the same manner, in a series alternating the sign of the ω_z component with downstream distance. This is shown clearly in the cut through the centre-plane between the cores in figure 4.32b. The wake vortices are again tilted slightly forwards (with the part near the cores further upstream than the part extending into the wake), but at a smaller angle when compared to those observed at $x/d_j = 15$. The wake structures appear to remain perpendicular to the jet trajectory, and again agrees with the jet fluid streaks appearing in the wake from the results of Smith & Mungal [58].

The three main structures observed in the near field are observed to persist in the far field in the form of hairpins (attached and detached), roller and wake vortices. Recall from the previous chapter that the mean rms velocity fields at $x/d_j = 30$ showed a very distinct 'kidney' shaped structure whose origin is not well understood. This can be explained using the Taylor reconstructions presented here. The kidney shape of the rms is composed of two peaks at the position of the cores of the CVP, the arch shaped contour connecting the two cores from above, and a narrow region of rms values along the centre-plane between the cores and the wake. To highlight the flow structures that form these mean rms contours, iso-surface contours of the entrophy field, calculated using the mean subtracted velocity (prime) field, Ω' is plotted in figures 4.33 and 4.34. The mean subtracted velocity field is calculated by subtracting the mean velocity in the CVP plane (i.e a time average of each measurement run performed) from each y-z slice in the reconstructed volumes. Both figures incorporate a colormap which highlights only strong positive (red) and negative (blue) events, with the ones in between having the same colour (white). The iso-surface contours are

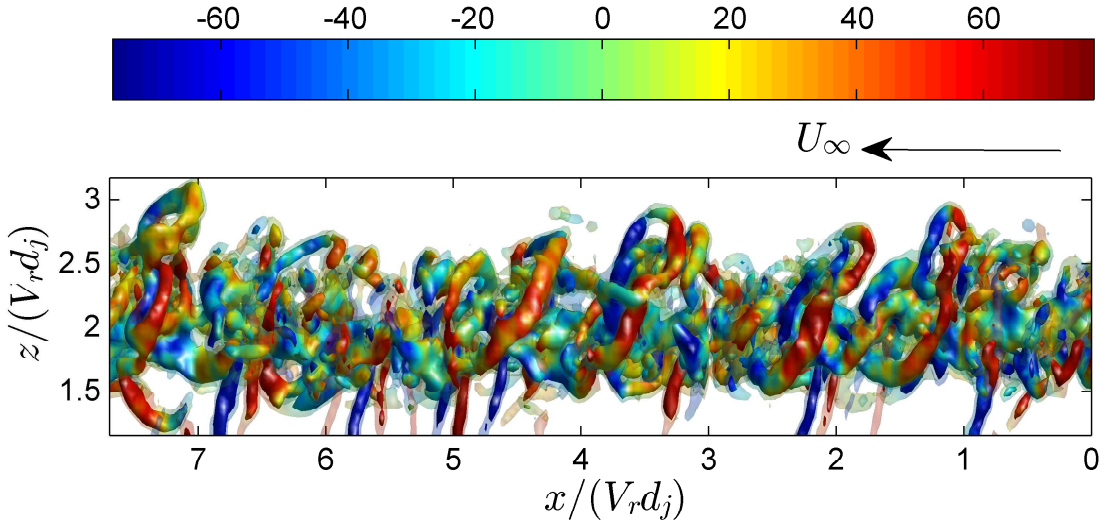

(a)

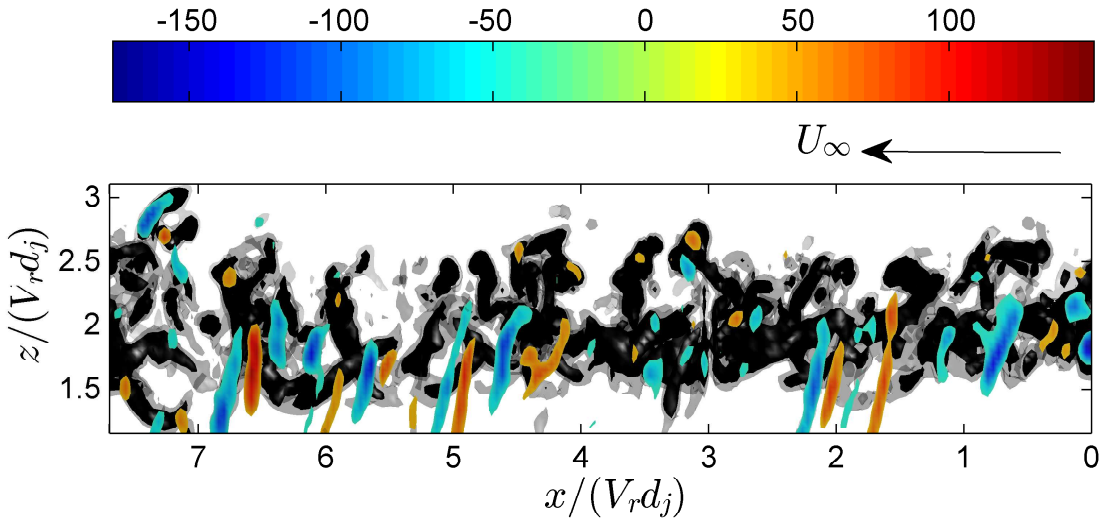

(b)

Figure 4.32: Volume 2 at $x/d_j = 30$: Visualisation of upright wake vortices from measurements at $x/d_j = 30$. (a) Iso-surfaces of $\Omega_{iso} = 0.1\Omega_{max}$ (solid) and $\Omega_{iso} = 0.05\Omega_{max}$ (transparent). Surface is coloured by the local value of $\omega_z(\mathrm{s}^{-1})$. (b) Cut through centre-plane of figure (a) showing contours of $\omega_z(\mathrm{s}^{-1})$ within the cut iso-surfaces (which are coloured black for clarity).

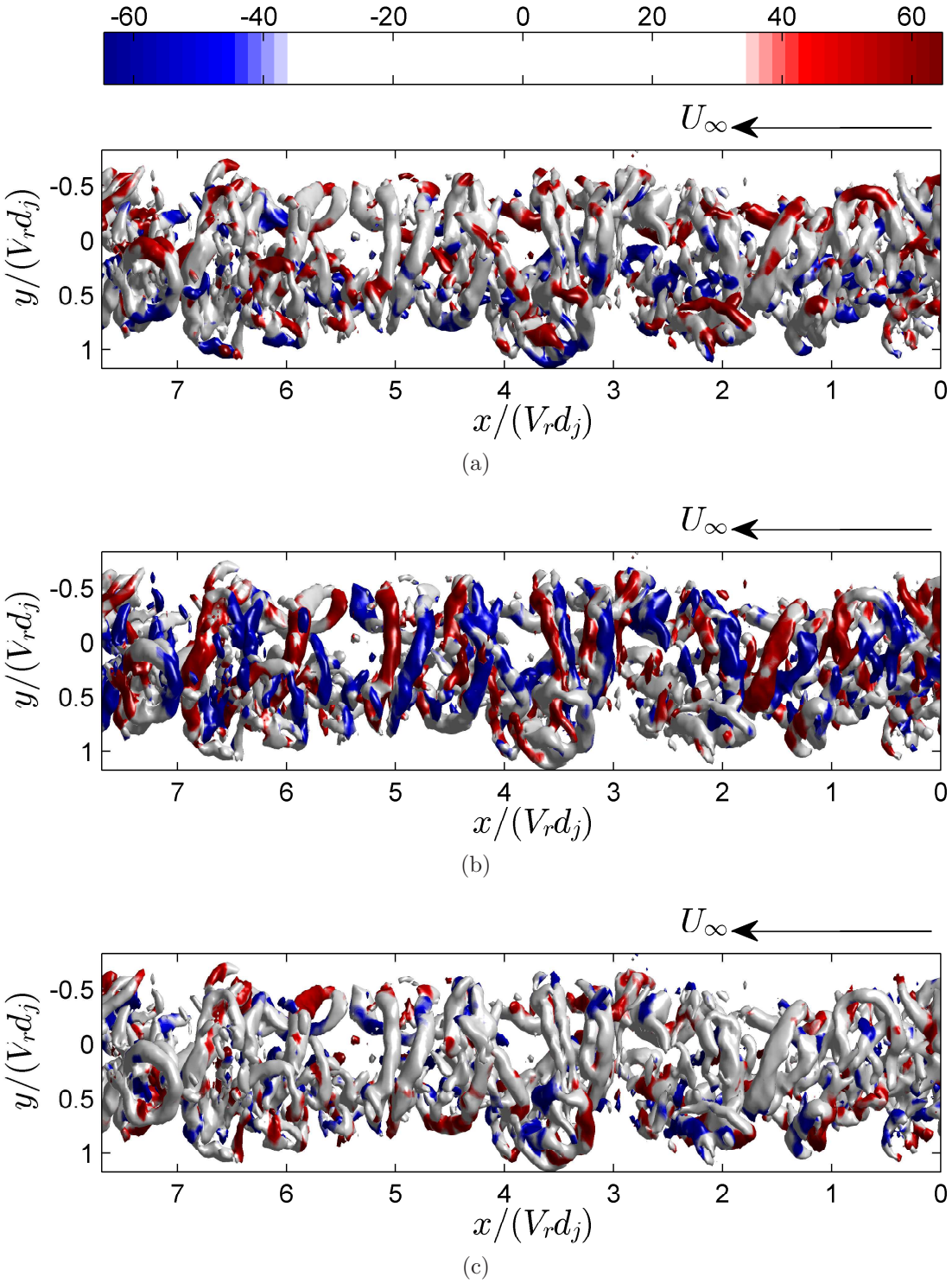

Figure 4.33: Volume 2 at $x/d_j = 30$: Visualisation of turbulent structures from measurements at $x/d_j = 30$. Top view of iso-surface contours of $\Omega'_{iso} = 0.10\Omega'_{max}$ coloured by the local value of (a) streamwise vorticity $\omega'_x(\mathrm{s}^{-1})$, (b) spanwise vorticity $\omega'_y(\mathrm{s}^{-1})$ and (c) wall-normal vorticity $\omega'_z(\mathrm{s}^{-1})$.

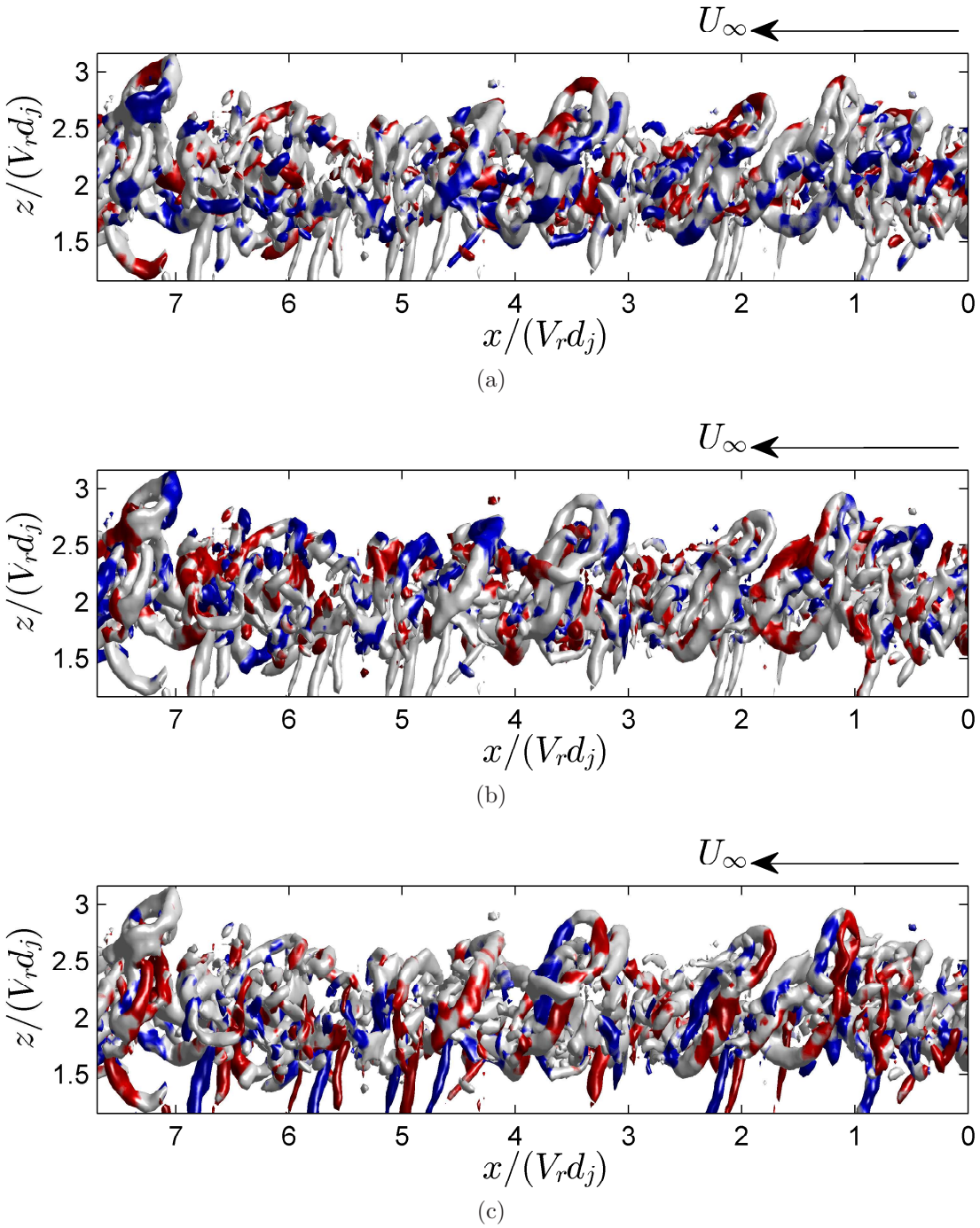

Figure 4.34: Volume 2 at $x/d_j = 30$: Visualisation of turbulent structures from measurements at $x/d_j = 30$. Side view of iso-surface contours of $\Omega'_{iso} = 0.10\Omega'_{max}$ coloured by the local value of (a) streamwise vorticity $\omega'_x(\mathrm{s}^{-1})$, (b) spanwise vorticity $\omega'_y(\mathrm{s}^{-1})$ and (c) wall-normal vorticity $\omega'_z(\mathrm{s}^{-1})$. Colormap is the same as that in figure 4.33.

calculated from the same velocity data used in figures 4.30 - 4.32 (Volume 2). Comparing the two figures showing the mean subtracted (prime) enstrophy field to the instantaneous one, the main difference is that the two cores are absent, with the windward and wake structures remaining.

Figures 4.33 and 4.34 show 3 top and side views of the volume thrice, each one having the iso-surfaces coloured by a different component of the vorticity vector, ω'_x, ω'_y and ω'_z. Figures 4.33a,c and 4.34a,c show that intense events of ω'_x and ω'_z are observed around the location of the cores where the legs of the hairpins end. These would induce all three velocity components u', v' and w' and explains the high rms velocities at the position of the cores. Figures 4.33b and 4.34b show the heads of the hairpins and rollers structures, alternating the sign of ω'_y which would induce an alternating sign of u' and w' component around the windward side of the jet. This explains the origin of the observed arch in the rms velocity contour plots connecting the two cores, and by extension the characteristic kidney shape of the CVP. This provides a mechanism for the shape of the rms profiles which has not been understood before. Furthermore since the structures are mainly aligned in the spanwise y-direction, they do not induce a v' component which explains the absence of an arch on the windward side in the $\sqrt{\overline{v'^2}}$ profiles. Finally figure 4.34c shows how the wake structures now have comparatively equal strength to the rest of the structures, appearing without the use of a second lower threshold being plotted. Given that they are observed to be positioned on the centreplane ($y = 0$) these would induce a u' and v' component in the area between the cores and the wake. This explains the contours of high rms velocity extending from and around the centreplane between the cores down into the wake in the $\sqrt{\overline{v'^2}}$ profiles, and to a lesser extent (lower rms velocity contours values) in the $\sqrt{\overline{u'^2}}$ profiles. This difference between the $\sqrt{\overline{v'^2}}$ and $\sqrt{\overline{u'^2}}$ profiles can be explained by to the interaction of the alternating ω'_z sign wake vortices. The wake structures interact to induce strong events of v' in the region between two opposite ω'_z signed vortices (similar to the large upwash in-between two counter-rotating vortices). The u' component is induced on the side of these structures where the interaction between the wake structures of alternating sign causes the induced velocity to reduce in strength.

The results from the measurements in the far field at $x/d_j = 85$ are now

analysed. Figure 4.35 shows a Taylor reconstruction of the enstrophy field with the iso-surfaces coloured by the value of the local streamwise vorticity covering approximately half a large-scale eddy turn-over time. Once again the two cores are visible. The cores become more clear by looking at the side and bottom views of the volume in figure 4.36. The bottom view in figure 4.36b shows how, when compared to the results at $x/d_j = 15$ and 30, the cores of the CVP seem to meander more about the $y = 0$ centre-plane.

The isometric and the side views show the presence of the spanwise windward structures. These become more clear by re-plotting the iso-surfaces in figure 4.35 but coloured by the local value of the spanwise vorticity ω_y in figure 4.37. Similar features to the data at $x/d_j = 30$ are observed with the windward structures aligned in the spanwise y-direction and alternating in sign with downstream distance. This shows that the hairpins and rollers generated in the near field persist well into the far field of the cross-flow jet and retain a surprising regularity in their relative positions. A top view shows this more clearly in figure 4.38a. As noted previously, the cores seem to meander more around the centre-plane and the top view shows how the windward structures follow the cores. This is consistent with the observation that the cores of the CVP are actually the tails of the hairpins structures generated in the near field. Figure 4.38b shows a cut through the centre-plane ($y = 0$) with contours of the spanwise vorticity component ω_y plotted showing how, like the results at $x/d_j = 30$, the hairpin heads and roller structures are at approximately the same wall-normal height. Note that the contours of ω_y between $x/(V_r d_j) = 7 - 10$ in the figure around the position of the cores ($z/(V_r d_j) = 2.7$) are from the cut through the cores due to them meandering through the centre-plane at these x-locations.

The results show that the structures at $x/d_j = 85$ appear to be less coherent when compared to those at $x/d_j = 30$, which is to be expected as we are moving further downstream. It is clear however that footprints of the hairpins and rollers do persist well into the far field and are observed throughout all of the reconstructions made from this measurement location. The degree of coherence is of course Reynolds number dependent. Similarly to the results at $x/d_j = 30$, there are expectedly less clear observations of the hairpin legs attaching to the tails (i.e the CVP core) or their interaction with each other but instances of them

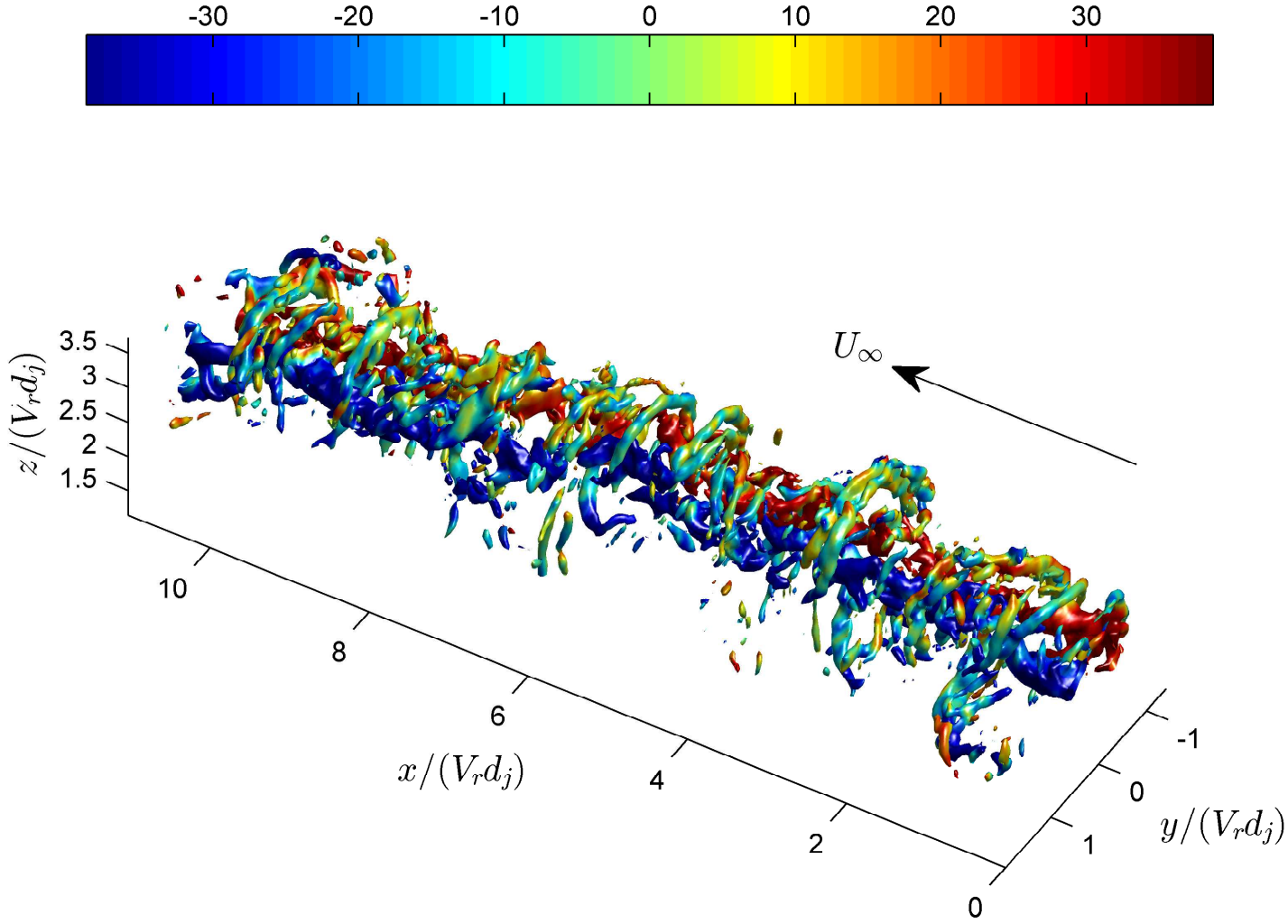

Figure 4.35: Volume 1 at $x/d_j = 85$: Enstrophy field structures. Iso-surfaces of $\Omega_{iso} = 0.1\Omega_{max}$. Surface is coloured by the local value of streamwise vorticity $\omega_x(\mathrm{s}^{-1})$.

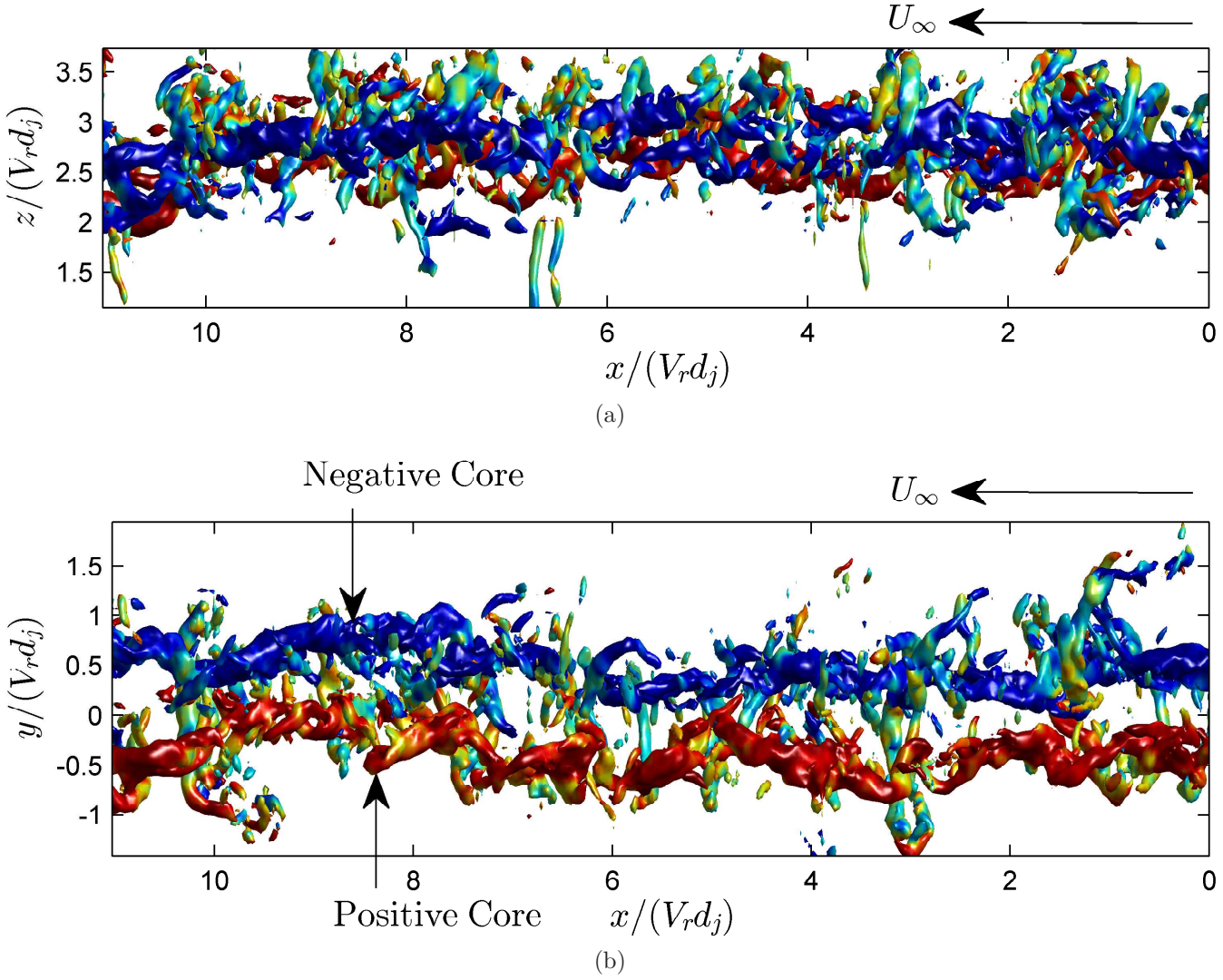

Figure 4.36: Volume 1 at $x/d_j = 85$: (a) Side and (b) Bottom view of figure 4.35. Iso-surfaces of $\Omega_{iso} = 0.1\Omega_{max}$. Surface is coloured by the local value of $\omega_x(\mathrm{s}^{-1})$.

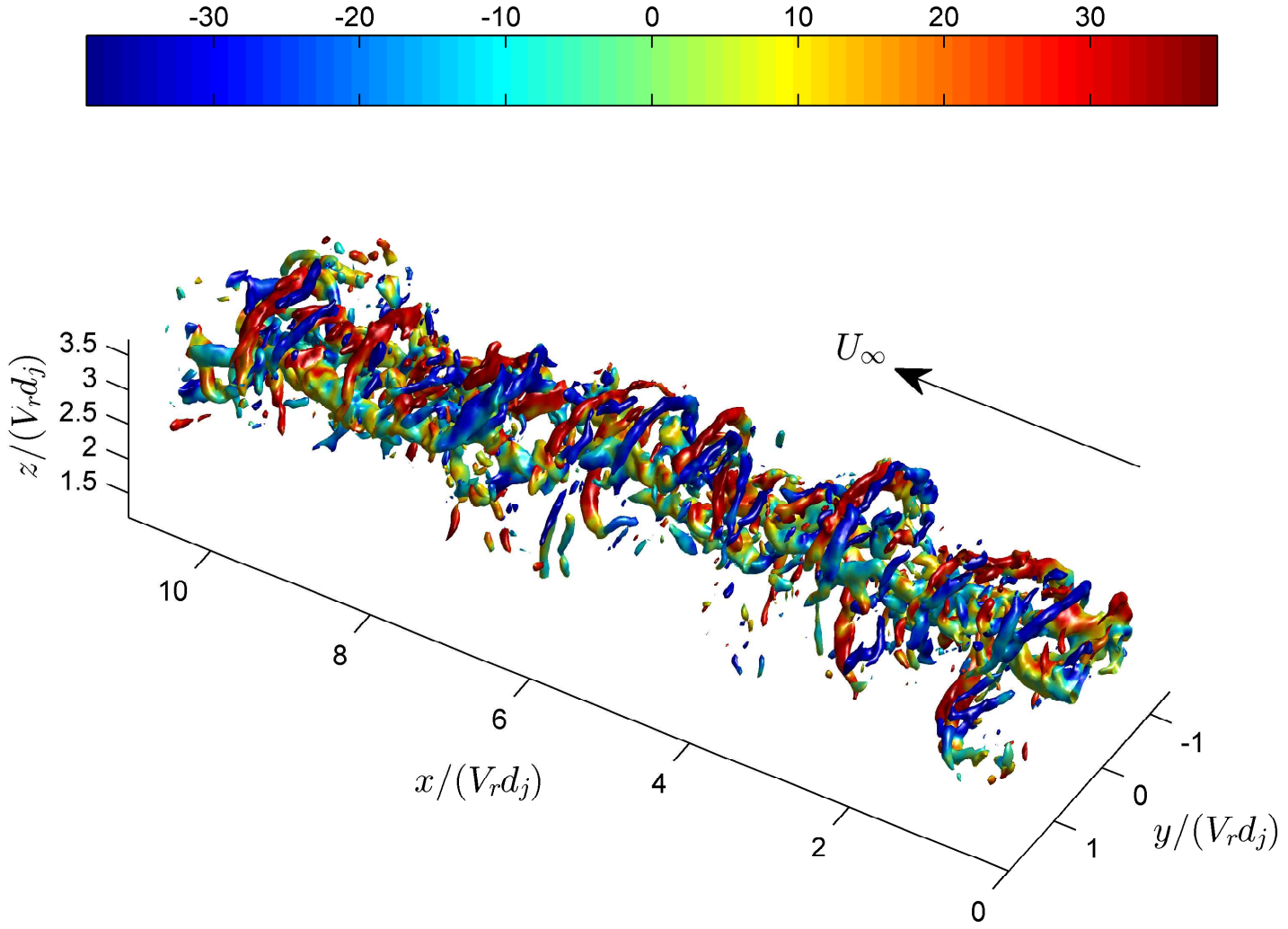

Figure 4.37: Volume 1 at $x/d_j = 85$: Enstrophy field structuresfrom Taylor reconstruction showing the persistence of spanwise windward structures well into the far field. Iso-surfaces of $\Omega_{iso} = 0.1\Omega_{max}$. Surface is coloured by the local value of spanwise vorticity $\omega_y(\mathrm{s}^{-1})$.

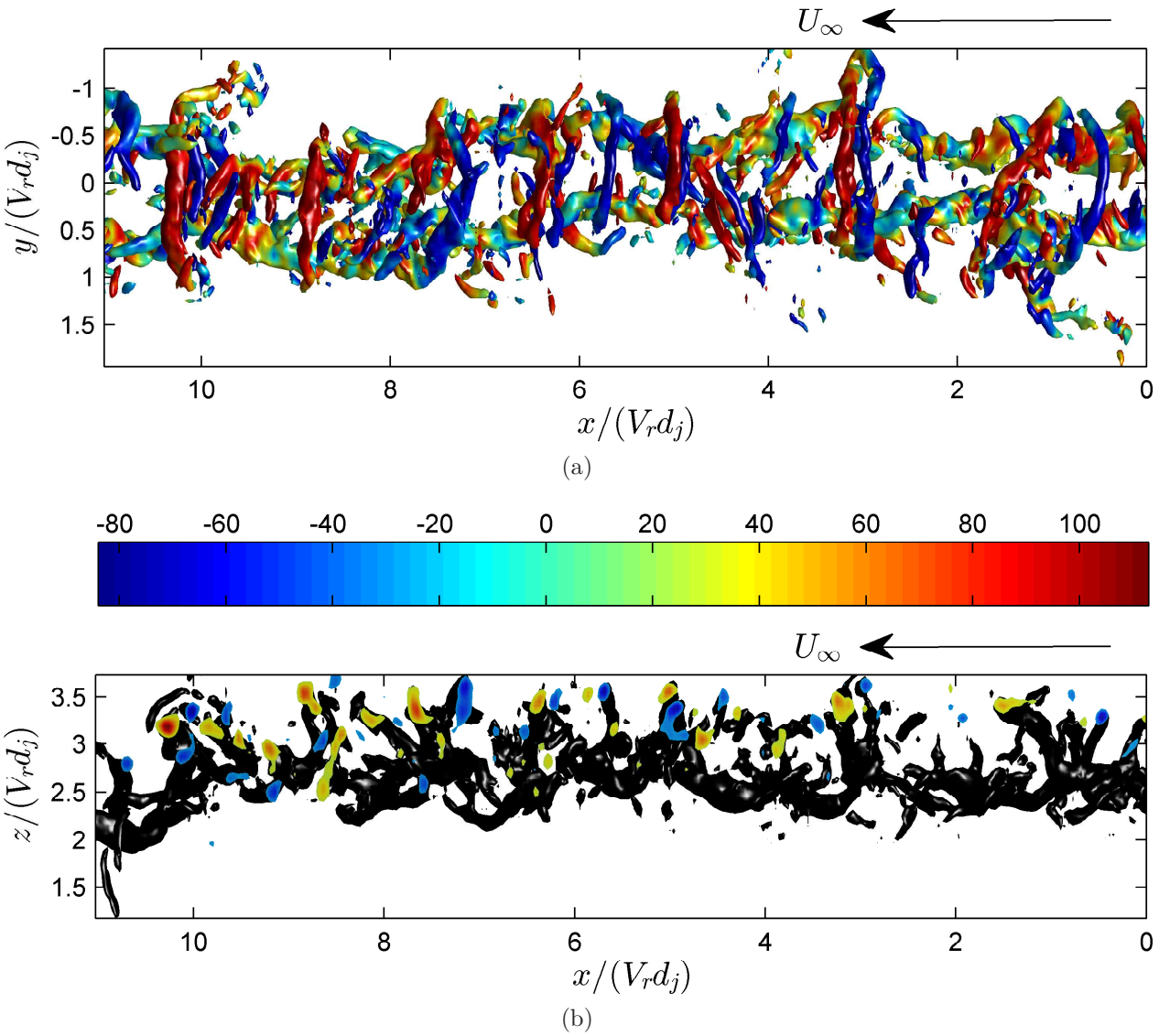

Figure 4.38: Volume 1 at $x/d_j = 85$: (a) Top view of figure 4.37 ($\Omega_{iso} = 0.1\Omega_{max}$). (b) Cut through centre-plane ($y = 0$) of (a) showing contours of $\omega_y(\mathrm{s}^{-1})$ within the cut iso-surfaces (coloured black for clarity).

can be observed. Figure 4.39 shows another reconstruction illustrating this. The structures here are a bit more clear allowing for their shape to be analysed in more detail. Once again the same pattern is observed on the windward side with the alternating hairpin heads and rollers. The two instances of the hairpin being attached or detached, as observed at $x/d_j = 30$, are annotated on the figure. The detached hairpin head has its legs detached from its tail, which is part of the CVP core, whereas the attached one has its leg still attached. The top and side views of the volume in figure 4.40 show that the apart from this difference between the two, the attached hairpin has its legs swept forward is it goes down and upstream and attaches to the CVP core. The detached hairpin head though has it's leg facing downwards, perpendicular to the streamwise direction appearing more similar to the roller structures, spanning the width of the two cores in an arch shape.

The side view in figure 4.36a and 4.40b shows that the wake structures also appear far downstream. As was illustrated with structures upstream, figure 4.41 shows a side view of the volume in figure 4.39 with the iso-surface coloured by the local value of the wall-normal vorticity component ω_z. A second lower threshold is needed to reveal the weaker wake structures, as was observed for the measurements further upstream. The pattern of the wake structures alternating the sign of ω_z with downstream distance continues indicating that the structures observed further upstream persist well downstream (at least until $x/d_j = 85$). The cut through the centre-plane shows that the wake vortices still extend from the area between the cores down into the wake, but their angle here seems to be perpendicular to the streamwise direction. Figure 4.42 shows a front view of the volume, with only the lower iso-contour value plotted, showing, the wake structures in the middle of the CVP. As shown in the cut through the centre plane in figure 4.41b the wake structures seem to almost start from the windward side of the jet and extend down into the wake.

Finally, the reconstructed volumes at the three measurement locations are combined together in such a way so as to show a pseudo-spatial representation of the instantaneous structure of the cross-flow jet in figure 4.43. The aim is to cover approximately one large scale eddy turnover time from each measurements position and combine the results to produce a single instantaneous example of

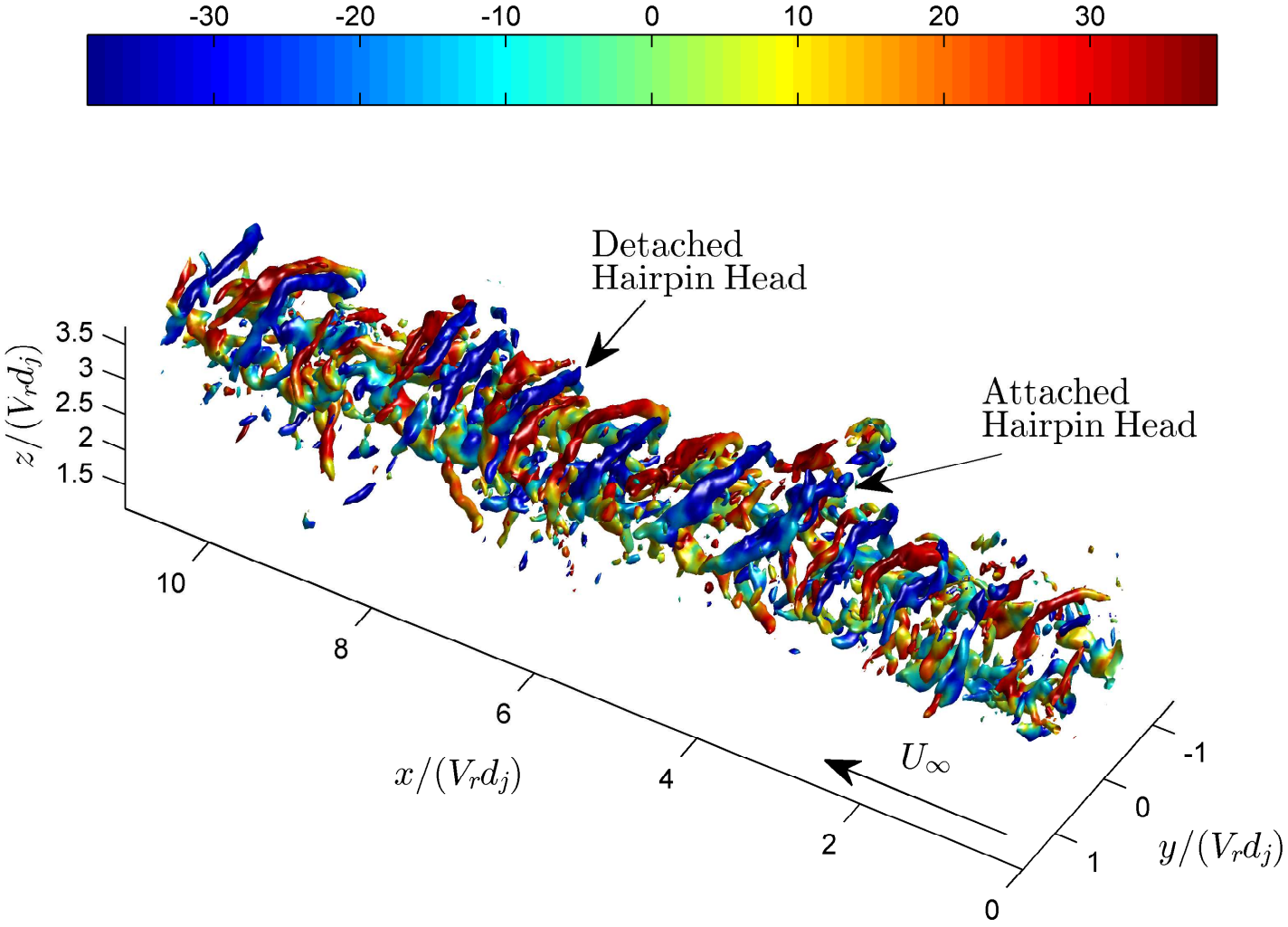

Figure 4.39: Volume 2 at $x/d_j = 85$: Enstrophy field structures from a different Taylor reconstruction showing the footprints of the hairpin and roller structures generated in the near field. Iso-surfaces of $\Omega_{iso} = 0.1\Omega_{max}$. Surface is coloured by the local value of spanwise vorticity $\omega_y(\mathrm{s}^{-1})$.

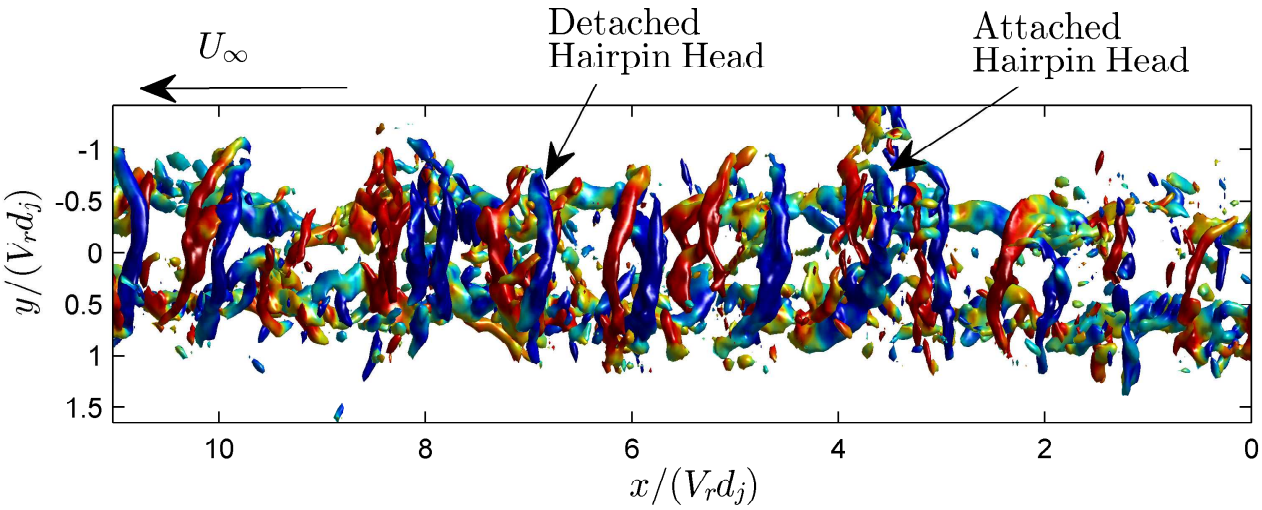

(a)

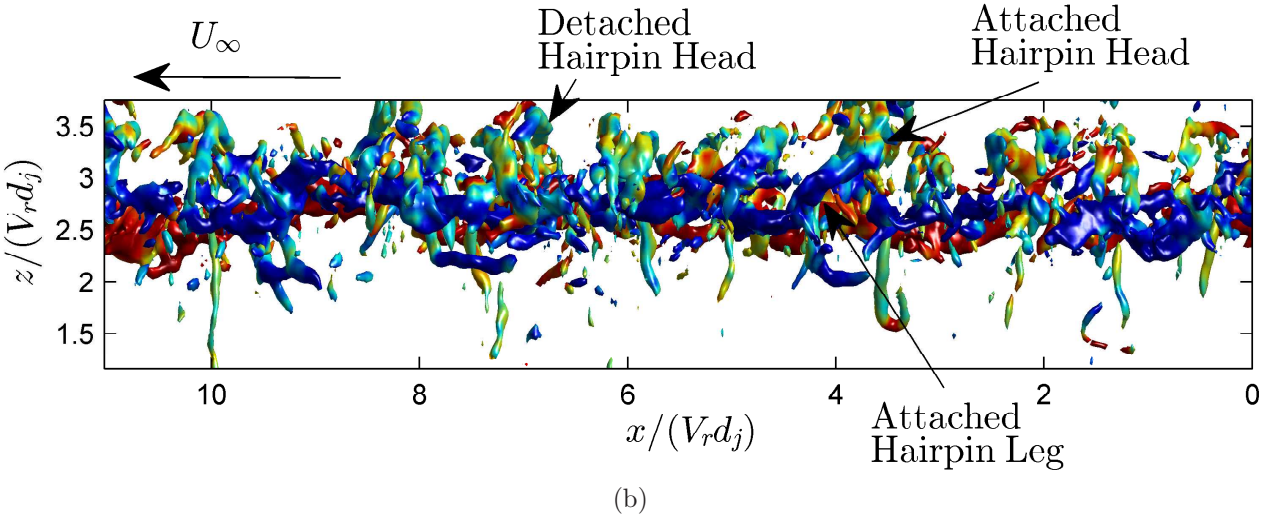

(b)

Figure 4.40: Volume 2 at $x/d_j = 85$: Top and side view visualisation of figure 4.39 showing attached and detached hairpin heads ($\Omega_{iso} = 0.1\Omega_{max}$). (a) Top view coloured by local value of $\omega_y(\mathrm{s}^{-1})$. (b) Side view coloured by local value of $\omega_x(\mathrm{s}^{-1})$.

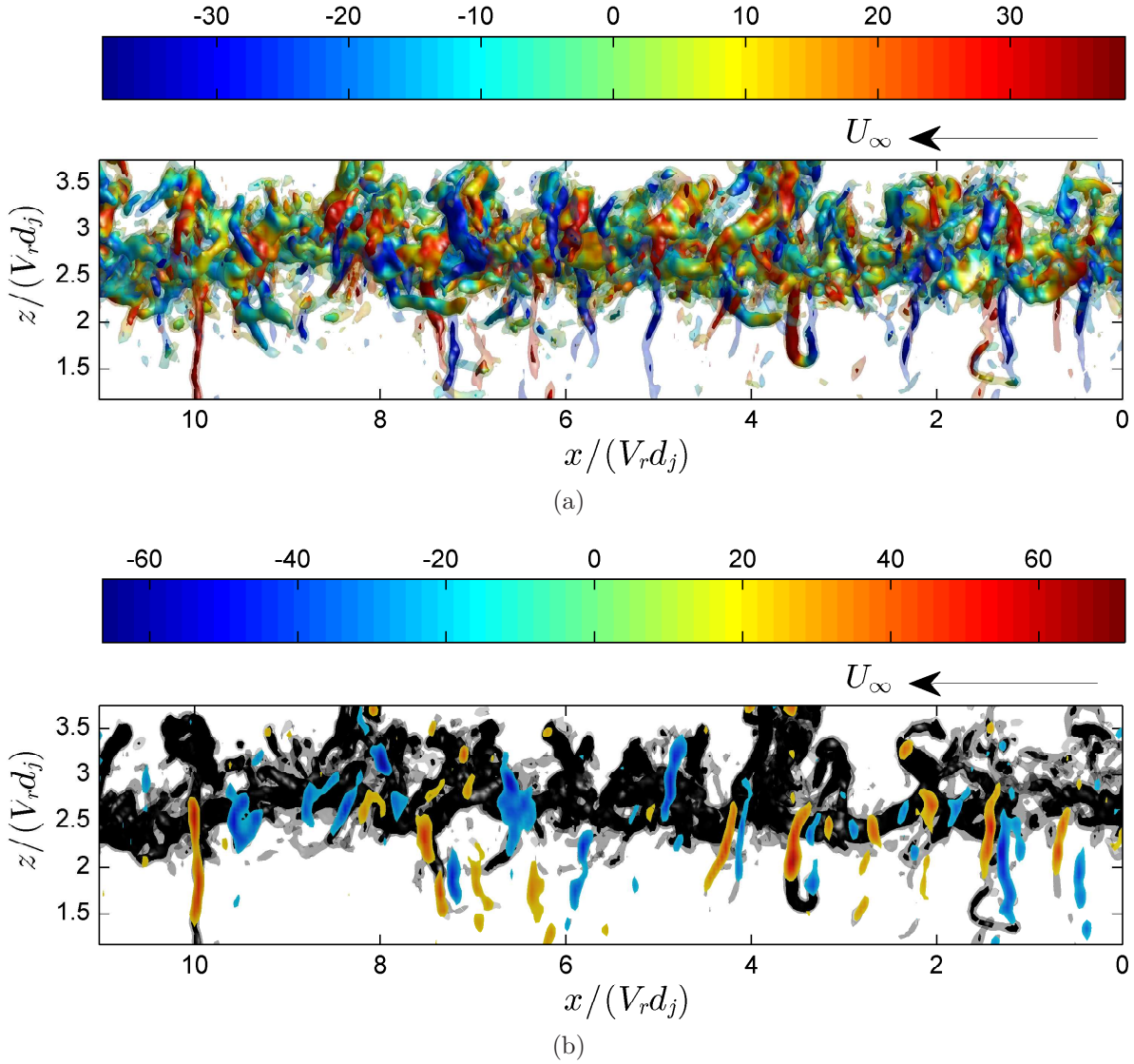

Figure 4.41: Volume 2 at $x/d_j = 85$: Side view visualisation showing wake structures. (a) Side view coloured by local value of $\omega_z(\mathrm{s}^{-1})$. Solid iso-surfaces $\Omega_{iso} = 0.1\Omega_{max}$. Transparent iso-surfaces $\Omega_{iso} = 0.05\Omega_{max}$. (b) Cut through the centre-plane (y = 0) of (a) showing contours of $\omega_z(\mathrm{s}^{-1})$ within the cut iso-surfaces (coloured black).

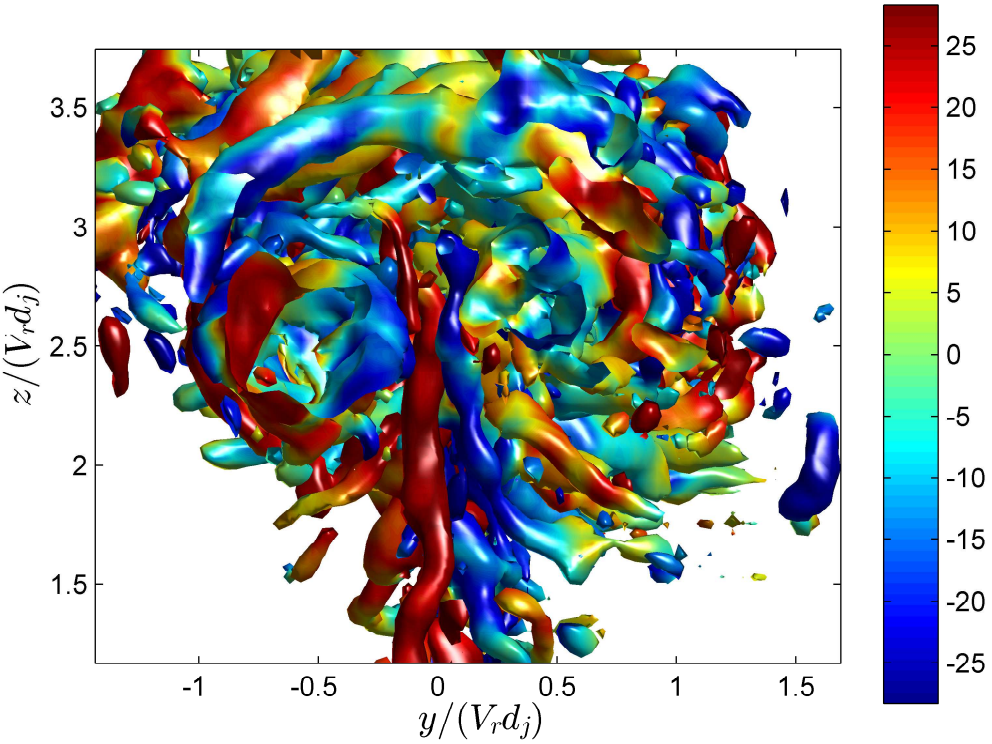

Figure 4.42: Volume 2 at $x/d_j = 85$: Front view visualisation of the CVP showing the wake structures extending from the CVP down into the wake. Iso-surfaces of $\Omega_{iso} = 0.05\Omega_{max}$ coloured by the local value of $\omega_z(\mathrm{s}^{-1})$.

the cross-flow jet. In the figure structures are reconstructed between $x/(V_r d_j) = 1.5-2.5$ using data from the measurements at $x/d_j = 15$, between $x/(V_r d_j) = 3-8$ using data from the measurements at $x/d_j = 30$ and between $x/(V_r d_j) = 8.5-13.5$ using data from the measurements at $x/d_j = 85$. The jet trajectory, as was calculated in the previous chapter using the fit suggested by Pratte & Baines [53], is shown in the figure as a solid black line. The gaps between the reconstructions are purposly left in order to distinguish their measurement location origin. Side and bottom views of the figure are shown in figure 4.44. These views show that the cores of the CVP are a prominent feature of the cross-flow jet, but the windward structures appear to be equally prominent and hence important feature.

Figure 4.45 shows the same reconstruction of the cross-flow jet as in figure 4.43, but with the iso-surfaces coloured by the local value of spanwise vorticity ω_y to emphasize the hairpin/roller structure. The figure shows how, as was noted before, the alternating sign windward structures persists far downstream and are hence an important feature of the cross-flow jet. A top view of the figure can be found in figure 4.46 showing them more clearly and how they evolve downstream.

4.4 Conditional Averaging

With the structures at all three downstream measurement locations studied a clearer picture about the large scale structure of the cross flow jet emerges. There are three main structures observed, the forward swept hairpins whose tails form the cores of the CVP, the rollers on the windward side of the jet occurring in between consecutive hairpin heads, and the wake vortices in the wake. However, these are observations made from a visual inspection of the reconstructed three-dimensional data volumes. Although the structures mentioned are relatively clear in the reconstructions due to their repeatable nature, and explain the mean statistical results in the previous chapter, their importance in producing the mean turbulence properties can be verified by looking at the conditionally averaged structure of the flow. This would confirm that these observed structures represent the 'average' flow structures appearing at the respective downstream positions and are not simply random events. In addition, this will provide some

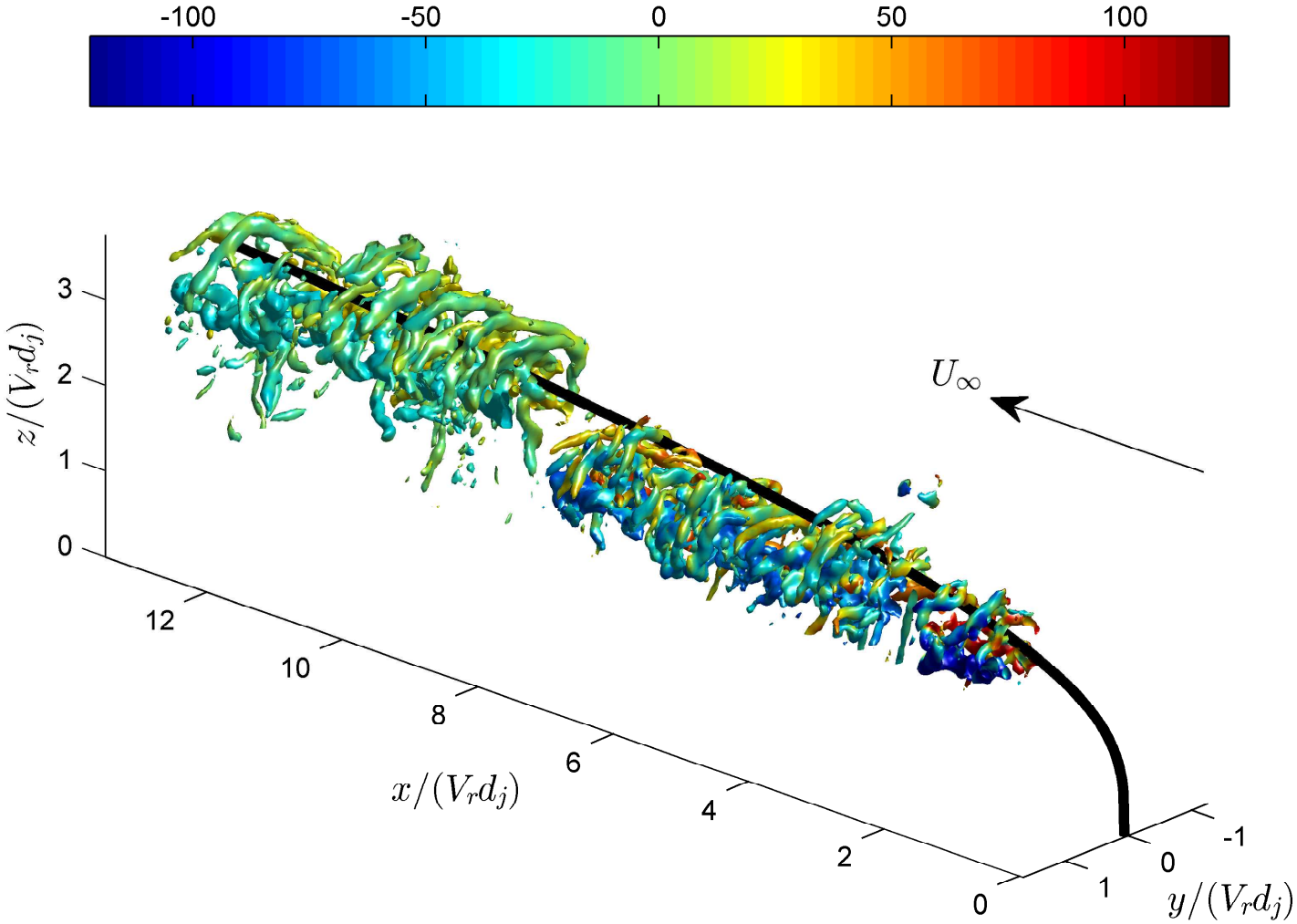

Figure 4.43: Enstrophy field structures of the cross-flow jet using data from all three measurement locations. Iso-surfaces of $\Omega_{iso} = 0.1\Omega_{max}$ at each downstream measurement location. Surface is coloured by the local value of streamwise vorticity $\omega_x(\mathrm{s}^{-1})$. Solid black line represents the jet trajectory as was calculated in the previous chapter

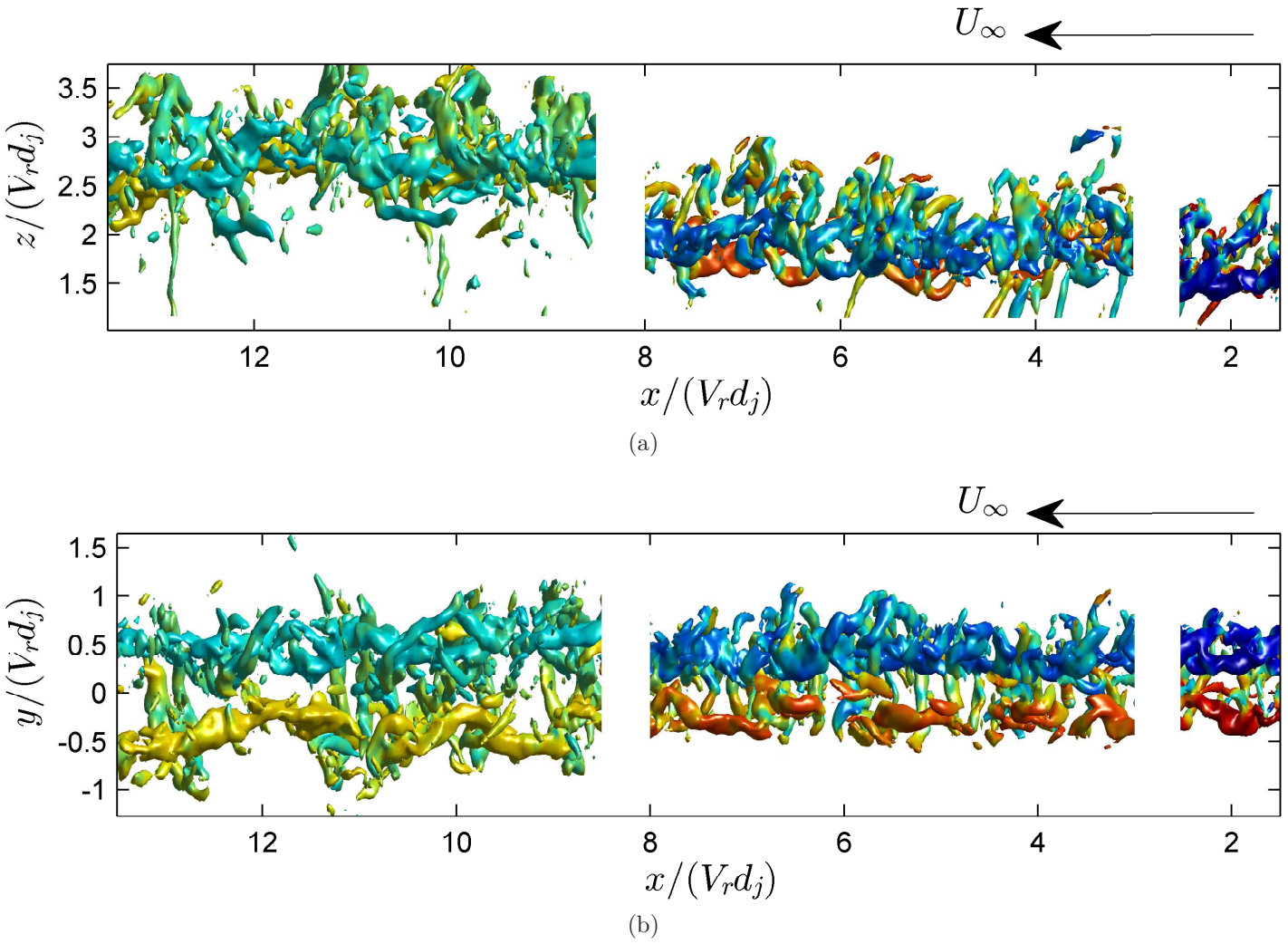

Figure 4.44: (a) Side and (b) Bottom view of figure 4.43 ($\Omega_{iso} = 0.1\Omega_{max}$). Iso-surfaces coloured by local value of $\omega_x(\mathrm{s}^{-1})$. Solid black line showing trajectory was removed for brevity.

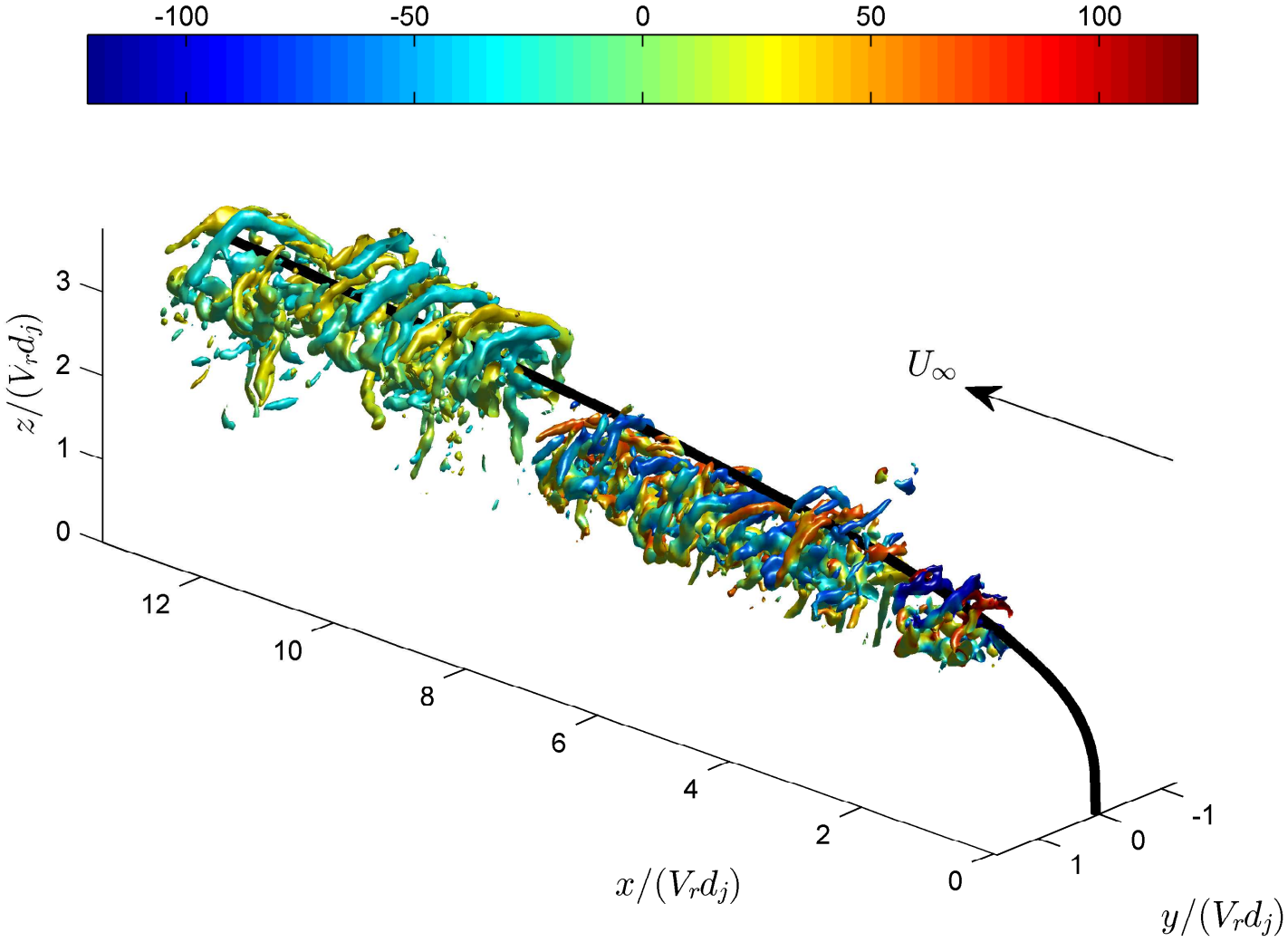

Figure 4.45: Enstrophy field structures of the cross-flow jet using data from all three measurement locations. Iso-surfaces of $\Omega_{iso} = 0.1\Omega_{max}$ at each downstream measurement location. Surface is coloured by the local value of streamwise vorticity $\omega_y(\mathrm{s}^{-1})$. Solid black line represents the jet trajectory as was calculated in the previous chapter

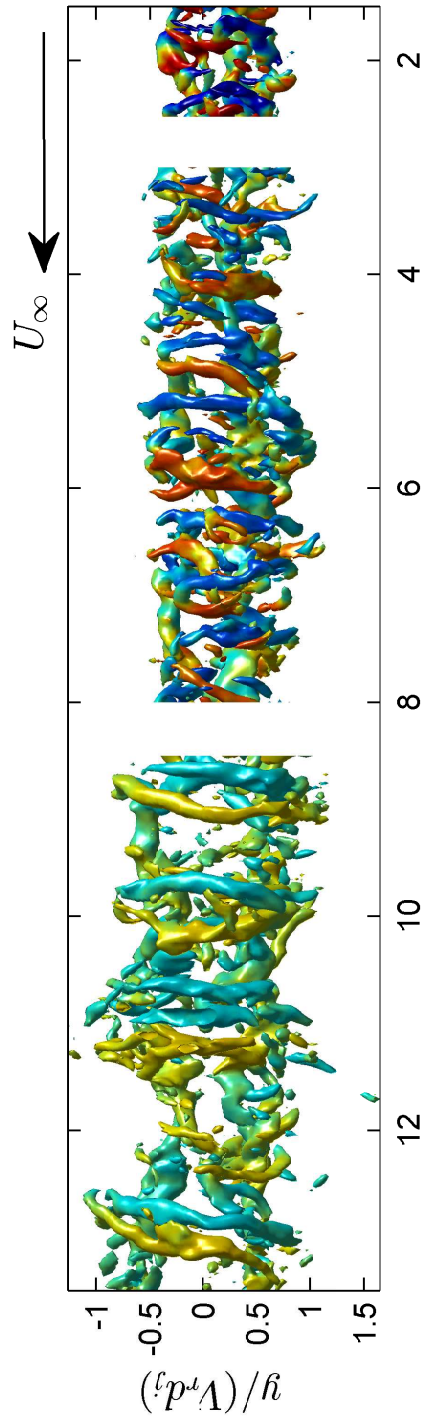

Figure 4.46: Top view of figure 4.45 ($\Omega_{iso} = 0.1\Omega_{max}$). Solid black line showing trajectory was removed for brevity.

insight into the average shape of the structures.

4.4.1 Procedure

The technique of conditional averaging, also known as conditional sampling, has been used by a large number of studies of turbulent flows. A description and a historical overview of the technique is given by Antonia [4]. As the name suggests, the technique produces a 'conditional average' obtained over an ensemble of events, selected based on the condition chosen. Given that the same condition is used for all events in the ensemble, the definition given by Blackwelder [7] arises as 'an ensemble average taken over many similar events'. Blackwelder [7] extends this definition to describe the technique as a special type of cross-correlation, where the data signal (which is to be conditionally average) is cross-correlated with a similar-events, or condition, signal. This study follows the approach used by Dennis & Nickels [18] who reconstructed 3D flow fields using Taylor's hypothesis from High-Speed Stereoscopic PIV measurements in a turbulent boundary layer. The definition given by the authors for the conditional average (which best applies here) is 'the ensemble average of a *selection* of the PIV fields'. The word selection is highlighted by the authors as it pin-points the main idea behind using conditional averaging. Only the PIV fields that meet a given condition, for example the velocity field around a strong vorticity event aligned in a given direction, are selected and added to the ensemble to be averaged. The same approach is used in the procedure to be performed here. Sub-regions of the three-dimensional reconstructions are extracted which satisfy the condition set forming an ensemble of sub-volumes which are averaged to produce the conditional-average. It should be noted that regardless of the condition used, it is always the velocity field that is extracted, stored and then averaged. From this conditionally averaged field other quantities can then be plotted.

Hayakawa [28] defines two 'implicit working rules' that are required in order to obtain a meaningful conditional average, which are repeated here, as: (a) the existence of identifiable, recurrent flow events and (b) the selection of similar events through conditioning. The first rule is perhaps the most important one when it comes to the results of the conditional averaging being subjective. In the case of

a perfectly random field, since the procedure creates an ensemble of events based on a condition, any pattern can be found given a large number of random field samples. The results from the conditional average is therefore not meaningful. Meeting the first rule though would make the results more meaningful and less subjective. The second rule refers to the use of the correct condition to extract the event/pattern under inspection. The first rule is clearly met, as was shown in the figures in section 4.3.5, with the recurrent hairpins, rollers and wake structures observed. For the second rule, given that three different structures are observed, different conditions will be used and depend on the event under inspection. Figure 4.47 illustrates how the procedure is carried out. The plot shows iso-contours of swirl λ_{ci} with an iso-value of $\lambda_{ci,iso} = 0.21\lambda_{ci,max}$. A search-area is selected, within which the condition of interest is searched for. This is indicated by the green transparent box. If the condition is met, then the velocity field around this position is extracted and stored. The sub-volume extracted is indicated by the yellow transparent box. The size of the sub-volume (yellow box) extracted is varied based on what structure is being conditioned, but is kept constant for the selected conditioning variable.

It is important to note that interpreting conditional averaged flow fields has to be done with care. With the explanation of the overall procedure above, it should come as no surprise that the event was conditioned will appear in the conditional averaged flow field. For example if the conditioning variable to be used was a strong value of spanwise swirl $\lambda_{ci,y}$, the result of a spanwise vortex tube appearing in the conditional averaged flow field provides no further physical insight into the flow structure. What should be examined is the appearance of an event not related to the condition set, e.g an wall-normal vortex tube. An example would be the results of Dennis & Nickels [18] who conditioned on events of strong spanwise swirl in a turbulent boundary layer, with the resulting averaged volumes revealing hairpin structures seating on top of low momentum fluid. This is best illustrated by the conditions set to extract the hairpin and roller structures mentioned. Since conditional averaging was only performed after analysis of the instantaneous reconstructions, the experiment was not optimised with conditional averaging in mind, specifically for the number of samples the can be extracted.

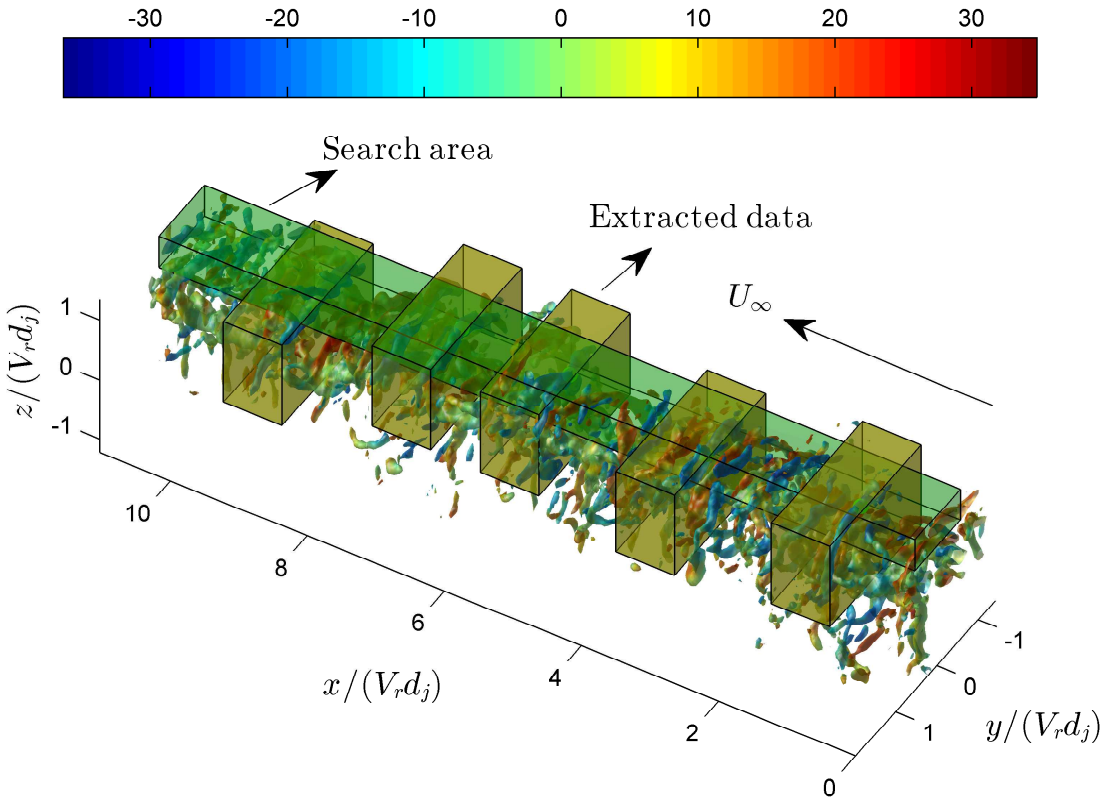

Figure 4.47: Example of the conditional averaging procedure. Plot shows the swirl field with iso-surface contours of $\lambda_{ci,iso} = 0.21\lambda_{ci,max}$. Green transparent box indicates search area. Yellow transparent boxes indicate selected vector field sub-volumes.

4.4.2 Conditioning for the Hairpin Structures

To find a suitable criterion to condition for hairpins, a cartoon of the hairpin structure is shown in figure 4.48. A number of conditions can be used in order to average. The streamwise velocity can be used, as high speed regions are created inside the hairpin head and legs as was shown in figure 4.22 and 4.23. Another condition could be vorticity, which is what was used to visualize the hairpins. One of the most striking features observed in the instantaneous enstrophy fields

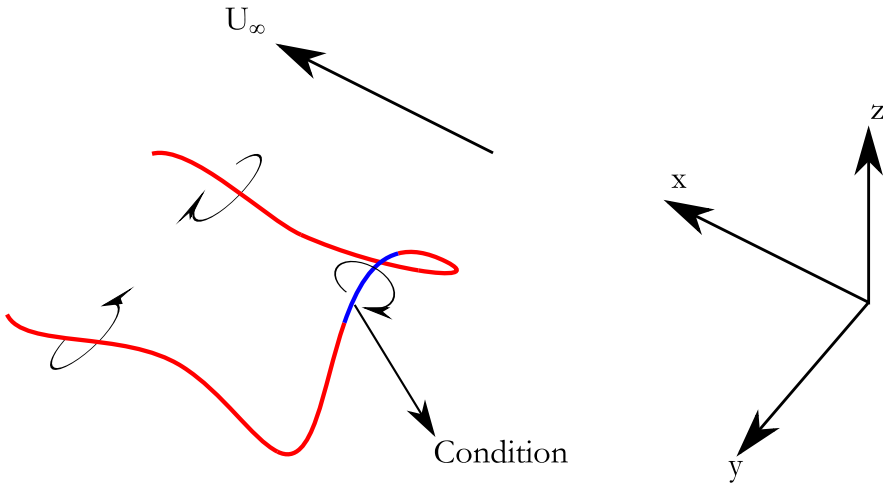

Figure 4.48: Cartoon of the hairpin structure. Blue part shows the head of the hairpin which has negative spanwise vorticity ω_y.

was the degree of organisation of the windward structures aligned in the spanwise direction. The structures with a negative spanwise vorticity component ω_y were observed to be part of the the hairpin structure, specifically the hairpin head, which is highlighted in the cartoon. One could therefore condition for strong negative spanwise vorticity, i.e the head of the hairpin (the blue part of the cartoon). The technique however is susceptible to noise as the vorticity condition does not distinguish between rotation and shear. Given that the condition is set for the detection of strong negative spanwise rotation, perhaps a more sensible choice would be that of strong negative spanwise swirl $\lambda_{ci,y}$, which is the condition used. The search area was centred around the windward side of the jet and the width and height of the sub-volume extracted was large enough to contain the

whole of the CVP, i.e the cores, part of the wake and the windward side, as shown in figure 4.47.

As was mentioned earlier, new physical insight is gained by applying this procedure from the unexpected part of the resulting conditionally average flow field. Therefore it is important to discuss what is expected. If we condition on spanwise vorticity a vortex tube aligned in the spanwise direction is expected. The length of the tube is unknown, but based on the observations in the instantaneous enstrophy fields, it would have a maximum length approximately equal to the CVP core separation. Furthermore the two cores of the CVP would also appear as they are always present and dominate the flow field. What will be interesting is the part, or parts, which deviate from this prediction. In the case of the hairpins, if they do represent the average structure, then we expect to see the legs appearing as well, which were not conditioned for. Table 4.8 summarises the properties of the conditional averaged volumes and resulting structures. The structures emerging from each downstream measurement location are analysed individually next.

Table 4.8: Summary of properties of the conditionally averaged hairpin structures

x/d_j	No. of Volumes	Leg Angle
15	56	114°
30	100	122°
85	168	114°

The conditionally averaged volume from an ensemble of 56 volumes from the measurements at $x/d_j = 15$ is shown in figure 4.49. The spanwise vortex tube together with the cores of the CVP are observed as expected in figure 4.49a. However a number of other structures are also observed. The hairpin head (which was conditioned for) is connected to the cores of the CVP by the hairpin legs which are slightly swept forwards in the downstream direction. This is consistent with the observations made in the instantaneous reconstructions that, on average, the windward structures are actually the heads of forward swept hairpins. A roller structure with a positive spanwise swirl component is observed in front and slightly below the hairpin head, which was also observed in the instantaneous

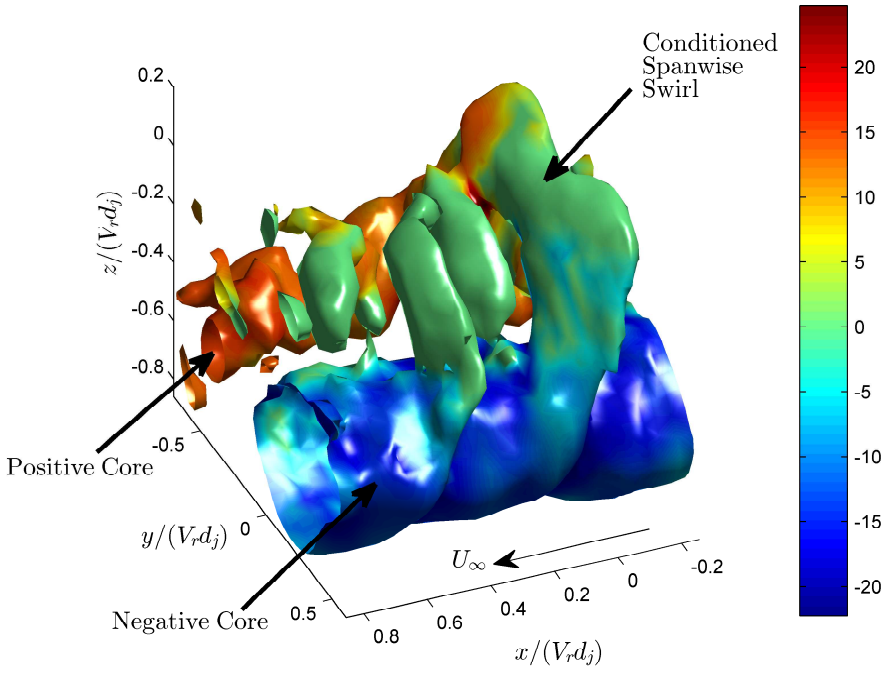

(a)

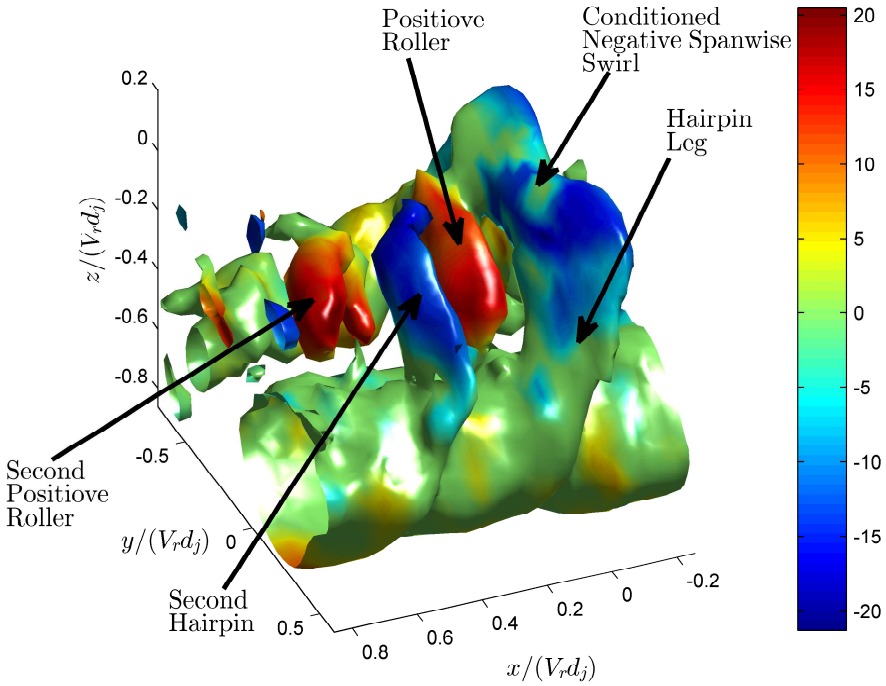

(b)

Figure 4.49: Conditionally averaged hairpin structure at $x/d_j = 15$. Iso-surfaces of $\lambda_{ci,iso} = 0.1\lambda_{ci,max}$. Surfaces coloured by the local value of (a) $\lambda_{ci,x}(\mathrm{s}^{-1})$ and (b) $\lambda_{ci,y}(\mathrm{s}^{-1})$.

fields. This structure was not conditioned for, but appears in the conditionally averaged field indicating that it consistently appears at this relative position to the conditioned hairpin structure. Furthermore, the hairpin-roller structure is repeated in the conditionally average field as a second pair is observed further downstream, although it is weaker in strength. This indicates that the hairpin-roller structure is organised in a regular fashion at $x/d_j = 15$. Given the near field dynamics of the cross-flow jet, this does not come as a big surprise as the the downstream position of $x/d_j = 15$ for a $V_r = 10$ jet can still considered as being in the 'near-field', but close to the branch point which denotes the far field according to Smith & Mungal [58].

Figure 4.50 shows a side view of the hairpin structure, showing the forward swept hairpin and the relative position of the roller structure more clearly. The side view in figure 4.50a reveals a third positive roller structure behind, i.e upstream, of the hairpin. This is most probably from a hairpin roller structure upstream of the conditioned hairpin. A slice through the centre plane in 4.50b shows the relative positions of the negative hairpin heads and positive rollers, with the rollers approximately a distance of $0.14V_r d_j$ below the hairpin heads. The roller structures that appear, which were not conditioned for, seem to be much weaker compared to the conditioned hairpin. This is to be expected as the flow is turbulent and not perfectly periodic so some degree of jitter in the relative positioning of the structures exists. The averaging procedure will decrease the strength of the appearing structures which were not conditioned for. However it should be noted that this may also be due to the fact that there is a limited number of volume samples. A slice through the negative core in figure 4.50c shows the leg of the hairpin and how its swept forward at an angle to the free stream direction. The angle of the hairpin leg to the free-stream direction (x-axis), indicated by the dashed lines, is approximately 114°.

The results from the conditionally averaging procedure applied to the data from the measurements at $x/d_j = 30$ are presented below. Figure 4.51 shows the conditionally averaged volume produced from an ensemble of 100 volume samples. Once again the spanwise (negative) vortex tube together with the cores of the CVP are observed as expected in figure 4.51a. The part which is not expected is the leg of the hairpin extending from the head (the negative spanwise

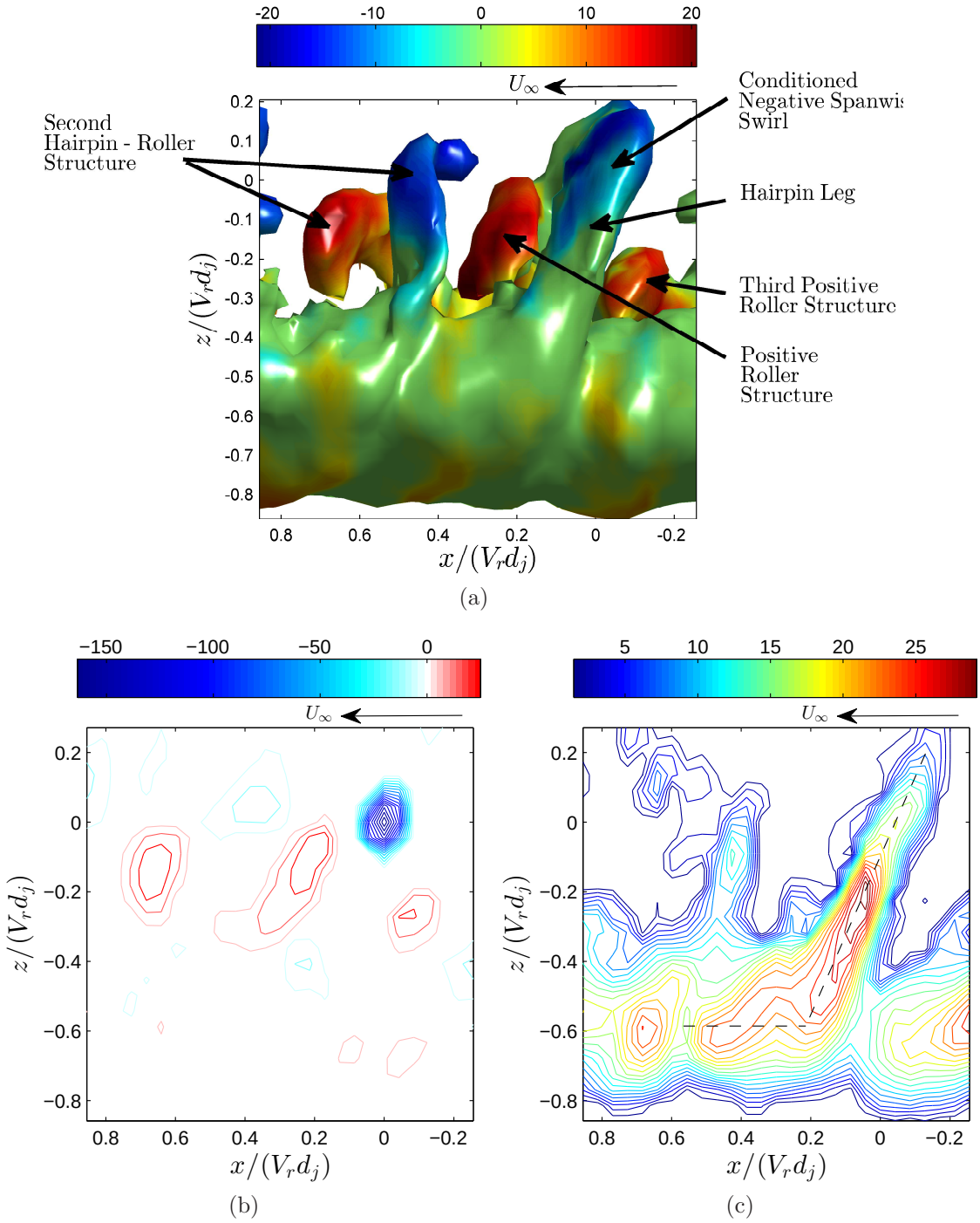

Figure 4.50: Side view of conditionally averaged hairpin structure at $x/d_j = 15$. (a) Iso-surfaces of $\lambda_{ci,iso} = 0.1\lambda_{ci,max}$. Surfaces coloured by the local value of $\lambda_{ci,y}(\mathrm{s}^{-1})$. (b) Slice through the centre- plane at $y/(V_r d_j) = 0$ showing contours of the spanwise swirl component $\lambda_{ci,y}$. (c) Slice through the negative core at $y/(V_r d_j) = 0.4$ showing contours of λ_{ci}. The angle between the dashed lines is 114°.

vortex tube) to the cores of the CVP connecting them and confirming that, on average, the windward structures with negative spanwise vorticity component are in fact the heads of hairpins. Although a series of these hairpins as well as positive roller structures are observed in the instantaneous reconstructions, no other structures appear in the conditionally average volume, unlike the case at $x/d_j = 15$. This could be explained by the increased turbulence of the jet at $x/d_j = 30$. The increased level of jitter in the relative positioning of the observed structures (hairpins, rollers and wake vortices) will prevent other structures that aren't conditioned for, to be smoothed out during the averaging procedure.

Figure 4.52a is a side view of the hairpin structure, showing how the hairpin is still swept forwards at an angle to the free stream direction at this downstream position as well. Figure 4.52b shows a slice through the positive core illustrating this more clearly. The angle of the hairpin leg to the free-stream direction (x-axis), indicated by the dashed lines, is approximately 122°.

Lastly, the conditionally averaged results from the measurements at $x/d_j = 85$ are presented. Similarly to before, figure 4.53 shows the swirl field of the conditionally averaged volume produced from an ensemble of 168 samples. Again the expected spanwise vortex tube together with the cores of the CVP are observed. And similar to the results at $x/d_j = 30$ the hairpin leg extending from the head to the cores is present in the average, but only for the negative core. The positive core does not appear to be connected to the head. This observation was made in the instantaneous reconstructions, where the windward structures, i. e the hairpin heads, appeared to be detached from the cores of the CVP, with a few examples of them being attached. This could be what is reflected in the conditionally averaged data, but it should also be taken into account that perhaps a larger ensemble is required (more than the 168 samples), as the flow time-scales increase downstream and therefore more samples are needed to build up averages. The asymmetry though is not surprising as the measurements are well in the far field and, as was mentioned in the previous chapter where the mean properties were studied, asymmetry in the cross-flow jet has been noted in the literature.

Figure 4.54a shows a side view (negative core) of the conditionally averaged hairpin structure in figure 4.53. Again the figure shows how the attached part of the hairpin is still swept at a forward angle to the free-stream direction. The

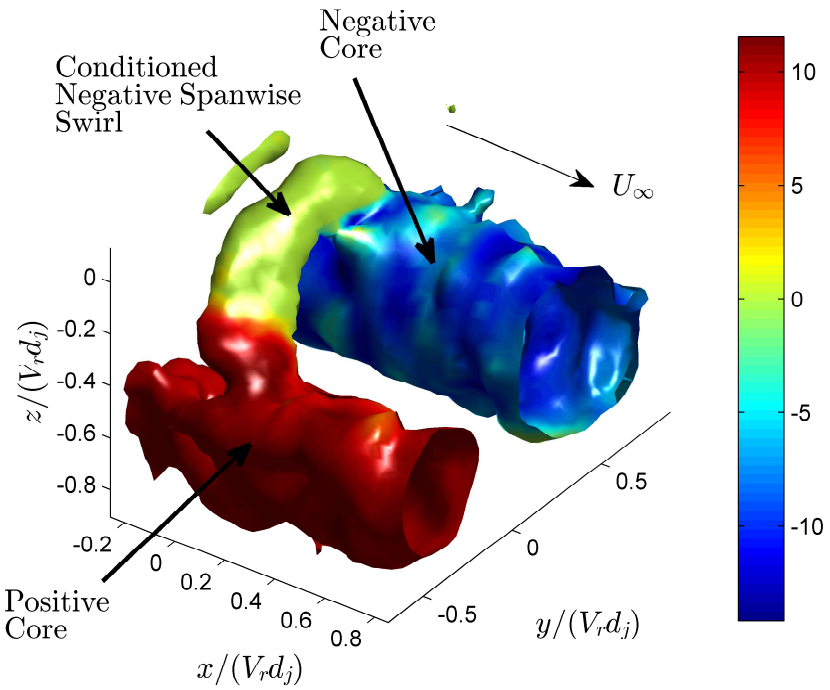

(a)

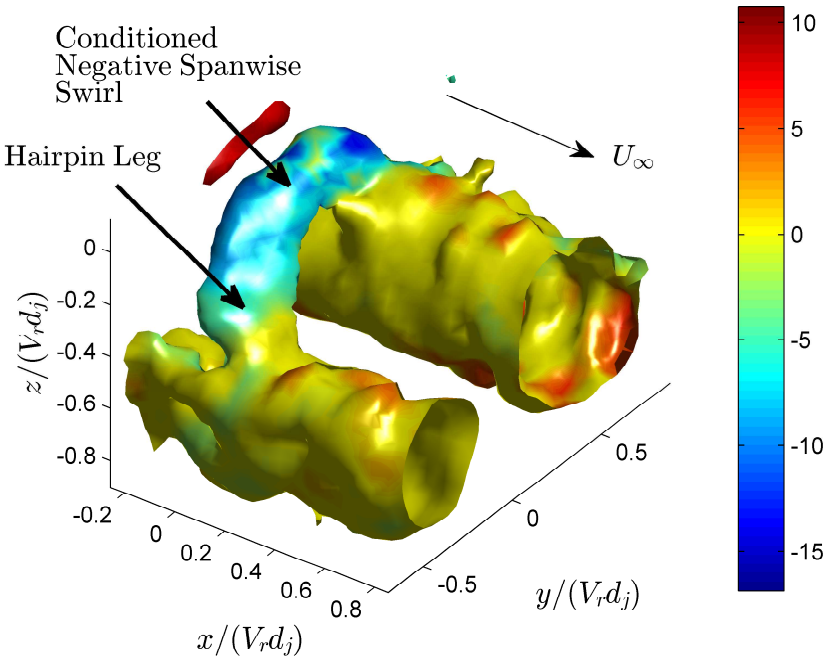

(b)

Figure 4.51: Conditionally averaged hairpin structure at $x/d_j = 30$. Iso-surfaces of $\lambda_{ci,iso} = 0.1\lambda_{ci,max}$. Surfaces coloured by the local value of (a) $\lambda_{ci,x}(\mathrm{s}^{-1})$ and (b) $\lambda_{ci,y}(\mathrm{s}^{-1})$.

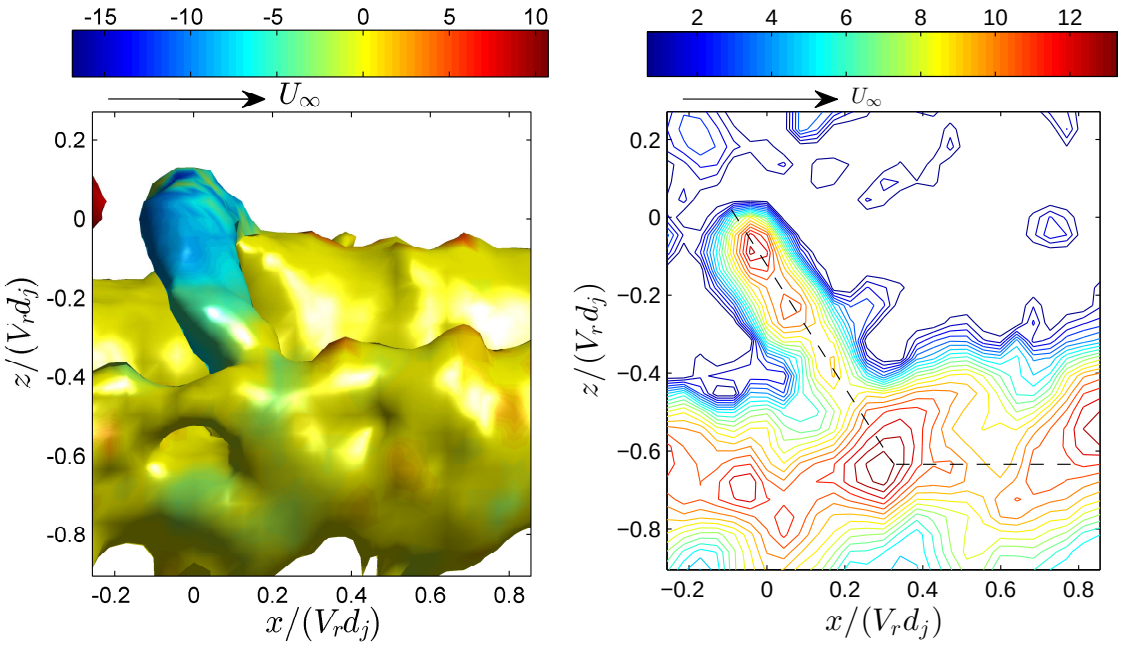

Figure 4.52: Side view of conditionally averaged hairpin structure at $x/d_j = 30$. (a) Iso-surfaces of $\lambda_{ci,iso} = 0.1\lambda_{ci,max}$. Surfaces coloured by the local value of $\lambda_{ci,y}(\mathrm{s}^{-1})$. (b) Slice through the positive core at $y/(V_r d_j) = -0.3$ showing contours of λ_{ci}. The angle between the dashed lines is 122°.

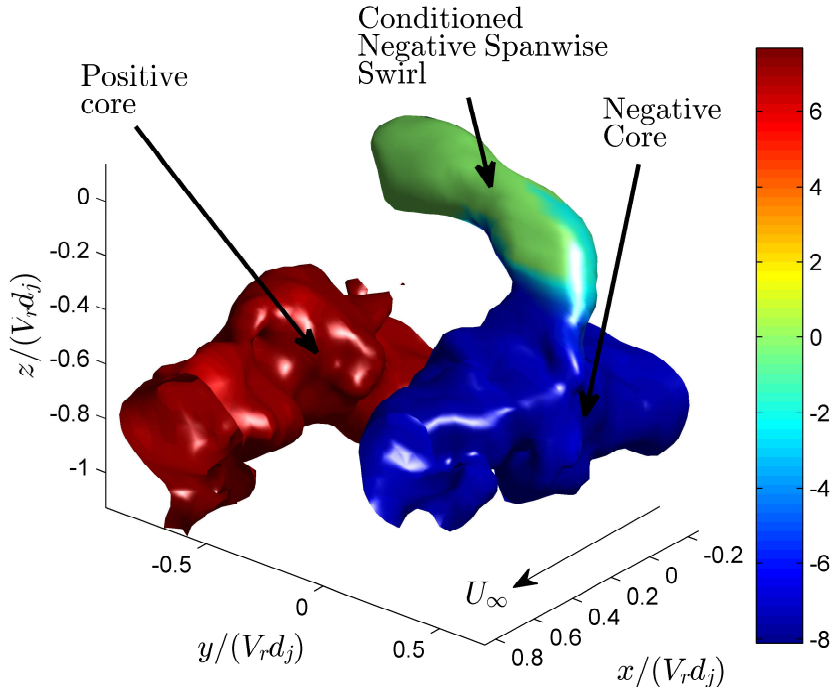

(a)

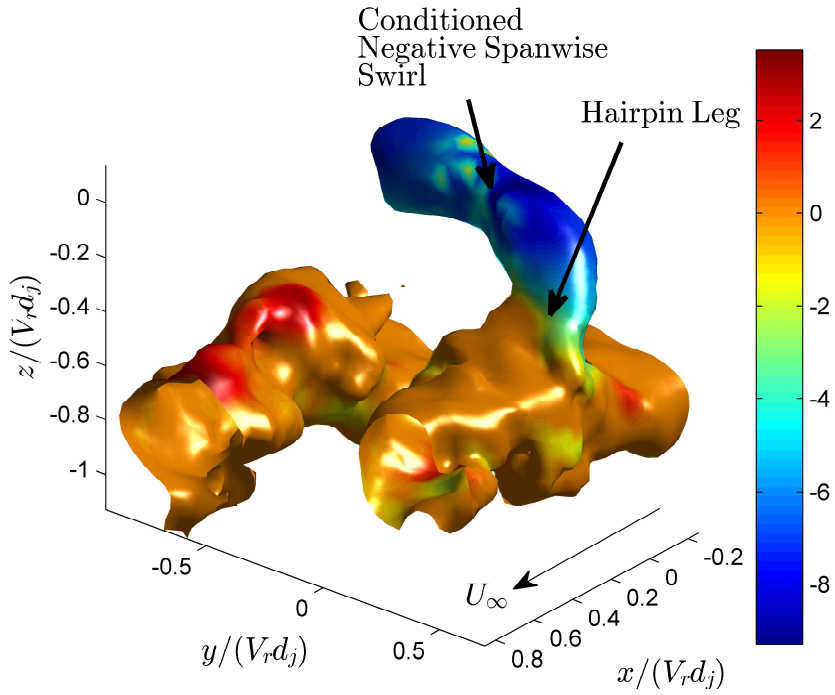

(b)

Figure 4.53: Conditionally averaged hairpin structure at $x/d_j = 85$. Iso-surfaces of $\lambda_{ci,iso} = 0.1\lambda_{ci,max}$. Surfaces coloured by the local value of (a) $\lambda_{ci,x}(\mathrm{s}^{-1})$ and (b) $\lambda_{ci,y}(\mathrm{s}^{-1})$.

angle is extracted by viewing a cut through the negative core of contours of swirl, shown in figure 4.54b. The angle, indicated by the dashed lines, of the hairpin head is approximately 114°. Furthermore, when compared to the results at $x/d_j = 15$ and 30, the length of the hairpin leg appears to decrease, with the one at $x/d_j = 85$ being the shortest one observed. This would agree with the observations that the hairpins head increasingly detach from the cores with downstream distance, but stay on the windward side of the jet.

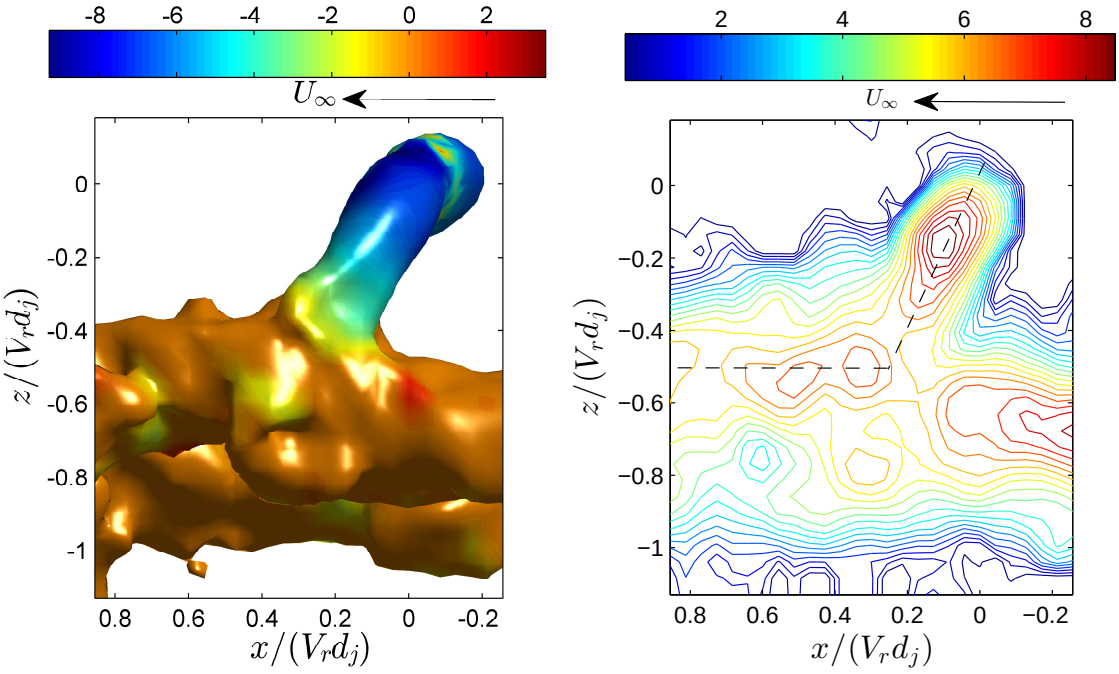

Figure 4.54: Side view of conditionally averaged hairpin structure at $x/d_j = 85$. (a) Iso-surfaces of $\lambda_{ci,iso} = 0.12\lambda_{ci,max}$. Surfaces coloured by the local value of $\lambda_{ci,y}(\mathrm{s}^{-1})$. (b) Slice through the positive core at $y/(V_r d_j) = 0.4$ showing contours of λ_{ci}. The angle between the dashed lines is 114°.

4.4.3 Conditioning for the Roller Structures

The second condition to be selected will be to extract the roller structures. Given that these structures appeared mainly on the windward side of the cross-flow

jet together with the hairpin heads, a similar approach is adopted as with the hairpin structures in the previous section, with the condition set for strong events of positive spanwise swirl $\lambda_{ci,y}$.

By conditioning on spanwise swirl, a vortex tube aligned in the spanwise direction is expected to appear. Again the length of the tube is unknown, but based on the observations made in the instantaneous reconstructions, it would have a maximum length approximately equal to the CVP core separation. Furthermore, as in the conditionally averaged hairpin volumes, the two cores of the CVP would also appear as they are always present and dominate the flow field. The parts which are not expected are the ones of interest. However, given that the positive roller structures were observed in the conditionally averaged volumes for the hairpin structures, it should be perhaps expected that the hairpin structures will be observed in the conditionally averaged volumes for the roller structures.

The conditionally averaged volume from an ensemble of 41 samples from the measurements at $x/d_j = 15$ is shown below. Figure 4.55 shows the swirl field of the volume. The spanwise vortex tube together with the cores of the CVP are observed in figure 4.55a as expected. A number of other (not conditioned for) structures appear, highlighted in figure 4.55b. The roller structure does not appear to have a leg connecting it to the cores, confirming the observations made in the instantaneous Taylor reconstructions, and simply appears on the windward side of the jet as a spanwise vortex tube. Furthermore a hairpin structure appears in front of the conditioned roller, and a second hairpin-roller structure appears further downstream. The resulting conditionally averaged volume produced by conditioning on the roller structure is therefore very similar to that produced by conditioning on the hairpin structure in figure 4.49. This confirms the conclusion made earlier that the hairpin-roller structure appears, to a large degree, periodically at $x/d_j = 15$.

Figure 4.56 is a side and top view of the volume, together with a different isometric view, which shows the hairpin and roller structures and their relative orientation more clearly. Figure 4.56a shows the hairpin structure appearing in front of the conditioned roller (hidden behind it in the figure). The side view in figure 4.56b shows how the roller, just like in figure 4.50, appears below the hairpin structure in front of it. The top view in figure 4.56c shows how the roller

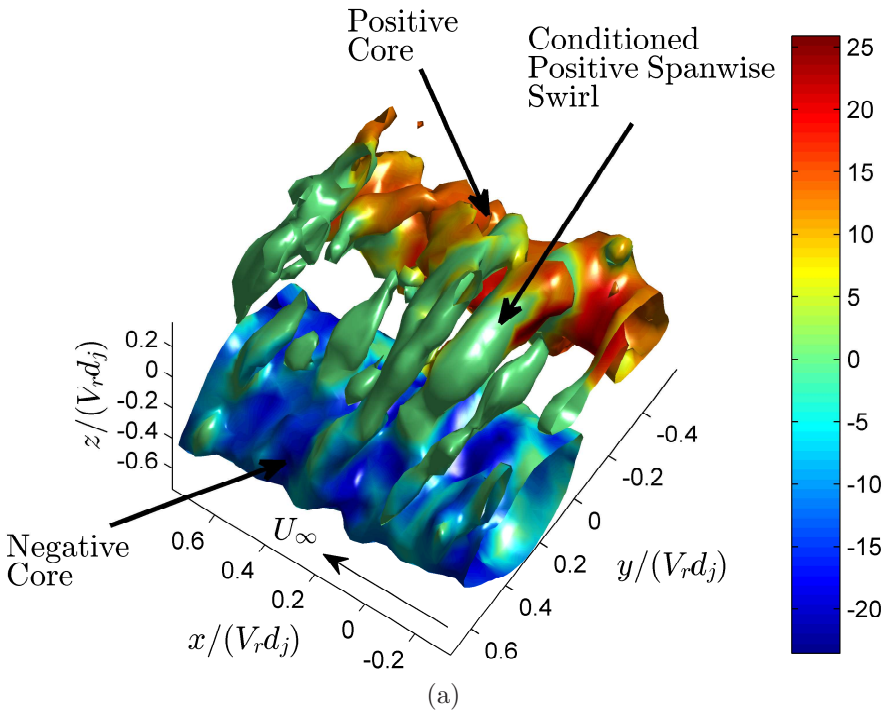

(a)

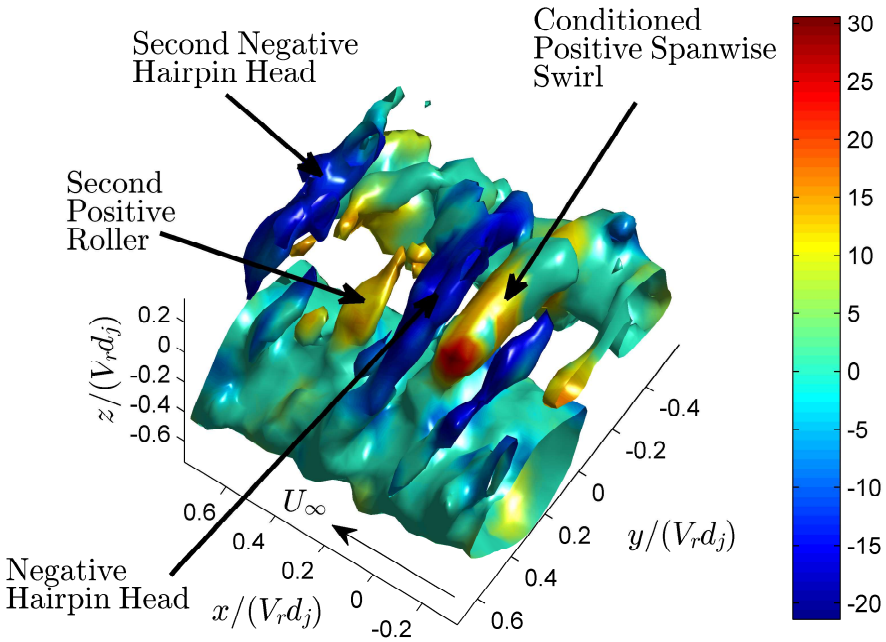

(b)

Figure 4.55: Conditionally averaged roller structure at $x/d_j = 15$. Iso-surfaces of $\lambda_{ci,iso} = 0.1\lambda_{ci,max}$. Surfaces coloured by the local value of (a) $\lambda_{ci,x}(\mathrm{s}^{-1})$ and (b) $\lambda_{ci,y}(\mathrm{s}^{-1})$.

structure is actually slightly shorter in length than the hairpin head, spanning a shorter length across the cores of the CVP.

The conditionally averaged volume from an ensemble of 91 samples from the measurements at $x/d_j = 30$ is examined below. The resulting swirl field is presented in figure 4.57. Figure 4.57a shows a 3D view where the expected spanwise vortex tube and two cores of the CVP are clearly observed, with no other unexpected structures or part appearing. Although only the expected structures are extracted this still useful. The roller structure is now observed to be slightly arched, similar to the arched hairpin head. A side view of the volume in figure 4.57b shows, unlike the hairpin head, that the roller is not angled to the free stream. From the side view it might appear as if the roller is actually connected to the cores, but a contour plot of swirl of a slice through the positive core in figure 4.57c shows that this is not the case as the swirl contours of the roller around $z/(V_r d_j) = 0$ do not extend to the cores at $z/(V_r d_j) = -0.6$ as for the hairpin in figure 4.52b, it is simply hovering above them. This therefore agrees once again with the observations made in the instantaneous reconstructions. Furthermore the hairpin structure does not appear as in the conditionally averaged volumes at $x/d_j = 15$, similarly to how the roller structures do not appear in the averaged volumes conditioned for the hairpin structures at $x/d_j = 30$. This would coincide with the explanation as to why, given for the averaged volume conditioned on hairpins at $x/d_j = 30$ before, being the increased level of turbulence of the jet.

Finally the conditionally averaged volume from an ensemble of 156 volume samples at $x/d_j = 85$ is shown in figure 4.58. The results are very similar to the averaged volumes from the measurements at $x/d_j = 30$. The 3D view in 4.58a shows the same spanwise vortex tube together with the cores of the CVP as expected. The roller is still slightly arched and not connected to the cores, hovering above them. Again no other structures appear in the volume, and this should have been expected given that the volume is extracted from data further downstream. A side view and a slice through the positive core in 4.58b and 4.58c respectively of the volume shows how the roller is detached form the cores and is not angled to the free stream, unlike the hairpin heads.

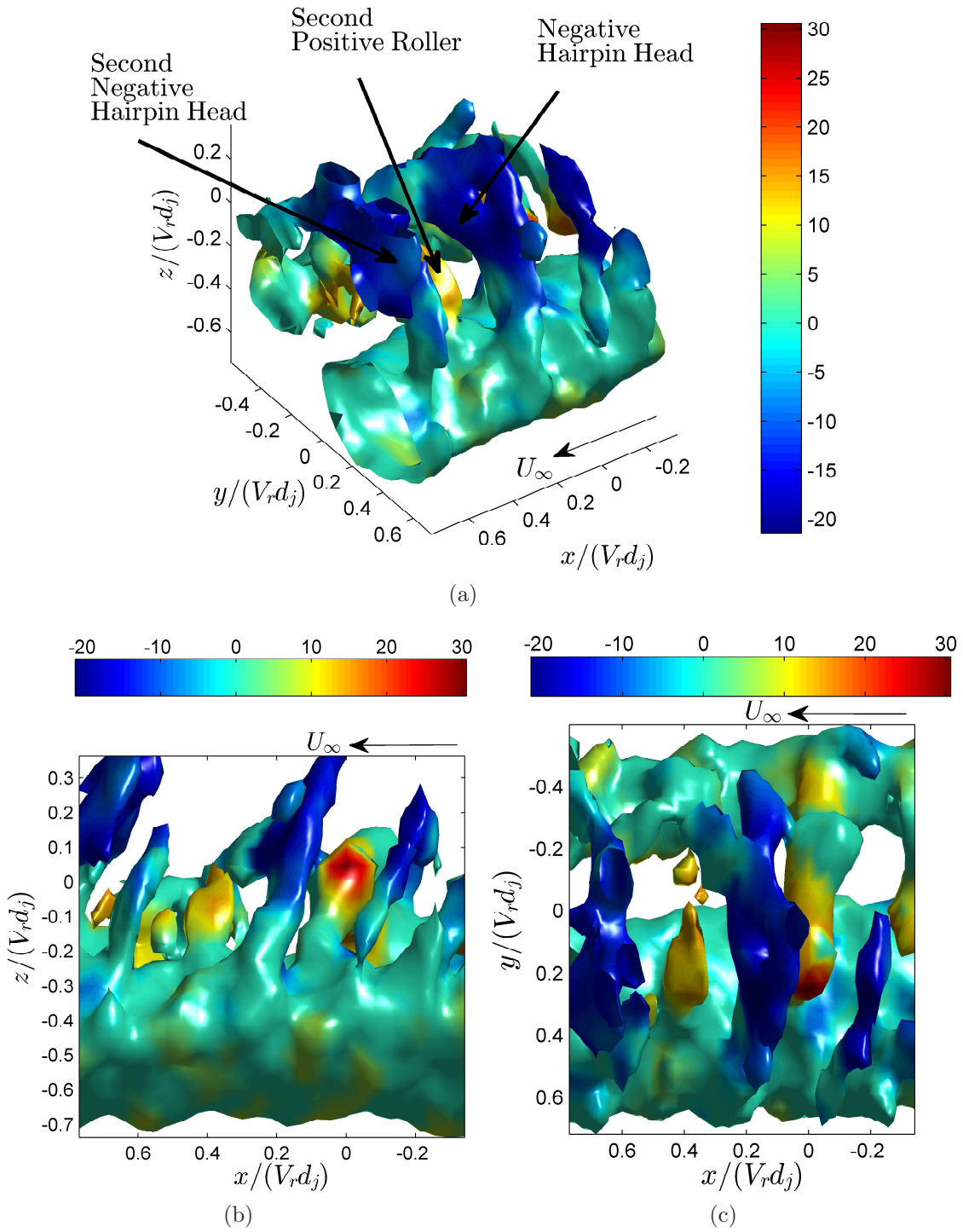

Figure 4.56: Various views of the conditionally averaged roller structure at $x/d_j = 15$. Iso-surfaces of $\lambda_{ci,iso} = 0.1\lambda_{ci,max}$ with surfaces coloured by the local value of $\lambda_{ci,y}(\mathrm{s}^{-1})$. (a) 3D view from the front looking upstream. (b) Side view and (c) Top view of the volume.

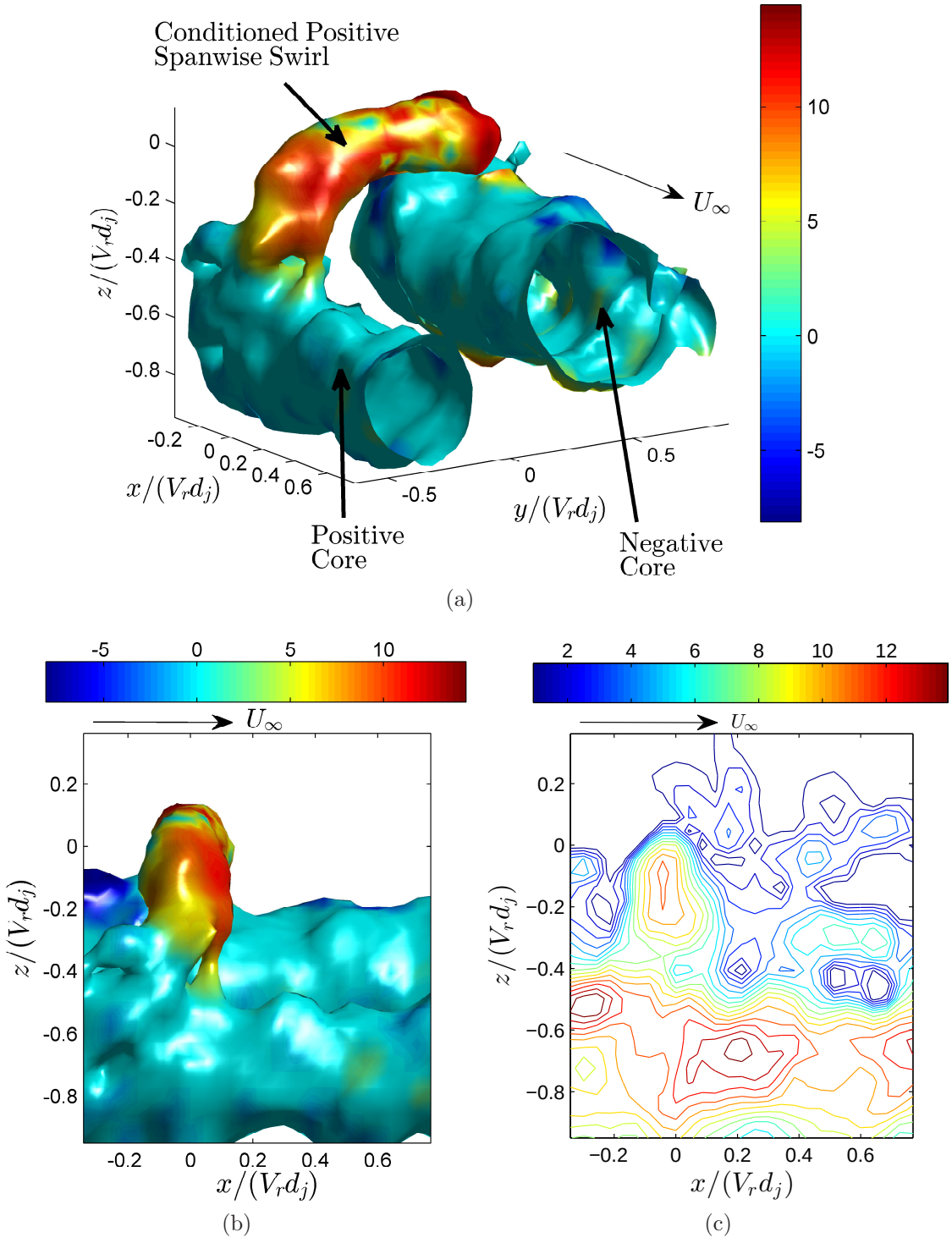

Figure 4.57: Conditionally averaged roller structure at $x/d_j = 30$. Iso-surfaces of $\lambda_{ci,iso} = 0.1\lambda_{ci,max}$ with surfaces coloured by the local value of $\lambda_{ci,y}(\mathrm{s}^{-1})$. (a) 3D view from the front looking upstream. (b) Side view of volume. (c) Slice through the positive core at $y/(V_r d_j) = -0.4$ showing contours of swirl λ_{ci}.

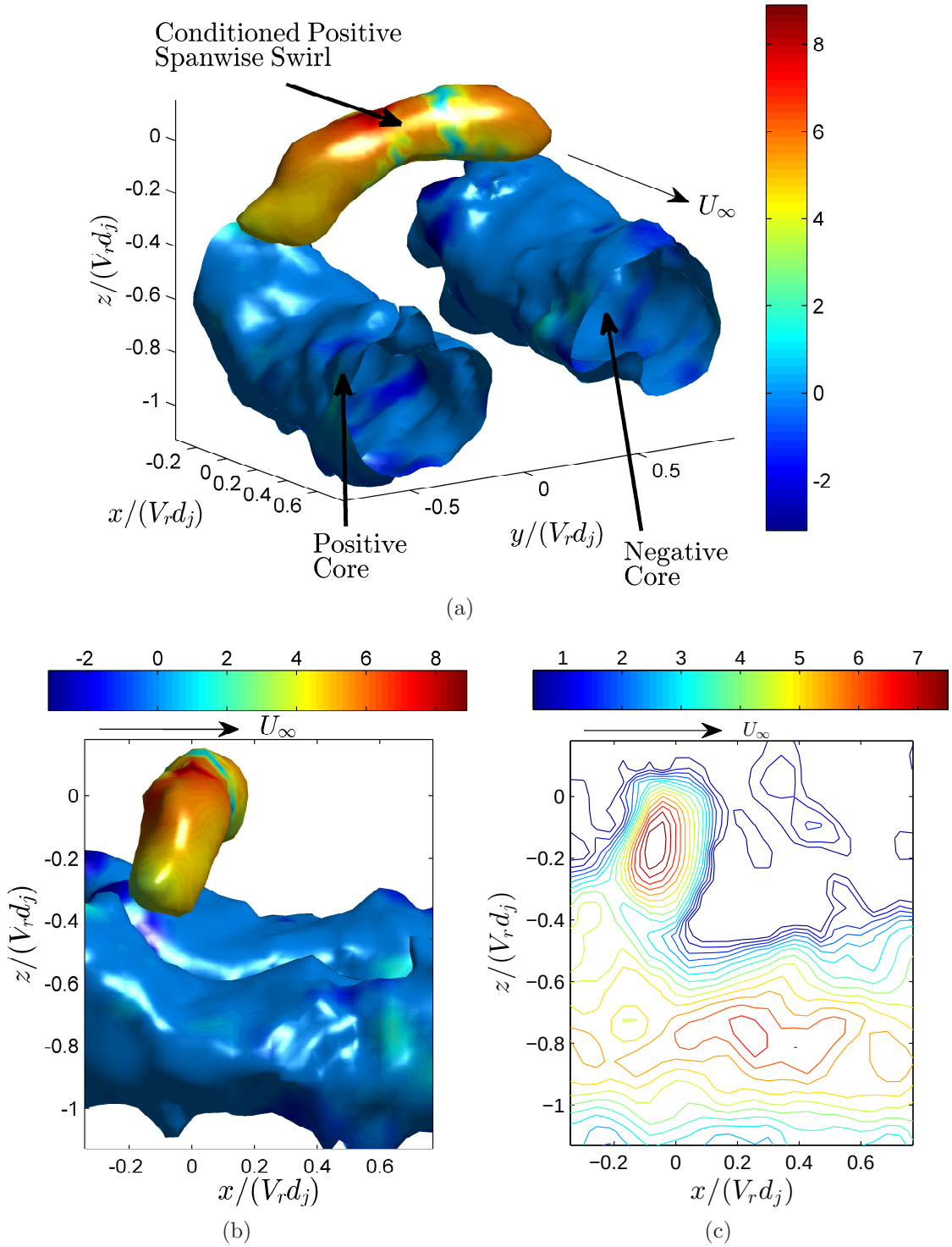

Figure 4.58: Conditionally averaged roller structure at $x/d_j = 85$. Iso-surfaces of $\lambda_{ci,iso} = 0.1\lambda_{ci,max}$ with surfaces coloured by the local value of $\lambda_{ci,y}(\mathrm{s}^{-1})$. (a) 3D view from the front looking upstream. (b) Side view of volume. (c) Slice through the positive core at $y/(V_r d_j) = -0.4$ showing contours of swirl λ_{ci}.

4.5 Discussion

The results presented in this chapter allow for a better understanding of the far field of the cross-flow jet, and specifically the mean properties in chapter 3, by looking at the coherent structures present. The Towed Jet-SPIV measurements showed that the cores of the CVP are made of a number of vortex tubes which wrap around each other in a helical structure with increasing downstream distance. This agreed with the observations made in the pdfs in section 3.3 of the number of vortex tubes present in the cores showing that instantaneously the cores consist of a number of interacting structures which persist far downstream. These structures were then studied by analysing the data from the High-Speed SPIV measurements converted to 3D volumes via the use of Taylors hypothesis.

The conditional averaging procedure confirmed that hairpins are representative of the mean structures having negative spanwise vorticity on the windward side of the jet. The tails of these hairpins make up the cores of the CVP. The wrapping of the vortex tubes in the Towed Jet experiment results together with the observation of the cores being made up of a number of tubes in the Multi-Scale SPIV measurements are a result of the interaction of the tails of successive hairpin structures as they are convected downstream by the cross-flow. The structures with positive spanwise vorticity were found to simply hover on the windward side of the jet and appear between successive hairpins. This repeatable pattern together with the shape of the representative mean structures found in the cross-flow jet are summarised in a cartoon in figure 4.59,. The figure shows two cartoons (both having a 3D and side view), one for the near field drawn from the results $x/d_j = 15$, and one for the far field drawn from the results at $x/d_j = 30$ and 85. In order to show the shape and relative orientation of the mean structures more clearly, the wake structures are not shown in the figure but their presence is confirmed through the instantaneous reconstructions. The difference between the near and far field structure is in the relative orientation of the hairpins and rollers as illustrated in the figure, together with the lower degree of coherency in the far field. This illustrates the idea that the hairpin and roller structures, as well as the wake vortices, can be used as idealised building blocks of the CVP far-field structure.

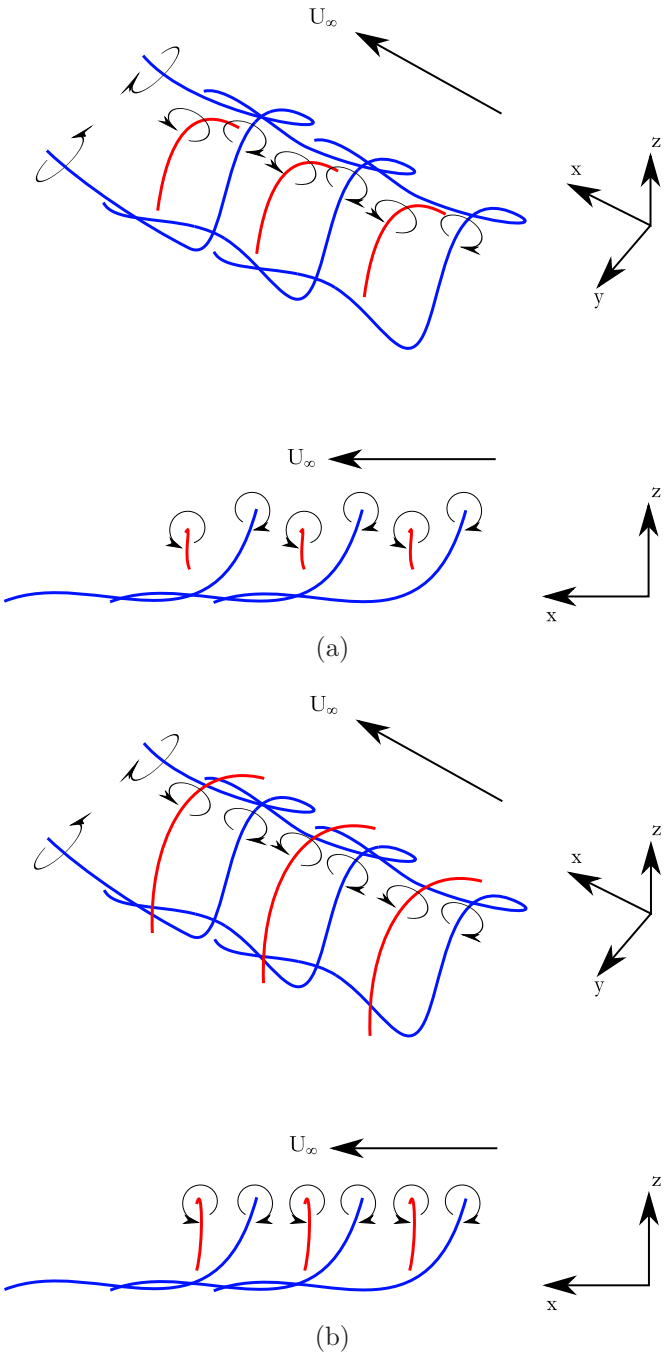

Figure 4.59: Cartoon of the coherent structures present in the (a) near and (b) far field of the cross-flow jet. The hairpins are coloured blue reflecting their negative spanwise vorticity component of the head, and the rollers are coloured red reflecting their positive spanwise vorticity component.

Chapter 5

Conclusions

In this thesis the turbulent structure of the jet in cross-flow was investigated experimentally by conducting statistical and time-resolved SPIV measurements in the CVP plane at a variety of downstream locations and velocity ratios. The literature review highlights that three main areas of interest have been the focus of previous research: i) the near field interaction of the jet with the cross-flow and resulting dynamics, ii) the wake area with the resulting wake structures from the near-field interaction and iii) the Counter-rotating Vortex Pair (CVP) in the far field. The work in this thesis is the first to study the CVP cross-plane using modern techniques of PIV for highly turbulent cases of large jet Reynolds number and velocity ratio. A series of low and high-speed SPIV measurements were undertaken in the CVP plane. The first involved a Multi-Scale SPIV measurement set-up performed in a water channel facility to obtain statistically independent two-dimensional three-component data at three different downstream locations x/d_j = 30, 55, 85, and three different velocity ratios V_r = 10, 15, 20. To gain insight into the 3D structure two sets of high-speed, time resolved, SPIV measurements were taken. The first was a towed-jet experiment conducted for three velocity ratios V_r = 9.1, 17, 23.5 which introduced the novel technique of changing the frame of reference from a stationary reference to a moving one by towing a jet in a tow tank facility. The second involved measurements in a stationary frame of reference in a water channel facility at three downstream locations of $x/d_j = 15, 30, 85$ for a velocity ratio of $V_r = 10$, converted to 3D volumes via the use of Taylor's hypothesis. With the details of the experimental set ups ex-

plained the SPIV measurements were then analysed for each case separately, after a statistical evaluation of each data set was performed.

5.1 Mean Flow Properties

To characterise the turbulent statistics and mean structure, Multi-Scale SPIV measurements were performed in the water channel facility in a stationary reference at the three downstream locations of $x/d_j = 30, 55, 85$ for three different velocity ratios $V_r = 10, 15, 20$. First the resolution and convergence of the measurements were assessed. The data was found to adequately resolve the large scales and inertial range, capturing most of the total turbulent kinetic energy. The statistical convergence was checked by quantifying the uncertainty involved in calculating the sample mean, for various turbulent quantities. The effect of decreasing the Interrogation Window (IW) size in the PIV processing procedure versus reducing the size of the Field of View (FoV) to achieve the same increase in resolution was assessed. This was done by measuring the increase in the percentage of total turbulent kinetic energy measured and by comparing the joint pdf between the invariants of the reduced Velocity Gradient Tensor, which exhibits a characteristic skewness if the data is resolved and not noisy. A reduction in IW size was found to add more noise to the data than decreasing the FoV.

The jet trajectory was found to collapse when using the classical scaling laws of Pratte & Baines [53] and Broadwell & Breidenthal [9], using the global length scale in the far-field $l = (\pi/4)^{\frac{1}{2}} V_r d_j$, which scales with $V_r d_j$. The constants used for the trajectory curve fit were $A = 1.58$ and $m = 0.28$ and fall within the range quoted in the literature. The mean vorticity field showed that the CVP is comprised of two cores that are slightly elongated in the wall-normal z-direction. The data was found to agree with the inviscid scaling laws for the far field suggested by the Broadwell & Breidenthal [9] vortex line model. However, the exponents of the power law relations for core spacing R and circulation Γ with downstream distance x were found to be different to the values predicted by the model, demonstrating the limitations of modelling the CVP as two vortex lines.

Instantaneous plots of the vorticity field showed that the cores are made of a number of small vortex tubes rather than a single vortex core. PDFs of the number of vortex tubes in each core demonstrated that many tubes of the same sign as mean is present on average, in addition to a smaller number tubes of opposite sign. Tubes of the same sign as the mean were also stronger than those of opposite sign. Performing the same analysis using the swirl field yielded almost identical results indicating that the CVP is made up by multiple vortex tubes. The spatial distribution of these tubes was analysed by calculating JPDFs of their in plane position and strength revealing that the strongest are concentrated around the position of the CVP core. Tubes of opposite sign are located in an arch on the windward side of the jet extending from the core with the same sign to the core of opposite sign. JPDFs of the in plane position of all vortex tubes (both positive and negative) reveals that the two cores are connected together by an arch of vorticity on the windward side, which result in the CVP having the characteristic kidney shape.

The resulting mean velocity field of the spanwise $\overline{V}$ and wall-normal $\overline{W}$ velocity component were in agreement with what one would expect of a CVP aligned in the streamwise direction. The streamwise velocity $\overline{U}$ component showed a wake profile, with a velocity deficit in the centre plane and a surplus on either side, at the position of the cores. The magnitude of all three components normalised by the free stream were observed to gradually decay with increasing $x/(V_r d_j)$. This is in agreement with the decay in circulation, as predicted by the Broadwell & Breidenthal [9] model. This gives some weight to the idea that the velocity field of a cross-flow jet with different inlet conditions can be collapsed using the global length-scale of $l = V_r d_j$, but the limited measurements were not made at numerous downstream locations to thoroughly test the circulation scaling.

The characteristic 'kidney' shape of the CVP widely reported in the literature was clearly illustrated in the turbulence intensity profiles of the streamwise and wall-normal velocity component, $\sqrt{\overline{u'^2}}$ and $\sqrt{\overline{w'^2}}$ respectively, where the two peaks present are connected by an arch of strong turbulence intensity on the windward side (top of the jet). The spanwise profile ($\sqrt{\overline{v'^2}}$) does not exhibit the same shape, but has the two cores connected by a strong turbulence intensity region on the wake side. The peaks of all three turbulence intensity profiles occur at

the position, which overlaps the position of maximum mean vorticity magnitude, i.e the cores of the CVP. The peaks in the spanwise and wall-normal turbulence intensity profiles can be attributed to the high concentration of strong streamwise vortex tubes around the cores. Evidence suggests that, given the absence of streamiwse vortex tubes in the wake region, the low but distinct turbulence intensity in this region results from wake vortices. The limitations of the planar measurements allows for only part of the features observed to be explained by vorticity structures aligned in the streamwise direction, with the peaks in the streamwise profiles and the absence of a windward high turbulence intensity arch in the spanwise profiles being attributed to different mechanisms.

The Reynolds stresses $\overline{u_i' u_j'}$ exhibit a high level of organisation. The $\overline{v'w'}$ stress has an 'ear' shaped profile with opposite signed stress in each side of the jet centreline, which remains the same for all inlet conditions. The $\overline{u'v'}$ and $\overline{u'w'}$ stresses show an evolving shape with increasing $x/V_r d_j$. A turbulent kinetic energy production analysis reveals that TKE is predominantly produced on the windward side of the jet between the cores, due to the shear generated between the jet and the cross-flow. Three out of the seven components that can be calculated provide most of the source of TKE, with $\overline{w'^2}\left(\partial\overline{W}/\partial z\right)$ being the largest contributor.

Two-point spatial correlations point to a structure whose mean shape generates the kidney shape observed in the rms velocity profiles. The correlations indicate a mean structure with an arched shaped, inclined to the free stream direction, on the windward side of the jet, a description consistent with the head of a hairpin structure. Furthermore wake structures of straight vortex tubes extending into the wake are also evident in the correlations with a possible link with the windward arch shaped structure observed. Importantly, for all the correlations, similar results are observed for all V_r and x/d_j, indicating that the structure of the CVP is common for the range of velocity ratios investigated and persists into the far-field.

5.2 Instantaneous Large-Scale Structure

To analyse the instantaneous 3D turbulent structure, reconstructed volumes from the high-speed SPIV measurements were constructed. The data was assessed by calculating the resolution and appropriate size of the volumes such that the data can be considered quasi-instantaneous. The accuracy of the reconstructions was assessed by performing a divergence error analysis, in line with other 3D measurements in the literature. In the towed-jet experiments the out-of-plane (streamwise direction) gradients could not be quantified. The resulting volumes enable a study of the downstream evolution of the CVP plane (the measurement plane) following the flow. In addition the towed-jet measurements could not offer any information about structures which advect with the mean flow. This was not the case for the stationary-frame measurements in the water channel facility, which enabled the presence of large-scale coherent structures that were advected with the mean flow to be detected. Crucially, the analysis showed that high magnitude gradients which would be associated with large scales coherent structures contain the lowest divergence error, meaning that they are less sensitive to the divergence errors.

The towed jet results revealed that each core of the CVP is made of a cluster of small vortex tubes rotating with the mean rotation of the respective core with downstream distance resulting in a twisting rope-like structure. By increasing V_r the number of vortex tubes were found to increase and spread out over a larger area within each core. This was in agreement with the observations made in the pdfs of vortex tubes number and location from the Multi-Scale SPIV measurements.

The use of Taylor hypothesis on high-speed Stereoscopic PIV data in a stationary frame of reference allowed for the understanding of the far field structure of the cross-flow jet through large-scale coherent turbulent structures. The resulting 3D reconstructions showed some very striking features. A series of structures on the windward side of the jet were very clearly observed to be aligned in the spanwise direction with alternating sign of spanwise vorticity component . Closer observations revealed that the structures with negative spanwise vorticity were on average part of a structure which strongly resembled the hairpin structures

found in turbulent boundary layers, but were inclined forward in the streamwise direction and more regular. The tail ends of the hairpins were aligned in the streamwise direction and formed the cores of the CVP, extending forwards and interacting with the hairpins in front. Structures with positive spanwise vorticity resembling 'roller' like structures were seated between successive hairpin structures, hovering on top of the cores. Wake structures were also observed, as straight rods extending from the area between the cores into the wake. All three structures were observed at all downstream measurement locations illustrating that they persist far downstream, albeit it with a gradual loss of coherency in the sense that the structures become less regular with downstream distance. Their presence provides a mechanistic origin of the characteristic 'kidney' shape, being attributed to the arched shape of the hairpin head and rollers, as well as a number of mean velocity and turbulent statistics features observed in mean turbulence measurements. Furthermore, the structures are consistent with observations made in scalar measurements from the literature.

Conditional averaging analysis demonstrated that the structures observed in the instantaneous reconstructions are on average represented by a hairpin and roller structure. The hairpin structures are inclined forwards at an angle between 114° and 122° and the roller structures have an arched shape. The extracted shape of the structures together with their repeatable nature observed in the instantaneous reconstructions shows that the hairpin and roller structures, as well as the wake vortices, can be considered idealised building blocks, that produce the turbulent structure of the CVP in the far field.

5.3 Final Remarks

In Chapter 1 it was highlighted that there are no extensive studies of the CVP cross-plane using modern techniques of PIV for highly turbulent cases of large Reynolds number and velocity ratio. The technique of Stereoscopic PIV was shown to be a very useful in performing measurements in the cross-plane. The Multi-Scale measurements allowed for a statistical description of the CVP to be made. The high-speed SPIV measurements with application of Taylor's Hypoth-

esis and the towed jet measurements, was shown to result in a very clear and detailed view of the cross-flow jet from a structural point of view.

This thesis has attempted to address what the turbulent structure of the CVP is and provide a physical explanation for the turbulence structure of the JICF. Investigating the JICF in a stationary and moving frame of reference has proved very useful in identifying key physics of the flow. The origin of the characteristic 'kidney' shape and large degree of spatial order observed in the far field mean flow properties was explained through the persistent presence of the hairpin, roller and wake structures and their relative spatial organisation. The wide parameter space of inlet conditions observed in the literature such as, the jet Reynolds number, V_r and nozzle condition (flush or protruding, angled to the cross-flow, round or elliptical) e.t.c, meant that only a small portion of it could be covered here. However, the mean results reported by others suggests that these results are likely to be general features of the JICF.

A study of different inlet conditions as well as comparisons with other flows should form part of future investigations. An important question not addressed here, but frequently discussed in the literature, is why the JICF acts as an efficient mixer. The degree of organisation in the far field does however explain why the scalar field shows anisotropic behaviour as reported by Shan & Dimotakis [57]. On the other hand the structures are likely responsible for enhanced entrainment. Another important question is how far downstream do these structures persist? Building on the current knowledge and that presented here, together with future investigations of the scalar field could lead to a deeper understanding of the mechanisms responsible for this and result in the complete physical modelling of the flow.

5.4 Future Work

The research in this thesis was performed in order to understand the complex structure of the far field for the simplest (or most fundamental) case of a flush round nozzle where the jet and cross flow fluid are the same. For future experimental work the same approach used here for different inlet conditions can be

utilised to begin building an understanding of the effect of the inlet conditions on the resulting far-field structure. High-Speed SPIV measurements in the lab frame were only performed for a $V_r = 10$, and although the mean flow properties indicate a similar structure for higher velocity ratios, higher velocity ratios would allow for it's effect to be studied. Furthermore simultaneous PIV and scalar measurements would also allow for the investigation of how the three main large-scale structures identified here transport the scalar, i.e how cross-flow fluid is entrained into the jet and mixed.

The structure of the JICF is a very complicated and elaborate one as is clearly illustrated by the work presented here. The fact that the CVP can be described as a 'train' of hairpins, rollers and wake structures means that the flow can be modelled using an eddy model, in a similar manner to the attached eddy ideas of Townsend [63]. With the successful extraction of these building blocks the next step would be to create an eddy model for the JICF. The idea of an eddy model for turbulent flows originated from Townsend [63] who suggested that, based on correlation measurements in turbulent free shear flows, the main turbulent motion is dominated by a pair of roller eddies (structures) inclined to the streamwise direction. Perry & Chong [46], Perry *et al.* [49] and Perry & Marusic [48] developed a model for the turbulent boundary layer to a varying degree of detail as a hierarchy of hairpin structures (distribution of geometrically similar structures of different sizes and population densities) after further experimental measurements and visualisations in the literature indicated this to be the dominant large-scale eddy. Using the Biot-Savart law they were then able to extract the mean velocity profiles and Reynolds shear stresses and associated spectra. Nickels & Perry [45] developed a model for axisymmetric turbulent jets in an analogous way as a random array of a single idealised structure, of one size, confined to a cross-plane (i.e a given downstream location). These idealised structures, or 'typical eddies', are constructed from a number of straight vortex lines which have a Gaussian distribution to avoid singularities within the cores in the induced velocity field.

The approach to be adopted for the cross-flow jet would be that of the axisymmetric jet. A set of the idealised structures, namely the hairpin, roller and wake structures, of one size and shape extracted from the conditional averaging procedure would be used for a given downstream location. The main difference,

compared to the turbulent boundary layer and the axisymmetric jet, would be that they are not randomly distributed in a given plane but rather form a series, or 'train', in the downstream direction. Jitter would be applied to the relative position within the 'train' of structures to a varying degree based on the downstream location. The aim would be to see if the mean velocity profiles and Reynolds shear stresses can be reproduced from such a model. This procedure illustrates the biggest difficulty with the eddy models, in that the shape of the idealised structures is critical which cannot be known 'a priori'. It is therefore necessary to know something about the shape of the flow structures before the model can be built. Complicated experiments and post-processing procedures are required to extract these structures with the best possible detail. Development of the model allows for a refinement of the geometry to best reproduce the mean flow properties and thus an even better understanding of the large-scale turbulent structures.

Appendix A

Additional Experimental Set-up Details

Images of the experimental set up

Figure A.1b shows a different view of the 'umbilical cord' water supply for the jet. Figure A.1a shows the pipe arrangement for the jet flow control unit. The reservoir tank is to the left side of the image. Figure A.1c shows the optics used for the creation of laser sheet. The laser beam exits from position of the yellow tag. It then passes through the beam expander where it is reduced in diameter and collimated. The beam is then directed into the cage system turning up towards the tank. It is finally expanded into a sheet using a hyperbolic lens.

Nozzle and Orifice Plate design

The drawings for the axisymmetric nozzles used to produce the jet are shown in figure A.2. The nozzles were made up of two parts, connected by screwing the top half (dark grey) into the lower half (copper yellow). Each half was milled out of a single cylindrical block of aluminium. The top half is the part that connects to the

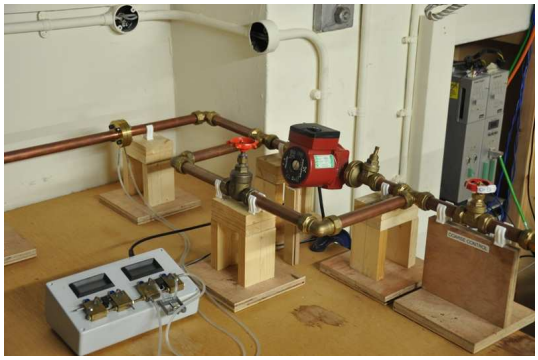

(a) Jet supply flow control unit

(b) Jet supply 'umbilical cord'

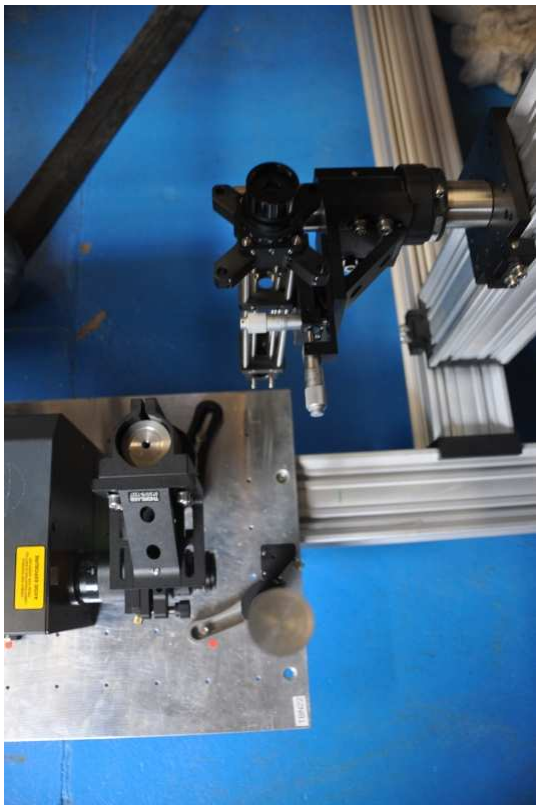

(c) Optical set up

Figure A.1: Pictures showing the experimental set up for the towed jet experiment

PVC hose pipe of the jet control unit via a brass hose pipe tail. The cylindrical chamber just above the contraction entrance houses the flow straightener. The lower half housed the 5th order polynomial profile nozzle.

The mas flow rate was measured using an orifice plate which was designed and constructed to the British Standard specifications of EN ISO 5167-2:2003, for an orifice to pipe-diameter ratio $\beta = 0.5$. The orifice plate itself was made from stainless-steel which was sandwiched between two cylindrical brass blocks, as shown in figure A.3. A gasket was place on each side of the orifice plate face as a seal to prevent water from leaking out. Hypo-tubes were inserted through the brass cylinders and the copper tube pipes at an angle, on each side of the orifice plate in order to measure the pressure drop across it. The hypo tubes were flush with the inner surface of the copper tubes.

Trigger System

Additional information regarding the timing set up for the laser and cameras is presented here.

A *National Instruments* PCI-6602 Counter/Timer connected to a BNC Terminal (BNC-2121) was used for the Water Channel measurements to create TTL signals with a low state of $0V$ and a high state of $5V$, where the duration of these states, i.e the frequency and pulse width, could be controlled. The camera frame rate was set as the reciprocal of the image pair temporal displacement $f_{cam} = 1/dt$. The shutter of the cameras were open for a time duration dt, i.e maximum possible. A start-up pulse is used to form datum point, i.e a $t = 0s$ point, for all subsequent pulses from which relative delays can be set.

Wiring and pulse diagrams for the Multi-Scale SPIV measurements are shown in figures A.4a and A.5a. The cameras were wired with a 'Master-Slave' configuration. A synchronisation signal, with frequency equal to the desired camera frame rate, was used to synchronise the exposure time of all cameras. Upon receiving the camera record trigger pulse, all cameras record 2 frames at the set frame rate and exposure time. The cameras then returned to a stand-by state until the next pulse is received. In order to make sure that the light from the laser

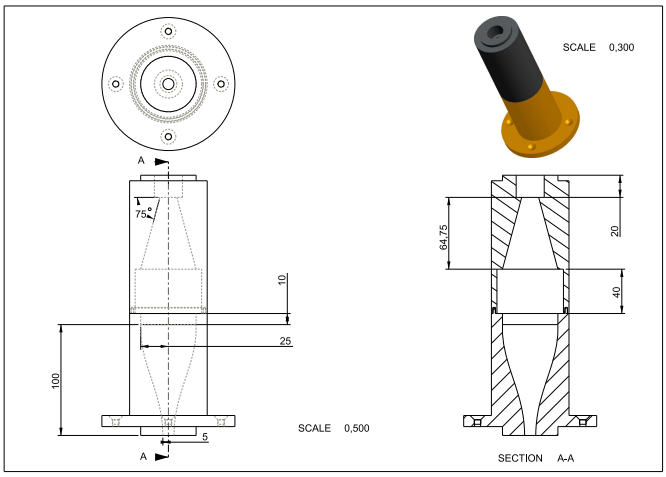

(a) Drawing for 10mm jet

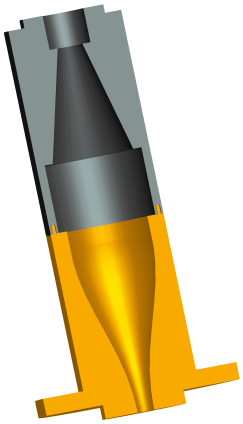

(b) 3D cross-section of 10mm jet

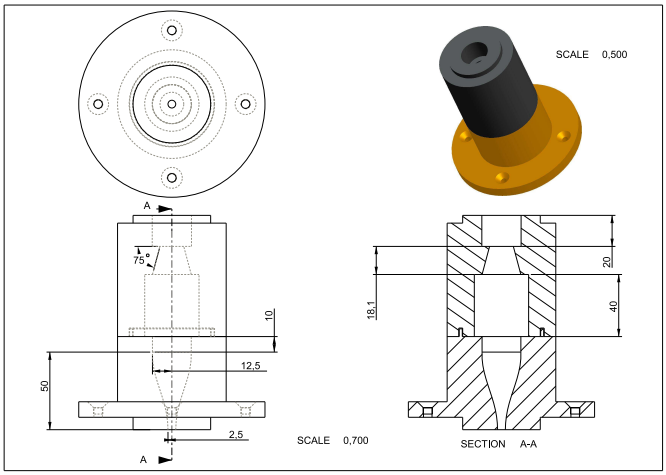

(c) Drawing for 5mm jet

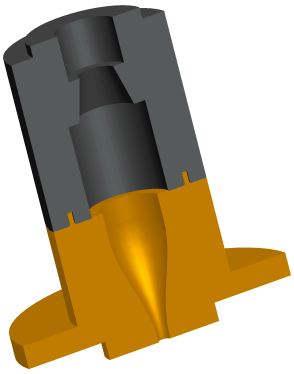

(d) 3D cross-section of 5mm jet

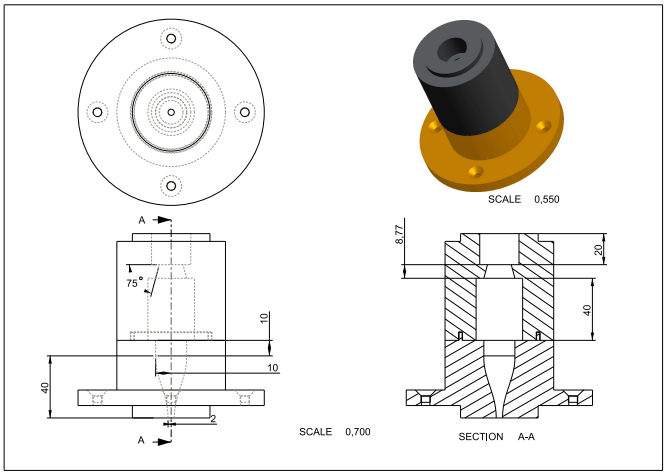

(e) Drawing for 5mm jet

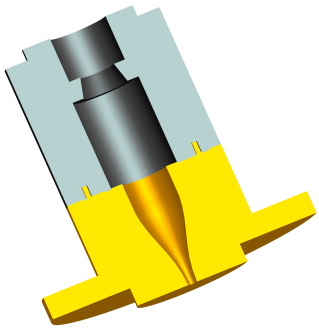

(f) 3D cross-section of 4mm jet

Figure A.2: Drawings of designed nozzles to generate the jet.

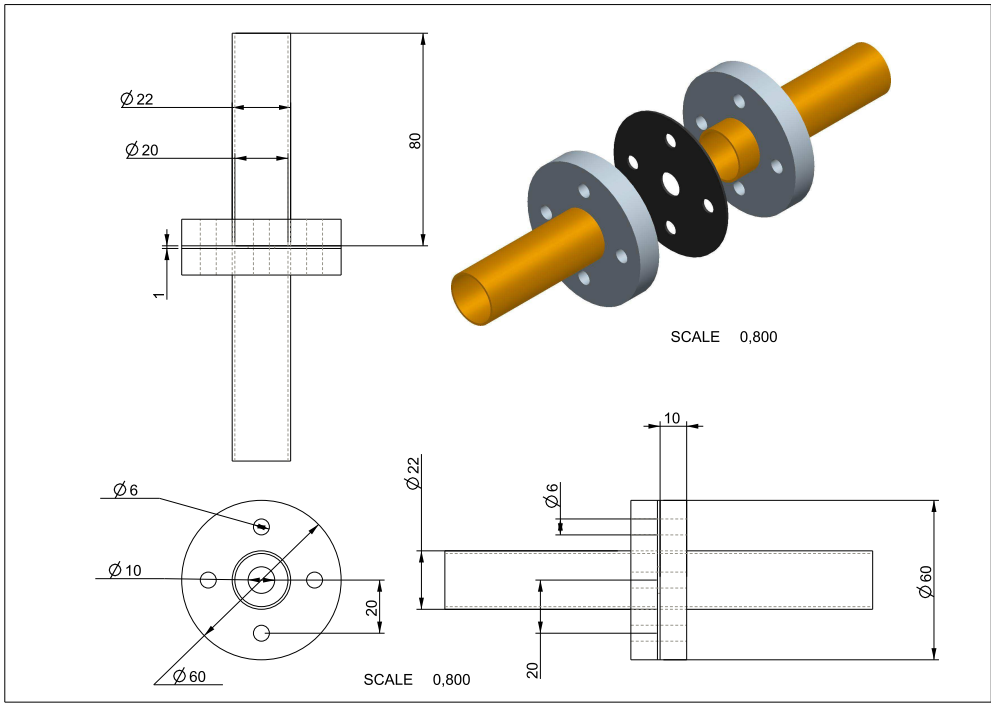

Figure A.3: Drawing of orifice plate used to measure the mass flow rate.

light sheet was captured by the cameras, a delayed pulse is used to trigger the first laser head. The delay is equal to half the exposure time of the camera, firing the laser in the middle of the time duration for which the shutter is open. The pulse for the second head is delayed by an additional time of dt thus generating the required temporal displacement between image pairs. The frequency of the laser trigger signals is the data/vector-field sampling frequency of the measurement performed, $f_s = 1/DT$.

The wiring for the High-Speed Taylor SPIV measurements is the same as for the Multi-Scale SPIV measurements, but has a different triggering set up as shown in figure A.5b. The cameras are again synchronised and upon receiving the single camera record trigger, start recording images at the set frame rate and exposure time until the memory buffer fills up. This results in a time series of 5457 images from each camera. Similar to the Multi-Scale SPIV measurements, a delayed pulse is used to trigger the laser with the difference that, since a high repetition rate laser is used, both laser heads are triggered at the same time at the set camera frame rate. This means that the temporal displacement between image pairs dt, is equal to the data/vector-field sampling time, i.e $f_s = 1/dt$.

The wiring for the Tow Tank measurements is shown in figure A.4b. In this set-up an analogue Thurlby TGP110 pulse generator was used to create the TTL signals. The resulting timing signals are similar to those of the High-Speed Taylor SPIV measurements, with the difference that there is no start up pulse. The cameras are synchronised using the camera exposure signal from the Master camera. A TTL signal from the Compax controller was used to generate the camera record trigger to start recording the time-series of images when the position of the centre of the carriage (i.e the nozzle) was at the measurement location. This meant that the first recording was consistently at x = 0m for all runs. The trigger for the laser was again delayed, with respect to the sync signal, so that the laser would fire in the middle of the time duration for which the camera shutter was open.

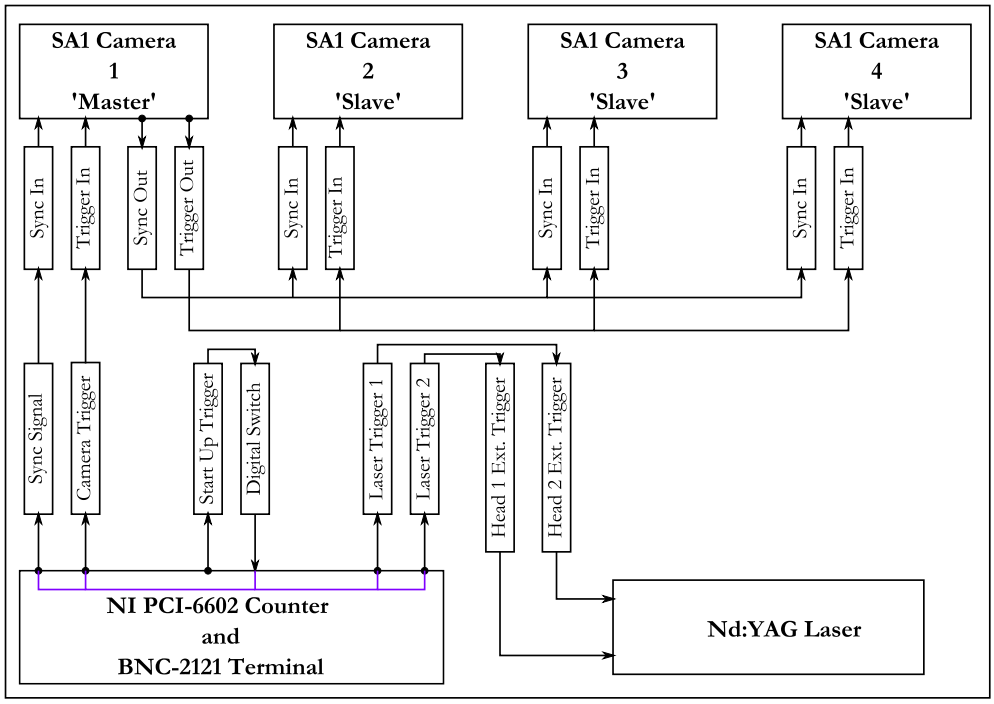

(a) MS-SPIV laser and camera wiring

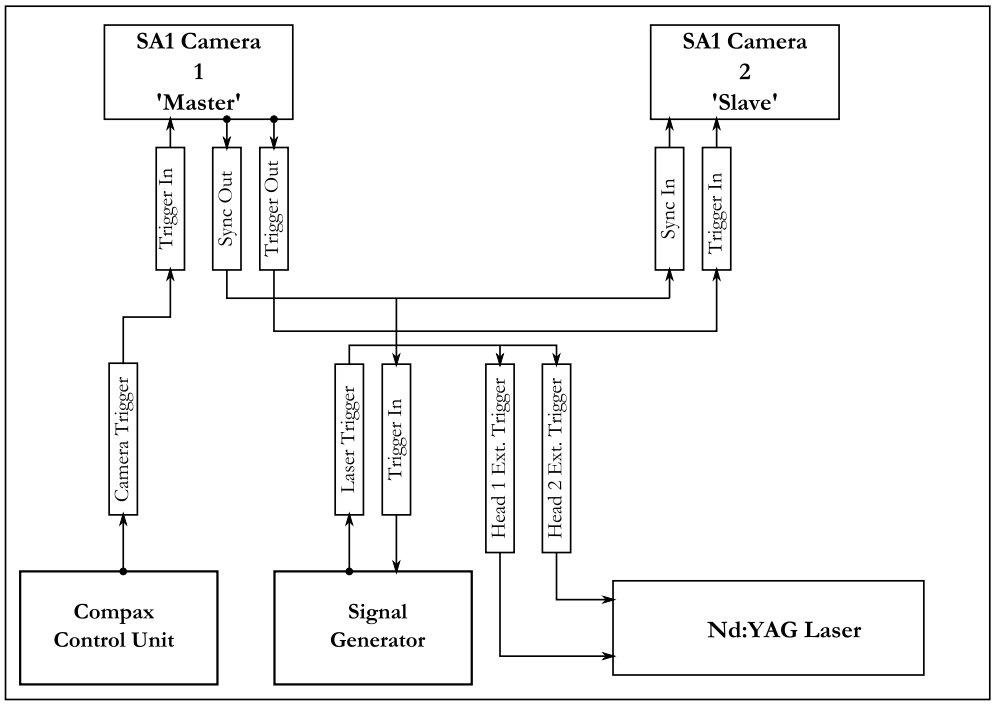

(b) T-SPIV and Tow-Tank SPIV laser and camera wiring

Figure A.4: Wiring diagrams

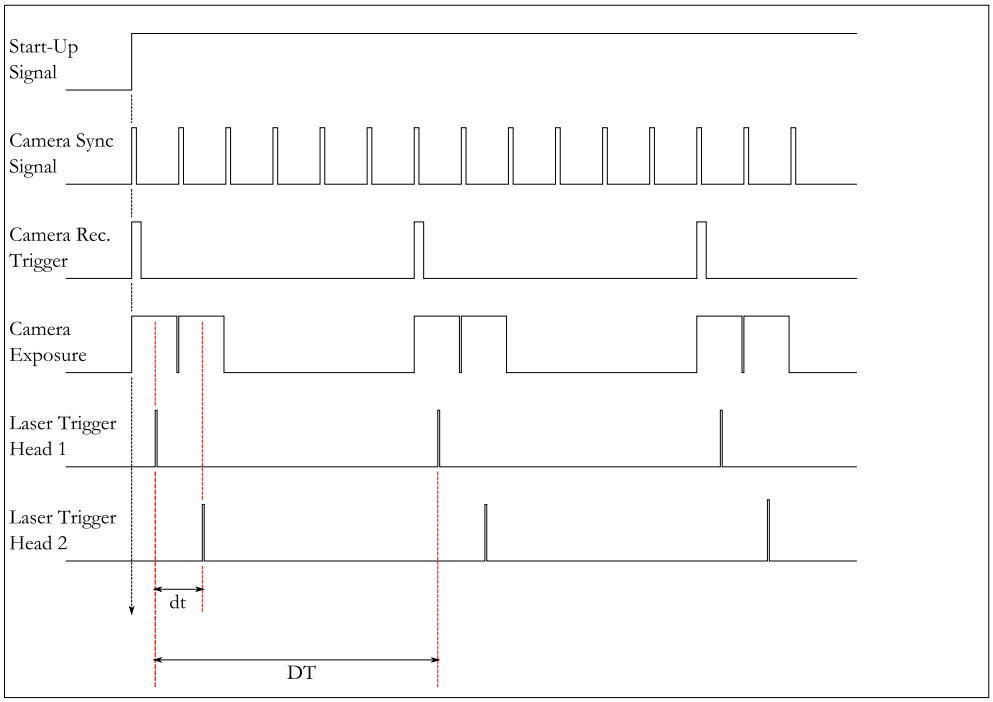

(a) MS-SPIV pulse diagram

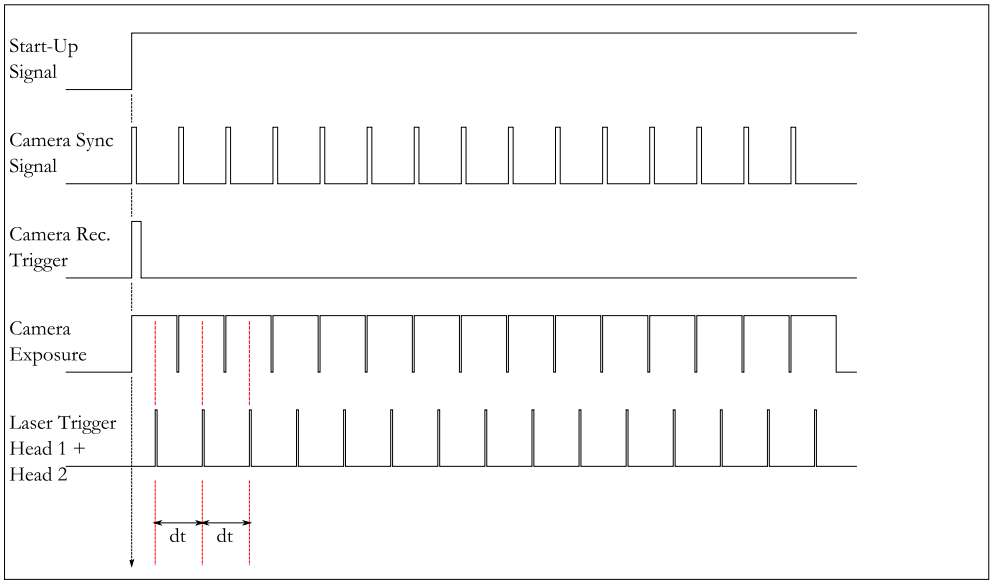

(b) T-SPIV and Tow-Tank SPIV pulse diagram

Figure A.5: Pulse diagrams

Appendix B

Additional Reconstructed Volumes from Towed-Jet SPIV Results

Additional 3D volume reconstructions are presented here showing similar results to those shown in section 4.2

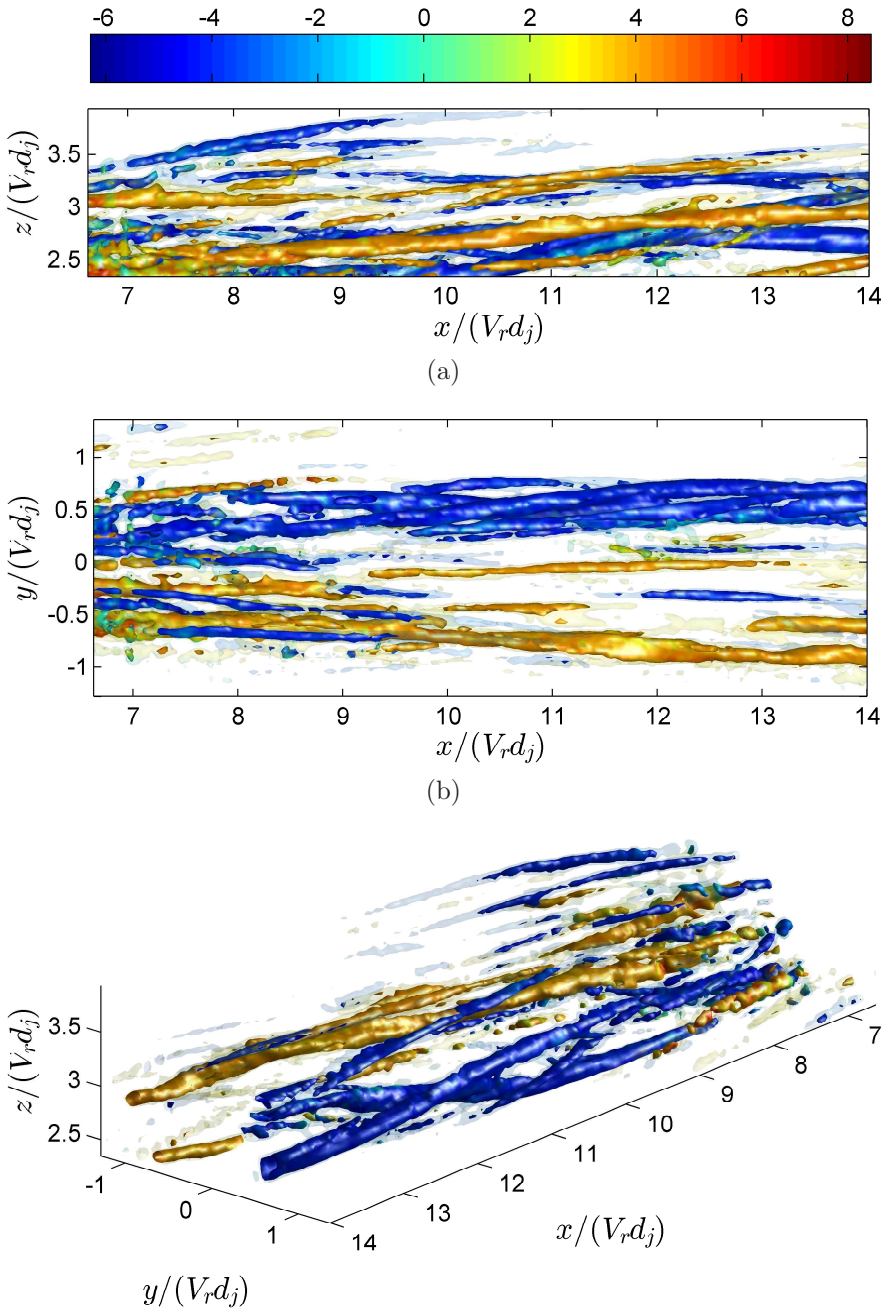

Figure B.1: Iso-contours of $\lambda_{ci,iso} = 0.25\lambda_{ci,max}$ (solid) and $\lambda_{ci,iso} = 0.15\lambda_{ci,max}$ (transparent) for $V_r = 9.1$. Surface is coloured by the local value of $\lambda_{ci,x}(\mathrm{s}^{-1})$. (a) Side view (x-z plane). (b) Top view (x-y plane). (c) 3D view.

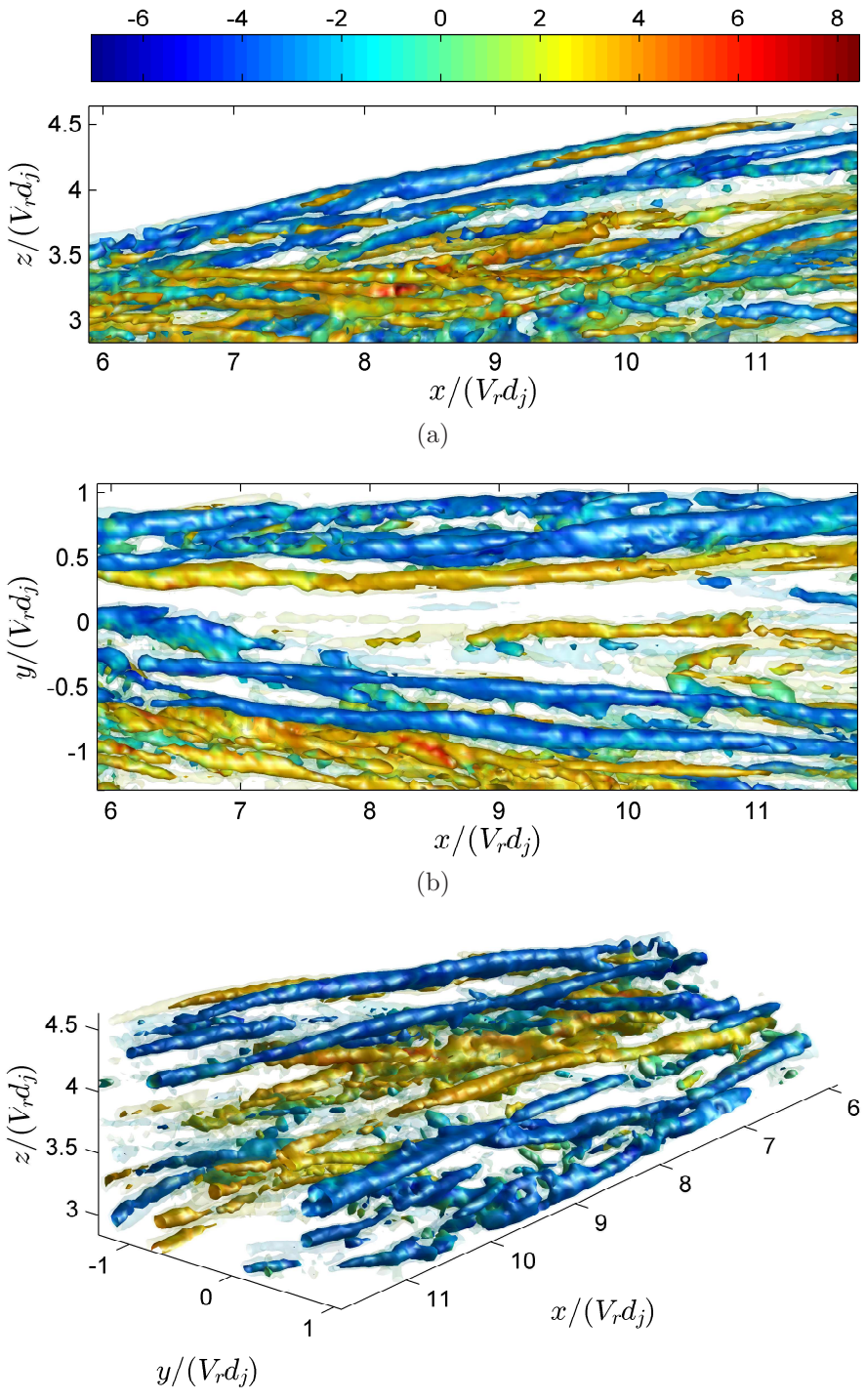

Figure B.2: Iso-contours of $\lambda_{ci,iso} = 0.25\lambda_{ci,max}$ (solid) and $\lambda_{ci,iso} = 0.15\lambda_{ci,max}$ (transparent) for $V_r = 17$. Surface is coloured by the local value of $\lambda_{ci,x}(\mathrm{s}^{-1})$. (a) Side view (x-z plane). (b) Top view (x-y plane). (c) 3D view.

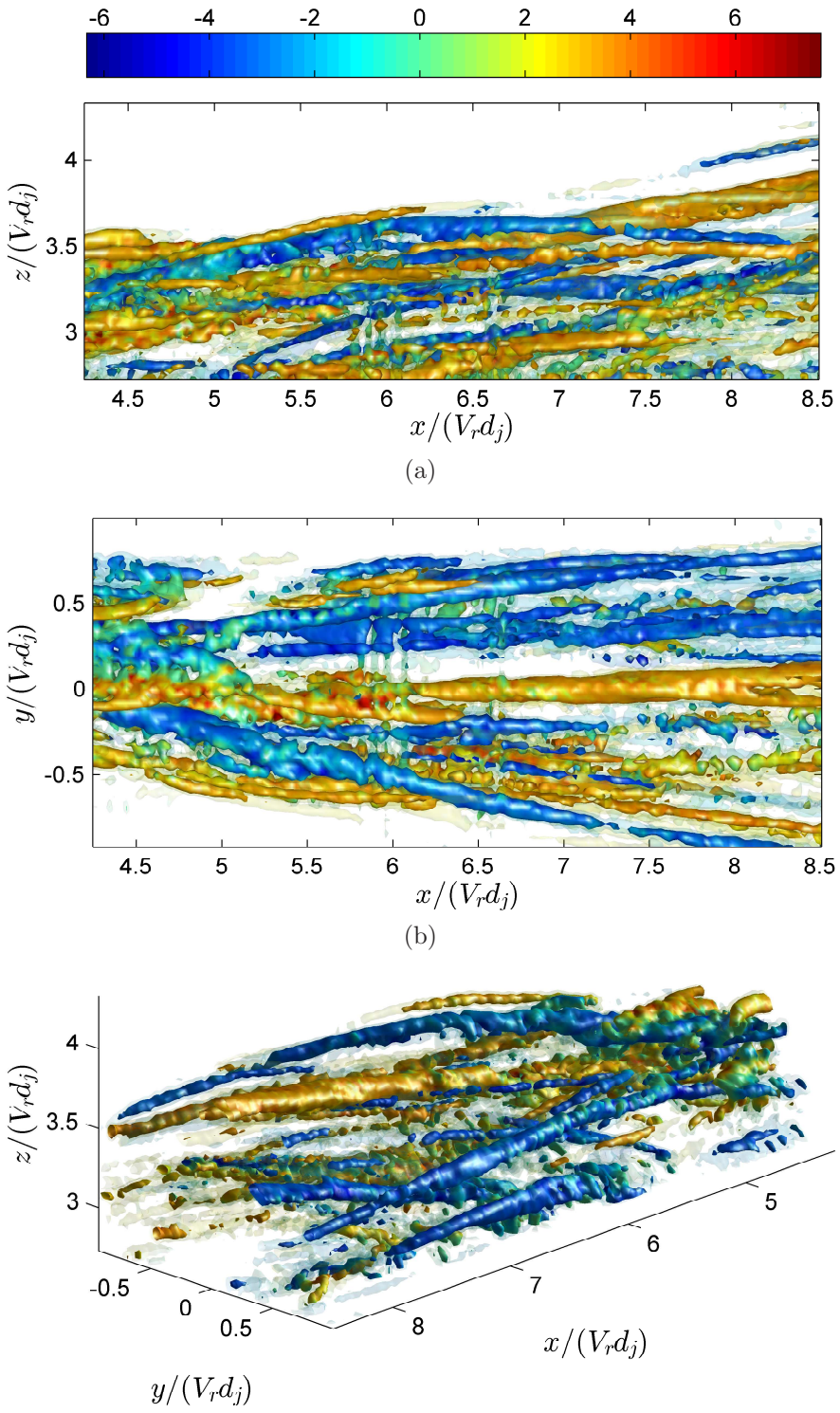

Figure B.3: Iso-contours of $\lambda_{ci,iso} = 0.25\lambda_{ci,max}$ (solid) and $\lambda_{ci,iso} = 0.15\lambda_{ci,max}$ (transparent) for $V_r = 23.5$. Surface is coloured by the local value of $\lambda_{ci,x}(\mathrm{s}^{-1})$. (a) Side view (x-z plane). (b) Top view (x-y plane). (c) 3D view.

References

[1] Adrian, R.J. (2005). Twenty years of particle image velocimetry. *Exp Fluids*, **39**, 159–169. 45

[2] Adrian, R.J., Meinhart, C.D. & Tomkins, C.D. (2000). Vortex organisation in the outer region of turbulent boundary layers. *J. Fluid Mech.*, **422**, 1–54. 3, 170

[3] Alamo, J.C.D. & Jimenez, J. (2009). Estimation of turbulent convection velocities and corrections to Taylor's approximation. *J. Fluid Mech.*, **640**, 5–26. 68

[4] Antonia, R.A. (1981). Conditional sampling in turbulence measurement. *Ann. Rev. Fluid Mech.*, **13**, 131–156. 207

[5] Benedict, L.H. & Gould, R.D. (1996). Towards better uncertainty estimates for turbulence statistics. *Exp Fluids*, **22**, 129–136. 81, 82

[6] Betchov, R. (1956). An inequality concerning the production of vorticity in isotropic turbulence. *J. Fluid Mech.*, **1**, 497–504. 89

[7] Blackwelder, R. (1977). On the role of phase information in conditional sampling. *Phys. Fluids*, **20**, S232–S242. 207

[8] Blevins, R.D. (2001). *Flow Induced Vibration*. Krieger Pub. Co., Malabar, Florida, 2nd edn. 17

[9] Broadwell, J.E. & Breidenthal, R.E. (1984). Structure and mixing of a transverse jet in incompressible flow. *J. Fluid Mech.*, **148**, 405–412. 1, 2, 4, 21, 22, 25, 30, 77, 92, 96, 112, 229, 230

[10] Buxton, O.R.H. (2011). *Fine Scale Features of Turbulent Shear Flows*. Ph.D. thesis, Imperial College London, Department of Aeronautics, Prince Consort Road, London. 57

[11] Buxton, O.R.H., Laizet, S. & Ganapathisubramani, B. (2011). The effects of resolution and noise on kinematic features of fine-scale turbulence. *Exp Fluids*, **52**, 1417–1437. 88

[12] Cardesa, J.I., Mistry, D., Gan, L. & Dawson, J.R. (2013). Invariants of the reduced velocity gradient tensor in turbulent flows. *J. Fluid Mech.*, **716**, 597–615. 89, 90

[13] Chong, M.S., Perry, A.E. & Cantwell, B.J. (1990). A general classification of three-dimensional flow fields. *Phys. Fluids.*, **2**, 765–777. 74

[14] Coelho, S.L.V. & Hunt, J.C.R. (1989). The dynamics of the near field of strong jets in crossflows. *J. Fluid Mech.*, **200**, 95–120. 11, 161

[15] Cortelezzi, L. & Karagozian, A.R. (2001). On the formation of the counter-rotating vortex pair in transverse jets. *J. Fluid Mech.*, **446**, 347–373. ix, 12, 13, 14, 161, 167

[16] Davidson, P.A. (2004). *Turbulence: An Introduction for Scientists and Engineers*. Oxford University Press, Oxford. 8

[17] Dennis, D.J.C. & Nickels, T.B. (2008). On the limitations of Taylor's hypothesis in constructing long structures in a turbulent boundary layer. *J. Fluid Mech.*, **614**, 197–206. 68, 134

[18] Dennis, D.J.C. & Nickels, T.B. (2011). Experimental measurement of large-scale three-dimensional structures in a turbulent boundary layer. Part 1. Vortex Packets. *J. Fluid Mech.*, **673**, 180–217. 3, 47, 58, 75, 170, 207, 208

[19] Eiff, O.S. & Keffer, J.F. (1997). On the structures in the near-wake region of an elevated turbulent jet in a crossflow. *J. Fluid. Mech.*, **333**, 161–195. 129, 161, 172

[20] Elsinga, G.E., Adrian, R.J., Oudheusden, B.W.V. & Scarano, F. (2010). Three dimensional vortex organisation in a high-Reynolds-number supersonic turbulent boundary layer. *J. Fluid Mech.*, **644**, 35–60. 3, 170

[21] Elsinga, G.E., Poelma, C., Schroder, A., Geisler, R., Scarano, F. & Westerweel, J. (2012). Tracking of vortices in a turbulent boundary layer. *J. Fluid Mech.*, **697**, 273–295. 68

[22] Fearn, R. & Weston, R.P. (1974). Vorticity associated with a jet in a cross flow. *AIAA J.*, **12**, 1666–1671. 2, 19, 123, 182

[23] Fric, T.F. & Roshko, A. (1994). Vortical structure in the wake of a transverse jet. *J. Fluid Mech.*, **48**, 73–74. ix, 17, 18, 32, 35, 172

[24] Ganapathisubramani, B., Lakshminarasimhan, K. & Clemens, N.T. (2008). Investigation of three-dimensional structures of fine scales in a turbulent jet by using cinematographic stereoscopic particle image velocimetry. *J. Fluid Mech.*, **598**, 141–175. 58, 60, 68, 155, 157, 158, 159

[25] Goldschmidt, V.W. & Young, M.F. (1981). Turbulent convective velocities (broadband and wavenumber dependent) in a plane jet. *J. Fluid Mech.*, **105**, 327–345. 68

[26] Hasselbrink, E.F. & Mungal, M.G. (2001). Transverse jets and jet flames. Part 1. Scaling laws for strong transverse jets. *J. Fluid Mech.*, **433**, 1–25. 25, 26, 30, 32, 92

[27] Hasselbrink, E.F. & Mungal, M.G. (2001). Transverse jets and jet flames. Part 2. Velocity and OH field imaging. *J. Fluid Mech.*, **433**, 27–68. 35, 76, 77, 81

[28] Hayakawa, M. (1994). Vorticity-based eduction of large-scale structures in turbulent shear flows. *Appl. Scie. Res.*, **53**, 203–225. 207

[29] Hussain, A.K.M.F. (1986). Coherent structures and turbulence. *J. Fluid Mech.*, **173**, 303–356. 152

[30] Hutchins, N., Hambleton, W.T. & Marusic, I. (2005). Inclined cross-stream stereo particle image velocimetry measurements in turbulent boundary layers. *J. Fluid Mech.*, **541**, 21–54. 3, 170

[31] Johnson, B.E., Elliot, G.S. & Christensen, K.T. (2013). Structural characteristics of a heated jet in a cross-flow emanating from a raised, circular stack. *Exp Fluids*, **54**, 1–17. 23, 75, 123, 182

[32] Karagozian, A.R. (2010). Transverse jets and their control. *Progress in Energy and Combustion Science*, 1–23, doi:10.1016/j.pecs.2010.01.001. ix, 1, 2, 123

[33] Kelso, R.M., Lim, T.T. & Perry, A.E. (1996). An experimental study of round jets in cross-flow. *J. Fluid Mech.*, **306**, 111–144. ix, 2, 11, 12, 18, 35, 161, 172

[34] Kuzo, M.D. (1995). *An Experimental study of the Turbulent Transverse Jet*. Ph.D. thesis, California Institute of Technology, Pa, California. ix, x, 20, 21, 22, 23, 33, 35, 182

[35] Kuzo, M.D. & Roshko, A. (1984). Observations on the wake region of the transverse jet. *Bull. Am. Phys. Soc.*, **29**, 1536. 18

[36] LaVision (2007). *Product-Manual:Flow Master for Davis 7.2*. LaVision GmbH, Gottingen, Germany. 45, 63

[37] Lim, T.T., New, T.H. & Luo, S.C. (2001). On the development of large-scale structures of a jet normal to a cross flow. *Phys. Fluids*, **13**, 770–775. ix, 2, 13, 14, 123, 161, 167

[38] Margason, R.J. (1993). Fifty years of jet in cross flow research. *AGARD Meeting on Computational and Experimental Assessment of Jets in Cross Flow*, 1–141. 1, 123

[39] Matsuda, T. & Sakakibara, J. (2005). On the vortical structure in a round jet. *Phys Fluids*, **17**, 1–11. 47, 58, 68, 69

[40] McMahon, M.H., Hester, D.D. & Palfrey, G.J. (1971). Vortex shedding from a turbulent jet in a cross-wind. *J. Fluid Mech.*, **48**, 73–80. 15

[41] Moin, P. (2009). Revisiting Taylor's hypothesis. *J. Fluid Mech.*, **640**, 1–4. 68

[42] Moussa, Z.M., Trischka, J.W. & Eskinazi, S. (1987). The near field in the mixing of a round jet with a cross stream. *J. Fluid Mech.*, **80**, 125–155. 11, 15, 19

[43] Mullin, J.A. & Dahm, W.J.A. (2006). Dual-plane stereo particle image velocimetry measurements of velocity gradient tensor fields in turbulent shear flow. I. Accuracy assessment. *Phys Fluids*, **18**, 1–18. 158, 159

[44] New, T.H., Lim, T.T. & Luo, S.C. (2006). Effects of jet velocity profiles on a round jet in cross flow. *Exp Fluids*, **40**, 859–875. 2, 15, 35

[45] Nickels, T.B. & Perry, A.E. (1996). An experimental and theoretical study of the turbulent coflowing jet. *J. Fluid Mech.*, **309**, 157–182. 235

[46] Perry, A.E. & Chong, M.S. (1982). On the mechanism of wall turbulence. *J. Fluid Mech.*, **119**, 173–217. 170, 235

[47] Perry, A.E. & Chong, M.S. (1987). A description of eddying motions and flow pattern using critical-point concepts. *Ann. Rev. Fluid Mech.*, **19**, 125–155. 74, 89

[48] Perry, A.E. & Marusic, I. (1995). A wall-wake model for the turbulence structure of boundary layers. Part 1. Extension of the attached eddy hypothesis. *J. Fluid Mech.*, **298**, 361–388. 170, 235

[49] Perry, A.E., Henbest, S. & Chong, M.S. (1986). A theoretical and experimental study of wall turbulence. *J. Fluid Mech.*, **165**, 163–199. 170, 235

[50] Phillip, J., Meneveau, C., de Silva, C.M. & Marusic, I. (2014). Multiscale analysis of fluxes at the turbulent/non-turbulent interface in high Reynolds number boundary layers. *Phys. Fluids.*, **26**, 015105. 57

[51] Pope, S.B. (2000). *Turbulent Flows*. Cambridge University Press, Cambridge. 6, 8

[52] Prasad, A.K. (2000). Stereoscopic particle image velocimetry. *Exp Fluids*, **29**, 103–116. 47

[53] Pratte, D.B. & Baines, M. (1967). Profiles of the round turbulent jet in a cross flow. *J. Hydronaut. Div. ASCE*, **92**, 53–64. 25, 91, 109, 202, 229

[54] Raffel, M., Willert, C., Wereley, S. & Kompenhans, J. (2007). *Particle Image Velocimetry: A Practical Guide*. Springer, New York. x, 45, 46, 48, 54, 61, 62, 65

[55] Rivero, A., Ferre, J.A. & Giralt, F. (2001). Organised motions in a jet in crossflow. *J. Fluid. Mech.*, **444**, 117–149. x, 23, 24, 35, 129, 172

[56] Schlegel, F., Wee, D., Marzouk, Y.M. & Ghoniem, A.F. (2011). Contributions of the wall boundary layer to the formation of the counter-rotating vortex pair in transverse jets. *J. Fluid Mech.*, **676**, 461–490. ix, 14, 16, 161, 167

[57] Shan, J.W. & Dimotakis, P.E. (2006). Reynolds-number effects and anisotropy in transverse-jet mixing. *J. Fluid Mech.*, **566**, 47–96. x, 1, 3, 28, 29, 30, 31, 35, 76, 77, 234

[58] Smith, S.H. & Mungal, M.G. (1998). Mixing, structure and scaling of the jet in crossflow. *J. Fluid Mech.*, **357**, 83–122. ix, x, 1, 3, 9, 18, 19, 26, 27, 28, 32, 35, 44, 76, 77, 92, 113, 123, 129, 147, 161, 172, 182, 187, 213

[59] Su, L. & Mungal, M.G. (2004). Simultaneous measurements of scalar and velocity field evolution in turbulent crossflowing jets. *J. Fluid Mech.*, **513**, 1–45. 3, 27, 28, 35, 76, 77

[60] Taylor, G.I. (1938). The spectrum of turbulence. *Proc. R. Soc. Lond.*, **164**, 476–490. 65

[61] Tennekes, H. & Lumley, J.L. (1972). *A First Course in Turbulence*. MIT Press, Cambridge, Massachusetts. 9, 49, 76

[62] Tomkins, C.D. & Adrian, R.J. (2003). Spanwise structure and scale growth in turbulent boundary layers. *J. Fluid Mech.*, **490**, 37–74. 170

[63] Townsend, A.A. (1976). *The Structure of Turbulent Shear Flow*. Cambridge University Press, Cambridge. 170, 235

[64] Tsinober, A., Kit, E. & Dracos, T. (1992). Experimental investigation of the field of velocity gradients in turbulent flows. *J. Fluid Mech.*, **242**, 169–192. 155

[65] van Doorne, C.W.H. & Westerweel, J. (2007). Measurement of laminar, transitional and turbulent pipe flow using Stereoscopic-PIV. *Exp Fluids*, **42**, 259–279. 47, 54, 58, 69

[66] Willert, C. (1997). Stereoscopic digital particle image velocimetry for applications in wind tunnel flows. *Meas. Sci. Technol.*, **8**, 1465–1479. x, 46, 47

[67] Wu, Z.J. & Wu, M.J. (1993). Interaction between a solid surface and a viscous compressible flow field. *J. Fluid Mech.*, **254**, 183–211. 18

[68] Zhang, J., Tao, B. & Katz, J. (1997). Turbulent flow measurement in a square duct with hybrid holographic PIV. *Exp Fluids*, **23**, 373–381. 155, 157, 158

[69] Zhou, J., Adrian, R.J., Balachandar, S. & Kendall, T.M. (1999). Mechanisms for generating coherent packets of hairpin vortices in channel flows. *J. Fluid Mech.*, **387**, 353–396. 75, 170